



Present-day fluid-rock interaction in a sedimentary basin: study case of the Granada Basin (Betic Cordillera, Spain)

Claire Lix

► To cite this version:

Claire Lix. Present-day fluid-rock interaction in a sedimentary basin: study case of the Granada Basin (Betic Cordillera, Spain). Earth Sciences. Sorbonne Université, 2019. English. NNT: 2019SORUS200 . tel-03171492

HAL Id: tel-03171492

<https://theses.hal.science/tel-03171492>

Submitted on 17 Mar 2021

HAL is a multi-disciplinary open access archive for the deposit and dissemination of scientific research documents, whether they are published or not. The documents may come from teaching and research institutions in France or abroad, or from public or private research centers.

L'archive ouverte pluridisciplinaire **HAL**, est destinée au dépôt et à la diffusion de documents scientifiques de niveau recherche, publiés ou non, émanant des établissements d'enseignement et de recherche français ou étrangers, des laboratoires publics ou privés.



Sorbonne Université

Géosciences, Ressources Naturelles et Environnement - ED 398

Institut des Sciences de la Terre de Paris (ISTeP)

UMR 7193, CNRS-Sorbonne Université, 4 Place Jussieu, 75252 Paris CEDEX 05

Present-day fluid-rock interaction in a sedimentary basin: Study case of the Granada Basin (Betic Cordillera, Spain)

Par **Claire LIX**

Thèse de doctorat de Sorbonne Université

Dirigée par Pierpaolo Zuddas

Xavier Guichet (Promoteur de thèse)

Présentée et soutenue publiquement le 15/03/2019

Devant un jury composé de :

Philippe SARDA	Professeur	Université Paris Sud	Rapporteur
Mohamed AZAROUAL	Directeur adjoint ISTO - HDR	Université d'Orléans	Rapporteur
Maryse ROUELLE	Maitre de conférences - HDR	Sorbonne Université	Examinateur
José BENAVENTE	Professeur	Université de Grenade	Examinateur
Pierpaolo ZUDDAS	Professeur	Sorbonne Université	Directeur de thèse
Xavier GUICHET	Ingénieur de recherche - Dr.	IFPEN	Promoteur de thèse
Mickaël BARBIER	Expert - Dr.		Invité

« Au milieu de l'hiver, j'apprenais enfin qu'il y avait en moi un été invincible. »

Albert Camus, L'Été (1954)

REMERCIEMENTS

Ces trois années de thèse arrivent à leur fin et je souhaiterais remercier les nombreuses personnes qui m'ont aidée, de près ou de loin, dans ce projet.

Tout d'abord, je voudrais remercier Mohamed Azaroual et Philippe Sarda de me faire l'honneur d'être rapporteurs de ma thèse, ainsi que Maryse Rouelle et José Benavente d'avoir accepté d'être examinateurs dans mon jury de thèse.

Je suis très reconnaissante envers l'IFP Energies Nouvelles d'avoir financé cette thèse et de m'avoir permis d'explorer ce sujet avec une grande liberté. Je tiens notamment à remercier la Direction Géosciences qui m'a fait confiance en acceptant ma candidature sur ce sujet de thèse.

Un grand merci à mon directeur de thèse, Pierpaolo Zuddas, et mes encadrants, Xavier Guichet et Mickaël Barbier, de m'avoir également fait confiance pour ce projet et de m'avoir soutenue tout au long de ces trois années. Merci Pierpaolo d'avoir accepté de diriger cette thèse. Vous m'avez beaucoup appris en géochimie et en matière de rigueur scientifique. Je vous remercie de m'avoir donné l'opportunité d'aller à l'INGV à Palerme. Xavier, merci pour ton aide et les nombreuses discussions sur tous les aspects de ma thèse, aussi bien sur la géologie que la géochimie ou la programmation. Ton enthousiasme pour ce projet, et la région andalouse dans son ensemble, était communicatif et m'a motivée à toujours aller plus loin. Et enfin, merci Mickaël d'avoir initié ce projet et de m'avoir soutenue tout au long, malgré le fait qu'il n'ait pas forcément pris le chemin escompté au départ. Je te remercie de m'avoir guidée dans la compréhension de la géologie régionale et d'avoir toujours été à l'écoute.

J'ai un merci tout particulier pour José Benavente, qui a accepté de prendre part à ce projet sur la géochimie des eaux profondes alors que son expertise est plutôt sur la ressource en eau. Merci de m'avoir transmis ta connaissance de l'hydrologie régionale et de l'histoire liée à Grenade. Je souhaite également remercier le département de Géodynamique de l'Université de Grenade, qui m'a permis de séjourner et travailler là-bas pendant un mois. Un grand merci à Juan Antonio Luqué et Virginia de l'IGME pour votre aide sur le terrain, que ce soit pour la prise de contact avec les propriétaires de puits ou pour l'échantillonnage en lui-même.

Merci à Claudio et Salvatore Inguaggiato de m'avoir accueillie à l'INGV à Palerme (Sicile) pour découvrir et comprendre les techniques analytiques des gaz rares. Merci à Claudio pour les nombreuses discussions sur la géochimie des gaz par la suite.

Je tiens à remercier les personnes des laboratoires de l'ISTeP et de METIS qui m'ont aidée au cours des analyses ou de la préparation de la mission de terrain. Je pense notamment à

Nathalie Labourdette pour son aide précieuse lors de la recherche de protocoles analytiques, pour sa parfaite gestion du matériel (très appréciable avant de partir sur le terrain !), et son oreille toujours attentive. Un grand merci à Emmanuel Aubry pour son aide pour les analyses à l'ICP-OES et en chromatographie ionique. Merci également à Alain Person de m'avoir fait (re)découvrir les analyses DRX. Je tiens également à remercier toutes les personnes de l'IFPEN, Pierre Bachaud, Virgile Rouchon, Daniel Pillot, Anne Batani, Christine Souque pour leur aide à différents moments de la thèse. Merci à Jamila pour son soutien et sa générosité.

Merci à l'ISTeP de m'avoir accueillie, à temps partiel, dans les locaux. Merci à Damien Do Couto, Laurent Jolivet et Laetitia Le Pourhiet pour les discussions sur les Bétiques ou sur ma thèse. Merci également à Dovy Tristani et Véronique Nantet pour toute l'aide administrative et logistique. Merci à la bande de thésards de l'ISTeP et de l'ED: Marianne, Lorella, Ella, Tiphaine, Lauriane, Juliana, Manfred, Guillaume, Maximilien, Lucie. Un merci tout particulier à mes co-bureaux, qui m'ont supportée et épaulée dans les montagnes russes émotionnelles de la thèse. Merci à vous Saliha, Maxime, Camille et Vincent !

Merci au groupe de thésards et anciens thésards de l'IFPEN pour les repas animés le midi, les pauses café et les événements Adifp : Pauline, Hamza, Aurélien, Anabel, Jean, Julie, Estelle, Marion, Arianne, Mona, Julia, Isabelle, Vincent, Arthur, Chakib, Dandan, Adriana, Cédric, Christopher, Marianne, Nicolas, Malik, Imane, Zaineb, Anouk, et j'en oublie... Un merci tout particulier à vous, Virginie, Richard, Sophie et Juliette, mes collègues et amis du bureau T-103.

Merci également à Antoine et Baudoin pour votre aide précieuse en Python et les nombreuses discussions sur ma thèse (et sur la société). Merci à mes (nombreux) amis jurassiens : Marie, Florine, Fiona, Yoann, Arnaud, Léa, Guillaume, Louise, Clément, Charles, Fur, pour votre présence physique ou téléphonique, votre soutien à toute épreuve et votre amour partagé pour le Jura ! Merci à toi, Geneviève... Thank you for your support despite the distance and the 8h time difference. I won't forget the long Skype conversations, it helped a lot! Merci à toi aussi, Paul, d'avoir rendu ces derniers mois de thèse plus faciles à vivre.

Enfin, un immense merci à mes parents et mes frères pour leur soutien inconditionnel, si précieux tout au long de ces années.

ABSTRACT

Understanding fluid circulations in sedimentary basins plays a critical role in the diverse fields of energy and natural resources: water resource management, petroleum production, development of geothermal resources, and CO₂ geological sequestration. However assessing and constraining groundwater circulation in sedimentary basins remain a challenge because of, among other factors, the different water origins and the multi-scale heterogeneity of the system. In this thesis, a geochemical approach is developed to characterize the present-day groundwater geochemistry and to investigate the reactions affecting a sedimentary system, taking the Granada Basin (southern Spain) as a regional study case. This combined study, including noble gas geochemistry, geothermal investigation and water geochemistry, is carried out to try to understand the flow paths in this Neogene intramountainous basin within the complex tectonic structure of the Betic Cordillera.

Helium isotopic composition of bubbling and dissolved gases has been investigated to set constraints on the lithospheric structure of the area. We found that the He isotopic composition has a dominant radiogenic component with a mantle-derived He contribution reaching mainly 1 %. The evaluation of helium transport mechanisms within the crust shows that the crustal system of the Betic Cordillera is currently dissociated from the mantle system. We therefore propose that the observed mantle-derived He could result from fossil mantle contribution associated to crustal production from Li-rich rocks.

Water-rock interactions in the Central Betic Cordillera have been investigated by characterizing the low- to medium-enthalpy thermal systems. This study, combining geothermometrical methods, shows a strong relationship between the temperature and the partial pressure of CO₂ (pCO₂) in the reservoir. The increasing buffering effect of aluminosilicates (in addition to carbonates and quartz) links to the reservoir temperature and pCO₂, highlighting the role of the potential mineral buffers of both the sedimentary infilling and the basement on the reactivity of CO₂. Further investigations on the reactivity within the Granada Basin allow us to give insights on the groundwater circulations at the scale of the whole basin. We show that the groundwaters evolve from carbonate-dominated waters in the basin borders to sulfate and chlorine-dominated waters within the basin. The evolution of the groundwater saturation with respect to carbonate, aluminosilicate, and sulfate minerals (barite, celestite, and gypsum) allows to assess the possible flow paths in the basin and to apprehend a conceptual reactive transport model.

Keywords: aqueous geochemistry, geochemical modeling, fluid-rock interaction, He isotopic composition, geothermal system, Betic Cordillera

RESUME ETENDU (FRANÇAIS)

Comprendre la circulation des fluides (eau et gaz) dans les bassins sédimentaires, tant du point de vue de la réaction que du transport, est crucial dans les divers domaines des ressources énergétiques : gestion des ressources en eau, production de pétrole, géothermie et séquestration géologique du CO₂. Toutefois, évaluer et contraindre les circulations des eaux souterraines dans les bassins sédimentaires restent un défi en raison, entre autres, des différences d'origine des eaux et de l'hétérogénéité multi-échelles du système.

L'objectif principal de mon projet de thèse est de suivre la circulation et la réactivité des fluides dans le bassin de Grenade, et plus globalement dans la Cordillère Bétique Centrale, en utilisant la géochimie des fluides inorganiques.

Structure de la Cordillère Bétique Centrale

La Cordillère Bétique Centrale se caractérise par la présence de nombreuses sources thermales, avec une concentration plus importante dans le bassin de Grenade. Des travaux géophysiques récents indiquent un possible retrait du panneau plongeant avec délamination, susceptible de favoriser des remontées de matériel mantellique à faible profondeur (<50 km) sous la zone étudiée. Selon les interprétations géophysiques, la Cordillère Bétique Centrale est également une zone de transition entre une lithosphère épaisse dans le domaine Ibérique et une lithosphère amincie dans le domaine Alboran. Ces hypothèses structurales nous ont amené à s'interroger sur l'influence possible du manteau sur les sources thermales observées dans la zone étudiée. Pour tester cette question, j'ai analysé la composition isotopique de l'hélium et du néon dans les gaz dissous et les bulles dans les sources thermales de la Cordillère Bétique Centrale.

Le gaz noble le plus léger, l'hélium, est chimiquement inerte et caractérisé par un fractionnement isotopique négligeable lors des processus d'interaction gaz-eau. Ces propriétés en font un très bon traceur de l'origine des fluides, à la fois libres et dissous. Il est possible de distinguer les trois sources d'hélium par leur signature isotopique : l'atmosphère terrestre; la croûte avec une production radiogénique par désintégration de l'uranium et du thorium; et le manteau contenant une signature primordiale.

De nombreuses données issues de précédentes études sur les gaz rares ont été collectés dans la région alpine européenne, notamment dans les Alpes, les Apennins et le bassin Pannonien montrant le contrôle tectonique de la distribution des isotopes des gaz rares et en particulier des isotopes de l'hélium. Cependant, très peu de données sur les gaz rares sont disponibles dans la Cordillère Bétique, avec seulement deux échantillons de gaz ayant été prélevés dans les

provinces de Grenade et d'Almeria.

Dans cette étude, nous avons montré que la composition isotopique de l'hélium avait une composante radiogénique dominante dans la Cordillère Bétique Centrale avec des rapports $^3\text{He}/^4\text{He}$ allant de 0,06 à 0,44 R_A pour les gaz dissous et entre 0,11 et 1,03 R_A dans des gaz libres. La contribution d'hélium provenant du manteau est globalement estimée à 1,4% pour la zone étudiée. Un seul échantillon, Capuchina de Lanjaron, situé sur l'important contact régional entre les complexes Alpujárride et Nevado-Filábride présente un rapport isotopique de l'He qui pourrait indiquer une contribution conséquente du manteau ($18 \pm 13\%$), malgré la forte proportion d'air.

Pour expliquer ces résultats, j'ai tout d'abord évalué les mécanismes potentiels de transport d'hélium à partir du manteau jusqu'à la surface. Dans un premier temps, j'ai estimé la diffusion d'hélium à travers la croûte ductile et montré que ce processus semblait trop lent pour expliquer la faible contribution d'hélium provenant du manteau mesurée à la surface. Ces résultats indiquent que le système de la croûte terrestre de la Cordillère Bétique semble actuellement dissocié du système du manteau. En considérant un transport advectif et en ré-analysant les données disponibles sur les complexes métamorphiques de la croûte terrestre, j'ai montré que la vitesse advective estimée était du même ordre de grandeur que les taux d'exhumation des complexes métamorphiques. J'ai alors proposé que l'incorporation de matériel asthénosphérique aurait pu entraîner un enrichissement relatif en ^3He lors de l'exhumation des complexes métamorphiques de la Cordillère Bétique. Cette hypothèse est confortée par la présence de xénolites dans la région. Cependant, une autre source possible ^3He pourrait être la production crustale de roches riches en Li. Les calculs de bilan massique tenant compte à la fois de la concentration en ^3He dérivée du manteau et celle dérivée de la production crustale ne permettent pas d'exclure une des deux sources. J'ai donc conclu que le léger excès de ^3He observé dans les fluides actuels pourrait résulter d'une signature fossile de manteau diluée par la production radiogénique locale au fil du temps.

Température et réactivité du CO_2 dans les eaux thermales de la Cordillère Bétique Centrale

Les régions du bassin de Grenade et de la Sierra Nevada ont le potentiel géothermique le plus élevé en Andalousie, avec de nombreuses sources thermales aux températures d'émergence comprises entre 20 et 50°C. Ces eaux thermales sont également principalement localisées aux niveaux d'accidents tectoniques majeurs structurant la région, comme la faille Cadix-Alicante ou le corridor de la faille NO-SE dans le bassin de Grenade. C'est une caractéristique intéressante dans cette région où les systèmes géothermiques sont contrôlés par fracture (c'est-

à-dire non magmatiques). Bien que très peu de données fiables soient disponibles dans cette région, aucun gradient géothermique ni flux de chaleur élevés n'a été reporté. De plus, ces sources thermales évoluent dans un environnement sédimentaire où les processus résultant de l'interaction entre l'eau, la roche et le CO₂ sont complexes. Par exemple, beaucoup d'interrogations existent encore sur la relation entre la pression partielle de CO₂ et la température en environnement sédimentaire, ainsi que les paramètres de contrôle du dégazage ou de la minéralisation du CO₂ dans cet environnement.

L'objectif est ici de caractériser la géochimie des réservoirs des eaux thermales de la Cordillère Bétique Centrale et le rôle du CO₂ dans ces systèmes thermiques de faible à moyenne enthalpie faible. Pour ce faire, j'ai d'abord caractérisé l'hydrochimie des eaux thermales dans les conditions de sortie en utilisant des calculs directs d'équilibre thermodynamique. Les températures dans le réservoir ont ensuite été estimées à l'aide de géothermomètres chimiques. Une modélisation hydrogéochimique a finalement été réalisée en système ouvert et fermé pour évaluer la composition chimique dans les conditions du réservoir et le long de la remontée de l'eau. Deux types d'assemblages de minéraux tampons ont été examinés: l'un avec seulement des carbonates et l'autre avec des carbonates et des aluminosilicates.

Ces résultats montrent que trois principaux groupes d'eaux peuvent être mis en évidence dans la Cordillère Bétique Centrale en fonction des caractéristiques géologiques, de la température, de l'assemblage de minéraux tampons et de la pCO₂ dans leur réservoir. Le premier groupe, correspondant aux eaux thermales situées dans les bassins sédimentaires, présente des températures allant de 70 à 90°C et une pCO₂ comprises entre 10⁻² et 10⁻¹ atm environ dans le réservoir. La chimie des réservoirs de ce groupe semble être principalement contrôlée par les carbonates et les évaporites.

Le deuxième groupe d'eaux correspond à celles situées dans le graben tectonique de la Valle de Lecrín, dans le complexe d'Alpujarride. Ce groupe affiche des températures et pCO₂ plus basses dans le réservoir (50-60°C et une gamme entre 10⁻³ et 10⁻² atm respectivement). Ce système est caractérisé par un assemblage de minéraux tampons en profondeur, composé principalement de carbonates, de quartz et d'alumino-silicates de calcium.

Enfin, le troisième groupe d'eaux, situé sur les détachements des complexes métamorphiques, présente les températures et pCO₂ estimées les plus élevées dans le réservoir (130 - 140°C et 1 à 10² atm respectivement). L'assemblage de minéraux tampons dans le réservoir pourrait être constitué d'alumino-silicates de calcium et magnésium, dolomite, et de quartz.

Les eaux des bassins sédimentaires présentent une variation de pCO₂ entre la profondeur et

la surface ($\Delta p\text{CO}_2$) de 10^{-1} atm pour les deux tampons minéralogiques (dolomite seule et assemblage carbonate et alumino-silicate). Le $\Delta p\text{CO}_2$ des eaux dont la température du réservoir est la plus basse (c'est-à-dire les eaux du graben) est plus élevée lorsque l'on considère le tampon de dolomite plutôt que l'assemblage carbonate/alumino-silicate, alors qu'il s'agit d'une tendance inverse pour les eaux avec les températures les plus élevées (c'est-à-dire dans les complexes métamorphiques).

Ce travail est la première étude reliant la géochimie des eaux thermales à l'environnement géologique de la Cordillère Bétique Centrale. Une forte relation entre la température et la $p\text{CO}_2$ dans le réservoir a été mise en évidence dans cette étude. Le rôle des tampons minéralogiques potentiels dans l'estimation de la $p\text{CO}_2$ apparaît comme crucial.

Vers un modèle de transport réactif

Le but de cette étude est d'obtenir un modèle d'évolution géochimique dans le bassin de Grenade qui pourrait ensuite être potentiellement couplé à un modèle de transport pour une modélisation ultérieure du transport réactif. L'accent est mis sur l'interaction eau-évacuoirite, ce qui a été motivé par la présence de plusieurs couches d'évacuoirites dans le bassin de Grenade avec une variabilité de distribution spatiale. Des évaporites triassiques sont présentes dans le socle du bassin, notamment dans la Zone Externe. Deux couches d'évacuoirite d'âge et de composition différents sont également présentes dans le remplissage sédimentaire du bassin. Les évaporites tortoniennes sont composées d'anhydrite et de halite, alors que les évaporites messiniennes sont principalement de l'anhydrite et du gypse. L'extension des évaporites messiniennes est plus grande que celle des tortoniennes et couvre presque tout le bassin. Deux massifs de célestine, associés aux évaporites, sont connus dans le bassin, formant l'un des plus gros gisements de strontium au monde.

D'un point de vue des ressources, le bassin de Grenade jouit d'un climat semi-aride où les ressources en eau sont soumises à une pression anthropique croissante (agriculture, industrie et tourisme). Les interactions importantes avec les évaporites modifient la qualité de l'eau en augmentant sa salinité, et diminue donc ses utilisations potentielles par la population. Les eaux à haute salinité, impropres à la consommation et à la plupart des cultures, sont également bien connues dans le bassin. L'eau dont la salinité est la plus élevée (environ 180 g / L de sels) est située à Salinas La Malaha, dans la zone évaporitique du bassin.

Certaines informations sur la circulation des eaux souterraines peuvent être obtenues à l'échelle de tout le bassin de Grenade en utilisant l'évolution de la composition de l'eau. Les eaux souterraines présentent de larges plages de température (de 6 à 40 ° C), de pH (de 5,8 à

8,0) et de conductivité électrique (de 0,09 à 187 mS / cm). La conductivité électrique (CE) sert de marqueur de la salinité tout au long de l'étude. L'augmentation de la CE depuis les bordures du bassin, proche des zones de recharge, jusqu'au centre du bassin, est liée à l'évolution des eaux carbonatées vers des eaux sulfatées et chlorurées.

Le contrôle des éléments majeurs (Ca, Mg, K, Na, HCO_3 et SO_4) a été évalué sur la base des états de saturation vis-à-vis des carbonates, aluminosilicates et des minéraux sulfatés. Les minéraux carbonatés, comprenant à la fois la calcite et la dolomite, semblent contrôler principalement les concentrations de Ca et de Mg, ainsi que le pH dans tout le bassin. Les alumino-silicates semblent exercer un fort contrôle sur le K, car les eaux sulfatées sont situées sur le point triple situé entre la kaolinite, la pyrophyllite et le microcline. Concernant le Na, les eaux à dominante sulfatée évoluent le long de la limite entre la kaolinite et la pyrophyllite.

Les chemins d'écoulement potentiels ont été discutés à l'aide de cartes de distribution de la saturation des eaux souterraines vis-à-vis des minéraux sulfatés (baryte, célestite et gypse). La saturation vis-à-vis des minéraux sulfatés montre que les eaux deviennent saturées en baritine, puis en célestine et enfin en gypse avec une CE croissante, des bordures vers le centre du bassin. Cette évolution donne des indications sur les chemins potentiels d'écoulement des eaux souterraines à l'échelle de l'ensemble du bassin de Grenade.

Enfin, les résultats de ce travail permettent de dégager plusieurs perspectives potentielles : étudier la composition isotopique de l'hélium au niveau des sources dans les massifs de péridotites, tester l'apport d'un modèle numérique de transport réactif dans le Bassin de Grenade et de discuter des cinétiques de dissolution/précipitation des évaporites.

TABLE OF CONTENT

GENERAL INTRODUCTION	3
CHAPTER 1:GEOLOGICAL AND GEODYNAMICAL SETTINGS.....	11
1.1. STRUCTURES AND GEODYNAMIC CONTEXT OF THE BETIC CORDILLERA	11
1.1.1. Geodynamic context	11
1.1.1.1. Geophysics and geodynamic models	12
1.1.2. Principal structural units of the Betics	15
1.1.2.1. External Zone.....	16
1.1.2.2. Internal Zone.....	17
1.1.2.3. Tectonic framework	18
1.2. GRANADA BASIN	19
1.2.1. Geodynamics and structure of the Granada Basin	19
1.2.2. Stratigraphy and geology of the Granada Basin	20
1.2.3. Focus on evaporites	24
1.2.3.1. Upper Tortonian evaporites	24
1.2.3.2. Messinian evaporites.....	26
1.2.4. Hydrogeology of the Granada Basin	26
1.2.4.1. Description of the aquifers	26
1.2.4.2. Thermal waters	29
CHAPTER 2:METHODOLOGY.....	33
2.1. SAMPLING SURVEY	33
2.1.1. Motivations and preparation	33
2.1.2. Water sampling	35
2.1.3. Gas sampling	36
2.2. ANALYTICAL METHODS	37
2.2.1. Field analyses	37
2.2.1.1. pH	37
2.2.1.2. Temperature	37
2.2.1.3. Electrical conductivity	37
2.2.1.4. Alkalinity	37
2.2.1.5. Redox potential and Iron.....	37
2.2.2. Laboratory analyses	38
2.2.2.1. Waters	38
2.2.2.2. Major elements	38
2.2.2.3. Minor elements	39
2.2.2.4. Silica	39
CHAPTER 3:CONSTRAINTS ON THE GEOLOGICAL STRUCTURE OF THE CENTRAL BETIC CORDILLERA FROM GAS GEOCHEMISTRY	43

3.1.	PRESENTATION	43
3.2.	NEW INSIGHTS ON BETIC CORDILLERA STRUCTURE FROM GAS GEOCHEMISTRY	45
3.2.1.	Abstract.....	45
3.2.2.	Introduction	46
3.2.3.	Geological settings and tectonic framework of the Betic Cordillera	47
3.2.3.1.	Iberian Domain	47
3.2.3.2.	Alboran Domain	48
3.2.3.3.	Neogene Basins.....	48
3.2.4.	Materials and Methods	51
3.2.4.1.	Sample location.....	51
3.2.4.2.	Sampling	51
3.2.4.3.	Laboratory gas analyses	51
3.2.5.	Results	53
3.2.5.1.	Fluid composition	53
3.1.1.1.	Noble gases	53
3.1.2.	Discussion.....	58
3.1.2.1.	A possible He diffusion mechanism	58
3.1.2.2.	Overall He transport and structural evolution of the Betic Cordillera	59
3.1.2.3.	Constraining ³ He origin by mass balance calculations	60
3.1.3.	Conclusions	62
3.2.	ADDITIONAL DATA	63
3.2.1.	Regional geodynamics.....	63
3.2.2.	Helium crustal production	65
3.1.1.	Results of a new sampling survey (June 2018).....	65
CHAPTER 4: THERMAL WATERS IN THE CENTRAL BETIC CORDILLERA		73
4.1.	PRESENTATION	73
4.2.	LOW TO MEDIUM ENTHALPY GEOTHERMAL SYSTEMS: ROLE OF CO ₂ . THE STUDY CASE OF THE CENTRAL BETIC CORDILLERA	75
4.2.1.	Abstract.....	75
4.2.2.	Introduction	76
4.2.3.	Geological setting	77
4.2.3.1.	Tectonic framework	78
4.2.3.2.	Lithostratigraphy	79
4.2.3.3.	Sample location.....	80
4.2.4.	Material and methods	81
4.2.4.1.	Water sampling	81
4.2.4.2.	Water analyses	81
4.2.4.3.	Gas analyses.....	82
4.2.4.4.	Geochemical calculations and modeling.....	82
4.2.5.	Results	86

4.2.5.1. Chemical characteristics of the waters	86
4.2.5.2. Saturation indices	87
4.2.5.1. CO ₂	88
4.2.5.2. Reservoir temperature and pressure	92
4.2.6. Discussion	104
4.2.6.1. Role of the mineral buffers in CO ₂ estimation	104
4.2.6.2. Relationship pCO ₂ and temperature	106
4.2.7. Conclusions	106
4.3. ADDITIONAL DATA	108
4.3.1. Relationship between hydrothermal characteristics and tectonics of the Central Betic Cordillera..	108
4.3.1.1. Supplementary information on the sampling points: tectonics and hydrogeological background	108
4.3.1.2. Results	109
4.3.2. Details of the hydrogeochemical simulations	110
CHAPTER 5: WATER-ROCK INTERACTIONS IN THE GRANADA BASIN.....	115
5.1. PRESENTATION	115
5.2. WATER-ROCK INTERACTION IN THE GRANADA BASIN (SOUTHERN SPAIN): A REGIONAL STUDY FOR GROUNDWATER REACTIVITY IN SEDIMENTARY BASINS	117
5.2.1. Introduction	117
5.2.2. Studied area	118
5.2.2.1. Geological and hydrogeological setting	118
5.2.3. Materials and methods	121
5.2.3.1. Water sampling	121
5.2.3.1. Water analyses	121
5.2.3.2. Geochemical calculations	122
5.2.4. Results	123
5.2.4.1. Chemical composition of waters	123
5.2.4.1. Saturation with respect to alumino-silicates	123
5.2.4.1. Saturation with respect to sulfate minerals	131
5.2.5. Discussion	133
5.2.5.1. Geochemical evolution	133
5.2.5.2. A possible conceptual reactive transport modeling?	134
5.2.6. Conclusions	136
5.3. ADDITIONAL RESULTS AND DISCUSSIONS	138
5.3.1. Kinetics and transport modeling	138
5.3.2. Influence of the Triassic evaporites in the External Zone	138
5.3.2.1. Motivations and geological setting	138
5.3.2.2. Materials and methods	143
5.3.2.3. Results and discussion	143
5.3.3. Origin of the salinity	145

5.3.4. Mineralization.....	147
SYNTHESIS AND CONCLUSIONS	151
PERSPECTIVES	159
REFERENCES.....	163
APPENDIX.....	181
LIST OF FIGURES	183
LIST OF TABLES	189

GENERAL INTRODUCTION

GENERAL INTRODUCTION

Understanding fluid (water and gas) circulations in sedimentary basins, both from the reaction and transport point of view, is crucial in the diverse fields of energy resources: water resource management, petroleum production, development of geothermal resources, and CO₂ geological sequestration. Both the chemistry of the fluid and its transport mechanisms need to be understood for all these energy resources to be economically viable. In the case of geothermal energy, several problems have been raised recently concerning the degassing of CO₂ and H₂S gas during the production. In the context of energetic transition, geothermal energy should be a clean non-carbon emitting energy to be a long-term environmental-friendly alternative to fossil-fuel. Evaluating the chemical reactions, susceptible to generate or consume CO₂, in geothermal systems are therefore necessary to efficiently predict the chemical behavior of future projects.

As fluids in sedimentary basins (including groundwaters, hydrocarbons, and/or gases) have been mobile through geological times, evaluating fluid circulations in the past is also of great interest in the energy industry. However, assessing and tracing fluid flow through geological time turns out to be a challenge and obtaining first a good comprehension of the present-day fluid flow is a major milestone to reach prior to transpose it in the past by the principle of actualism. This last point is of particular interest for IFPEN, which develops a basin modeling software, TemisFlow. This software dynamically simulate the evolution of sedimentary basins through geological times and the generation, migration, and accumulation processes of hydrocarbons. In addition, aqueous fluid flows may have effects on diagenesis and therefore on porosity and permeability and would hence control the migration and accumulation of oil and gas. The fluid circulations and the mineralogical changes that they induced may therefore exert a strong feedback on rock flow properties.

Apprehending current fluid flow at the basin scale remains a challenge in geosciences because of the heterogeneity of the multi-scale system formed by the sedimentary basin, of the diversity of fluid types, and of the complexity of chemical reactions encountered. One of the first key points that need to be addressed is how to define a sedimentary basin. Among all the definitions of sedimentary basins that have been formulated, two points of view catch my attention. On the first hand, geologists might consider a sedimentary basin as an accommodation space in the basement filled with sediments (Einsele, 2013). The focus of the

geologist would be on the sedimentary infillings itself and its geometrical structure. On the other hand, hydrogeologists might see the sedimentary basin as an object at the interface between the atmosphere, the lithosphere, and the hydrosphere, in which water flows (Garven, 1995).

The water chemistry sampled in the sedimentary basin cannot be dissociated from the interaction with the sedimentary infillings, but also the basement rocks of the basin, and the potential exchanges with the atmosphere (e.g., meteoric waters). Therefore, the sedimentary basin can be considered as a complex multi-scale system, in which the interaction with fluids can be investigated by different, but complementary, approaches. Indeed, the relationship between the fluid geochemistry and the structure of the sedimentary system can be apprehended at different scales (Figure I-1):

- with the basement of the basin and the underlying lithosphere (crust and mantle),
- with the fault systems affecting both the basement and the sedimentary infilling (i.e. pluri-kilometric scale of the crust)
- within the sedimentary infilling through fracture network (metric scale) and porous media (micrometric to centimetric scale).

The following work is dedicated to regional flow and hence focus on the lithospheric and fault scales.

This is in this context that I focused my PhD project on the present-day aqueous fluid circulations in the sedimentary basins, with the case study of the Granada Basin. This basin is a relatively small Neogene intramountain sedimentary basin (40 x 60 km²) within the Betic Cordillera (southern Spain), which belongs to the Alpine peri-Mediterranean orogenic belt. The formation of the basin was initiated ~15 Ma ago, reflecting a recent active geodynamic evolution of the investigated area. Major tectonic discontinuities structure the area and the rocks forming the basement of the basin crop out in the mountainous area surrounding the basin. The basin is also characterized by the occurrence of evaporites within the basement and the sedimentary infilling. All these features make of this basin an interesting study case for the fluid-rock interaction considering the different scales.

Different types of fluids can be investigated in sedimentary basins, including waters, hydrocarbons, and gases. My main interest in this work is the aqueous fluids and more specifically groundwater. Groundwater, contrary to the surface water, may interact with rocks up to several

kilometers depth. There is a large diversity of groundwater types and one possible way to classify them is according to their physical-chemical characteristics, e.g. temperature or salinity. In this research project, three types of groundwaters have been studied: (1) the thermal waters (temperature $> 20^{\circ}\text{C}$) related to the fault systems in the Central Betic Cordillera; (2) fresh low-mineralized waters corresponding to the waters in the mountainous recharge area of the Granada Basin; and (3) saline waters (brackish waters and brines) circulating within the sedimentary basin.

In parallel to the groundwater studies, dissolved and bubbling gases in water were also investigated in some of the water points of the Central Betic Cordillera. The gas abundance and the isotopic composition can allow to assess the gas-water-rock system and the interactions with the underlying lithosphere.

Groundwater in sedimentary basin may also be derived from different sources (Bjorlykke, 1993) including: (1) meteoric waters; (2) seawater; (3) deep fluids from the underlying basement; (4) waters resulting from dehydration of minerals (e.g. water resulting from the transformation of gypsum to anhydrite); (5) subaerially produced brines fossilized into the basin. The differences in the physical-chemical properties of groundwater might be partially explained by the origins of the fluids.

The overall chemical composition of water results from chemical reactions, including fluid-minerals (e.g. dissolution, precipitation, and redox-reactions) and reactions within the fluids (e.g. complexation). In order to describe these reactions affecting the sedimentary system at the large spatial and temporal scales, we defined a geochemical approach based on thermodynamic calculations. This approach is governed by groundwater equilibrium of the groundwater with respect to a set of minerals during one or several stages of its chemical evolution. This mineral assemblage, or mineral buffer, is a key parameter of this geochemical strategy to apprehend fluid reactivity.

In this PhD project, fluid geochemistry is used as a tool to follow the groundwater evolution and to get insights on the flow path in sedimentary basins. The chemistry of the sampled water corresponds to the final stage of the whole history of water and we intend to estimate the intermediate and initial stages of the chemical composition. In the case of meteoric waters circulating in the sedimentary basins, they evolve from low-mineralized waters in the recharge areas to mineralized or saline waters within the basin due to increasing water-mineral interactions. The Granada Basin is an interesting study case for investigating the groundwater

geochemical evolution at the basin-scale as the water mineralization might allow recording the progressive water-evaporite interactions in the basin. This basin is characterized by several evaporite layers of different mineralogies (anhydrite, gypsum, and halite) with distinct spatial distribution.

The reaction model obtained from this hydrogeochemical approach might be then coupled with a transport model, taking into consideration pressure gradient, water flow velocity, and residence time, to carry out reactive transport modeling. The reactive transport modeling is a popular approach in hydrogeology (e.g. water contamination assessment) which allow getting insights into the feedbacks of the fluid circulations on flow properties through coupled numerical equations. In our study, the original geochemical modeling provides qualitative information on the regional circulations without numerical flow calculations. The limitations of this approach will be discussed relative to the reactive transport modeling at the basin scale.

The main objective of my PhD project is to trace the fluid reactivity and circulations in the Granada Basin, and more globally in the Central Betic Cordillera, using the inorganic fluid geochemistry.

The following are the main questions addressed in this thesis:

- Can we constrain the geological structure of the Central Betic Cordillera from the gas geochemistry? (Chapter 3)
- How to constrain the relationship between $p\text{CO}_2$ and temperature in low enthalpy geothermal systems? (Chapter 4)
- What is the evolution of the water-rock reactivity in the Granada basin? (Chapter 5)

This thesis is structured in five chapters and assesses the potential of fluid geochemistry to trace fluid circulations and reactivity at different scales in a sedimentary basin.

Chapter 1 presents the geodynamics and the geology of the Betic Cordillera, as well as the geology and hydrogeology of the Granada Basin.

Chapter 2 describes the methods that I developed during my PhD project and that are used in all subsequent chapters. Our motivations and approach to prepare the sampling survey are presented in this chapter, including the construction of a geochemical database and the development of a numerical program to query the database and select sampling points. Finally, the analytical methods used to investigate fluid geochemistry are described.

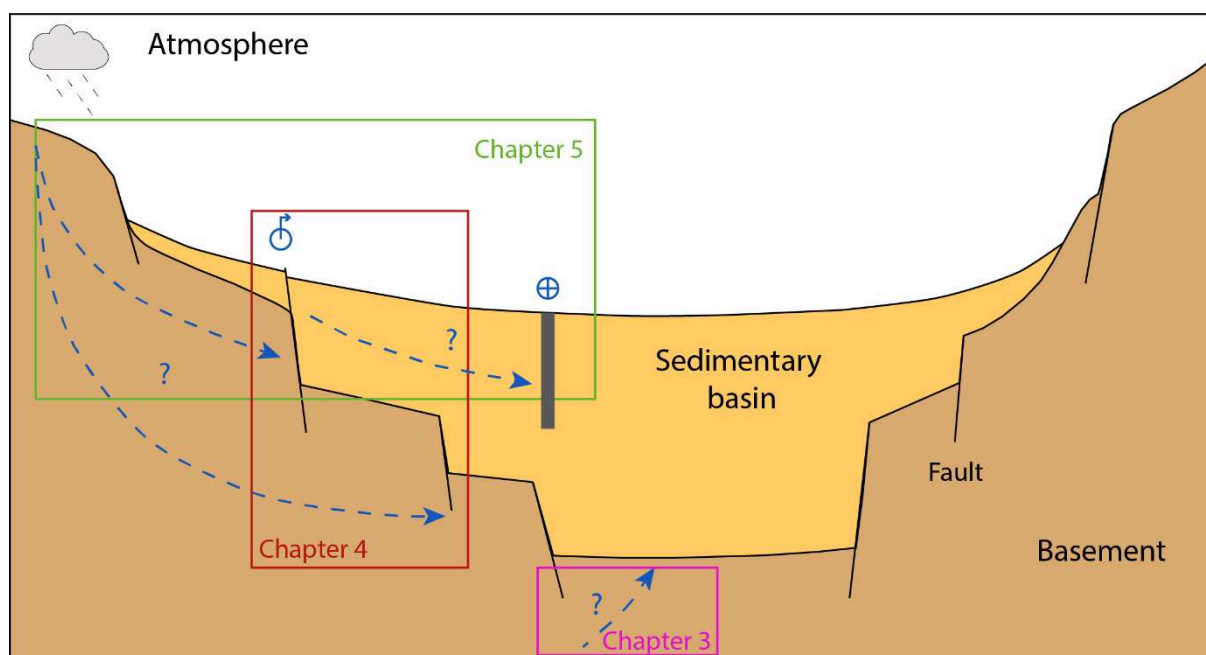


Figure I-1: Schematic representation of a sedimentary basin and the fluid circulations

The chapters 3 to 5 present the results of the studies of fluid-rock interaction at the different scales (Figure I-1). Chapter 3 constrains the mantle influence on the gas geochemistry in the complex tectonic structure of the Central Betic Cordillera. A study of the helium isotopic composition is presented, as well as an evaluation of the possible helium transport mechanisms.

Chapter 4 focuses on the characterization of the low- to medium-enthalpy thermal systems in the Central Betic Cordillera. This study combines classical geothermometrical methods to discuss the role of CO₂ in these systems.

Chapter 5 presents the groundwater geochemical evolution in the Granada Basin as a whole system. The interaction with the evaporites, and with sulfate minerals in particular, allows to assess the possible flow paths in the basin and to apprehend a conceptual reactive transport.

Finally, a conclusion highlights the main findings of this work and future leads are suggested in perspective with regards to these results.

CHAPTER 1

GEOLOGICAL SETTINGS

CHAPTER 1: GEOLOGICAL AND GEODYNAMICAL SETTINGS

1.1. STRUCTURES AND GEODYNAMIC CONTEXT OF THE BETIC CORDILLERA

1.1.1. Geodynamic context

The Betic Cordillera is the present-day European western part of the Alpine peri Mediterranean orogenic belt resulting from the Africa-Iberia plate convergence since the Upper Cretaceous (Dewey et al., 1989; Rosenbaum et al., 2002). The Betic Cordillera in southern Spain forms, together with the Rif in northern Morocco, the Gibraltar Arc enclosing the Alborán Sea, which corresponds to the westernmost part of the Mediterranean Sea (Figure 1-1).

The region of the Betic Cordillera is currently subject to a NW-SE convergence of 4-6 mm/yr (Platt et al., 2013). This convergent movement has controlled the movement of strike-slip faults since the late Miocene.

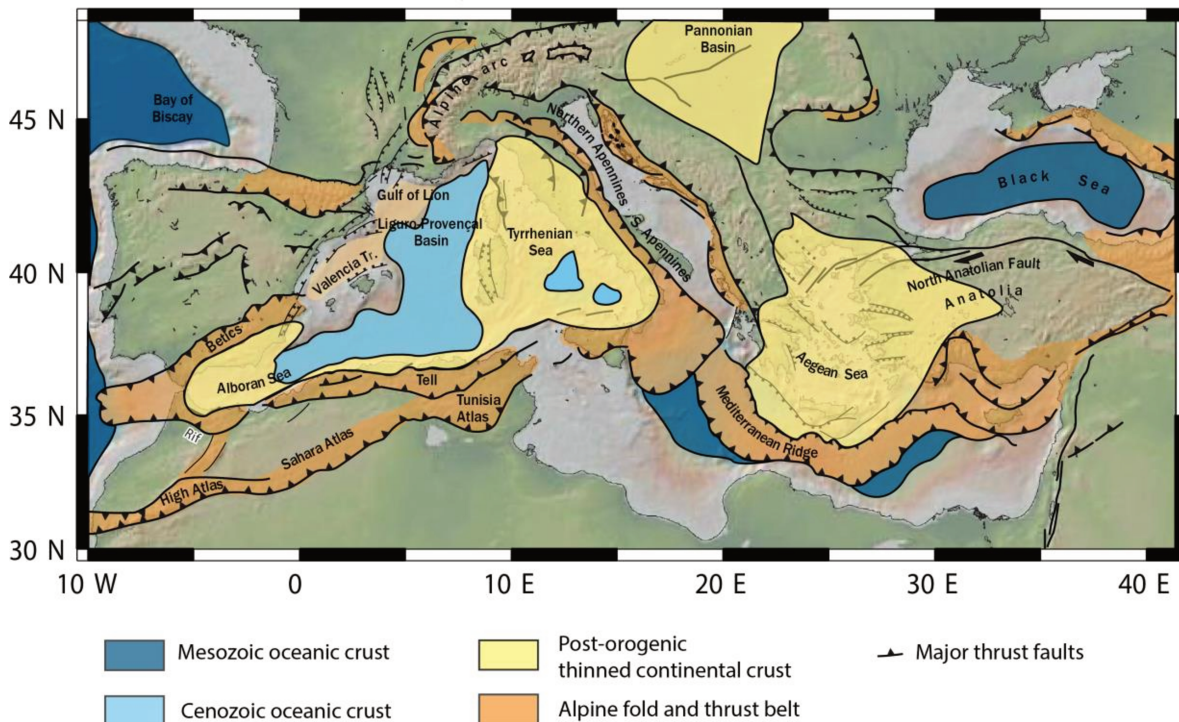


Figure 1-1: Tectonic map of the Mediterranean modified after Jolivet et al. (2009) and Do Couto (2014) showing the position of the thrust fronts and subduction zones and the nature of crust.

1.1.1.1. Geophysics and geodynamic models

Several geophysical studies have been carried out in order to understand the lithospheric structure under the Gibraltar Arc and more especially the Betic Cordillera (Galindo-Zaldívar et al., 1999; Jabaloy et al., 1997; Mancilla et al., 2015; Palomeras et al., 2017; Pérez-Peña et al., 2012; Rosell et al., 2011).

Geodynamic models of the Betic Cordillera

The mechanisms for the development and evolution of the Betic-Rif orogeny and the following extension are still subject of debates (Jolivet et al., 2008; Jolivet and Faccenna, 2000; Platt et al., 2013; Platt and Vissers, 1989; Vergés and Fernández, 2012). Several models have been developed to explain the extension episode and the genesis of the Alborán sea including slab rollback (Lonergan and White, 1997; Royden, 1993) with or without mantle delamination (Calvert et al., 2000), convective removal of gravitationally unstable lithosphere (Platt and Vissers, 1989), and slab break-off (Blanco and Spakman, 1993) (Figure 1-2).

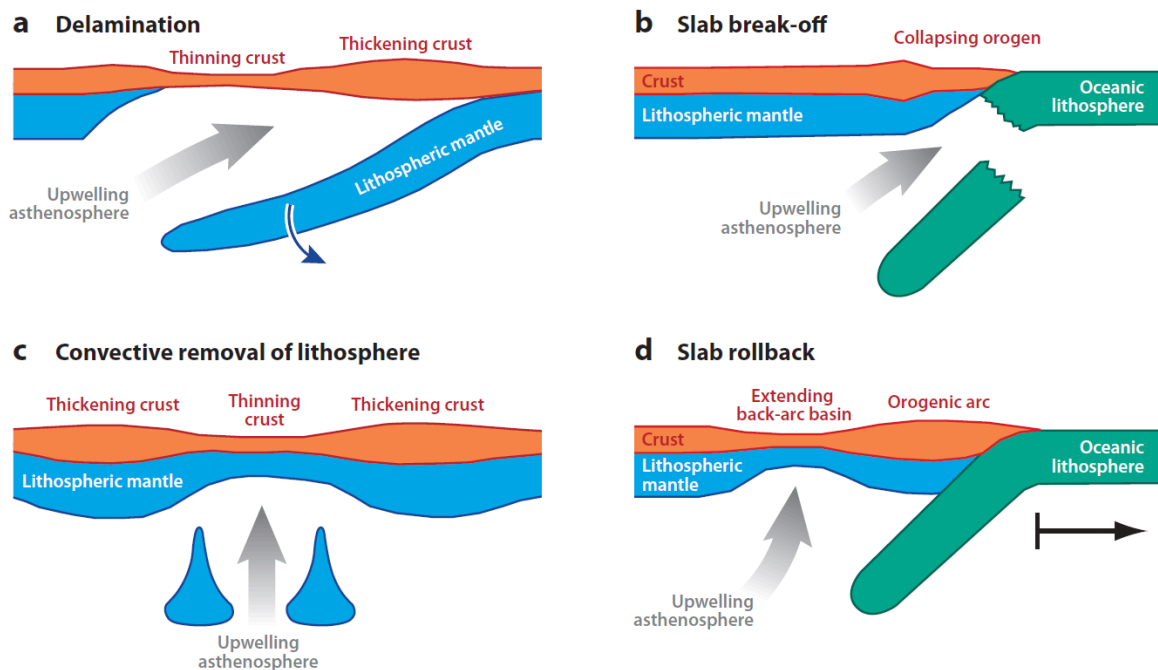


Figure 1-2: Models of the four upper mantle processes beneath the Alboran Domain invoked to explain geodynamics (Platt et al., 2013). (a) Delamination (e.g., Calvert et al. 2000), (b) slab break-off (e.g., Blanco and Spackman, 1993), (c) convective removal of the lithosphere (Platt and Vissers, 1989), (d) slab rollback (Lonergan and White, 1997; Royden, 1993).

Geophysical studies

Recent geophysical studies (Bonnin et al., 2014; Gutscher et al., 2002; Mancilla et al., 2018, 2015; Rosell et al., 2011) support the slab detachment models. A model of subduction rollback and tearing for the westernmost Mediterranean has been proposed by Mancilla et al. (2015). They obtained cross-sections by interpreting receiver functions (Figure 1-3) and showed strong lithospheric and crustal thickness gradients between the eastern and western Betics. It supports the idea of a continental slab detachment of the South Iberian subducted lithosphere under the eastern Betics producing a mantle edge delamination. They noticed that the lithosphere under the Granada Basin is 35 km deeper than under the Sierra Nevada, which they interpreted as the presence of the Iberian lithosphere beneath the basin and its absence to the East (Figure 1-4) (Mancilla et al., 2013, 2015).

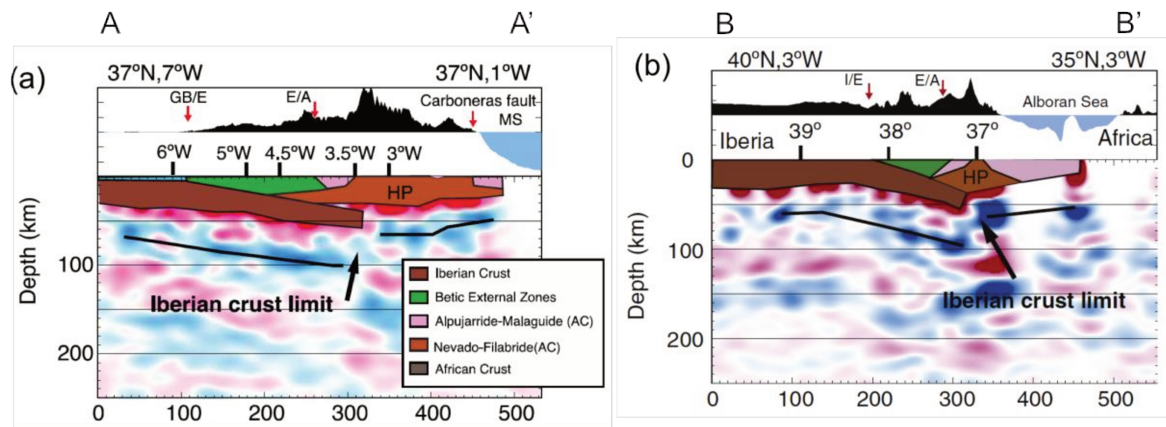


Figure 1-3: EW- and NS-interpreted cross-sections across the Betic Cordillera from Mancilla et al. (2015), localized in Figure 3.4. The topography is displayed at the top of the profiles.

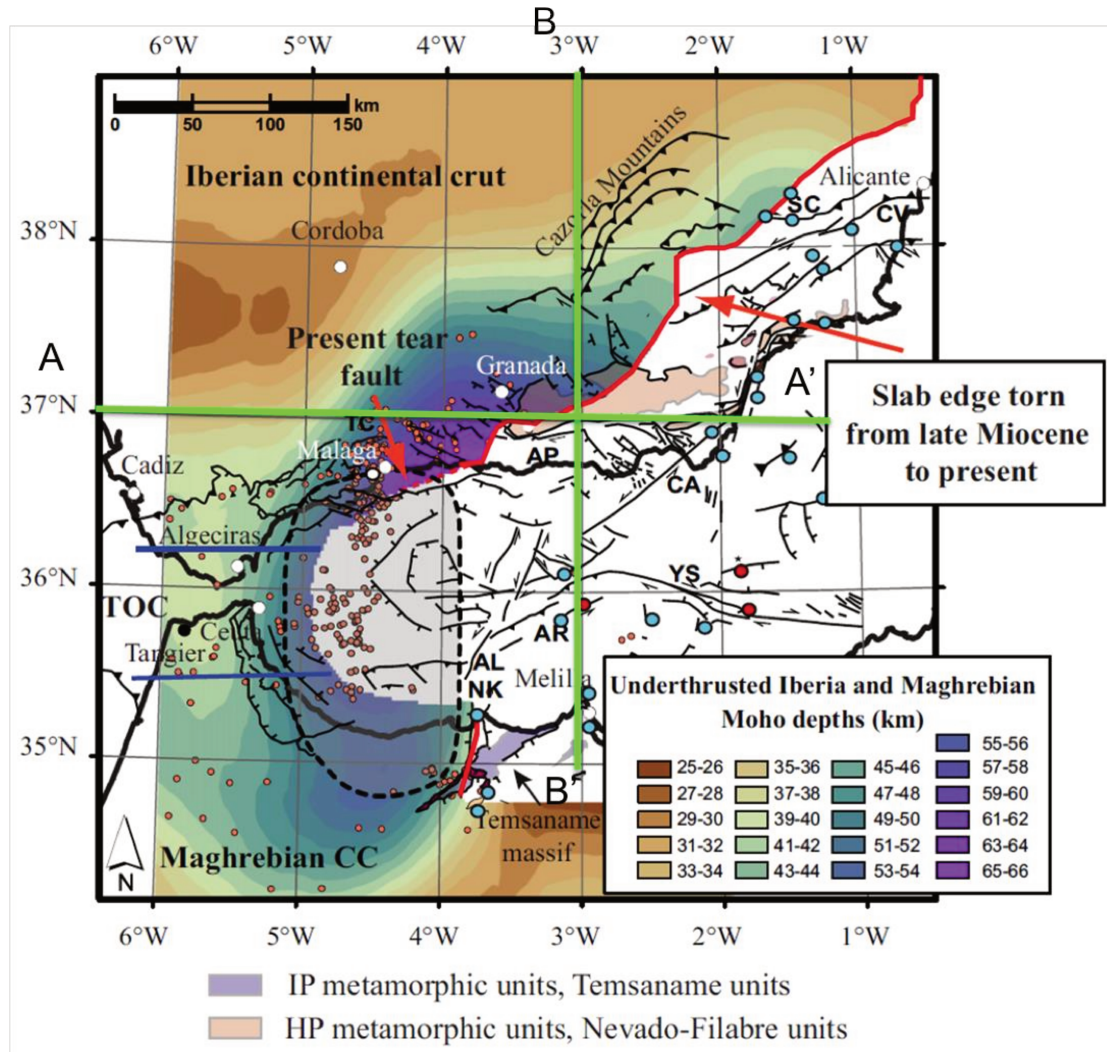


Figure 1-4: Moho depths of the Iberian and Maghrebian subducted continental slabs. The continuous red line marks the interpretation of the edge of the south Iberian Moho imaged by the P-receiver functions and the dashed red line the extrapolation of the torn slab edge toward the east (modified from Mancilla et al. (2015)). The two green solid lines correspond to the cross-sections presented in Figure 1-5.

Rosell et al. (2011) presented a deep electrical resistivity distribution model of the lithospheric structure beneath the Betic Cordillera based on magnetotelluric data. They showed a low-resistivity anomaly at lithospheric mantle depth (~ 50 km), which they interpreted as an intrusion of asthenospheric material (Figure 1-5). The location of the intrusion (east of the 4° W meridian) coincides with the zone of Alhama de Granada located at the SW border of the Granada Basin. Some historic baths (Banos Alhama de Granada), whose water has high temperature (40°C), are well-known in the region. Their model suggests that the intruding asthenospheric material results from the westward roll-back of the E-directed subducting slab and the following slab break-off and detachment.

The Betic Cordillera is still subject to extension according to the new GPS data of (Galindo-Zaldívar et al., 2015). They revealed oblique displacement of the Betic Cordillera relative to the NW-SE Eurasian-African plate convergent movement, with increasing extensional deformation affecting the crust towards the Alboran Sea and the western part of the Betics. These data are also in accordance with the roll-back subduction model.

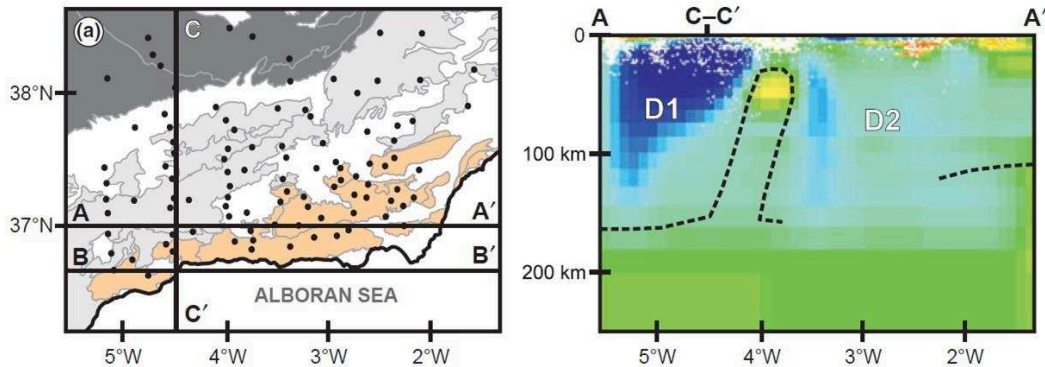


Figure 1-5: Map of the Betics showing the locations of the magnetotelluric sites (black dots) and the cross-sections. *AA'* side view cross section of the 3D resistivity model, from Rosell et al. (2011).

1.1.2. Principal structural units of the Betics

The Betic Cordillera is a complex structure that is commonly subdivided into two domains with very distinct histories: (1) the External Zones and (2) the Internal Zones (Figure 1.6). The External zone is separated from the Internal Zone by a major shear zone called the Internal External Boundary Zone (IEBZ), which had a dextral movement at the beginning of the orogeny (Lonergan et al., 1994; Sanz de Galdeano, 1990).

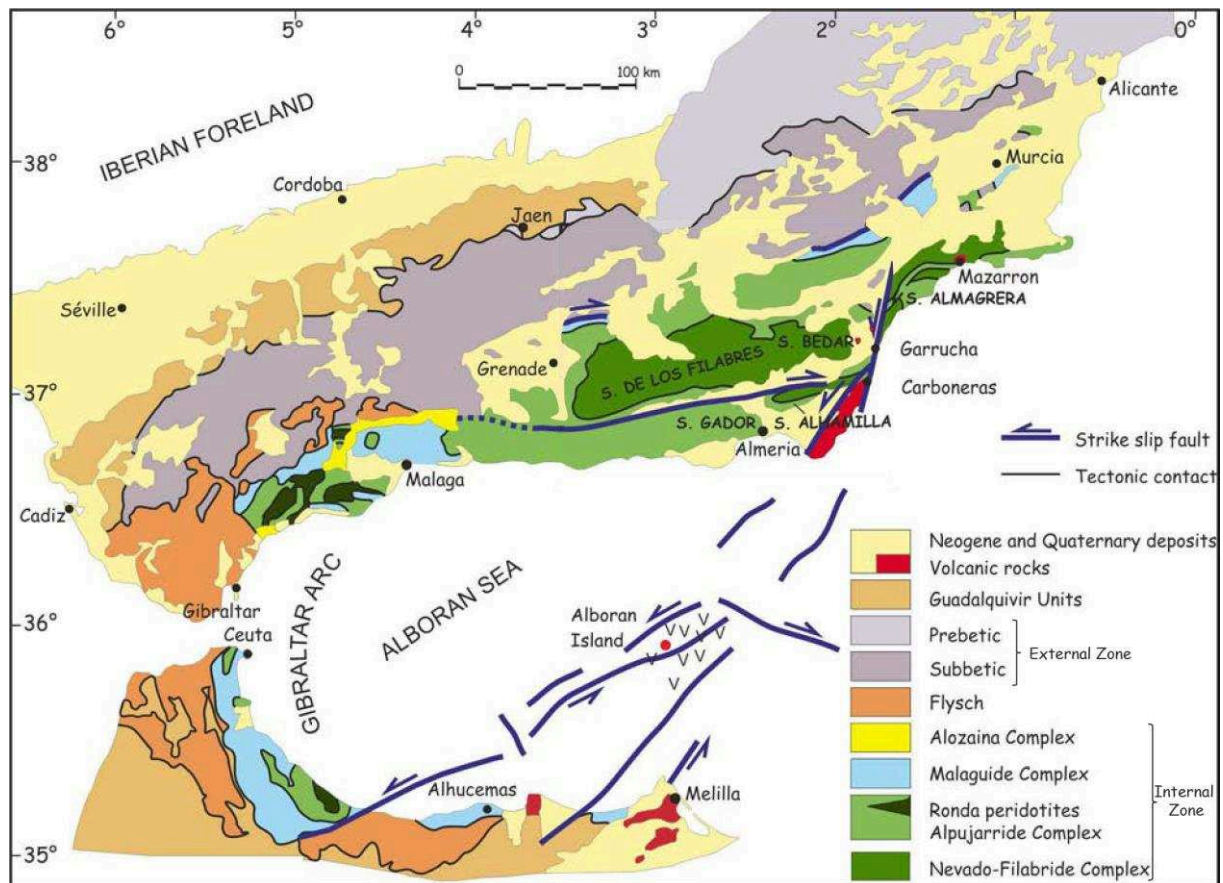


Figure 1-6: Geological sketch map of the Gibraltar Arc in the western Mediterranean, modified after Dyja (2014), Sánchez-Gómez et al. (2002), and Comas et al. (1999)

1.1.2.1. External Zone

The External Zone, which is the northern border of the Cordillera, corresponds to mesozoic and tertiary sedimentary rocks of the continental Iberian paleo-margin of the Tethys Ocean (García-Hernández et al., 1980). This non-metamorphic zone did not undergo the subduction of the Iberian plate under the Meso-Mediterranean micro-plate (Dyja, 2014; Vera, 2001). Nevertheless, the Meso-Cenozoic cover has been tectonically deformed into thrust nappes, whose tectonic contacts took root into the Triassic evaporitic sequence (Keuper facies). The External Zone can be subdivided into two subunits, the Prebetic and Subbetic zones respectively (Figure 1-6). The Prebetic zone, which is located in the north, is formed of continental to shallow shelf facies dated from the Triassic to the Middle Miocene and is considered as the autochthonous domain (Braga et al., 2003). On the other hand, the allochthonous Subbetic zone, which is situated in the south, is dominated by deep-water marine facies from the early Jurassic (generally limestones and marls) and frequent interbedded submarine volcanic rocks.

Flyschs units, mainly located at the west of the Cordillera (Figure 1-6) may be associated with the External Zone. The flyschs are mainly composed of Upper Cretaceous and Lower

Miocene turbidites and hemipelagic sediments (Durand Delga, 1980). These nappes are structurally located over the External Zone.

1.1.2.2. Internal Zone

The Internal Zone consists of three tectonically stacked metamorphic complexes from the base to the top: (1) the Nevado-Filábride, (2) the Alpujarride, and (3) the Maláguide (Figure 1-2). These complexes are distinguished from their metamorphism degree and their position in the subduction (geodynamic and structural histories). They are described as following from the highest degree of metamorphism to the lowest.

- (1) The Nevado-Filábride complex crops out in local tectonic windows in the Sierra Nevada and Sierra de los Filábres, forming the high summits of the Betic Cordillera (Figure 1-2). It comprises Paleozoic or older metamorphic rocks (Gómez-Pugnaire, 1979; Gómez-Pugnaire et al., 2000) strongly affected by high-pressure Alpine metamorphism. The basement is mainly composed of mica schist and separated from the Permo-Triassic overburden by a Hercynian discordance. The cover comprises from the base to the top: mica schist, a meta-evaporite interval, and marble associated with calc-schist (Brouwer, 1926).
- (2) The Alpujarride complex extends over 400 km long in the Internal Zone of the Betic Cordillera and is structurally located between the Nevado-Filábride and the Maláguide complexes (Figure 1-2). It is composed of a series of nappes of Paleozoic-Mesozoic metasediments (Azañón et al., 1998, 1995). The pre-Mesozoic basement, consisting of graphite mica schist for the Pre-Permian rocks, underwent Variscan metamorphism. This metamorphic basement is overlain by meta-sandstones, conglomerates, and schists, which are in turn overlain by Triassic carbonates (limestone, dolomitic limestone and dolostone) (Martín and Braga, 1987). Mesozoic pelagic marls form the top the Alpujarride complex.
- (3) The Maláguide complex crops out in small windows at the junction between the Internal and External Zones in the Betic Cordillera (Figure 1-2). This complex is made up of non-metamorphic clastic and carbonate Paleozoic sediments covered by Mesozoic mixed sediments (carbonate, evaporite and siliciclastic) (García-Tortosa et al., 2000).

A phase of crustal thickening in the Betic Cordillera began about 51 My as the result of the collision of the African and Iberian plates and lasted until approximately 24 Ma, i.e. during the

larger Alpine Orogeny. This episode has been followed by a crustal-scale extension during the early to middle Miocene (Monié et al., 1991). The metamorphic rocks of the Nevado-Filábride and Alpujárride complexes have been exhumed during that time as shown by a sharp decompression in their P-T path (Braga et al. (2003) and references wherein).

1.1.2.3. Tectonic framework

Major accidents have accommodated the convergent movement in the Betic Cordillera such as the Cadix-Alicante fault. The Cadix-Alicante fault, crossing a large part of the south of Spain from Cadix (SW) to Alicante (E) and extending from 550 km (Figure 1-3). This long fault has been first described as a whole major accident by Sanz de Galdeano (1983) but its existence is still debated by some authors. The Cadix-Alicante accident is mainly reported as a zone of parallel faults rather than a single fault. However, the architecture and the movement of the Cadix-Alicante fault vary depending of the location. At the East (between Alicante and Bullas) the fault is well defined and called Crevillente Fault (Foucault, 1974; Sanz de Galdeano, 2008). Between the Granada Basin and the Guadix-Baza Basin it forms a corridor of dextral strike-slip faults (Sanz de Galdeano and Alfaro, 2004; Soria et al., 1993).

The Carboneras and Palomeras fault zones are two other well-known major strike-slip fault systems in the South-East of the Betic Cordillera (Figure 1-7). The Palomeras Fault Zone (PFZ) and the Carboneras fault system are two sinistral strike-slip fault systems linking areas subject to NW/SE shortening (Booth-Rea et al., 2004a; Faulkner et al., 2003; Keller et al., 1995). Another major strike-slip fault is located in the southern part of the Sierra Nevada (Martínez-Martínez et al., 2006) (Figure 1-7). It corresponds to a 40-km long dextral strike-slip fault accommodating the present extension and the westward movement (Martínez-Martínez et al., 2006). It acts as a transfer fault of the normal faults.

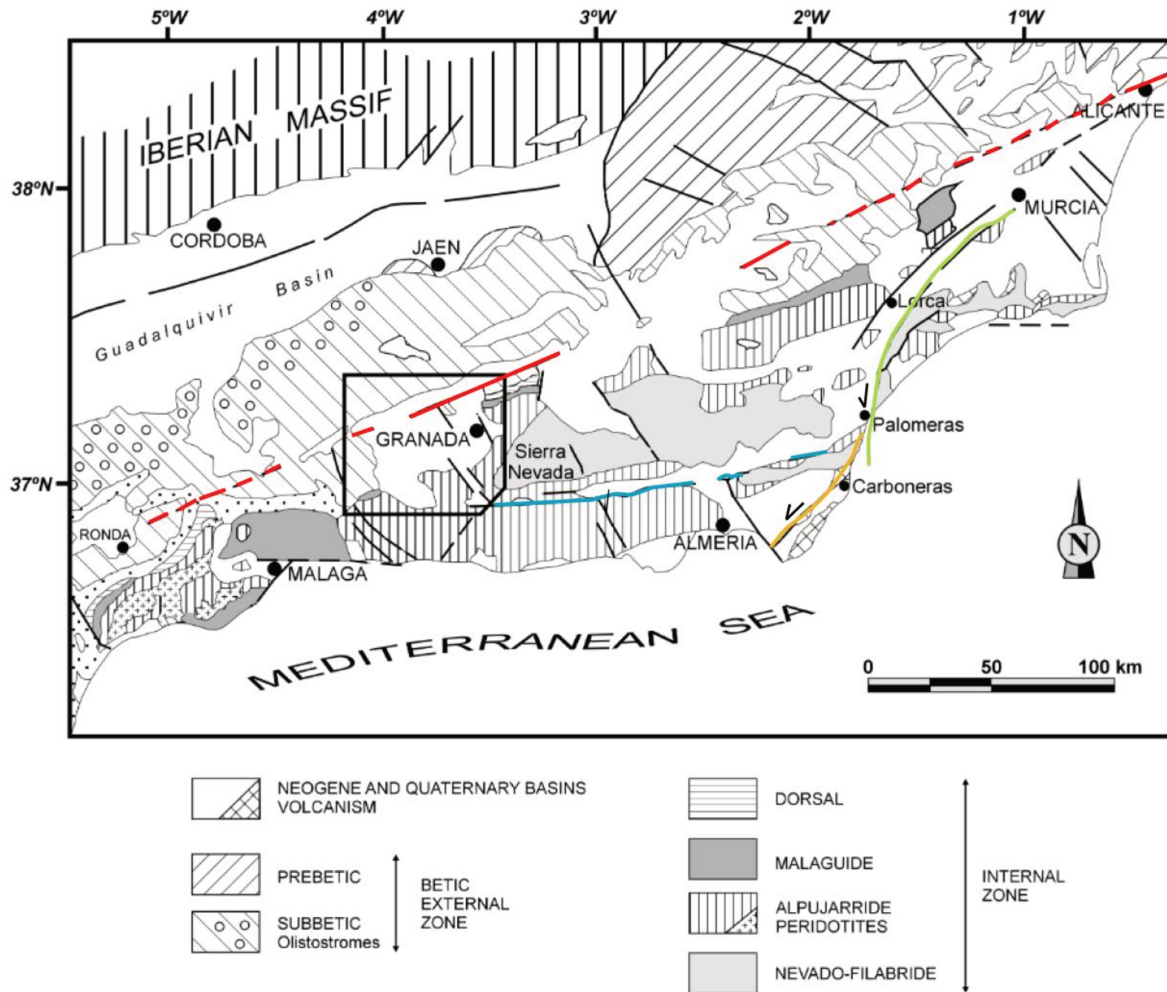


Figure 1-7: Structural map of the Betics modified from Sanz de Galdeano et al. (2003). Red line: Cadix-Alicante fault; blue line: transfer fault; green line: Palomeras Fault Zone; and yellow line: Carboneras fault.

1.2. GRANADA BASIN

1.2.1. Geodynamics and structure of the Granada Basin

The Granada Basin is a Neogene intramountain basin within the Betic Cordillera. It is located at the junction between the Internal and External zones (Figure 1-6). The basement structure of the basin has been well defined by Morales et al., (1990) and Rodríguez-Fernández and Sanz de Galdeano (2006). Two sets of normal faults affect the basement and the sedimentary infilling of the basin: one set of E-W faults with low angle dip ($< 30^\circ$) toward the south and the north; and a second one with NE-SW faults, dipping westward (Figure 1-8) (Galindo-Zaldívar et al., 2015; Rodríguez-Fernández and Sanz de Galdeano, 2006a; Sanz de Galdeano and Peláez, 2011). The NE-SW faults are mainly located in the NE of the basin (Figure 1-8). The fault movements were controlled by the extension affecting the Granada Basin

since the Upper Tortonian. The NE-SW normal faults are still tectonically active resulting in a large number of small-magnitude earthquakes ($m_b < 5$) and lower occurrence of moderate and high-magnitude seismic events (Galindo-Zaldívar et al., 1999; Morales et al., 1997; Sanz de Galdeano et al., 2003). The Granada Basin constitutes one of the most seismically active area in the Iberian Peninsula (Gil et al., 2002).

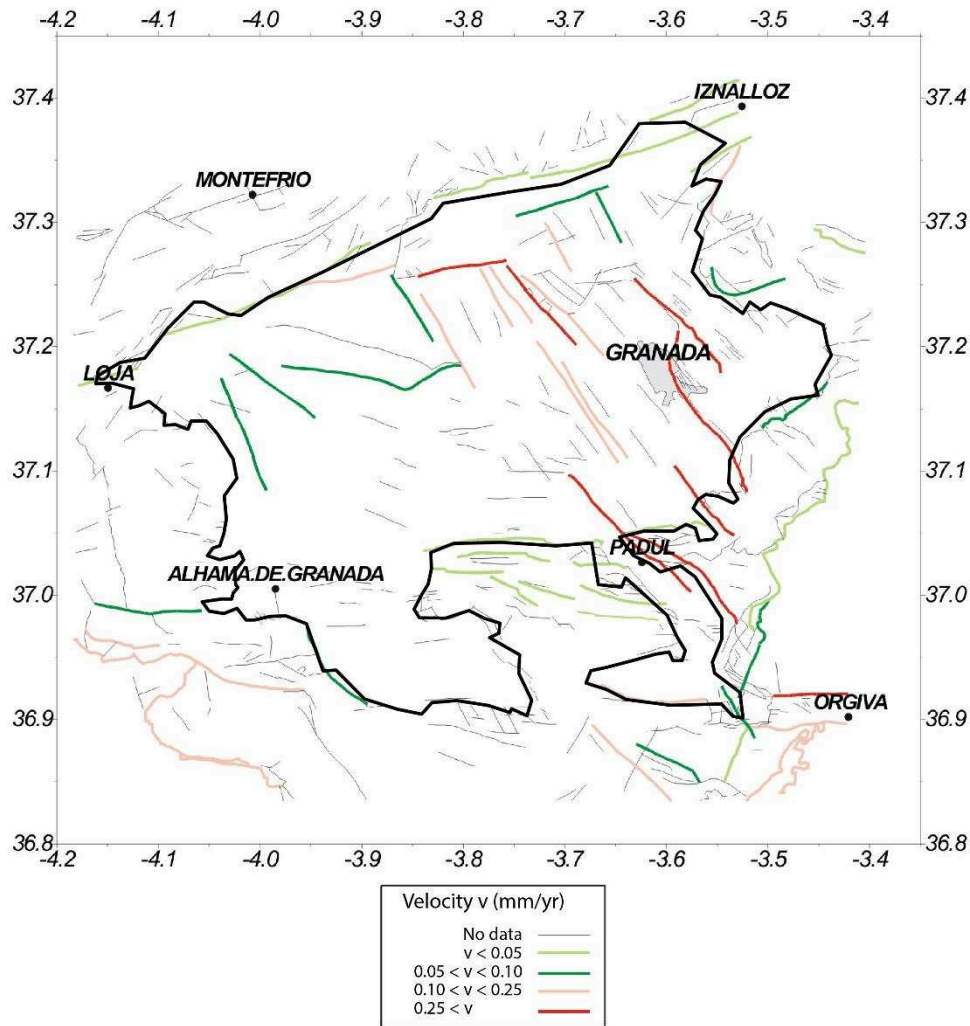


Figure 1-8: Map of the network of active faults in the Granada Basin modified after Sanz de Galdeano and Peláez (2011). Colors indicate the calculated velocity of the displacement.

1.2.2. Stratigraphy and geology of the Granada Basin

The sedimentary infilling of the Granada Basin ranges from the Miocene to the Quaternary (Braga et al., 2003; Corbí et al., 2012). It can be subdivided into four units (I, II, III, IV), defined

on tectono-sedimentary and age criteria. From bottom to top, the Units I and II are dated from Langhian to Tortonian whereas the Units III and IV are from Messinian to Quaternary (Figures 1-9 and 1-10). The transition between the Units II and III marks the evolution of the basin from marine to continental conditions (Braga et al., 2003, 1990, Martín et al., 2014, 1984). During the Upper Tortonian the Granada Basin was connected to the Atlantic Ocean to the northwest and to the Mediterranean Sea to the south and west (Braga et al., 1990; Martín et al., 2014). As the basin was uplifted, the marine connections were interrupted first to the Atlantic Ocean and then to the Mediterranean Sea. The basin began to desiccate and sedimentation evolved to become predominantly fluvial and lacustrine (Martín et al., 1984).

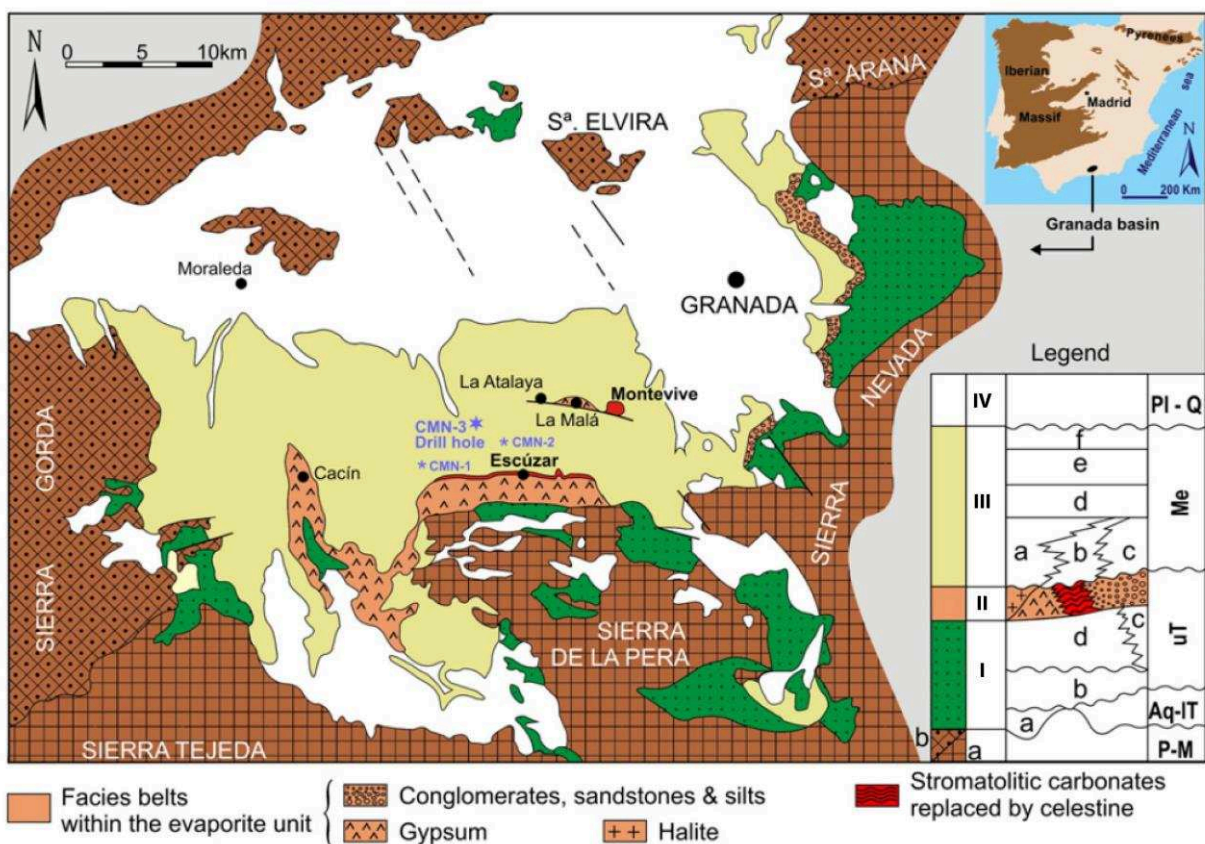


Figure 1-9: Simplified map of the Granada Basin (Modified from Martín et al. (1984) and Dabrio et al. (1982)). The Unit I, II, III and IV are described in section 1.2.2.

Unit I is subdivided into four subunits (Subunit I-a, I-b, I-c, and I-d). The Subunit I-a and locally I-b overly the metamorphic Triassic basement of the Internal Zone with an angular discordance. At the base of Unit I, the Subunit I-a corresponds to siliciclastic sediments (red conglomerates, sandstones, and silts) dated of the early to middle Miocene (Langhian, Serravalian, and lower Tortonian) (Figure 1-10). According to Martín Suarez et al. (1993),

Serravalian age has been determined for the red silts in the Granada Basin thanks to micromammal fossils. The sediments of the Subunit I-a correspond to deltaic environments that crop out only locally at the margins of the basin (Braga et al., 2003; Rodríguez-Fernández and Sanz de Galdeano, 2006a) (Figure 1-10). The Subunit I-b is made up of bioclastic calcareous sandstones, calcarenites, calcirudites, and mixed siliciclastic-carbonate sediments including coral reefs. The detrital and conglomeratic sediments were deposited in proximal deltaic environment and the carbonates were deposited on platforms around the margins of the basin between 8.3 and 7.8 My (Corbí et al., 2012) followed by coral-reef carbonates between 7.8 and 7.3 My (Braga et al., 2003; Corbí et al., 2012). The sediments of this unit is also called "Tortonian Temperate Carbonates" (TTC) and have been have been studied for diagenetic purposes by López-Quirós et al. (2016). These rocks contain abundant fragments of bryozoans, bivalves, and coralline algae; and in smaller quantity: echinoids, benthic foraminifers and brachiopods. The uppermost part of the Unit I, is subdivided into the Subunits I-c and I-d (Figure 1-10) depending of the paleo-environment of deposition and the resulting facies. The Subunit I-c is composed of conglomerates, sandstones, and silts, which were deposited in fan-delta environments. These deposits record the uplift of the northeastern (Sierra Arana) and eastern (Sierra Nevada) edges of the Granada Basin (Braga et al., 2003, 1990; Dabrio et al., 1978; Martín and Braga, 1987). The Subunit I-d is made up of planktonic marls that were deposited in open-marine distal environments in the center of the basin (Dabrio et al., 1978; Martín et al., 1984).

Unit II corresponds to the Tortonian evaporite unit in the Granada Basin, dated from the Upper Tortonian (7.3 to 7.2 My). This unit comprises different facies evolving from conglomerates, sandstones and silts (Subunit II-a); carbonate stromatolites partly- or fully-mineralized by celestine (Subunit II-b); and selenitic gypsum and halite (Subunit II-c) (Dabrio et al., 1982; Martín et al., 1984) (Figure 1-10). The detrital sediments were deposited in fan-delta at the eastern border of the evaporitic basin close to the Sierra Nevada (Dabrio et al., 1982). The stromatolites developed in the margin of the basin forming a coastal belt (Martín et al., 1984). The replacement of the stromatolite carbonate by celestine was interpreted by Martín et al. (1984) as an early diagenetic process in the evaporitic context. According to Martín et al. (1984), the evaporites were deposited in a marine shallow-basin evaporitic environment, where selenitic gypsum precipitated in shallow-water areas and halite in the center.

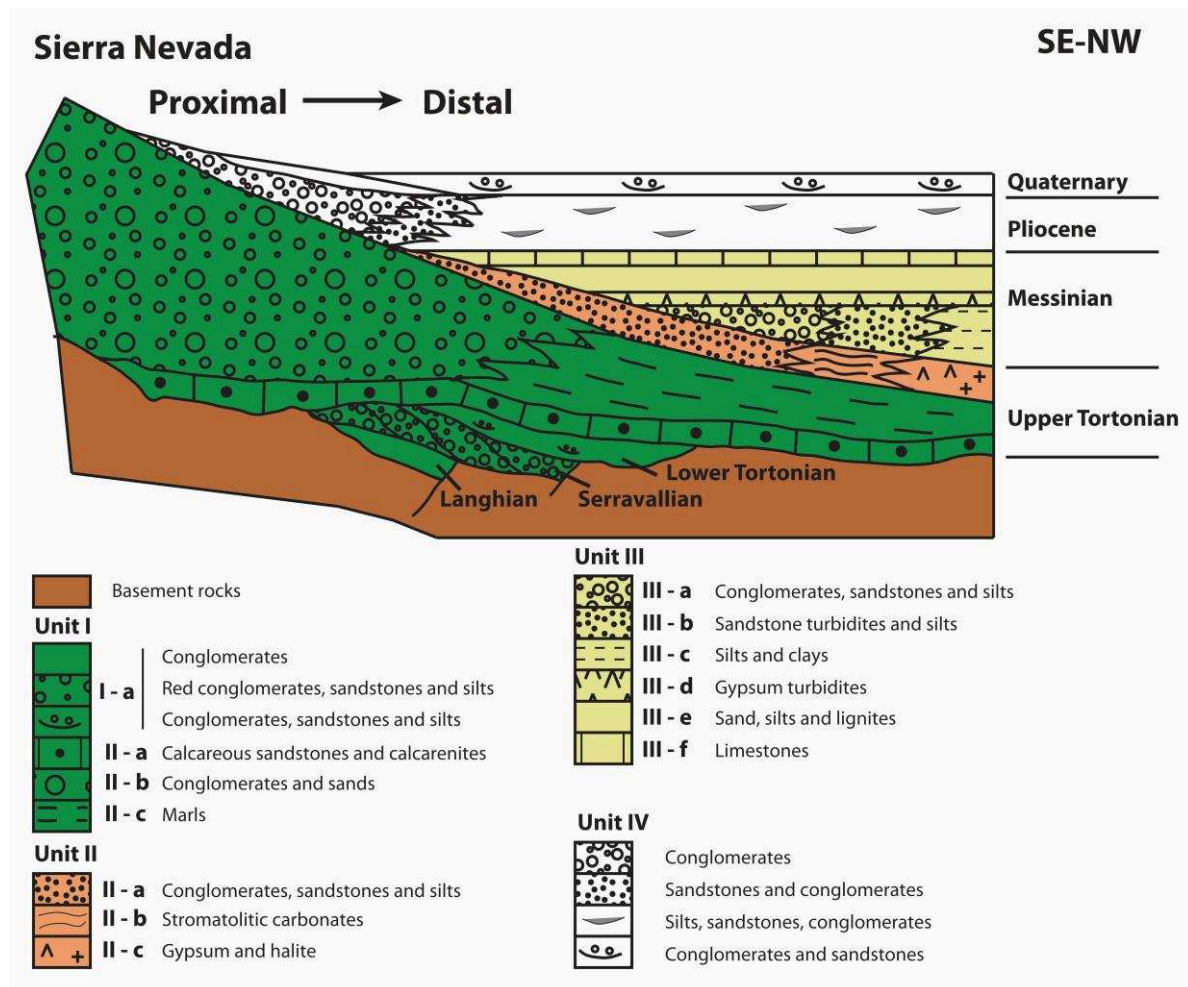


Figure 1-10: Stratigraphy of the Granada Basin (Modified from Braga et al. (1990)).

Unit III is dated of Messinian and is subdivided into six subunits depending of their lithologies and paleo-environments (Figure 1-10). The whole unit has a thickness ranging from few meters to more than 500 m (Rodríguez-Fernández and Sanz de Galdeano, 2006b). At the base of the Unit III, three subunits are distinguished (III-a, III-b, III-c) and show lateral evolution of facies (García-Alix et al., 2008). Subunit III-a corresponds to conglomerates, sands and silts that have been accumulated into marginal and fluvial environments. Subunit III-b is made up sandstones turbidites and silts, which have been deposited into proximal-lake environment. Subunit III-c is composed of silts and clays corresponding to distal-lake deposits (García-Alix et al., 2008). Overlying these three subunits, the Subunit III-d is formed of sandy-gypsum beds interpreted as gypsum turbidites (Dabrio et al., 1982) (Figure 1-10). These Messinian evaporites were deposited in lacustrine environments with turbidite originating from, at least partially, the surrection of the Sierra Tejeda and Sierra Gorda (Dabrio et al., 1982; Martín et al., 1984; García-Alix et al., 2008). The uplifting of these reliefs results in the erosion and resedimentation of the gypsum beds of the Subunit II-c. Subunit III-e covers the evaporites

of the subunit III-d and is formed of sands, silts, lutites and coal (lignites). These sediments were deposited in deltaic and lacustrine environment (García-Alix et al., 2008). The uppermost subunit of the Unit III is the Subunit III-f, which is composed of micritic limestones riched in gasteropods (Boné et al., 1978). The deposition of these limestones was in a small lake (García-Alix et al., 2008).

Unit IV consists of detrital deposits from the Zanclean and Plaisancian (Pliocene) to Quaternary, whose the precise ages have not been determined in details. They are conglomerates, sand and silts (Figure 1-10), deposited in alluvial and lacustrine systems (Morales et al., 1990; García-Alix et al., 2008). High-subsidence depocenters, controlled by laterally limited faults, are formed (Pérez-Peña et al., 2015; Rodríguez-Fernández and Sanz de Galdeano, 2006). The Pliocene-Quaternary sediments reach a considerable thickness locally, up to 1250 m (Rodríguez-Fernández and Sanz de Galdeano, 2006).

1.2.3. Focus on evaporites

Two phases of evaporite deposition can be revealed in the Granada Basin: during the Upper Tortonian (Unit II) and the Messinian (Subunit III-d) (Figures 1-9 and 1-10). The study of these evaporites was possible thanks to outcrops mainly located at the south of the basin and three boreholes (CMN-1, -2, and -3), which were drilled by the Rio Tinto Company in 2006 and 2007. The well CMN-3 is located close to the village of Ventas de Huelma in the center of the Granada Basin (N 37°06'46.3", W 3°47'20.3") (Figure 1-9). The core is available at the Granada University and have been studied by the IFPEN team for diagenetic purposes (López-Quirós et al., 2018).

1.2.3.1. Upper Tortonian evaporites

The Upper Tortonian evaporites (i.e. the Unit II described in section 1.2.2) are located in the southern and central part of the Granada Basin (Figure 1-11) and have a thickness ranging from ap- proximately 200 to 550 m. These evaporites are referred as the "Lower Evaporite Unit" (LHU) according to Dabrio et al. (1982). They consist of selenetic gypsum (Dabrio et al., 1982; Dabrio and Martín, 1981; Rouchy and Pierre, 1979) and halite in chevron (García-Veigas et al., 2013). The selenitic gypsum alternated locally with secondary gypsum, which has been transformed via deshydration (anhydrite formation) and rehydration process. The evaporites were deposited in a marine shallow-basin evaporitic environment evolving to a salt-pan strongly

isolated to the sea. This phase of dessication marks the transition between the marine and continental conditions in the Granada Basin. García-Veigas et al. (2013) studied the late Tortonian evaporites in the CMN-3 core including their isotopic compositions ($\delta^{18}\text{O}_{\text{sulfate}}$, $\delta^{34}\text{S}_{\text{sulfate}}$ and $^{87}\text{Sr}/^{86}\text{Sr}$) and the fluid inclusion compositions in halite. They showed a mixture of water inflows with different origins in the basin and the evolution from marine to continental conditions. The celestine deposits replacing the stromatolite carbonates were interpreted by Martín et al. (1984) as an early diagenetic process in the mixing zone close to the evaporitic basin. García-Veigas et al. (2015) proposed a model for the formation of celestine ore deposits (Montevive and Escúzar), present in the Unit II, involving gypsum dissolution by SO_4^{2-} -poor and Sr^{2+} -rich, CaCl_2 hydrothermal water associated with low meteoric input. These evaporites have been deposited before the well-known "Messinian salinity crisis" of the Mediterranean Sea.

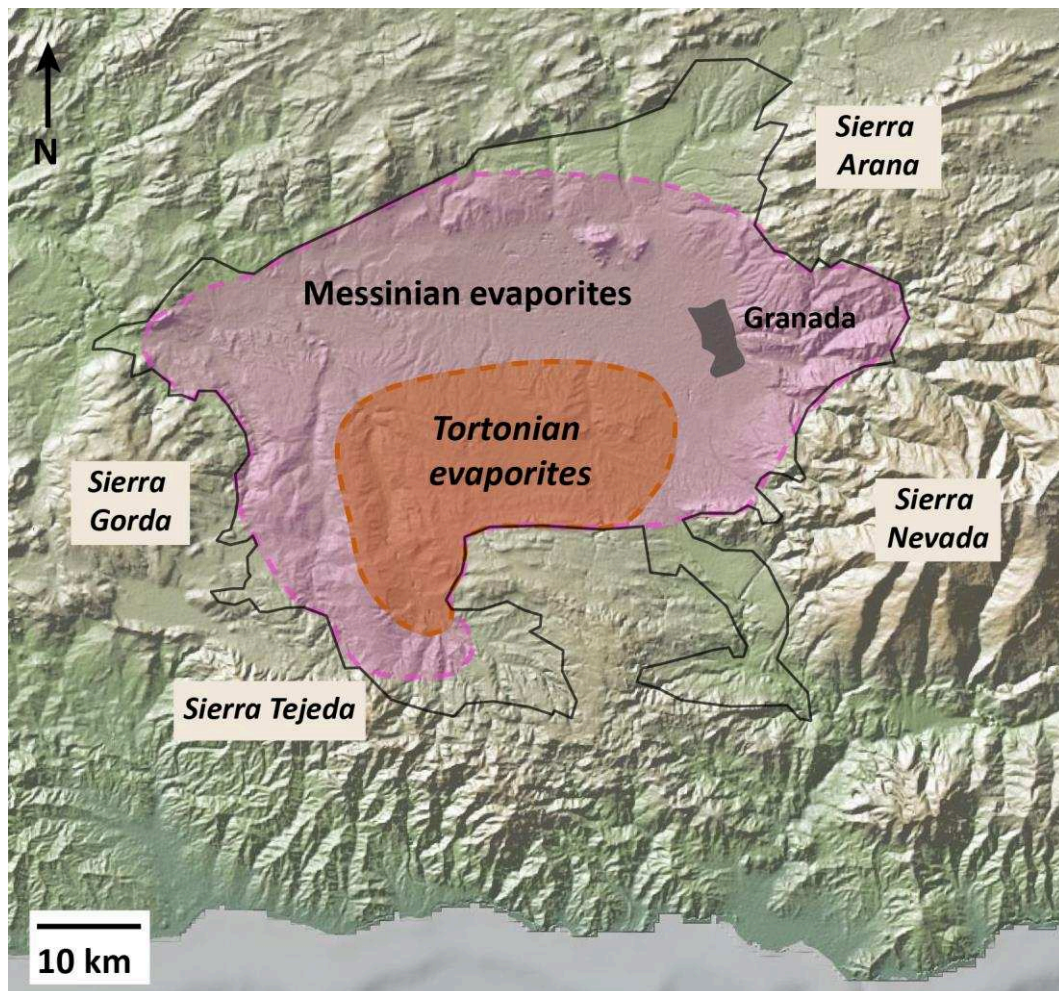


Figure 1-11: Presumed distribution map of the Tortonian and Messinian evaporites in the Granada Basin defined after Dabrio et al. (1982) and García-Veigas et al. (2013).

1.2.3.2. Messinian evaporites

The Messinian evaporites (Subunit III-d) have a larger extension than the Tortonian evaporites and cover almost the whole Granada Basin (Figure 1-11). The Messinian evaporites correspond to "Upper Evaporite Unit" sensus (Dabrio et al., 1982). These evaporites consist of a sequence of cm-scale turbiditic gypsum alternating with lutites and sandstones. This turbiditic gypsum sedimentation could be interpreted as the result of the resedimentation of eroded gypsum layer of Unit II during the uplifting of the western and south-western reliefs of the basin (Sierra Tejeda and Sierra Gorda) (García-Alix et al., 2008). No halite has been formed during this evaporitic phase.

1.2.4. Hydrogeology of the Granada Basin

The Granada Basin is currently a semiarid area with low precipitation, where the groundwater recharge is mainly localized in the high elevation area surrounding the basin itself (Kohfahl et al., 2008a). The mean annual rainfall ranges from approximately 460 mm/y in the basin to about 1000 mm/y in the Sierra Nevada (IGME, 1990).

1.2.4.1. Description of the aquifers

The terms of hydrological units (HU) (unidad hidrogeológica) and groundwater masses (Masas de Agua Subterránea or MASub) are often used to describe the hydrogeology of the Granada Basin (IGME, 1990). However, these terminologies are employed in legal and management purposes. A hydrological unit or MASub may comprise a number of different aquifers or groundwater flow systems. Scientifically, it makes more sense to link a spring or well water to an aquifer or a groundwater reservoir. For this reason, the notion of aquifer will be preferred. An aquifer is water-saturated geological medium capable of storing and transmitting groundwater whereas an aquitard does not really transmit water although it might have high water content (Clark, 2015). Two main types of aquifer can be distinguished in the Granada Basin: the highly permeable aquifers (Vega de Granada Aquifer and carbonate aquifers) and the low-permeability minor aquifers (Campos, 2006).

Highly permeable aquifers

Within the highly permeable aquifer, the Vega de Granada Aquifer is an important aquifer

in the Granada Basin with a surface area of 200 km² (22 x 8 km) and a thickness of about 250 m locally (Castillo, 1995; Sprenger, 2006) (Figure 1-12). It supplies water for a large part of the population and for irrigation of several cultures (poplar grove, cereal, olive, corn and vegetables). It takes its name from the agricultural use of this very fertile area as the word Vega means “cultivated land” in Spanish. This aquifer has been intensively studied and is still closely monitored to avoid any pollution, e.g. nitrates related to agriculture. Hence, there are a lot of data of the flow system, hydraulic characteristics and chemical composition available for this aquifer. Geologically, it is made of detrital Quaternary alluvial material (gravel, sand, silt) deposited from the numerous rivers that flows in the area (Monachil, Darro, Dilar and Genil). The hydraulic gradient, i.e. the difference of hydraulic heads between two points in an aquifer, is higher at the NE of the Vega de Granada aquifer (1.5 %) than in the southeastern and southwestern parts (0.2-0.4 %) creating an east to west flow (Sprenger, 2006). The direction of the flow is in accordance with the regional flow of the rivers (Figure 1-13). Hydraulic characteristics have evolved through time due to increasing anthropogenic activity (over exploitation, urbanization, and reservoir building) impacting the flow system (IGME, 1990; Castillo, 1995).

The carbonate aquifers in the Granada Basin are important aquifers, covering more than 1300 km². They form the mountain areas bordering the Granada Basin (e.g., Sierra de la Peza, Sierra de Padul, Sierra Arana, Sierra Elvira, Sierra Gorda, Almjara-La Guajaras, Albunuelas, Sierra Tejeda) (IGME, 1990) (Figure 1-12). The aquifers in the Internal Zone are made up of Triassic and Jurassic limestones, dolostones, and marbles from the Alpujárride Complex whereas the aquifers in the External Zone consist of Jurassic carbonate formations. The carbonate aquifers have generally an high permeability due to karstification (Campos, 2006). These aquifers are directly linked with the adjacent aquifers (e.g. the Vega de Granada Aquifer) and constitute their main recharge. The discharge of these carbonate aquifers is highly dependent of the precipitations as the residence time of the water is relatively short. Hence, the spring flows are relatively high during the rainy season and highly reduced during the dry season (Campos, 2006).

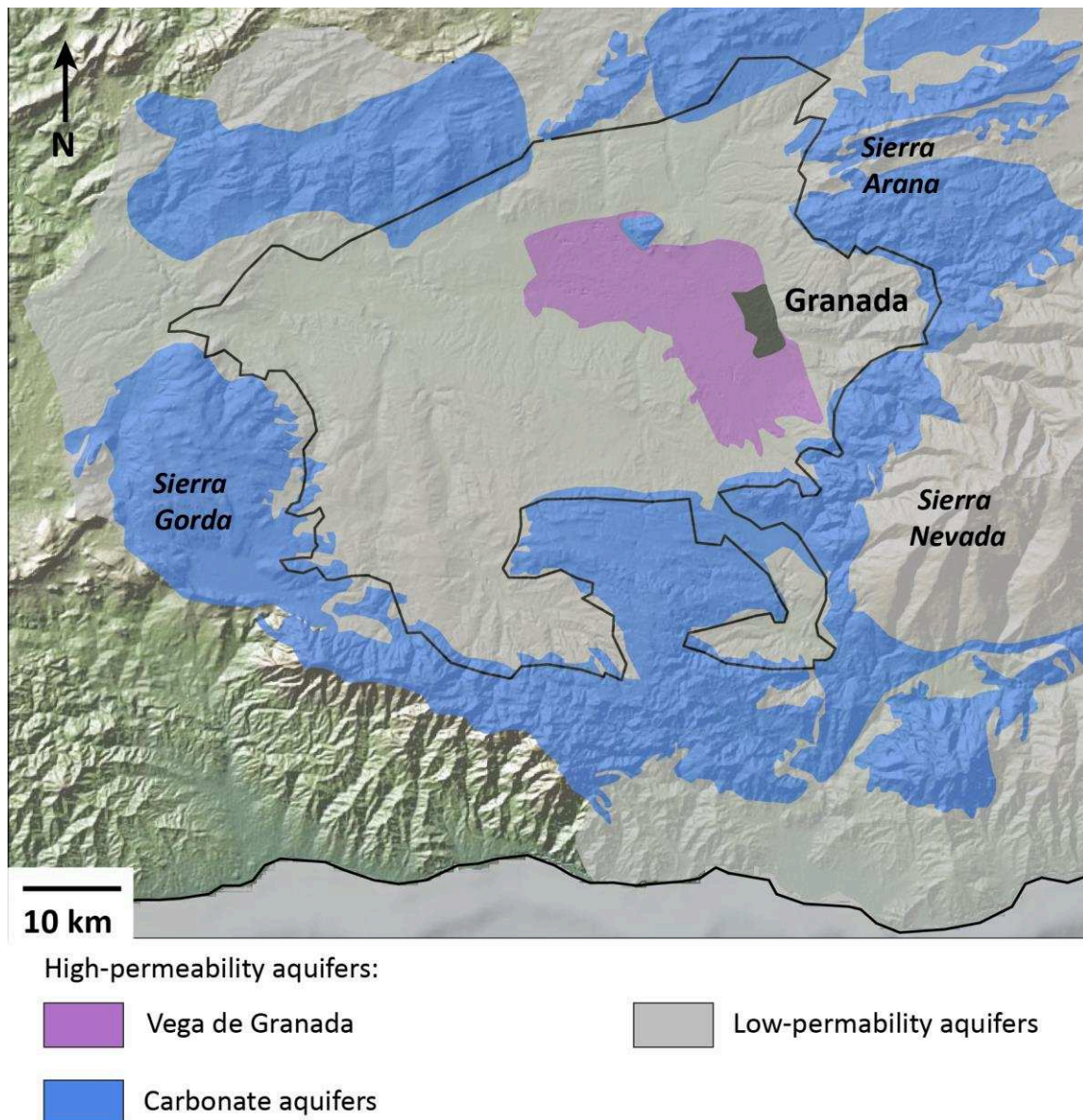


Figure 1-12: Map of the aquifers of the Granada Basin modified after Campos (2006).

Low-permeability minor aquifers

Low-permeable to impermeable zones in the Granada Basin (Figure 1-12) form minor aquifers with significantly lower permeability. They can be subdivided into two groups in the Granada Basin depending of their lithology: the schists of the Nevado-Filabride Complex and the detrital and carbonated Mio-Pliocene basin deposits, although they are not distinguished in Figure 1-12. The Triassic micaschists and quartzites of the Nevado-Filabride complex constituting a low-permeability aquifer are located in the highest mountain area in the eastern part of the Sierra Nevada. These metamorphic rocks have low permeabilities (Gómez-Pugnaire

et al., 2000). However, these low-permeability rocks have been partially altered by glaciogenic processes and may have relatively high permeabilities locally (Castillo, 2000). The Mio-Pliocene basin deposits, constituting most of the sedimentary infilling of the Granada Basin, are considered as moderate to low permeability aquifer according to IGME (1990). This aquifer covers between 800 km² and 1350 km² in the Granada Basin (IGME, 1990; Sprenger, 2006) and is composed of very heterogeneous sediments (i.e. terrigenous, carbonated, and evaporitic). This aquifer is not well defined as a result of little available data on the groundwater flow (Sprenger, 2006).

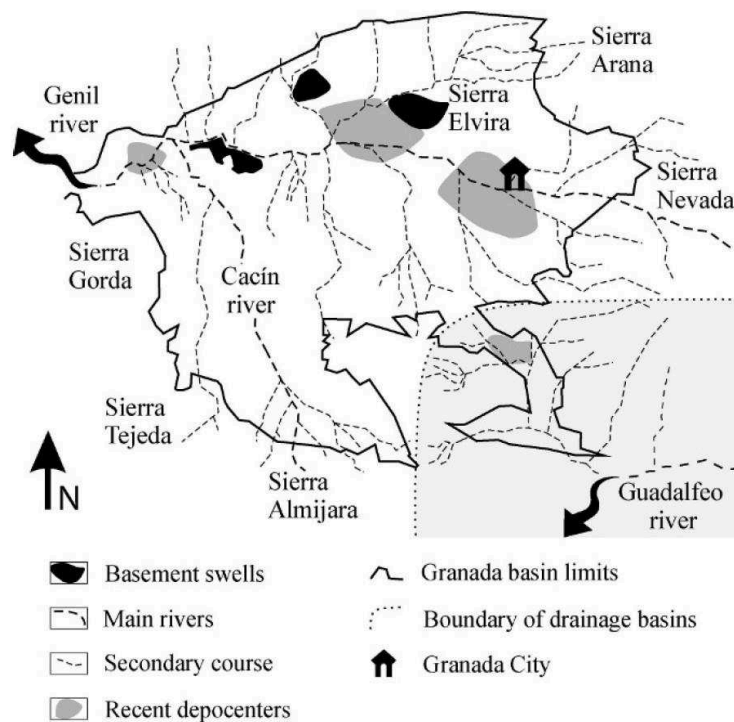


Figure 1-13: Current drainage of the Granada Basin from García-Alix et al. (2009).

1.2.4.2. Thermal waters

The hydrogeology of the Granada is also characterized by the presence of numerous thermal springs. As there are several definitions of a thermal water (Gilli et al., 2008; Sonney, 2010), we considered here that a thermal spring has an emergence temperature higher than 4°C compared to the annual average air temperature of the site, i.e. 16°C in the Granada Basin. This is the norm that is applied in France to define a thermal water (Lepiller, 2006).

The thermal spring of Baños Nuevos Alhama de Granada (40°C) is particularly well-known in the Granada Basin. Located close to the village of Alhama de Granada in the southwest of the basin, it appeared after the Andalusian earthquake in December 1884 (Terremoto de

Andalucia) (Kohfahl et al., 2008a; López-Chicano et al., 2001a). Another spring (Baños Viejos), located few hundreds of meter nearby, was already used as thermal bath during the Roman and Islamic times. It appears that part of the local hydrothermal activity may be related to the intense tectonic activity of the region (Azañón et al., 2004; Pérez-Peña et al., 2010, 2015). Other thermal springs, such as Baños de La Malahá (30°C) and Baños Sierra Elvira (39°C), are located close to NE-SW and E-W normal faults in the center and north of the Granada Basin.

In the whole Granada province, there are other occurrences of thermal springs (e.g., Baños Alicun de las Torres, Baños Zujar, and Baños Sierra Alhamilla), spread over several hundreds of kilometres. The high concentration of thermal springs in the Granada Basin makes of that basin an interesting study case for hydrothermalism purposes.

CHAPTER 2

METHODOLOGY

CHAPTER 2: METHODOLOGY

2.1. SAMPLING SURVEY

2.1.1. Motivations and preparation

As my PhD project focus on the fluid circulation in the Granada Basin through their geochemistry, I needed to collect samples for further analyses. I prepared and actively participated to a fluid sampling survey in November 2016 in the Betic Cordillera and more especially in the Granada Basin. This sampling survey was carried out to complete the geochemical water dataset acquired from a first sampling campaign in June 2015, which has been completed in the framework of Daniel Muñoz-Lopez's internship at IFPEN. Based on the composition (major and minor elements) of 11 collected water samples, I was able to draw a first conceptual model of evolution of water geochemistry in the Granada Basin. In this model, the carbonated waters at the border of the basin evolve to sulfated waters in the center of the basin. The new sampling campaign was therefore organized to refine this first conceptual model and check the representativeness of the samples.

In order to prepare the field work, I proceeded to a selection of new sampling points based on the large existing water database of the Instituto Geológico y Minero de España (IGME) available online in open-access (<http://info.igme.es/bdaguas/>). An important quantity of data is available for water points (springs, wells, surveys, tunnels, and others) all around Spain with several types of information: piezometric, hydrometric, and physicochemical data (pH, electrical conductivity, temperature, geochemical composition). The water points are georeferenced which enable to include them into our QGis project and see their spatial distribution on geological and hydrogeological maps. Piezometric, hydrometric, and physicochemical data may not be available all together for each water point. In addition, there is a monitoring of some of the water points that allow to get the evolution of the geochemical composition through the 40 last years. These are precious information that allow us to have quality control for some of the water points. IGME's website provides an interface to select water points depending of their localization or their alphanumerical data (e.g. type of data, nature of the water points, type of utilization, depth of the well, year of the measurement, or water flow).

In our case, waters from the townships in the Granada Basin and the close surroundings were selected resulting in the listing of 4360 water points, whose 1749 springs and 2993 water

points with geochemical data. This database is aimed at a wide audience (e.g., farmers, private individuals, and companies) and thus it is not shaped and organized to scientists (hydrologists or geochemists).

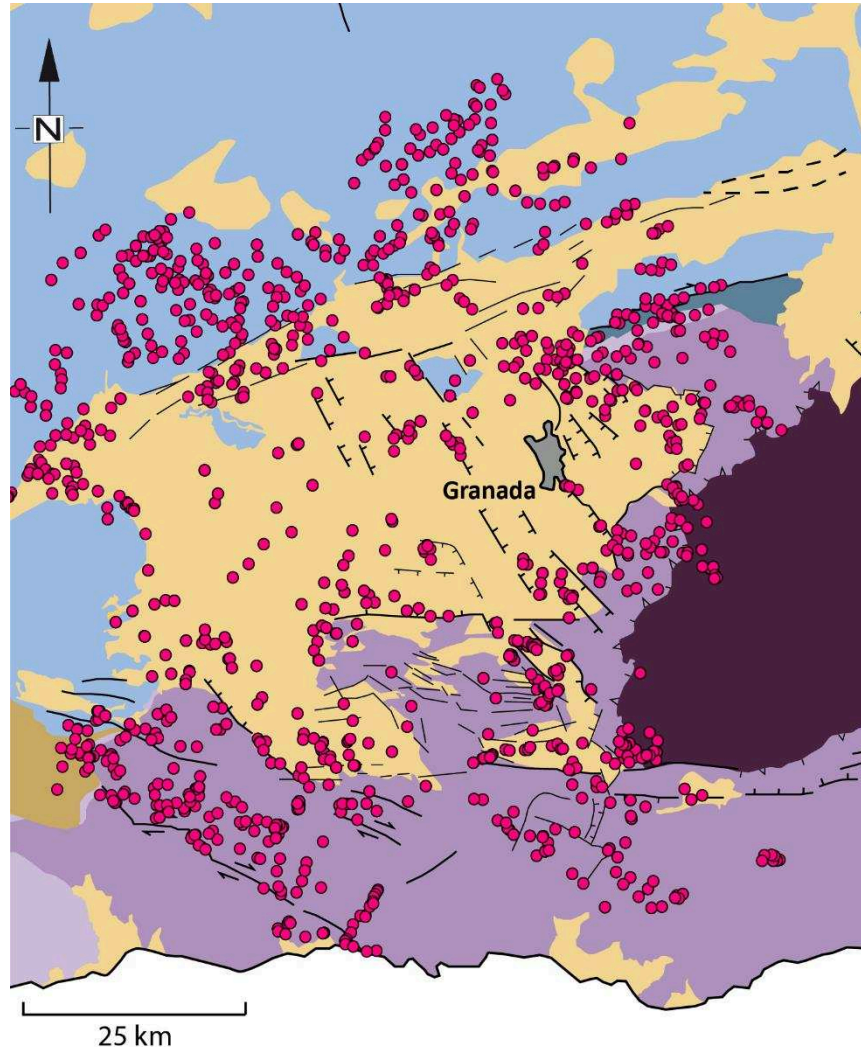


Figure 2-1: Map of the 1749 springs in the Granada Basin and its surrounding. The background geological map has been modified after Sanz de Galdeano and Peláez, (2011).

To deal with this large number of data, I made a numerical code, written in Python, to compile all these data and construct my own geochemical database of the water points, based on the IGME's database, where I grouped the physicochemical data, the location, and the nature of the water points available in the Granada Basin. This code also allows applying several filters to those compiled data with a set of criteria, to proceed to geochemical calculations, and to generate graphical outputs from several thousand data available in the Granada Basin (Figure 2-2). This code was created in the first place to select sampling points whose water geochemistry could complete my first conceptual geochemical model of fluid circulation within

the basin. It is an effective and fast tool to explore the large quantity of data in our possession and also to valorize the data collected after the analyses thanks to the graphical outputs.

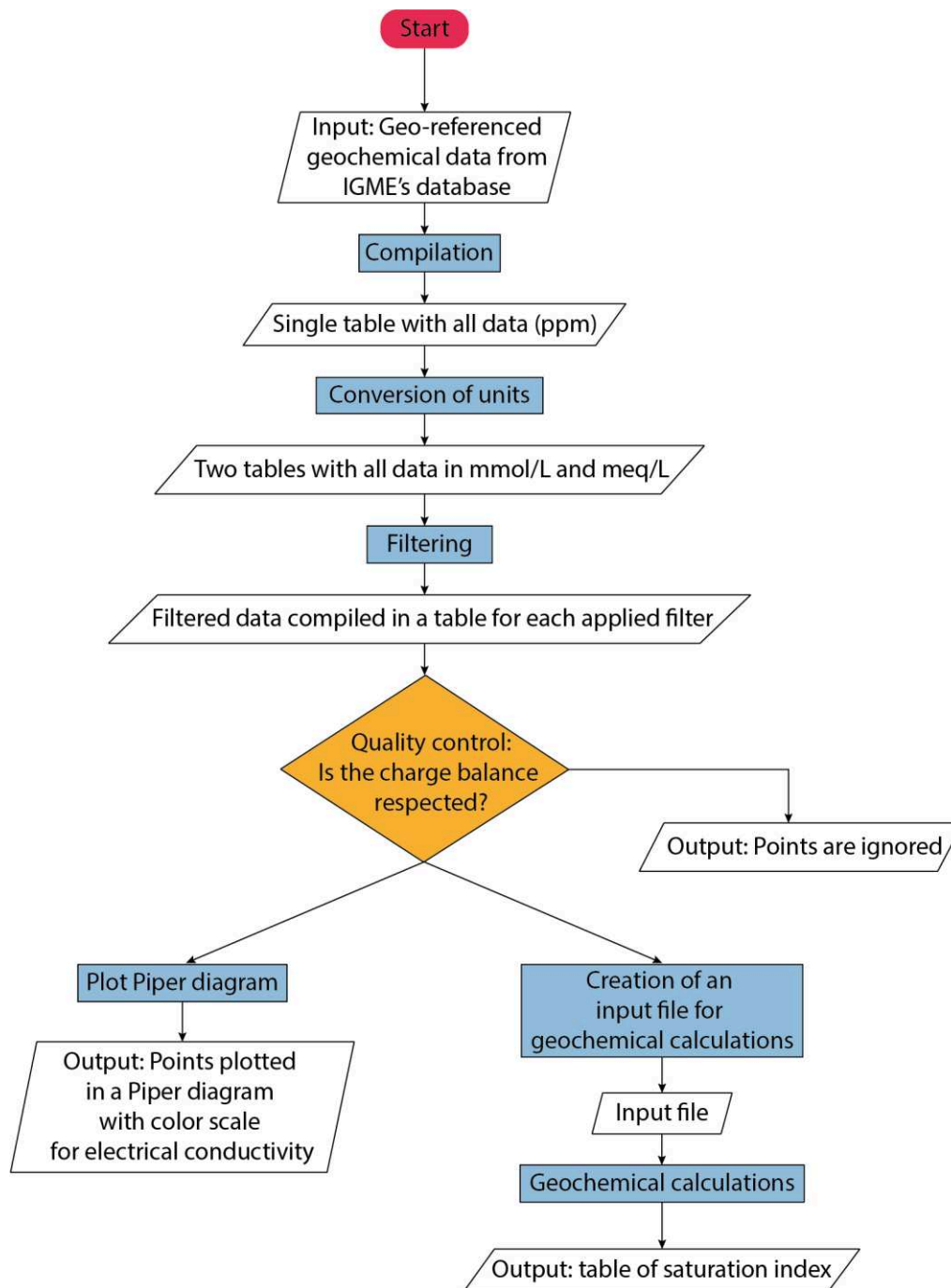


Figure 2-2: Algorithm scheme of the developed numerical program.

2.1.2. Water sampling

Thirty water samples were collected in the Granada Basin and in the Betic Cordillera, from 20 springs and 10 well heads. Two wells were artesian whereas the other water samples were pumped. Although the overall depth of the wells is usually known, it is difficult to estimate the

depth from which water comes from because of possible incomplete tubing. Some of the wells that were planned to sample were clogged at our arrival because of improper water for drinking purpose. Thanks to the support of the IGME team, it was possible to sample other wells. The GPS coordinates of the water points and their type specifications are indicated in the Chapters 3 to 5.

Specific precautions were taken during the selection of the sampling area including avoiding iron tubing for wells and at the outlet of the spring or making sure to have a sufficient flow rate. Ten polypropylene capped Falcon® tubes of 14 mL were filled for each spring to subsequent analyses (cations, anions, trace elements, Al). The water samples were filtered with 0.45 µm membrane filters immediately after sampling to prevent loss of constituents through precipitation and sorption. Samples assigned to trace elements and Al analyses were filtered with 0.2 µm membrane filters to remove colloidal oxyhydroxides of iron and manganese and clay particles, which can pass through larger pores. The water samples dedicated to cations, minor and Al analyses were acidified using suprapure nitric acid (HNO₃). All Falcon® tubes and brown glass bottles were sealed with parafilm to avoid evaporation.

2.1.3. Gas sampling

The sampling of bubbling and dissolved gases was carried out in twelve water points in the Betic Cordillera, located along tectonic boundaries and faults, and within the Granada Basin. Eleven dissolved gas samples were sampled in seven springs and three wells including one artesian and two pumped water samples. Dissolved gases were collected in filling 142 ml glass bottles with the water samples without filtering while taking care not to include air bubble. The glass bottles were sealed under water with silicon/rubber septa to avoid atmospheric contamination.

Four bubbling samples were collected using an upside-down funnel submerged in the water connected to a syringe via a Teflon tube. The gases were then stored in glass flasks with two vacuum stopcocks (Inguaggiato et al., 2016).

This whole sampling process was carried out with the help and the expertise of Claudio Inguaggiato and is detailed in the Chapter 3.

2.2. ANALYTICAL METHODS

2.2.1. Field analyses

2.2.1.1. pH

Measurement of pH was performed with a portable pH-meter (VWR pH110) with a combination pH electrode. The electrode was calibrated with boric acid, potassium chloride and sodium hydroxyde standard buffer solutions of pH 4.0, 7.0 and 10.0 (25°C) (CertiPUR® Reference material). The uncertainty of the measurement was ± 0.1 pH unit.

2.2.1.2. Temperature

Temperature was measured with the probe connected to the pH-meter. The uncertainty of the measurement was $\pm 1^\circ\text{C}$.

2.2.1.3. Electrical conductivity

Electrical conductivity was measured with a portable conductimeter (VWR CO310). The electrode was calibrated with two potassium chloride standard solutions of 1.41 mS/cm and 12.8 mS/cm (25°C) (CertiPUR® Reference material) depending of the conductivity of the sample. The precision of the measurement was considered to be $\pm 5\%$.

2.2.1.4. Alkalinity

Alkalinity was determined on the field by titration with an 0.01M or 0.1M hydrochloric acid solution depending of the encountered alkalinity range. The pH evolution was measured with the VWR portable pH-meter and the HCl solution was added with an Eppendorf pipette (1000 μL). The chemical equilibrium between HCO_3^- and H_2CO_3 was attained with a pH in the range of 4.3 - 4.6. The equivalent volume was determined with the Gran's method (Gran, 1952). The analytical error of the alkalinity measurements is of approximatively $\pm 10\%$.

2.2.1.5. Redox potential and Iron

Redox potential, also known as Eh, was measured with an ORP probe (VWR ORP15). The precision of the measurement is of ± 1 mV. Due to a dysfunction of the device on the field, the redox potential has been only measured for the first seven samples. Another way to assess the

redox potential of the water was through the determination of the total Fe and Fe^{2+} concentrations. The concentrations were determined by colorimetric method with CHEMets® Visual Kit for Fe concentrations ranging from 0 to 1 ppm, and 1 to 10 ppm. The uncertainty of the measurement was of $\pm 10\%$.

2.2.2. Laboratory analyses

2.2.2.1. Waters

I carried out all the analyses of the major and minor elements, as well as the re-titration of the alkalinity and the determination of silica concentration by spectrophotometry at UPMC.

2.2.2.2. Major elements

The major cations and anions (Ca^{2+} , Mg^{2+} , K^+ , Na^+ , SO_4^{2-} , and Cl^-) were analyzed by ionic chromatography with the device Dionex ICS-3000 at the laboratory METIS. Cations and anions were analysed in two separate columns. The concentration of each element was calibrated up to 100 ppm by dilution of the standard material.

The device requires having waters with Total Dissolved Solute (TDS) lower than 10 g/l. Therefore, samples with expected high TDS, estimated from their conductivities, were diluted with MilliQ water by weighting the quantities of samples and MilliQ water. The dilution factors were ranging between 2 and 1000 due to the broad range of ionic strength of the studied waters. Two set of analyses were necessary to find the appropriate dilution factors and fit the calibration curve. A set of internal standards (one for anions and one for cations at 50 ppm) were analyzed every 10 samples to detect analytical errors and the analytical drift of the device through the analyses. Certified reference natural waters ION-96.4 and HAMIL-20.2 were analyzed at the beginning or the end of analyses to detect analytical errors. The uncertainty of Mg, K, Na, SO_4 determination is $\pm 5\%$ whereas that on Ca and Cl is estimated to $\pm 10\%$.

Alkalinity was re-titrated in the laboratory by the Gran's method with a 0.01M or 0.1M hydrochloric acid solution depending of the encountered alkalinity range. I weighted the water samples to get a more precise measure of the alkalinity of the highly saline samples. Duplicate analyses were done for each sample. The analytical error of the alkalinity measurements is of approximatively $\pm 5\%$.

The ionic balance was calculated for each sample, including HCO_3^- determined from

alkalinity, to verify the results. When the balance exceeded 10%, the sample was re-analyzed. The final ionic balance does not exceed 8%.

2.2.2.3. Minor elements

Minor and trace elements (Ba, Sr, Al, Fe) were analyzed by Inductively Coupled Plasma Optical Emission Spectrometry ICP-OES (5100 SVDV Agilent) at the platform ALIPP6 of UPMC Sorbonne Universités. The concentration of each element was calibrated between 1 ppb and 5 ppm by dilution of the standard references materials. The standard of 100 ppb was analyzed every 10 samples to detect analytical errors and the analytical drift of the device through the analyses. A certified reference material (TMDA-64.3 which is a trace element fortified water sample) was analyzed at the beginning or the end of analyses to detect analytical errors. Two wavelengths were investigated for each element in taking into consideration potential interference with other elements mentioned in the software of the ICP-OES.

The device requires having waters with total dissolved solute (TDS) lower than 1 g/l and especially Cl^- concentrations lower than 100 ppm. Therefore, water samples were diluted with MilliQ water by weighting the quantities of samples and MilliQ water. The dilution factors were ranging between 1.5 and 1000 due to the broad range of TDS values of the water samples.

The processing of the results was done manually, checking first the quality of each peak of the calibration and then adapting the calibration range for each element. 6.4 and HAMIL-20.2 were analyzed at the beginning or the end of analyses to detect analytical errors. The uncertainty of Ba and Sr determination is $\pm 10\%$ whereas that on Al is estimated to $\pm 20\%$.

The boron concentration was also analyzed by ICP-OES. However, contamination of the capillaries have been observed for this element due to the use of boric acid employed for rock analyses.

2.2.2.4. Silica

The silica concentrations obtained from the analysis with the ICP-OES were highly underestimated for the certified reference water sample and were therefore ignored. I had to define another analytical protocol to determine the silica concentration. It was therefore determined by spectrophotometric method with the device Milton Roy Spectronic-301. I used the protocol from Centre d'Expertise en Analyse Environnementale du Québec (2016) for these samples as it is suitable for natural groundwater with Si concentration ranging from 0 to 20 mg/l. This colorimetric method allows measuring only the reactive silica, i.e., the portion of

silica reacting with molybdate.

I adapted the protocol for waters with high ionic strength by preparing NaCl-enriched calibration solutions in the same range of ionic strength. Extra care was also taken for iron-rich water samples because of the presence of iron oxide particles in suspension in the filtered waters, which provoke turbidity. I had to re-filtered the waters to remove the particles in order to apply the protocol.

A certified reference material (ION-96.4) was also analyzed to detect analytical errors. As the certified reference ION-96.4 has low Si concentration (0.28 ppm), I used a bottled mineral water at known SiO₂ concentration (15 ppm) as a supplementary standard. The results were compared with respect to the previous measurements available in the literature. The uncertainty on the results was estimated at 10%.

CHAPTER 3

CONSTRAINTS ON THE GEOLOGICAL STRUCTURE OF THE CENTRAL BETIC CORDILLERA FROM GAS GEOCHEMISTRY

CHAPTER 3: CONSTRAINTS ON THE GEOLOGICAL STRUCTURE OF THE CENTRAL BETIC CORDILLERA FROM GAS GEOCHEMISTRY

3.1. PRESENTATION

The initial aim of this work was to investigate the low to medium thermal systems observed in the Central Betic Cordillera and to deduce a potential link with the lithospheric structure. The Central Betic Cordillera is characterized by several occurrences of thermal springs with a greater concentration in the Granada Basin. Recent geophysical works (Mancilla et al., 2015 and Rosell et al., 2011) indicate a possible slab rollback with delamination susceptible to promote mantle influx at shallow depth (< 50 km) beneath the studied area (see Chapter 1). According to geophysical interpretations, the Central Betic Cordillera is also a transition zone between a thick lithosphere in the Iberian domain and a thin lithosphere in the Alboran domain. These structural hypotheses bring into questions the possible mantle influence on the observed thermal springs in the studied area. To test this question, the helium and neon isotopic composition of dissolved and bubbling gases were analyzed in springs in the Central Betic Cordillera.

The lightest noble gas, helium, is chemically inert and characterized by negligible isotopic fractionation during gas-water interaction processes. Those properties make of it a very good tracer of the origin of fluids, both free and dissolved gases. This is possible to isotopically distinguished helium from three well-known sources: the terrestrial atmosphere; the crust with radiogenic production by decay of uranium and thorium; and the mantle containing a primordial signature (Sano and Wakita, 1985). Numerous data of noble gases have been collected in the European Alpine region, including the Alps (Marty et al., 1992), the Apennines (Caracausi and Paternoster, 2015) and the Pannonian Basin (Bräuer et al., 2016; Marty et al., 1992) showing the tectonic control of the noble gas isotopes distribution and especially helium isotopes. However, very little data on noble gases are available in the Betic Cordillera with gas samples collected in two locations in Granada and Almeria provinces (Pérez et al., 1996; Rey et al., 2012).

In this study, we showed that the helium isotopic composition have a dominant radiogenic component in the Central Betic Cordillera with $^3\text{He}/^4\text{He}$ ratios of the dissolved gases ranging

from 0.06 to 0.44 R_A for dissolved gases and $^3\text{He}/^4\text{He}$ in bubbling gases spanning from 0.11 to 1.03 R_A . The mantle-derived He contribution is estimated at mainly 1.4 % for the investigated area. Only one sample, Capuchina de Lanjaron, situated on the important regional contact between Alpujárride and Nevado-Filábride complexes has a He isotopic ratio that could indicate a potential mantle contribution (18 ± 13 %) despite the high air proportion.

To explain these results, I evaluated first the potential He transport mechanisms from the mantle of the surface. First, I estimated He diffusion through the ductile crust and showed that this process appears to be too slow to explain the low mantle-derived He contribution measured at the surface. These results indicate that the crustal system of the Betic Cordillera, is currently dissociated from the mantle system. While considering an advective transport and reanalyzing the available data of the crustal metamorphic complexes, I showed that the estimated advective velocity is on the same order of magnitude than the exhumation rates of the metamorphic complexes. I propose that incorporation of asthenospheric material might have led to a relative enrichment in ^3He during the exhumation of the metamorphic complexes of the Betic Cordillera. This hypothesis is supported by presence of xenoliths in the region. However, the possible source ^3He of the measured He isotopic ratio could also result from crustal production of Li-rich rocks. He mass-balance calculations considering both mantle-derived ^3He and crustal production do not allow excluding one of the two sources. I therefore concluded that the slight ^3He excess observed in the present-day fluids might result from a fossil mantle signature diluted by local radiogenic production over time.

Finally, the results of a new sampling survey of dissolved gases, which was performed in June 2018, are presented at the end of this chapter.

3.2. NEW INSIGHTS ON BETIC CORDILLERA STRUCTURE FROM GAS GEOCHEMISTRY

C. Lix^{1,2,3}, P. Zuddas², C. Inguaggiato⁴, X. Guichet¹, J. Benavente³ and M. Barbier¹

¹ IFP Energies Nouvelles, 1 et 4 avenue de Bois-Préau, 92852 Rueil-Malmaison, France.

² Sorbonne Université, CNRS-INSU, Institut des Sciences de la Terre de Paris, IStEP UMR 7193, F-75000 Paris, Campus Pierre et Marie Curie - 4 place Jussieu 75005 Paris, France.

³ Departamento de Geodinámica e Instituto de Investigación del Agua, Universidad de Granada, Granada, Spain.

⁴ Departamento de Geología, Centro de Investigación Científica y de Educación Superior de Ensenada (CICESE), Carretera Ensenada-Tijuana 3918, Ensenada, Baja California, México.

3.2.1. Abstract

The current lithospheric structure of the Betic Cordillera results from active geodynamic system related to slab retreat slowdown in western Mediterranean. A sharp change in lithospheric thickness has been imaged beneath the Betic Cordillera, potentially resulting from a near-vertical subduction-transform-edge-propagator fault (STEP) towards the surface with possible mantle influx. In this study, we use helium isotopic composition of bubbling and dissolved gases in groundwater samples of the central part of the Betic Cordillera to evaluate the origin of gases and to set constraints on its lithospheric structure. We found that helium isotopic composition have a dominant radiogenic component with a mantle-derived He contribution reaching mainly 1 % for the investigated area. Estimation of He diffusion within the ductile crust indicates that this process is potentially too slow to explain the low mantle-derived He contribution measured at the surface. A new analysis of the available data of the crustal metamorphic complexes allows us to suggest that the crust could be dissociated from the mantle with no evidence of asthenospheric influx. The weak mantle He signature could reflect a mantle material earlier incorporated in the crustal metamorphic complexes of the Betic Cordillera during their exhumation. In light of mass-balance calculations, we propose that the slight ³He excess observed in the present-day fluids might result from a fossil mantle signature diluted by local radiogenic production over time.

Reference: Lix, C., Zuddas, P., Inguaggiato, C., Guichet, X., Benavente, J., and Barbier, M. (2018). New Insights on Betic Cordillera Structure from Gas Geochemistry. *Geochemistry, Geophysics, Geosystems*.

3.2.2. Introduction

The Betic Cordillera (Spain) corresponds to the Western European region of the Alpine peri-Mediterranean orogenic belt and forms the Gibraltar arc with the Rif (Morocco) enclosing the Alboran Sea. This region results from the convergence of the Iberian and African plates since the Mesozoic. Several hypotheses have been proposed to explain the geometry and the formation of this tightly arcuate structure including convective removal of thickened continental lithosphere (Platt and Vissers, 1989), delamination of subducted continental lithosphere (Calvert et al., 2000), and slab rollback (Faccenna et al., 2004; and reference therein). Recent tomographic studies supports the theory of slab rollback with (Heit et al., 2017; Mancilla et al., 2015) or without lithospheric delamination (Spakman and Wortel, 2004). The present position of the slab involves a westward slab tearing beneath the Betic Cordillera resulting in large variations of the lithospheric thickness (Mancilla et al., 2015). The Betic Cordillera lithosphere corresponds to a transition zone between the thick Iberian crust and the thin Alboran crust. Mancilla et al. (2018) have recently suggested that this sharp transition would result from a near-vertical subduction-transform-edge-propagator fault (STEP) spreading towards the surface as a flower-shaped tectonic structure in the crust. In contrast, Rosell et al. (2011) proposed that lithospheric tearing might have resulted in a hot asthenospheric material intrusion displayed by a low-resistivity anomaly beneath the cordillera at shallow depth (< 50 km). Both the anomaly and the transition between thick and thin lithospheres are located beneath the Granada Basin and the Sierra Nevada. This area is also characterized by recent active tectonic movements and low to medium enthalpy geothermal springs historically used as thermal baths (baños) (Bufo et al., 2004; López-Chicano et al., 2001a).

In this work, we investigate the noble gas isotopic composition of fluids of the Betic Cordillera to refine our understanding on the structural relationship between mantle, ductile lower crust, and fragile upper crust. Noble gases are inert elements and thus their isotopic composition reflect that of the fluid sources making them excellent tracers of fluids origin (Ballentine et al., 2002). Terrestrial atmosphere, mantle, and crust have distinct helium isotopic ratios. ^3He is a primordial isotope acquired during the Earth accretion and enriched in the mantle over ^4He . This latter is continuously produced by radiogenic decay of U, Th in the crust (Ballentine and Burnard, 2002). Here, we present a study of the chemical composition and helium isotopes of bubbling and dissolved gases in groundwater in the central Betic Cordillera and analyze possible origin of fluid composition in this complex tectonic region.

3.2.3. Geological settings and tectonic framework of the Betic Cordillera

Our sampling area is located in the tectonically active central region of the Betic Cordillera, with a concentration of sampling points in the Granada Basin to the west of the Sierra Nevada massif. Presently, westward tectonic movement actively deforms the Sierra Nevada with higher displacement in the western part (Galindo-Zaldívar et al., 2015). The Granada Basin is an active Neogene intramountainous basin in the Betic Cordillera with NW–SE to NNW-SSE normal faults dipping westwards.

Two main parts may be distinguished into the complex structure of the Betic Cordillera: (1) the Iberian Domain including the non-metamorphic External Zone and (2) the Alboran Domain corresponding to the metamorphic Internal Zones (Figure 3-1a). The External Zone is separated from the Internal Zone by a major shear zone called the Internal External Boundary Zone (IEBZ, Figure 3-1) (Sanz de Galdeano, 1990). In the NE part of the Granada Basin, this tectonic accident becomes nearly coincident with the so-called Cadix-Alicante faults system (CAFS, Figure 3-1a and 3-1b) extending from 550 km across the Betic Cordillera. This fault system represents one of the major tectonic accidents in the region with crustal discontinuity exceeding 7 km depth (Sanz de Galdeano, 2008 and references therein). Another significant tectonic accident of concern in this study is the so-called Alpujarras fault corridor (AFC, Figure 3-1a and 1b), which has a general E-W dextral strike-slip component and limits the Sierra Nevada massif to the south. The cross-sections I-I' and II-II' (Figure 3-2a and 3-2b) illustrates the westward termination of the Sierra Nevada massif at lithospheric scale. The cross-section I-I' (Figure 3-2a) has been drawn by compiling current interpretations of previous geophysical investigations (Mancilla et al., 2015, 2018, Palomeras et al., 2017; Thurner et al., 2014) and Moho depths determined by Diaz et al. (2016). The cross-section II-II' (Figure 3-2b) has been modified from Crespo-Blanc and Frizon de Lamotte (2006).

3.2.3.1. Iberian Domain

The Iberian Domain is composed of a hercynian basement (Iberian Meseta) and the External Zone, which corresponds to the Iberian paleo-margin cover and is made up of sedimentary rocks deformed into fold-and-thrust belt during the early Miocene (Crespo-Blanc and Frizon de Lamotte, 2006). The Iberian Domain is characterized by a variable crustal thickness increasing from 35 to 40 km from west to east respectively (Diaz et al., 2016;

Mancilla et al., 2015). The transition between the fragile upper crust and the ductile lower crust occurs at around 20 km (Fernández-Ibáñez et al., 2005).

3.2.3.2. Alboran Domain

The Alboran Domain or Internal Zone consists of three stacked metamorphic complexes distinguished from top to bottom by variable metamorphic degree: (1) the Maláguide with low grade metamorphism of greenschist facies (García-Tortosa et al., 2000); (2) the Alpujárride with HP/LT metamorphism of blueschist facies (Azañón and Crespo-Blanc, 2000); and (3) the Nevado-Filábride with HP/LT metamorphism of eclogitic and blueschist facies (Gómez-Pugnaire and Fernández-Soler, 1987). The accretion and the exhumation of the Alboran Domain occurred during the pre-Miocene intracontinental collision and the early Miocene extensional phase, respectively (Azañón and Crespo-Blanc, 2000; Martínez-Martínez and Azañón, 1997). This accretion event was coeval with thin-skinned thrusting of the External Zone. During the Miocene exhumation, the metamorphic complexes were re-organized by low-angle normal faults shaping the present-day upper crust (Booth-Rea et al., 2004b). The base of the Alpujárride Complex in the western part of the Betic Cordillera is characterized by the presence of structurally intercalated bodies of peridotite (Tubía et al., 1992) (Figure 3-1a). Today, the depth of Alboran Domain Moho is estimated to be at ~ 20-25 km depth (Diaz et al., 2016; Mancilla et al., 2015).

3.2.3.3. Neogene Basins

The Iberian and Alboran domains are the basement of several intramountainous basins (e.g. Tabernas, Sorbas, Guadix-Baza, Granada), which were formed during the last ~13 Myr (Braga et al., 2003). The infilling of these basin includes a variety of rocks, mainly clayey conglomerates, calcareous sandstones, marls and silts, gypsum/anhydrite (and locally halite), lacustrine limestones, cemented breccias and alluviums from bottom to top. Significant southwestward displacement is currently observed in the Granada Basin due to extensional deformation, whereas the eastern basins display low movements (Galindo-Zaldívar et al., 2015).

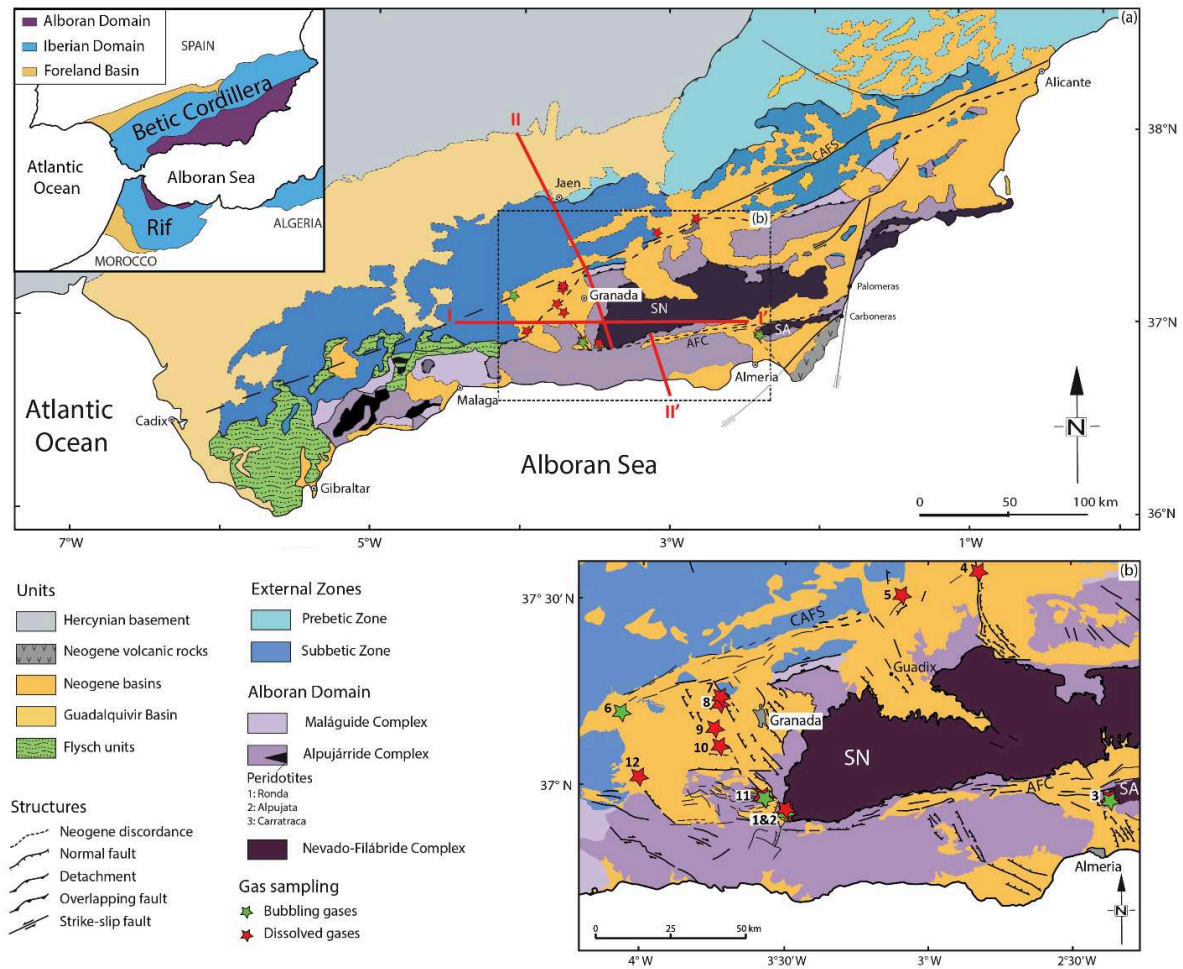


Figure 3-1: (a) Structural map of the Betic Cordillera (Spain) including the main lithological units and structures. Bold red lines shows the location of the cross-sections presented in Figure 3-2 and discussed in text. Structural map modified after Augier (2004). Inset indicates the main tectonic domains of the peri-Alboran orogenic system modified after Janowski et al. (2016). (b) Detailed structural map of the Central Betic Cordillera, modified after Sanz de Galdeano and Peláez (2011), showing the main tectonic domains and faults. SN and SA are Sierra Nevada and Sierra Alhamilla massifs respectively. Sampling points are: (1) Baños Salado de Lanjaron, (2) Capuchina de Lanjaron, (3) Baños Alhamilla, (4) Baños Zujar, (5) Baños Alicun de las Torres, (6) Frontil, (7) Sierra Elvira, (8) Vivero Arco, (9) Baños Santa Fe, (10) Salinas la Malaha, (11) Baños Urquizar Grande and (12) Baños Alhama de Granada.

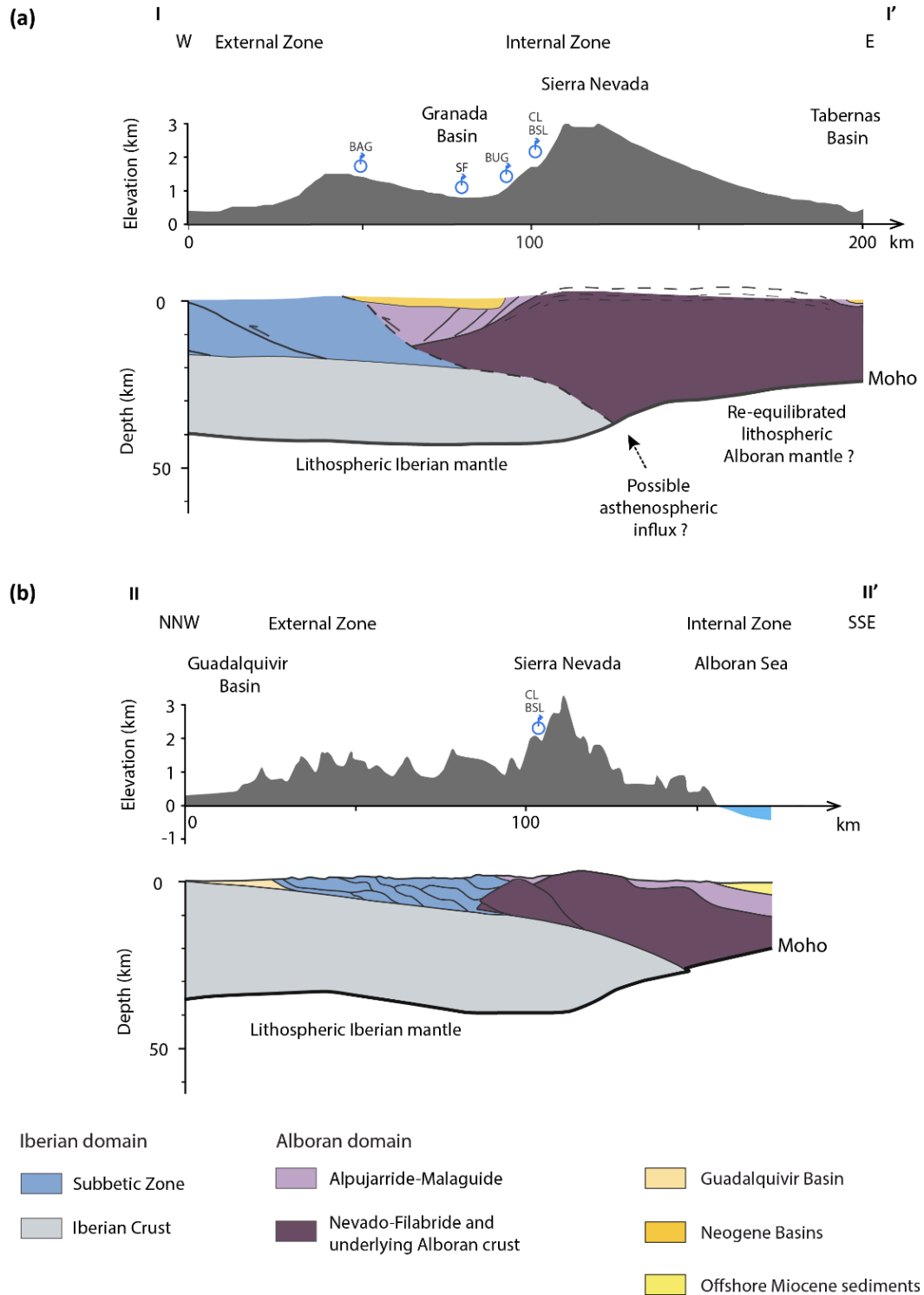


Figure 3-2: (a) Original W-E cross-section showing the lithospheric structure of the Betic Cordillera. Five sampling points have been projected on the topographic section. Moho profile was constrained using Diaz et al. (2016)'s data from deep seismic sounding experiments and receiver functions studies. (b) NNW-SSE cross-section of the Betic Cordillera modified from Crespo-Blanc and Frizon de Lamotte (2006). Two sampling points have been projected on the topographic section.

3.2.4. Materials and Methods

3.2.4.1. Sample location

We sampled bubbling and dissolved gases in twelve locations of the central Betic Cordillera. Nine springs and three wells were selected over ~ 200 km along the main tectonic boundaries (Figure 3-1b). Baño Salado de Lanjaron and Capuchina de Lanjaron springs (points 1 and 2) are located in the Sierra Nevada along the detachment between Nevado-Filábride and Alpujárride complexes. Baños Alhamilla spring (point 3) is situated further to the east in the Sierra Alhamilla along the same tectonic contact, where it intersects the trace of an important strike-slip fault of near N30E direction. Baños de Zujar, Baños de Alicun de las Torres, Frontil, Sierra Elvira, and Vivero Arco (points 4 to 8) are close to the above mentioned CAFS. The two last points of this group (7 and 8) are also located on the trace of an active fault, belonging to the NW to NNW directed fault system that continues toward the city of Granada. Baños Santa Fe, Salinas la Malaha, Baños Urquizar Grande (points 9 to 11) are also aligned along a fault striking N30E. Finally, Baños Alhama de Granada (point 12), Baños Santa Fe (point 9) are presumably close to the IEBZ.

3.2.4.2. Sampling

At every sampling point, physico-chemical parameters of the waters, including temperature, pH, alkalinity and electrical conductivity (EC) were measured. The collected samples correspond to eleven waters and four bubbling springs.

Waters were collected by filling 142 mL and 242 mL Pyrex glass bottles to analyze chemical composition and helium isotope composition, respectively, of dissolved gases (Capasso and Inguaggiato, 1998; Inguaggiato and Rizzo, 2004). The glass bottles were sealed under water with silicon/rubber septa to minimize the atmospheric contamination (Capasso and Inguaggiato, 1998).

The bubbling gas samples were collected using an upside-down funnel submerged in the water and connected to a three-way valve. The gas accumulated in the funnel was sucked and pushed in the glass flasks (equipped with two vacuum stopcocks) through a syringe connected to the three way valve (Inguaggiato et al., 2016, and references therein).

3.2.4.3. Laboratory gas analyses

Laboratory gas analyses were carried out at the Istituto Nazionale di Geofisica e Vulcanologia - Palermo (Italy). Dissolved gases were extracted following the method described

by Capasso and Inguaggiato (1998) and Inguaggiato and Rizzo (2004). A known volume of host gas was injected into the upside-down glass bottles while drawing out the equivalent water volume through needles. After equilibration for 24 hours allowing the equilibrium partition of gas species between the liquid phase and the host gas phase, a variable gas volume was extracted for analyses by injecting water into the glass bottles.

Elemental and isotopic gas analyses were performed in 15 days from the date of sampling. Gas species (O_2 , N_2 , CH_4 , CO_2 and He) were analyzed by gas chromatography (Clarus 500, Perkin Elmer instrument with Carboxen 1000 columns with a hot wire detector and a flame ionization detector) using Ar carrier gas. The composition of dissolved gases, expressed in cm^3 (STP)/ L_{water} , was calculated taking into account the volume of gas extracted, the volume of water sample, and the solubility of each gas species (Bunsen coefficient in cm^3_{gas} (STP)/ L_{water}). The composition of bubbling gases was expressed in either %vol or ppmv. The uncertainty (1σ) for elemental gases determination is within 5 %.

The gas mixture was purified in a stainless steel preparation line in order to remove all the species except noble gases. He and Ne were then separated from each other by a cryogenic trap first cooled down to $-263.15^\circ C$ to adsorb both species, second rising the temperature at $-233.15^\circ C$ to release helium and to $-193.15^\circ C$ to release neon, and finally separately admitted into the appropriate mass spectrometers. Helium isotope composition and ^{20}Ne concentration were determined by a GVI-Helix SFT mass spectrometer and a ThermoFisher-Helix MC plus multi-collector mass spectrometer respectively (Rizzo et al., 2016, and references therein). For each analytical session, we analyzed at least one standard of He and Ne that had previously been purified from air following the above procedure of separation by cryogenic trap. The uncertainty (1σ) of the $^3He/^4He$ ratio is 3 %, while for 4He and ^{20}Ne is 5 % for both free or dissolved gases. The $^3He/^4He$ isotopic ratio, R , was normalized to atmospheric composition ($R_A = 1.384 \times 10^{-6}$; Clarke et al., 1976) and then corrected for the atmospheric contamination using the following equation:

$$(R/R_A)_c = [(R/R_A)_s * X - 1]/(X - 1) \quad (3-1)$$

where R is the measured ($^3He/^4He$) isotopic ratio, R_A is the air ($^3He/^4He$) isotopic ratio, the subscripts s and c refer to measured and corrected ratios respectively, and X , corresponding to a proportionality factor between the sample and the air isotopic contribution, is estimated by:

$$X = \left(\frac{^4He}{^{20}Ne} \right)_s / \left(\frac{^4He}{^{20}Ne} \right)_{air} \times \beta_{Ne}/\beta_{He} \quad (3-1a)$$

where β are the Ne and He Bunsen coefficients (Weiss, 1971).

3.2.5. Results

3.2.5.1. Fluid composition

Temperatures of the sampled fluids were between 17°C and 51°C with the lowest values observed in the central part of the Granada Basin (Salinas la Malaha and Vivero Arco, 17°C and 20°C respectively). All water samples have EC, pH and alkalinity values ranging from 1.5 to 187.1 mS/cm, 5.8 to 7.4 and 2.53×10^{-3} to 1.29×10^{-2} mol/L respectively. High EC were observed in water samples located near the evaporitic rocks of the Granada Basin. Capuchina de Lanjaron differs from the others sampling points because of higher alkalinity (1.29×10^{-2} mol/L) and lower pH (6.1).

The chemical composition of dissolved and bubbling gases is displayed in Figure 3-3 and the data table is presented in Appendix. We found that the proportion of CO₂ is close to 15 % in the sedimentary Granada Basin and reaches 50 % along the Cadix-Alicante fault system. Baños Salado and Capuchina de Lanjaron springs, located near the detachment between the Nevado-Filábride and the Alpujarride complexes, have more than 95 % of CO₂.

3.1.1.1. Noble gases

The concentration and isotopic composition of He are reported in Table 3-1. In both dissolved and bubbling gases, we found that He concentration ranges by two orders of magnitude reaching values up to 5.34×10^{-3} cm³ (STP)/L_{water} and 120.76 ppmv respectively and are significantly higher compared to both air-saturated water (ASW) and air. We found that He concentration exceeds 1.46×10^{-3} cm³ (STP)/L_{water} when the water temperature is above 30°C, whereas it is lower than 6.21×10^{-4} cm³ (STP)/L_{water} when water temperature is under 25°C. The helium isotopic composition of the dissolved gases ranges from 0.06 to 0.44 R_A, while ³He/⁴He in bubbling gases spans from 0.11 to 1.03 R_A. The ⁴He/²⁰Ne ratio ranges from 0.40 to 32.87 and 0.46 to 10.46 for dissolved and bubbling gases, respectively. Four samples have a ⁴He/²⁰Ne ratio lower than 1, reflecting a He atmospheric contribution of more than 20 %. The air-corrected helium isotopic compositions (³He/⁴He)_c of both dissolved and bubbling gases display much lower values, ranging from 0.017 ± 0.007 to 0.106 ± 0.004 R_A.

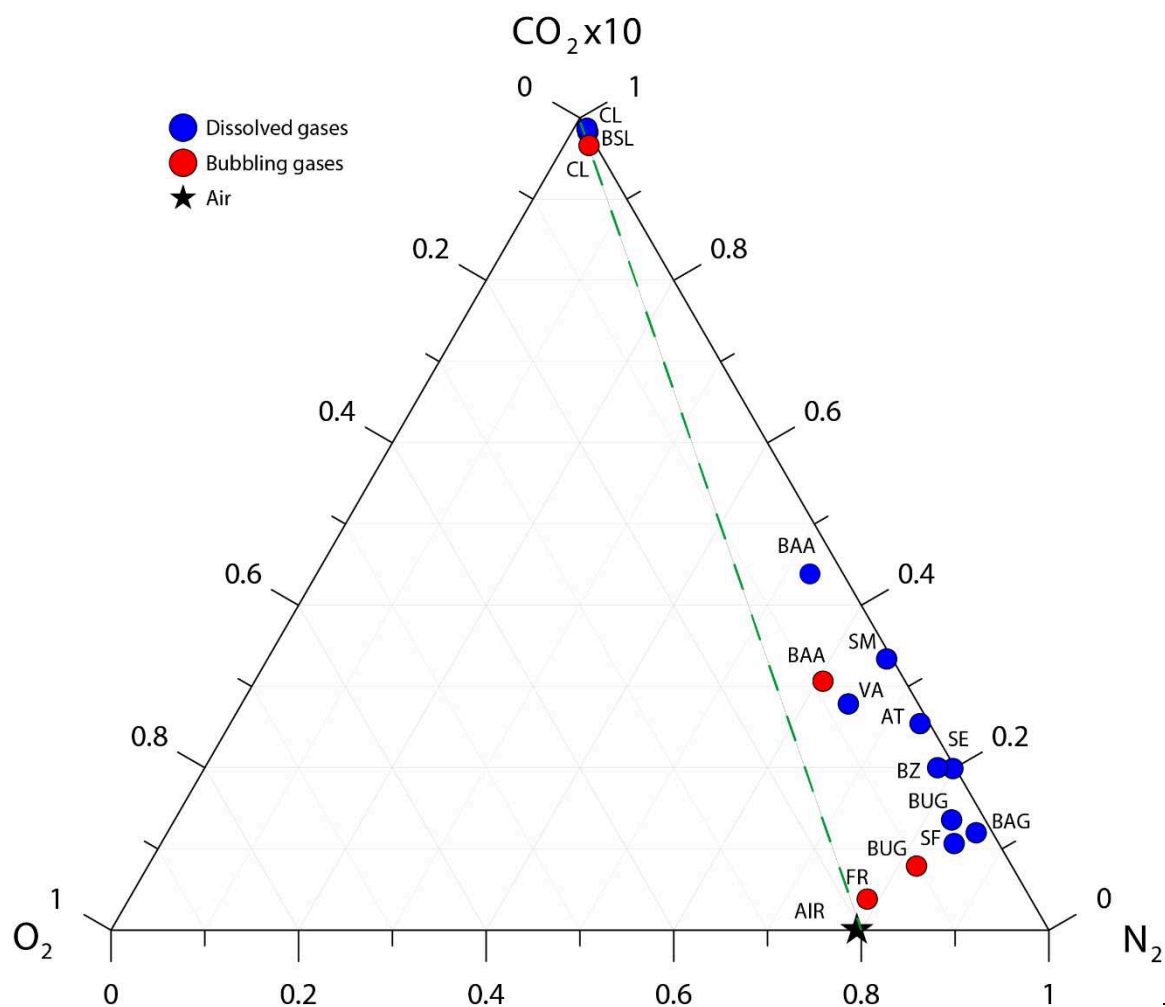


Figure 3-3: Triangular plot of the relative pressure of CO_2 , N_2 , and O_2 . The air value is also reported for comparison; the green dotted line represents the theoretical mixing between air dominated system and CO_2 -rich fluid.

Sampling points ^a	Code	Ref. number	T (°C)	pH	EC ^b (mS/cm)	Alkalinity (x10 ⁻³ mol/L)	Gas type ^c	He ^d	³ He/ ⁴ He ^e	(³ He/ ⁴ He) _c ^f	⁴ He/ ²⁰ Ne
Baños Santa Fe (W)	SF	9	39	7.0	4.69	2.58	D	1.46E-3 (7)	0.067 (2)	0.024 (4)	5.9 (3)
Sierra Elvira (S)	SE	7	30	6.9	3.82	3.77	D	1.74E-3 (9)	0.083 (2)	0.057 (3)	9.2 (5)
Vivero Arco (W)	VA	8	17	7.1	2.01	7.44	D	9.1E-5 (5)	0.44 (2)	na	0.40 (2)
Baños Alicun de las Torres (S)	AT	5	34	6.7	2.24	7.94	D	3.3E-3 (2)	0.119 (4)	0.106 (4)	18.1 (9)
Baños Alhama de Granada (S)	BAG	12	40	7.4	1.13	3.05	D	2.0E-3 (1)	0.135 (4)	0.105 (5)	7.8 (4)
Baños Salado de Lanjaron (S)	BSL	1	26	5.8	8.18	4.72	D	1.66E-4 (8)	0.158 (5)	na	1.04 (5)
Baños de Zujar (W)	BZ	4	35	6.8	12.82	2.06	D	5.3E-3 (3)	0.057 (2)	0.049 (2)	33 (2)
Salinas Malaha (S)	SM	10	20	6.8	187.10	3.81	D	nm	nm	na	nm
Baños Alhamilla (S)	BAA	3	51	7.1	1.92	4.32	D	1.54E-3 (8)	0.124 (4)	0.071 (5)	4.9 (2)
							B	121 (6)	0.108 (3)	0.083 (4)	10.5 (5)
Baños Urquizar Grande (S)	BUG	11	23	7.3	1.50	2.89	D	6.2E-4 (3)	0.096 (3)	0.017 (7)	3.0 (2)
							B	46 (2)	0.165 (5)	0.06 (1)	2.6 (1)
Capuchina Lanjaron (S)	CL	2	21	6.1	34.15	12.87	D	nm	nm	na	nm
							B	3.1 (0.2)	1.03 (3)	1.1 (5)	0.46 (2)
Frontil (S)	FR	6	17	7.5	0.67	6.15	B	14.3 (7)	0.43 (1)	0.06 (8)	0.72 (4)

Notes. nm = not measured. na = not applicable.

1σ uncertainties are displayed as last significant figures in parentheses.

^aSample collected in: Spring (S) and Well (W).

^bEC: electrical conductivity.

^cB: bubbling gas. D: dissolved gas.

^dHelium concentrations are expressed in cm³ (STP)/L_{water} for dissolved gases and in ppmv for bubbling gases.

Standard conditions are p = 101.325 kPa and T = 25°C.

^eHelium isotopic composition is expressed as R/R_A, where R is the ³He/⁴He ratio of the samples normalised to the atmospheric ratio (R_A = 1.39 x 10⁻⁶).

^fHelium isotopic composition, expressed as R/R_A, corrected for the atmospheric contamination

Table 3-1: Physical and chemical parameters of the waters sampling sites and helium isotopic composition of dissolved and bubbling gases

Plotting the measured $^3\text{He}/^4\text{He}$ ratio versus the $^4\text{He}/^{20}\text{Ne}$ ratio for both dissolved and bubbling gas samples (Figure 3-4), we found that our samples can be described by a mixing proportion between three end-members: air or ASW, crust, and mantle. We assume that the crust end-member has a $^3\text{He}/^4\text{He}$ ratio value of $0.02 \pm 0.01 R_A$ (Sano and Marty, 1995) and a $^4\text{He}/^{20}\text{Ne}$ ratio ranging from 900 to 10,000 (Sano and Wakita, 1985). The mantle $^3\text{He}/^4\text{He}$ ratio is here assumed to be equivalent to that of the sub-continental lithospheric mantle (SCLM) of $6 \pm 0.9 R_A$ (Gautheron and Moreira, 2002). The atmosphere-derived ratios are well constrained ($^3\text{He}/^4\text{He} = 1 \pm 0.0009 R_A$ and $^4\text{He}/^{20}\text{Ne} = 0.318$ for air; $^3\text{He}/^4\text{He} = 0.983 R_A$ and $^4\text{He}/^{20}\text{Ne} = 0.285$ for ASW; Benson and Krause, 1980 and Ozima and Podosek, 2002). However, excess of air might be present in water due to bubbling effect with consequent lowering of the $^4\text{He}/^{20}\text{Ne}$ ratio down to 0.19 (Gilfillan et al., 2011; Kipfer et al., 2002).

Plotting our data on mixing lines between air-crust-SCLM end-members, we found that the majority of He in our fluids results from a mixing of atmosphere-derived and 1 % mantle – 99 % crust end-members with an atmospheric contribution mainly spanning between 1 and 10 % (Figure 3-4). The uncertainty in the mixing proportion is represented in Figure 3-4 by the surface area around the hyperbolas.

We estimated more precisely the mantle contribution in the binary mantle/crust system using the constrained mantle and crustal $^3\text{He}/^4\text{He}$ end-members and the air-corrected $^3\text{He}/^4\text{He}$ ratio. The mantle contribution of He in samples AT, SE, BAG, BAA, and BZ varies between 0.5 ± 0.2 and 1.4 ± 0.3 %. The samples VA, FR, BSL, BUG, and SF have a mantle contribution lower than 0.3 ± 0.2 %, fitting on the mixing line between air/ASW and crust end-members (Figure 3-4). However, we found that Capuchina de Lanjaron, situated on the important regional contact between Alpujárride and Nevado-Filábride complexes has a He mantle contribution of 18 ± 13 % and more than 95 % of CO_2 . The He isotopic ratio could indicate a potential mantle contribution despite the high air proportion.

Estimations of 0.5 to 1.4 % magmatic fluids in 5 samples within the 1σ uncertainty can be considered as a minimum given the possible excess air in water samples and the potential presence of crustal ^{20}Ne . Both assumptions would decrease the air correction and increase the mantle contribution (0.1 % rise assuming the $^4\text{He}/^{20}\text{Ne}$ ratio of our samples to be 30 % higher).

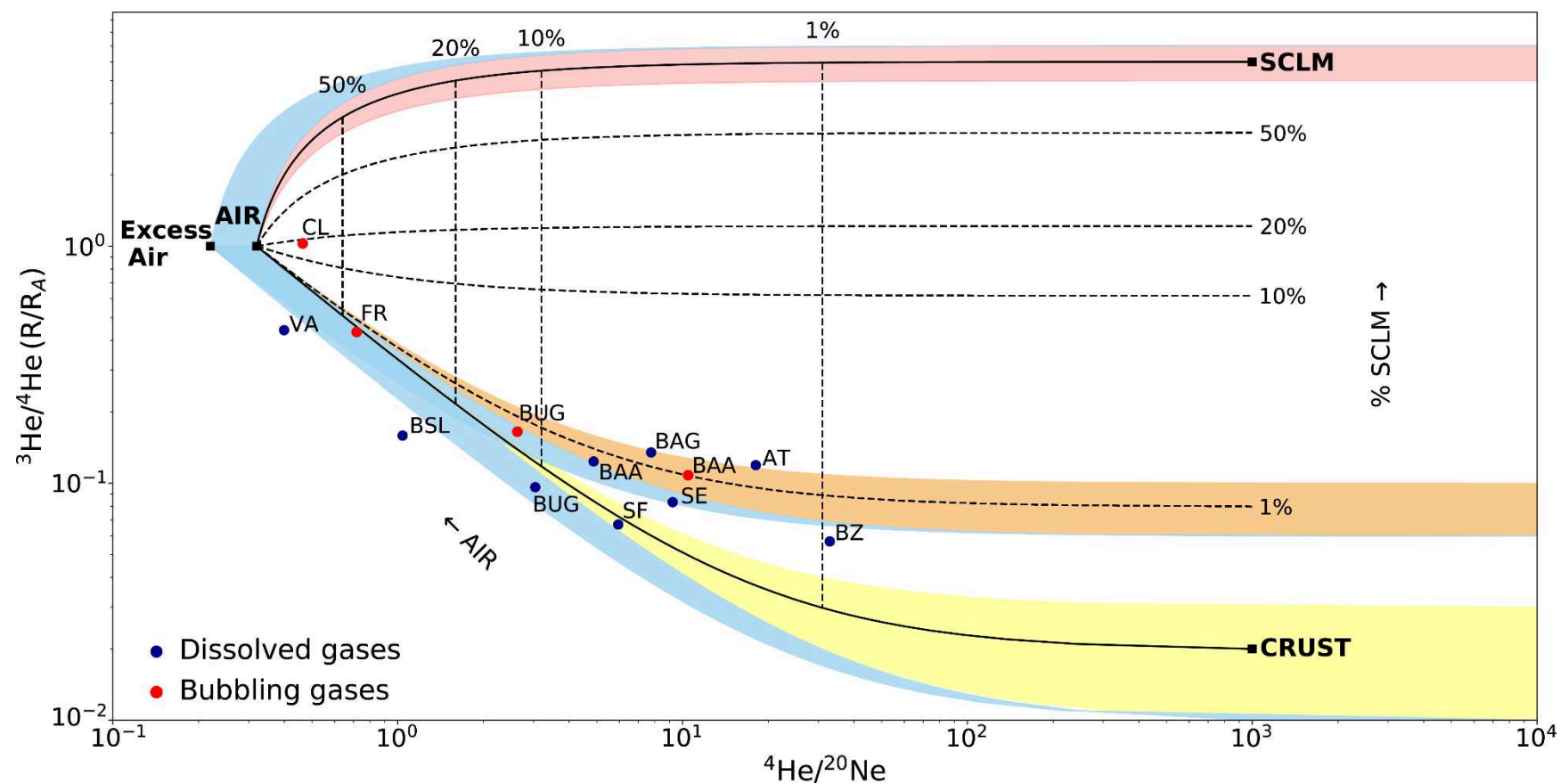


Figure 3-4: $^3\text{He}/^4\text{He}$ (R/R_A) values vs. $^4\text{He}/^{20}\text{Ne}$ ratios diagram. The uncertainties (1σ) are within the size of the symbols.

3.1.2. Discussion

Helium in surface manifestations along the Betic Cordillera has only 1.4 % maximum mantle contribution. This calls in question which transport mechanism can cause this anomaly. We initially test a simple diffusion mechanism and thus He transport processes that were constrained by tentative mass-balance calculation.

3.1.2.1. A possible He diffusion mechanism

We initially test whether diffusion in the ductile lower crust could be a viable transport mechanism for mantle-derived helium. We assume that ^3He diffuses from the mantle into the ductile lower crust before being advected in the upper crust through the major faults. Based on our cross-sections (Figure 3-2), we estimate the minimum distance (d) for mantle-derived helium to cross the lower crust at 25 ± 10 km. The characteristic time of He degassing can be evaluated considering the thermal event dated at 20 Ma in the Alboran Domain related to the beginning of both extensional phase and metamorphic exhumation (Vergés and Fernández, 2012). Considering a 1D diffusion model, the ^3He concentration within the ductile lower crust has been evaluated by an analytical solution of the diffusion equation expressed by the following equation:

$$C(z, t) = C_m + (C_s - C_m) \times \text{erf}\left(\frac{z}{2\sqrt{Dt}}\right) \quad (3-2)$$

where $C(z, t)$ is the ^3He concentration within the ductile lower crust at time (t) and distance from the Moho (z); $C_s = C(d, 0) = 0$ is the initial ^3He concentration at the lower-upper crust limit; $C_m = C(0, t)$ is the mantle-derived ^3He concentration constant, and D is the apparent He diffusion coefficient.

Equation 3-2 yields an apparent He diffusion coefficient D ranging from 2.7×10^{-8} to $1.5 \times 10^{-7} \text{ m}^2 \cdot \text{s}^{-1}$ when considering: the minimum 1 % mantle-derived helium measured at the surface and a time range of 20 Myr (e.g., $C(d, 20 \text{ Myr}) = 1 \% C_m$). To apprehend the validity of this calculation, we compare our estimated apparent He diffusion coefficient to that in minerals and pore waters potentially present in the lower crust. Crystal lattice diffusion is an extremely slow process in minerals like muscovite and hornblende, which could be representative of the lower crust, with helium diffusion coefficient close to $10^{-12} \text{ m}^2 \cdot \text{s}^{-1}$ at 500°C (Lippolt and Weigel, 1988). Helium diffusion coefficient in He-rich minerals (eg, apatite, zircon) ranges between 10^{-11}

10^{-15} to 10^{-14} $\text{m}^2.\text{s}^{-1}$ at 500°C (Cherniak et al., 2009). These values are more than 5 orders of magnitude lower than our estimated He apparent diffusion coefficient. For pure water, there is no data of He diffusion coefficient at 500°C . However, the diffusion coefficient of ions having a similar radii-sized (i.e., H^+ and Li^+) in water up to 500°C does not exceed 10^{-8} $\text{m}^2.\text{s}^{-1}$ (Oelkers and Helgeson, 1988). The amount of “free water” in the ductile lower crust generally estimated to be less than 1 % (Hyndman and Shearer, 1989) implying that the He diffusion coefficient should be reduced by several orders of magnitude.

The result of this calculation supports the hypothesis that diffusion alone is not efficient enough to transport ^3He from mantle to fragile upper crust in the Betic Cordillera indicating that other mechanisms such as advection and/or convection could control the eventual mantle-derived He transport in this complex geological region.

3.1.2.2. Overall He transport and structural evolution of the Betic Cordillera

In order to constrain He transport mechanisms in the area, we scale the previously estimated apparent He transport coefficient to an “advective” velocities (v) using the following Equation 3-3 (Jähne et al., 1987):

$$v = D/(d\varphi) \quad (3-3)$$

where d is the distance that ^3He would have to cross to reach the surface, ranging from 15 to 35 km, and φ is the porosity assumed to be 1 % (Hyndman and Klemperer, 1989).

According to Equation 3, we found an “advective” velocity, representing the average rate at which ^3He should have crossed the complex crustal structure to reach the surface during the last 20 Myr, ranges from 2.4 to 13.2 mm/yr. The velocity estimated here is on the same order of magnitude of the Nevado-Filábride Complex exhumation rates estimated to be of 0.5 and 2.8 mm/yr (Vergés and Fernández 2012). The complex tectonic and geologic history of the Betic Cordillera is in fact characterized by important vertical displacements of rocks, including burial and exhumation of the metamorphic complexes, since the early Miocene.

Reanalyzing the pressure-temperature exhumation paths of the Alpujárride and Nevado-Filábride complexes from thermo-barometric data of Augier et al. (2005), Azañón and Crespo-Blanc (2000), and Gómez-Pugnaire and Fernández-Soler (1987) we found that:

At ~ 20 Ma, the Alpujárride and Nevado-Filábride complexes, previously dragged into the subduction channel, might be located down to 30 and 40 km depth respectively according to thermochronology data (Augier et al., 2005; Janowski et al., 2016, and references therein).

Since the Nevado-Filábride Complex was close to the Alboran asthenospheric mantle and heated subducted material allows movement of low viscosity rocks inside the accretionary complex (Jolivet et al., 2003), asthenospheric materials could be easily incorporated. This process is in agreement with the presence of serpentinite layers found in the Nevado-Filábride Complex (Dyja-Person et al., 2018) and is also consistent with the known peridotite massifs and xenoliths, with low $^3\text{He}/^4\text{He}$ values ranging from 1.4 to 5.7 R/R_A , intercalated into the Alpujarride Complex (Martelli et al., 2011; Tubía et al., 1992).

At ~ 15 Ma, the metamorphic complexes were exhumed initially through a ductile shear zone in the lower crust and then through low-angle detachment faults in the fragile upper crust. This two-stage exhumation model proposed here is in agreement with the results of the thermo-mechanical numerical modeling of Burov et al. (2001) and Jolivet et al. (2003).

Since the Betic Cordillera crust contain mantle-derived material incorporated during its burial and exhumation history, we propose that the 1 % mantle-derived helium found in the present-day fluids results from a progressive degassing of the paleo-asthenospheric material incorporated in the crust. Our study indicates that convective movements associated with the metamorphic complex exhumation appear to be faster than He diffusion through the lower crust. Nevertheless, the different geodynamic models (slab rollback, delamination of the lithosphere, and convective removal of thickened continental lithosphere) responsible for the exhumation cannot be still discriminated.

3.1.2.3. Constraining ^3He origin by mass balance calculations

Although we cannot exclude a low $^3\text{He}/^4\text{He}$ fractionation during release from minerals (Tolstikhin et al., 1999) to explain the measured He isotopic ratio in the Betic Cordillera, the possible source ^3He could result from both mantle material and crustal production of Li-rich rocks.

To assess the volume of mantle-derived material incorporated into the crust, we ideally use a mass balance approach using ^4He crustal production and the ^3He abundance in xenoliths. To assess the ^4He crustal production, we consider an average upper crust composition ($[U] = 2.8 \pm 1.3$ ppm and $[Th] = 9 \pm 3$ ppm) (Rudnick and Fountain, 1995) and a crust density of 2.7 ± 0.1 g/cm³. Using Steiger and Jäger (1977)'s decay constants, we find that ^4He crustal production rate is $7.1 \pm 2.9 \times 10^{-11}$ mol/m³/yr. The $[^4\text{He}]$ in the crust was estimated assuming that the sampled fluids are in closed system conditions with a residence time between 10^3 and 10^5 years. We found that the overall production of ^4He in the crust ranges from 7×10^{-8} to 7×10^{-6} mol/m³.

Since ^3He abundance in mantle-derived materials (MORB and xenoliths) varies between 10^{-14} and $10^{-10} \text{ cm}^3 \text{ (STP)/g}$ (Martelli et al., 2011; Ozima and Podosek, 2002) and assuming a rock density of $3 \pm 0.1 \text{ g/cm}^3$, the $[^3\text{He}]$ spans between 10^{-12} and 10^{-8} mol/m^3 . Thus, the average volume of mantle-derived material that would be incorporated into 1 m^3 of current crustal material should be determined by the proportion between the ^3He abundances and 1 % of the estimated ^4He crustal production. Our estimation gives an average volume of mantle-derived material between $3 \cdot 10^{-2}$ and 10^5 m^3 . The result of this calculation gives partially non-realistic values (volume_{mantle material} > volume_{crustal material}). However, the possible minimum value obtained in this estimation may correspond to an eventual MORB signature. This calculation indicates that the He mass-balance modeling cannot be simply constrained by the mantle He hypothesis alone and that Li-rich rocks potentially present in the crust should be invoked as source of ^3He excess.

In rocks like granite, shale, sandstone, and evaporites, the crustal ^3He production, derived from ^6Li concentration, ranges from at least 1.0×10^{-19} to $1.3 \times 10^{-17} \text{ mol/m}^3/\text{yr}$ (Lehmann et al., 2003; Tolstikhin et al., 2011; Tolstikhin et al., 1996). We estimate the complete He transfer from rock to water under the closed-system assumption, using the following (Tolstikhin et al., 1996) equation:

$$^4\text{He}_{\text{water}} = ^4\text{He}_{\text{rock}} \times \left(\frac{1 - \varphi}{\varphi} \right) \times \left(\frac{\rho_r}{\rho_w} \right) \quad (3-4)$$

where φ is the average porosity assumed to be 3 % for the whole crust, ρ_r is the average rock density assumed to be 2.7 g/cm^3 and ρ_w is the average water density assumed to be 1 g/cm^3 .

We found that the crustal ^3He concentration in water would range from 3×10^{-15} to $4 \times 10^{-11} \text{ mol/m}^3$, whereas the crustal ^4He concentration in water would be between 1×10^{-6} and $3 \times 10^{-4} \text{ mol/m}^3$. In Figure 3-5, we report ^3He and ^4He concentrations in water calculated from crustal production and measured in our samples ($4.1 \times 10^{-6} < ^4\text{He} < 2.4 \times 10^{-4} \text{ mol/m}^3$ and $1.6 \times 10^{-12} < ^3\text{He} < 2.4 \times 10^{-11} \text{ mol/m}^3$).

We found that, considering groundwater residence time of 10^5 yr , the ^3He crustal production is in agreement with the measured values while ^4He crustal production corresponds to the limit of the ^4He measured values. On the other hand, considering a groundwater residence time of 10^4 yr , ^4He crustal production matches the average measured concentrations while ^3He crustal production corresponds to the lower boundary of measured values. This suggests that Li-enriched rocks alone cannot constrain the origin of ^3He excess.

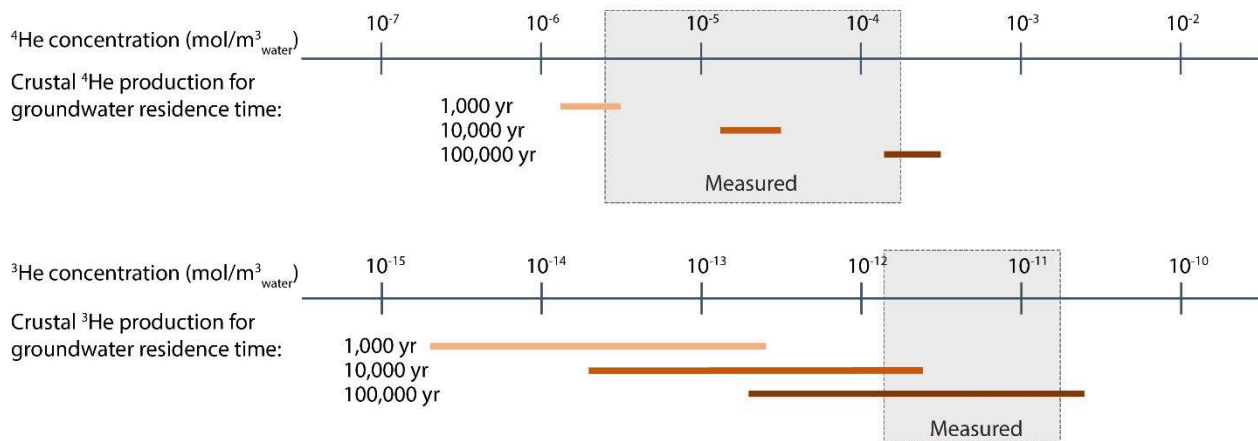


Figure 3-5: Comparison of ^4He and ^3He concentrations in water between measured and calculated values for groundwater residence time of 10^3 , 10^4 and 10^5 years. He concentrations in water from crustal production are calculated with the hypothesis of 3 % porosity.

We finally propose that the ^3He signature observed in our samples might result from both crustal production (related to enriched Li content) and incorporation of mantle material during the exhumation of the metamorphic complexes but the proportion of the two potential sources still remains not evaluated.

3.1.3. Conclusions

Gas geochemistry from groundwater samples have been investigated for the first time in the central Betic Cordillera. Helium isotopic compositions of bubbling and dissolved gases show that the crustal radiogenic He signal is predominant whereas the mantle-derived He contribution reaches mainly 1 %. The helium isotopic signature is relatively homogeneous at the scale of the metamorphic complexes of the Betic Cordillera, although at Capuchina de Lanjaron where a higher He mantle contribution has been detected. Transport of mantle-derived He by diffusion within the ductile lower crust cannot provide a suitable explanation for the observed 1 % mantle-derived contribution measured at the surface, diffusion being a slow process at geological timescale. Therefore, our results show that the crustal system of the Betic Cordillera, is currently dissociated from the mantle system. We propose that, during the exhumation of the metamorphic complexes of the Betic Cordillera, incorporation of asthenospheric material might have led to a relative enrichment in ^3He . The presence of xenoliths in the Betic Cordillera supports this hypothesis, however He mass balance calculations do not allow excluding ^3He production from crustal Li-rich rocks associated to the fossil mantle signature.

3.2. ADDITIONAL DATA

3.2.1. Regional geodynamics

As mentioned in section 1.1.1.1, geodynamics of the Betic Cordillera is still subject to a lot of debates. Although our gas data do not allow a unique solution of the complex geodynamics of the Betic Cordillera, I propose here a detailed schematic chronology in Figure 3-6 using the most commonly accepted hypothesis of slab rollback. In this figure, I reanalyzed the pressure-temperature exhumation paths of the Alpujárride and Nevado-Filábride complexes from thermo-barometric data of Augier et al. (2005), Azañón and Crespo-Blanc (2000), Gómez-Pugnaire and Fernandez-Soler (1987) and the kinematic models from Vergés and Fernández (2012) and Behr and Platt (2012).

At ~ 20 Ma, the Alpujárride and Nevado-Filábride complexes, previously dragged into the subduction channel, might be located down to 30 and 40 km depth respectively according to thermochronology data (Augier et al., 2005; Janowski et al., 2016, and references therein). Since the Nevado-Filábride Complex was close to the Alboran asthenospheric mantle and heated subducted material allows movement of low viscosity rocks inside the accretionary complex (Jolivet et al., 2003), asthenospheric materials could be easily incorporated. This process can explain the presence of serpentinite layers found in the Nevado-Filábride Complex (Dyja-Person et al., 2018) and is also consistent with the known peridotite massifs and xenoliths intercalated into the Alpujárride Complex (Tubía et al., 1992).

At ~ 15 Ma, the metamorphic complexes were exhumed, as a result of the slab rollback and tearing (Augier et al., 2005; Kirchner et al., 2016). The exhumation is initially driven by the formation of a ductile shear zone in the lower crust and pursued with low-angle detachment faults in the fragile upper crust. The proposed two-stage exhumation model is in agreement with the thermo-mechanical numerical modeling of Burov et al. (2001) and Jolivet et al. (2003). Under the W-E extensional conditions occurring at that time, the Nevado-Filábride Complex outcropped in the eastern Sierra Nevada whereas only the Alpujárride Complex was unroofed in the western part, as evidenced by clasts in the sedimentary basins (Braga et al., 2003).

At ~ 10 Ma, the W-E extension still occurred with normal faults responsible for the continuous exhumation of the Nevado-Filábride Complex, which has continued until the present-day.

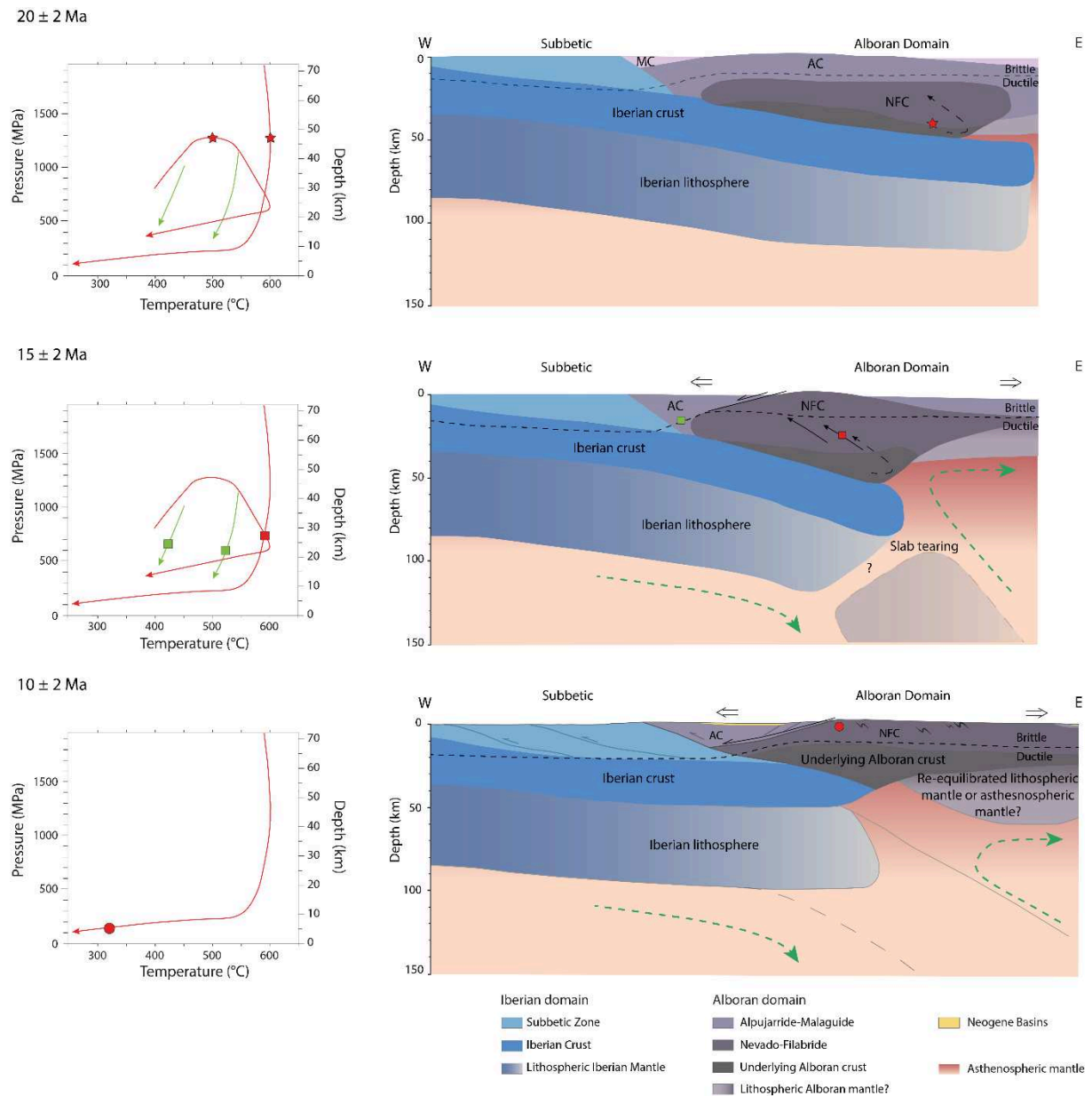


Figure 3-6: Geodynamic evolution of the Betic Cordillera since the last 20 Ma. NFC: Nevado-Filábride Complex; AC: Alpujarride Complex; MC: Maláguide Complex. Insets represents the pressure-temperature exhumation paths for the Alpujarride Complex in green (Azañón and Crespo-Blanc, 2000) and for the Nevado-Filábride Complex in red (Augier et al., 2005; Gómez-Pugnaire and Fernández-Soler, 1987). Green and red symbols correspond to the pressure-temperature conditions of the metamorphic complexes during their exhumation path

3.2.2. Helium crustal production

As mentioned in the article (section 3.1.2.3), it is possible to constrain the crustal He isotopic production in the studied area using the values derived from ^6Li in different rocks forming the Earth crust (e.g. granite, shale, sandstone). The results are presented in Figure 3-7 showing both the crustal He isotopic production for the different rocks and the He isotopic abundances in our water samples.

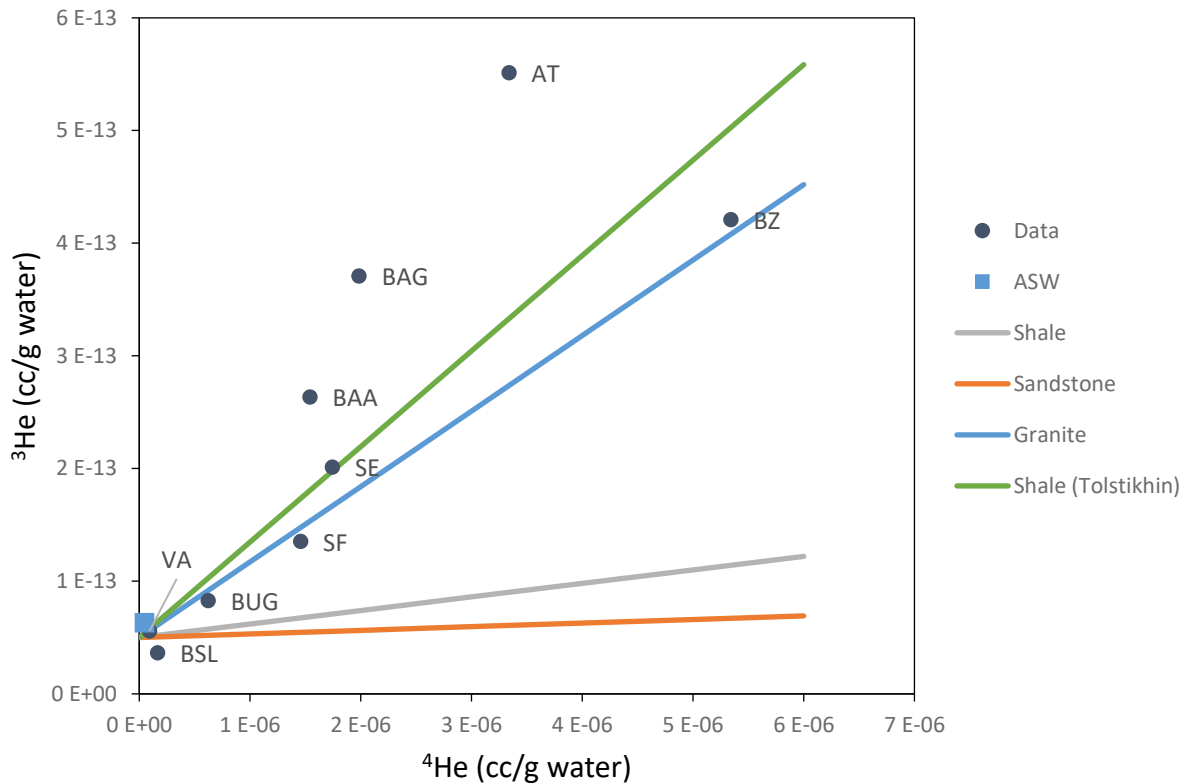


Figure 3-7: Crustal He isotopic production (lines) and measured He isotopic abundance in our water samples (circles). The crustal helium isotopic production is represented for different rocks (shale, granite, sandstone).

3.1.1. Results of a new sampling survey (June 2018)

I carried out a second sampling survey of the dissolved gases in few springs, four in total, in June 2018 to check the results of the first sampling survey and analyze the dissolved gases of another spring on the large accident bordering the southern part of the Sierra Nevada (Alpujaras Fault Corridor, AFC). Our main question was: Is the ~15% He mantle contribution observed in the bubbling gases of the Capuchina de Lanjaron sample significant? This spring is located on the detachment of the metamorphic Nevado-Filabride Complex and might be linked with the AFC. That is why the spring of Fuente Agria de Portugos (FAP), known as a

CO₂-rich spring (Rosino, 2015), has been sampled. The location of the springs is presented in Figure 3-8.

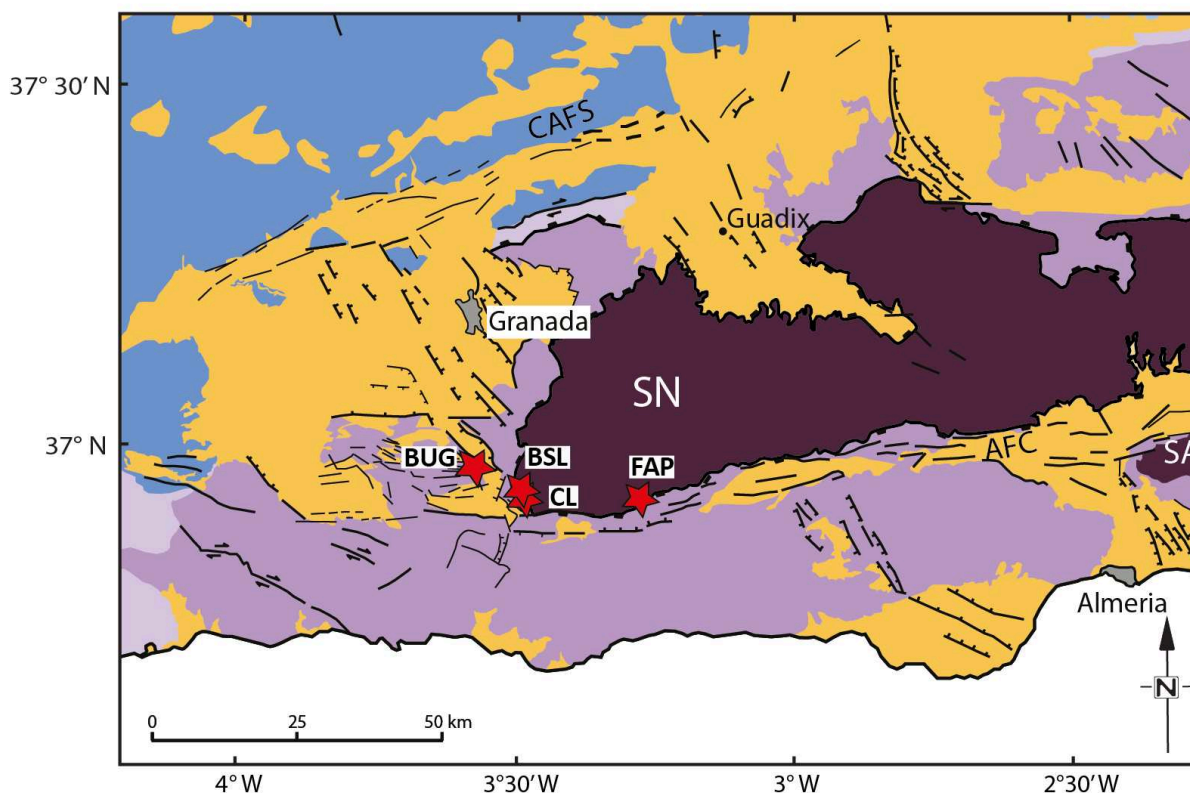


Figure 3-8: Structural map of the Central Betic Cordillera, modified after Sanz de Galdeano and Peláez (2011), showing the main tectonic domains, faults, and the location of the dissolved gas samples collected in four springs during the 2018 survey. SN and SA are Sierra Nevada and Sierra Alhamilla massifs respectively.

The chemical composition of dissolved gases is displayed in Figure 3-9 and the major gases are mainly CO₂ ($\geq 80\%$) and N₂ ($\leq 20\%$). Only three of the four samples have been analyzed because of a broken glass bottle during the shipping. The concentration and isotopic composition of He are reported in Table 3-2. The measured $^3\text{He}/^4\text{He}$ ratio versus the $^4\text{He}/^{20}\text{Ne}$ ratio for dissolved gas samples were plotted in Figure 3-10, together with the values from the 2016 sampling survey for the common sampled points (BUG, CL and BSL). We found that the majority of He in our fluids results from a mixing of the atmosphere-derived and the crust end-members, or a mixing of the atmosphere-derived and 1 % mantle – 99 % crust end-members. All these samples display a quite large atmospheric contribution ($> 10\%$).

Moreover, these results are consistent with those obtained during the first sampling survey in 2016. The radiogenic component of the He isotopic composition is predominant in these samples and the $\sim 15\%$ He mantle contribution observed for the bubbling gas sample of CL in

2016 could not be confirmed with the second sampling.

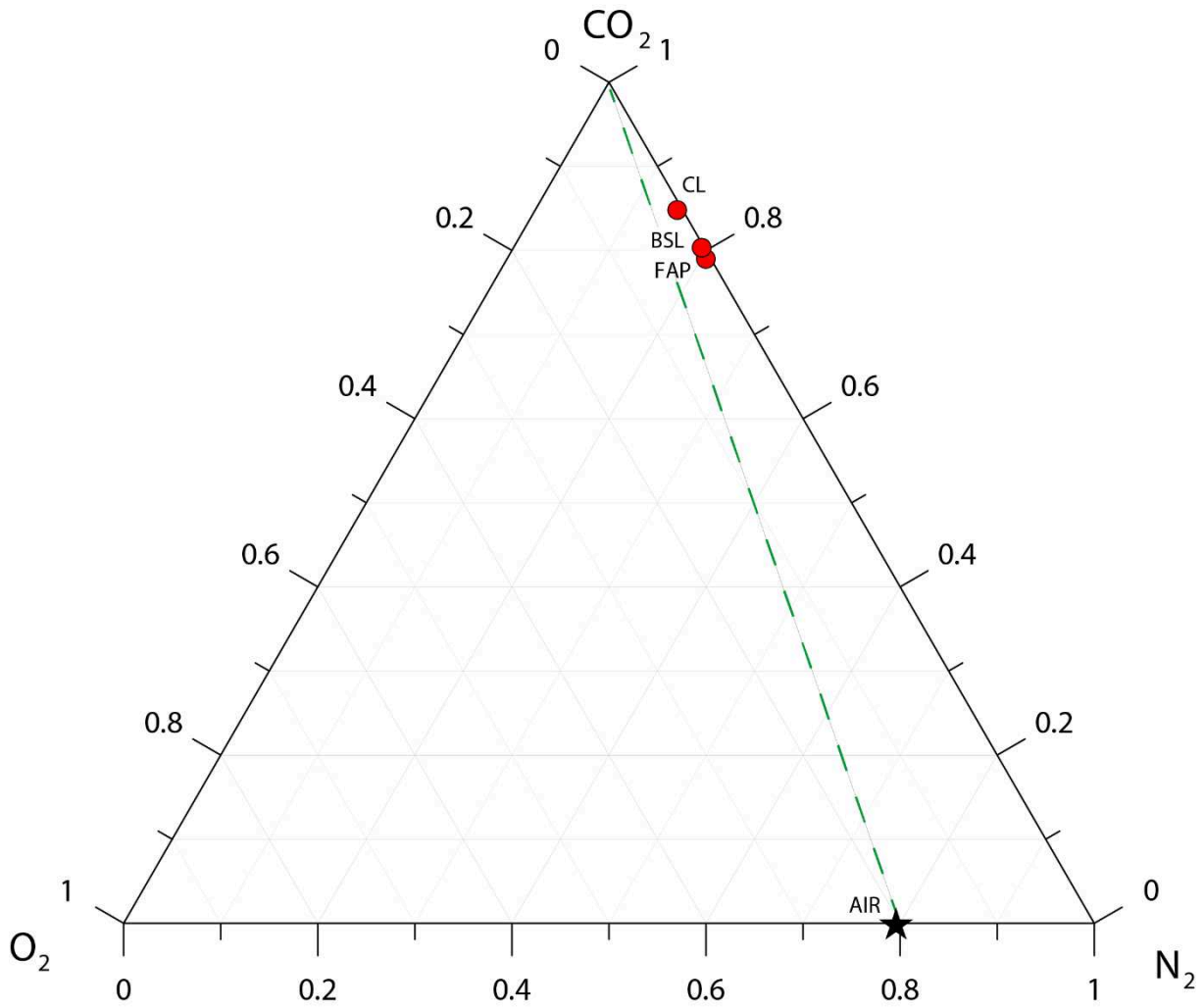


Figure 3-9: Triangular plot of the relative pressure of CO_2 , N_2 , and O_2 . The air value is also reported for comparison; the green dotted line represents the theoretical mixing between air dominated system and CO_2 -rich fluid.

Sampling points	Code	T (°C)	pH	EC ^a (mS/cm)	Alkalinity (x 10 ⁻³ mol/L)	Gas type ^b	He ^c (x 10 ⁻³ cm ³ (STP)/L _{water})	³ He/ ⁴ He ^d	(³ He/ ⁴ He) _c ^e	⁴ He/ ²⁰ Ne
Capuchina Lanjaron (S)	CL	20.5	6.0	25.9	29.85	D	0.0335 (2)	0.75 (2)	0.39 (2)	0.48 (2)
Baños Urquizar Grande (S)	BUG	23.5	7.3	1.15	4.79	D	0.509 (3)	0.156 (2)	0.037 (2)	2.3 (1)
Fuente Agria de Portugos (S)	FAP	14.2	5.24	0.33	3.28	D	0.0612 (3)	0.51 (1)	0.24 (1)	0.82 (4)
Baños Salado de Lanjaron (S)	BSL	25.5	5.7	5.84	12.62	D	0.114 (1)	0.260 (4)	0.141 (7)	2.1 (1)

Notes. nm = not measured. na = not applicable.

1σ uncertainties are displayed as last significant figures in parentheses.

^aEC: electrical conductivity.

^bB: bubbling gas. D: dissolved gas.

^cHelium concentrations are expressed in cm³ (STP)/L_{water} for dissolved gases and in ppmv for bubbling gases.

Standard conditions are p = 101.325 kPa and T = 25°C.

^dHelium isotopic composition is expressed as R/R_A, where R is the ³He/⁴He ratio of the samples normalised to the atmospheric ratio (R_A= 1.39 x 10⁻⁶).

^eHelium isotopic composition, expressed as R/R_A, corrected for the atmospheric contamination.

Table 3-2: Physical and chemical parameters of the waters sampling sites and helium isotopic composition of dissolved gases, which were sampled during the second sampling survey in June 2018.

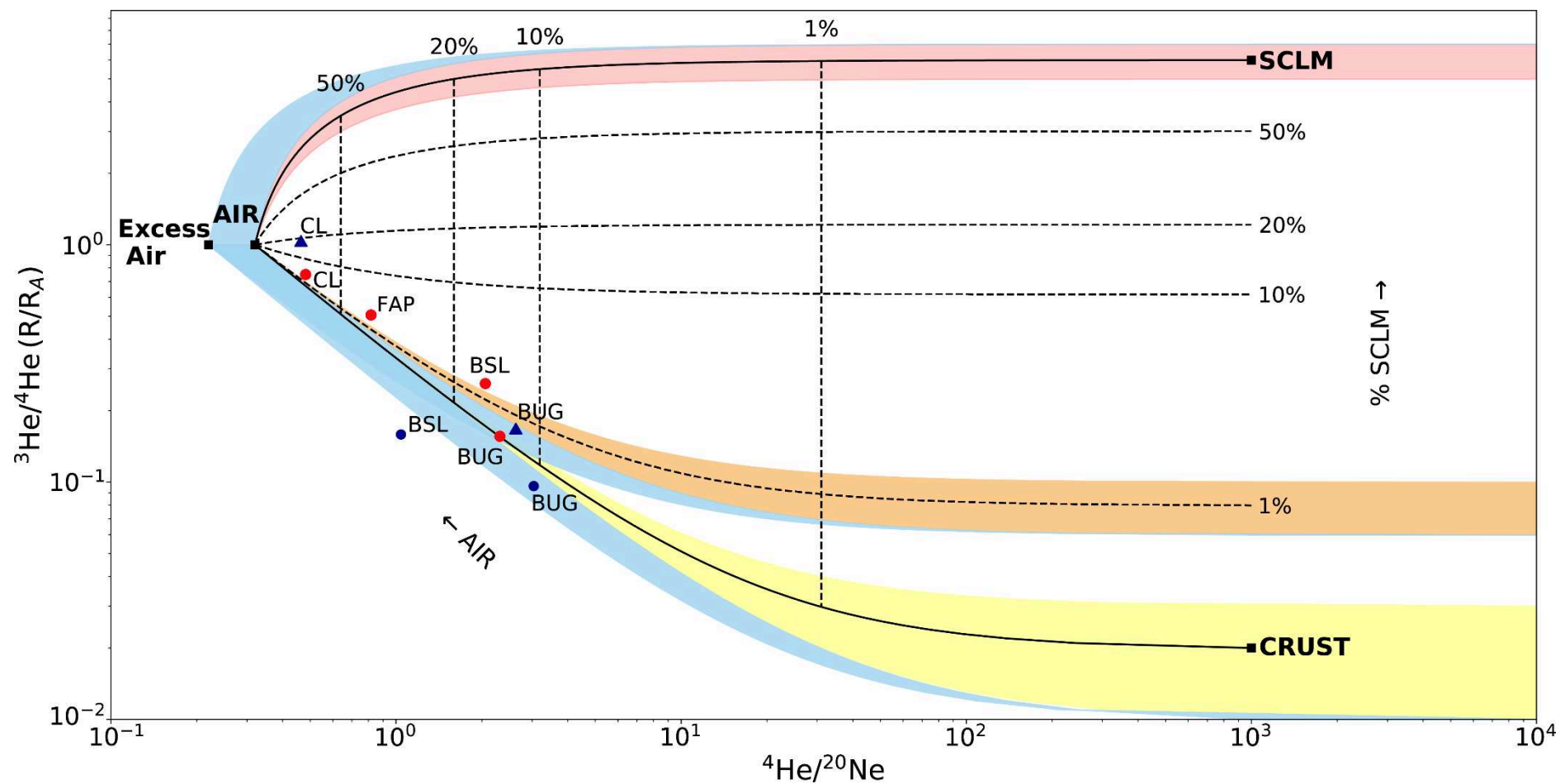


Figure 3-10: $^3\text{He}/^4\text{He}$ (R/R_A) values vs. $^4\text{He}/^{20}\text{Ne}$ ratios diagram. The circles and triangle symbols correspond to dissolved and bubbling gas samples respectively and the blue and red colors designate samples from the 2016 and 2018 surveys respectively. The uncertainties (1σ) are within the size of the symbols.

CHAPTER 4

THERMAL WATERS IN CENTRAL BETIC CORDILLERA

CHAPTER 4: THERMAL WATERS IN THE CENTRAL BETIC CORDILLERA

4.1. PRESENTATION

This chapter focuses on the thermal waters in the Central Betic Cordillera and on the reservoir chemistry and P-T conditions of these waters. As mentioned in section 1.2.4.2, numerous occurrences of thermal waters are displayed in the Central Betic Cordillera, with outlet temperature ranging from 20 to 50°C. Some of these thermal springs have been exploited as bath since the Roman times (~200 B.C.), as well as under the domination of the Arabs from the 8th to 15th century. The use of these thermal waters is restricted to balneotherapy nowadays but the development of heat pumps might be considered in future. These characteristics make of the Granada Basin and the Sierra Nevada one of the region in Andalucía with the highest geothermal potential (Arrizabalaga et al., 2015; Cerón and López-Chicano, 2002; Sánchez Guzmán and García de la Noceda, 2010).

These thermal waters are also mainly located on major tectonic accidents structuring the region, as the Cadix-Alicante fault or the NW-SE fault corridor in the Granada Basin. This is an interesting feature in this region where the geothermal systems are fracture-controlled (i.e. non-magmatic). Although very few reliable data are available in this area (Fernández et al., 1998), no high geothermal gradient or heat fluxes have been reported. Heat flux have been estimated below 50 mW/m² in the Betic Cordillera and the geothermal gradient ranges from 20 to 45°C (Cerón and López-Chicano, 2002).

In addition, these thermal springs evolve in sedimentary environment where the processes resulting from the interaction between water, rock and CO₂ are complex. For example, the relationship between the partial pressure of CO₂ and temperature is still actively questioned in sedimentary environment, as well as the controlling parameters of the degassing or mineralization of CO₂ in this environment.

The objective of this study is to characterize the reservoir geochemistry of the thermal waters in the Central Betic Cordillera and the role of CO₂ this low- to medium- enthalpy thermal systems. To do so, I characterized first the hydrochemistry of thermal waters in the outlet conditions using direct thermodynamic equilibrium calculations. Temperatures in the reservoir were then estimated using chemical geothermometers. Hydrogeochemical modeling were finally performed in open and closed system conditions to assess the chemical composition in

the reservoir conditions and along the water ascent. Two types of buffering mineral assemblages were considered: one with carbonates only, and the other with carbonates and alumino-silicates.

Our result show that three main water groups can be determined in the Central Betic Cordillera depending on the geological features, the temperature, the buffering mineral assemblage, and the $p\text{CO}_2$ in their reservoir. The first group, corresponding to the thermal waters located in the sedimentary basins show temperatures ranging from 70 to 90°C and $p\text{CO}_2$ spanning from $\sim 6 \times 10^{-2}$ and 6×10^{-1} atm in the reservoir. The reservoir chemistry of this group seems to be mainly controlled by carbonates and evaporites.

The second group of waters corresponds to those located in the Valle de Lecrín tectonic graben in the Alpujarride Complex. This group displays lower temperature (50-60°C) and $p\text{CO}_2$ in the reservoir (from 10^{-3} to 10^{-2} atm). A buffering mineral assemblage in depth, mainly composed of carbonates, quartz, and Ca alumino-silicates characterizes this system.

Finally, the third group of waters, located on the detachments of the metamorphic complexes, show the highest estimated temperatures (130 – 140°C) and $p\text{CO}_2$ in the reservoir (1 to 10^2 atm). The buffering mineral assemblage in the reservoir might be dolomite, quartz, Mg and Ca alumino-silicates.

The waters of the sedimentary basins display a variation in $p\text{CO}_2$ between the depth and the surface ($\Delta p\text{CO}_2$) of 10^{-1} atm for both mineral buffers (dolomite only and carbonate and alumino-silicate assemblage). The $\Delta p\text{CO}_2$ of the waters with the lowest reservoir temperature (i.e. the waters in the graben) is higher when considering the dolomite buffer than the carbonate and alumino-silicate buffer, whereas it is inverse trend for the waters with the highest temperature (i.e. the waters in the metamorphic complexes).

This study is one of the first attempt to link the geochemistry of the thermal waters to the geological environment in the Central Betic Cordillera. A strong relationship between the temperature and the $p\text{CO}_2$ in the reservoir has been hence evidenced in this study. The role of the potential mineral buffers on the estimation of the $p\text{CO}_2$ appears to be crucial, especially at the border of the evaporitic basins.

4.2. LOW TO MEDIUM ENTHALPY GEOTHERMAL SYSTEMS: ROLE OF CO₂. THE STUDY CASE OF THE CENTRAL BETIC CORDILLERA .

C. Lix^{1,2*}, P. Zuddas², X. Guichet¹, J. Benavente³, J.A. Luque-Espinar⁴, and M. Barbier¹

¹ IFP Energies Nouvelles, 1 et 4 avenue de Bois-Préau, 92852 Rueil-Malmaison, France

² Sorbonne Université, CNRS-INSU, Institut des Sciences de la Terre Paris, ITeP UMR 7193, F-75000 Paris, Campus Pierre et Marie Curie - 4 place Jussieu 75005 Paris, France

³ Departamento de Geodinámica e Instituto de Investigación del Agua, Universidad de Granada, Granada, Spain

⁴ Instituto Geológico y Minero de España, Granada, Spain

This section corresponds to an article in preparation to be submitted in Science of the Total Environment.

4.2.1. Abstract

There is growing interest in geothermal energy, which is considered as an efficient energetic solution to mitigate rising atmospheric CO₂. Besides known high enthalpy geothermal systems, increasing attention is paid on low- to medium- temperature geothermal systems, as they are suitable for domestic or local use (heat pump or greenhouse). Although geothermal production seems to be an environmentally advantageous renewable energy, it might result in significant CO₂ emissions. In this study, we investigate the relationship between the temperature, pCO₂, and mineral buffers in the reservoir conditions, taking the low- to medium-enthalpy thermal waters in the Central Betic Cordillera as study case. This area is characterized by evaporitic sedimentary basins, whose basement is constituted of sedimentary rocks and metamorphic sedimentary complexes, and by fracture-controlled (non-magmatic) geothermal systems. Using geothermometrical and geochemical thermodynamic modeling, three main groups of waters have been determined depending on the temperature, the buffering mineral assemblage, and the pCO₂ in their reservoir. A group of waters with a reservoir temperature ranging from 70 to 90°C and located in the sedimentary basins shows a pCO₂ in depth ranging from $\sim 6 \times 10^{-2}$ and 6×10^{-1} atm. The reservoir chemistry of this group seems to be mainly controlled by carbonates and evaporites. This set of waters display a variation in pCO₂ between the depth and the surface ($\Delta p\text{CO}_2$) of 10^{-1} atm. Another group of waters, located in a graben, displays lower temperature (50-60°C) and pCO₂ in the reservoir (from 10^{-3} to 10^{-2} atm). Finally,

the third group of waters, located on the detachments of the metamorphic complexes, show the highest estimated temperatures (130 – 140°C) and $p\text{CO}_2$ in the reservoir (1 to 10^2 atm). The two later groups show increasing buffering effect of alumino-silicates, in addition to carbonates and quartz. Therefore, we showed a strong relationship between the temperature and the $p\text{CO}_2$ in the reservoir as well as the potential mineral buffers.

4.2.2. Introduction

Geothermal energy has been widely developed across Europe and the World for the last 50 years, with main focus on the conventional high-temperature geothermal reservoirs. Nevertheless, low (30°C to 100°C) to medium (100 – 150°C) enthalpy geothermal systems have been recently subject to increasing interest (Blasco et al., 2017; Capecchiacci et al., 2015; Fusari et al., 2017) as they may be easily exploited for ground-source heat pump or greenhouses (Battistel et al., 2016). In the current context of global warming and energy transition, geothermal is generally considered to be an environmentally advantageous renewable source energy. However, emissions of greenhouse gases, and especially CO_2 , might be generated by geothermal exploitation. Although CO_2 release from geothermal utilization has been shown to be significantly lower than from fossil fuel (Ármannsson, 2003; Hunt, 2001), the efficiency of this energy to mitigate rising atmospheric CO_2 is a major concern for society acceptance. The expansion of the geothermal sector leads to consider broader range of geothermal resources resulting in possible large CO_2 emissions, even in low- and medium- enthalpy geothermal systems. Scientific research programs have been recently dedicated in development of cost-effective non-carbon emitting geothermal energy (e.g., “Geothermal Emission Gas Control”, Horizon 2020, European program).

The CO_2 concentration in geothermal waters is strongly related to the geology, and more specifically the lithology, of the reservoir. Higher CO_2 fluid concentrations might be expected in medium- to high- temperature carbonate-hosted geothermal systems than in other geothermal systems (Ármannsson et al., 2005). Carbonate dissolution or thermal decomposition of carbonates might be major sources of CO_2 in fluid whereas carbonate precipitation in the reservoir or in the ascent of the water might be a sink of geothermal CO_2 . The equilibrium relative to the carbonates minerals and the alumino-silicate minerals, often associated to the chemical water-rock interactions, is an important parameter to consider as it “buffers” the fluid chemical composition and the CO_2 degassing. Therefore, understanding the relationship between the mineral buffer, the partial pressure of CO_2 ($p\text{CO}_2$), and the temperature in the

reservoir, is crucial to estimate the CO₂ release in geothermal systems.

The Central Betic Cordillera, in the South of Spain, has an interesting geothermal potential with abundant low to medium geothermal resources (Arrizabalaga et al., 2015; Sánchez Guzmán and García de la Noceda, 2010), major fault systems allowing a rapid ascent of the deep hot water (Cerón and López-Chicano, 2002), and moderate-intensity seismic activity. This region is characterized by several occurrences of thermal springs (water with temperature of more than 20°C, according to the average air temperature of this area), known as baños, which have been used, for some of them, as thermal bath since the Roman times. They are mainly exploited for balneotherapy or spa nowadays. The thermal waters in the Central Betic Cordillera are also characterized by large variability in pCO₂. Low pCO₂ are observed in the sulfated waters (e.g., Baños Alhama de Granada) whereas large amount of CO₂ degassing are known in few springs (e.g., Capuchina de Lanjaron) (Pérez del Villar, 2009). The thermal springs of Baños Alicun de la Torres have been studied as natural analogue for CO₂ storage (Prado-Pérez and Pérez del Villar, 2011). Nevertheless, only old Spanish studies have been considered globally the thermal waters in the Central Betic Cordillera (Benavente Herrera and Sanz de Galdeano, 1985; Cruz-Sanjulián et al., 1972; Cruz Sanjulián and Granda, 1979). Recent studies (Campos, 2006; López-Chicano et al., 2001a; Prado-Pérez and Pérez del Villar, 2011) characterized the geochemical and hydrogeological properties in specific individual thermal system.

The aim of this study is to evaluate the suitability of the thermal waters for the geothermal exploitation in the Central Betic Cordillera in regards of CO₂ emissions. Geochemical and isotopic indicators and thermodynamic calculations can be applied to get insights on the fluid geochemistry, temperature, and pCO₂ of the reservoir using the measured physical-chemical characteristics at the surface. The present study attempt to assess the potential mineral assemblages buffering the waters in the reservoir and the variations of pCO₂ at the regional scale.

4.2.3. Geological setting

The sampled thermal waters (springs and wells) are located in the central region of the Betic Cordillera with a greater concentration of points in the Granada Basin (Figure 4-1). The Central Betic Cordillera is a complex structure, resulting from the convergence of the Iberian and African plate convergence, which can be subdivided into: (1) the non-metamorphic External Zone, (2) the metamorphic Internal Zones, (3) the Neogene basins. The External Zone is

separated from the Internal Zone by a major shear zone called the Internal External Boundary Zone (IEBZ) (Sanz de Galdeano, 1990). The Granada Basin is one of the Neogene intramontainous basin in the Central Betic Cordillera, located at the junction between the Internal and External zones.

4.2.3.1. Tectonic framework

The Central Betic Cordillera is a tectonically active region structured by several crustal faults (Bufo et al., 2004; Sanz de Galdeano and Peláez, 2011). In the NE part of the Granada Basin, the IEBZ, mentioned above, becomes nearly coincident with the so-called Cadiz-Alicante faults system (CAFS, Figure 4-1) extending from 550 km across the Betic Cordillera. This fault system forms a corridor of dextral strike-slip faults generating crustal discontinuities of at least 7 km depth (Sanz de Galdeano, 2008 and references therein). Besides, two main sets of normal faults affect the basement and the sedimentary infilling of the Granada Basin: one set of E-W faults with low angle dip ($< 30^\circ$) toward the south and the north; and a second one with NE-SW faults, which dip westward, mainly located in the NE of the basin (Figure 4-1) (Galindo-Zaldívar et al., 2015; Rodríguez-Fernández and Sanz de Galdeano, 2006a). The thermal waters are strongly related to the faults in the Central Betic Cordillera as the thermal systems are convective fracture-controlled systems (Benavente Herrera and Sanz de Galdeano, 1985; Cruz-Sanjulián et al., 1972).

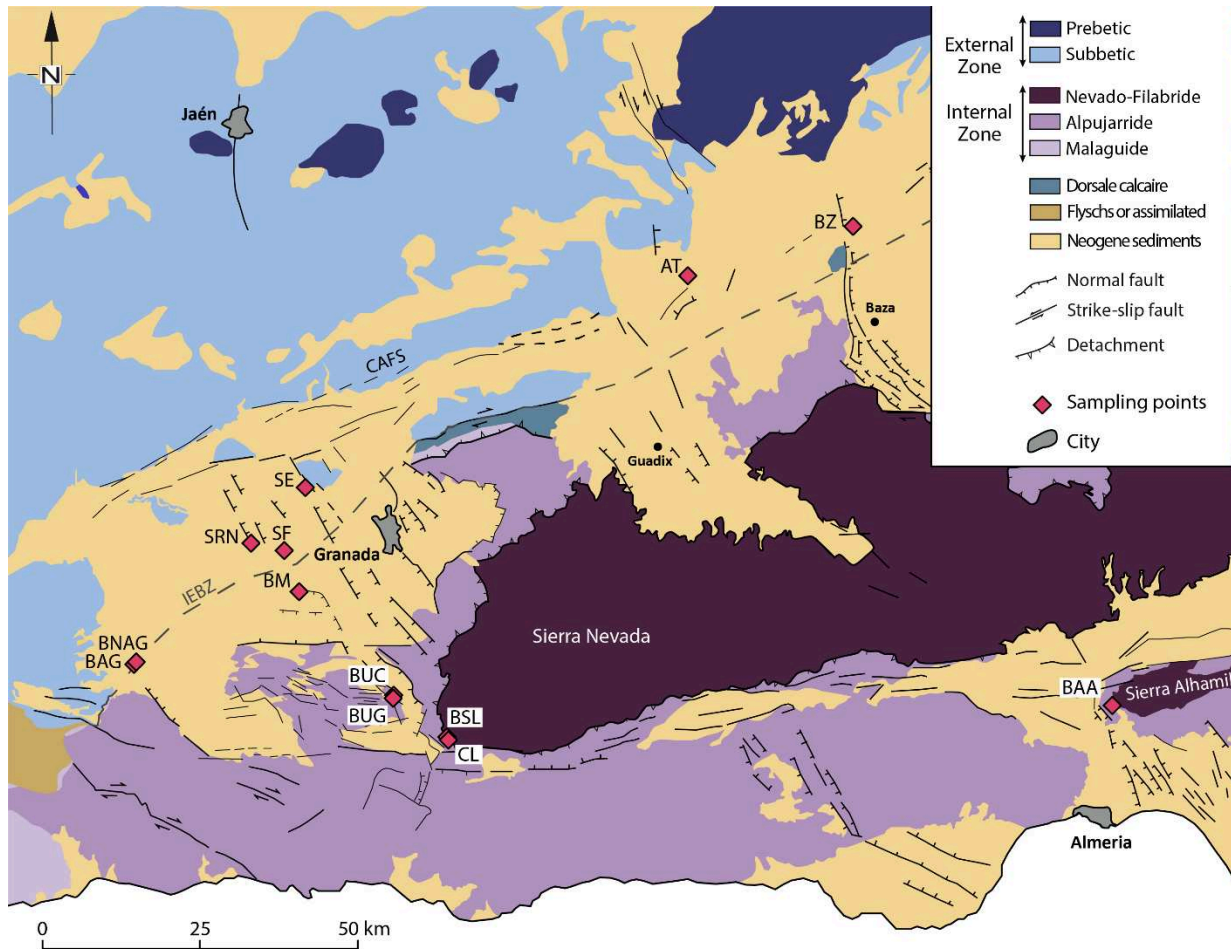


Figure 4-1: Location of the thermal water samples in the Central Betic Cordillera and geological map of the area modified after Sanz de Galdeano and Peláez (2011).

4.2.3.2. Lithostratigraphy

The material of the Internal Zone corresponds to Paleozoic to Mesozoic metasediments differentiated into three stacked metamorphic complexes, from the top to the base, by different metamorphic degree and structural position: (1) Maláguide, (2) Alpujarride, and (3) Nevado-Filábride. The Alpujarride Complex, well represented in our study area, consists in a series of nappes of Paleozoic-Mesozoic HP/LT metasediments (Azañón et al., 1998; Azañón and Crespo-Blanc, 2000). The base of the nappes consists of Paleozoic graphite mica schists, which are overlain by Permo-Triassic metapelites with layers of meta-sandstones, dolomite, and limestone. These meta-sediments are in turn overlain by middle-upper Triassic marbles with interbedded gypsum layers and Mesozoic pelagic marls forming the top of the nappes (Martín and Braga, 1987; Prado-Pérez and Pérez del Villar, 2011). The HP/LT Nevado-Filábride materials, outcropping in the Sierra Nevada and Sierra Alhamilla, comprise from the base to

the top: Paleozoic graphitic schists, Permo-Triassic mica schists associated with metapelites, Triassic dolomite and marbles, and heterogeneous rocks with Jurassic metabasite inclusions (Gomez-Pugnaire et Fernandez-Soler, 1987; Gómez-Pugnaire et al., 2000).

The External Zone forms the northern part of the Granada Basin basement and crops out in Sierra Elvira and Alicún de las Torres. It is mainly composed of Mesozoic sedimentary rocks, with Triassic evaporitic-bearing marls, dolomitic limestones, and interbedded marls (Braga et al., 2003; Sanz de Galdeano and Vera, 1992).

The sedimentary infilling of the Granada Basin ranges from the Miocene to the Quaternary and is composed, from bottom to top, of clayey conglomerates, calcareous sandstones, marls and silts, gypsum/anhydrite (and locally halite), lacustrine limestones, cemented breccias and alluviums (Braga et al., 2003; Corbí et al., 2012).

4.2.3.3. Sample location

The thermal waters are mainly situated close to major tectonic and geological structures. The sampling points can be gathered into three groups depending of the nature of the geological features:

- The thermal waters related to the metamorphic complexes: Baño Salado de Lanjaron and Capuchina de Lanjaron springs (BSL and CL) are located in the Sierra Nevada along the detachment between Nevado-Filábride and Alpujárride complexes. Baños Alhamilla spring (BAA) is situated further to the east in the Sierra Alhamilla along the same tectonic contact, where it is also close to the trace of an important strike-slip fault of near N30E direction.
- The thermal waters located in the evaporitic basins (Granada Basin and Guadix-Baza Basin): Baños Santa Fe (SF), Baños de la Malahá (BM), and Sondeo Romilla de la Nueva (SRN) are wells situated in the Granada Basin. Baños Alhama de Granada (BAG), Baños Nuevo Alhama de Granada (BNAG), and Sierra Elvira (SE) are springs located in the Granada Basin. SE is also located on the trace of an active fault, belonging to the NW to NNW directed fault system. Baños de Zujar (BZ) and Baños de Alicún de las Torres (AT) are springs located in the Guadix-Baza Basin, close to the above mentioned IEBZ and CAFS. The springs SE, BZ, and AT are linked by faults to small Subbetic carbonate outcrops.
- The thermal waters linked to the Baños Urquizar Chico (BUC) and Baños Urquizar Grande (BUG) are located within the Valle de Lecrin tectonic graben within the

Alpujarride Complex along faults striking N30E, forming the western termination of the Sierra Nevada Massif.

4.2.4. Material and methods

4.2.4.1. Water sampling

Thirteen thermal water samples were collected in the Granada Basin and in the Betic Cordillera, from nine springs and four wells. Two wells were artesian whereas the other water samples were pumped. All water samples were filtered with 0.45 μm membrane filters and samples assigned to trace elements and Al analyses were filtered with 0.2 μm membrane filters. The water samples dedicated to cations, minor and Al analyses were acidified using suprapure nitric acid (HNO_3).

Dissolved gases were collected in filling 142 ml glass bottles with the water samples without filtering. The glass bottles were sealed under water with silicon/rubber septa to avoid atmospheric contamination.

4.2.4.2. Water analyses

Physical-chemical properties

Physical-chemical parameters of the waters, including temperature, pH, electrical conductivity (EC), and alkalinity were measured directly on the field. The combination pH electrode was calibrated with three buffer solutions at pH 4.0, 7.0 and 10.0 (25°C) (CertiPUR® Reference material) and the EC electrode with two potassium chloride standard solutions of 1.41 mS/cm and 12.8 mS/cm (25°C) (CertiPUR® Reference material). The uncertainties on the measurements of temperature, pH, and EC were of $\pm 1^\circ\text{C}$, ± 0.1 , and ± 0.01 mS/cm respectively. Alkalinity was determined by titration with an 0.01M or 0.1M hydrochloric acid solution depending on the encountered alkalinity range and by following the pH evolution with the pH-meter. The equivalent volume was determined with the Gran's method (Gran, 1952) and the analytical error of the alkalinity measurements was of approximately $\pm 5\%$.

Laboratory chemical analyses

The major cations and anions (Ca^{2+} , Mg^{2+} , K^+ , Na^+ , SO_4^{2-} , and Cl^-) were analyzed by ionic chromatography. The uncertainty of Mg^{2+} , K^+ , Na^+ , SO_4^{2-} determination is $\pm 5\%$ whereas that on Ca^{2+} and Cl^- is estimated to be $\pm 10\%$. Minor and trace elements (Ba, Sr, Al, Fe) were

analyzed by Inductively Coupled Plasma Optical Emission Spectrometry ICP-OES. The uncertainty of Ba and Sr determination is $\pm 10\%$ whereas that on Al is estimated to $\pm 20\%$. The silica concentration were determined by spectrophotometric method following the protocol from Centre d'Expertise en Analyse Environnementale du Québec, (2016), suitable for natural groundwater with Si concentration ranging from 0 to 20 mg/l. The total ionic balance does not exceed 8% for all water samples.

4.2.4.3. Gas analyses

Extraction and analyses of dissolved gases

The extraction of the dissolved gases was carried out following the method described by Capasso and Inguaggiato (1998) and Inguaggiato and Rizzo (2004). A known volume of host gas was injected into the upside-down glass bottles while drawing out the equivalent water volume through needles. After equilibration for 24 hours, a variable gas volume was extracted for analyses by injecting Millipore water into the glass bottles.

Gas species (O_2 , N_2 , CH_4 , CO_2 and He) were analyzed by gas chromatography (Clarus 500, Perkin Elmer instrument with Carboxen 1000 columns with a hot wire detector and a flame ionization detector) using argon as carrier gas. The composition of dissolved gases, expressed in $cc.l^{-1}$ STP (Standard Temperature and Pressure), was calculated taking into account the volume of gas extracted, the volume of water sample, and the solubility of each gas species (Bunsen coefficient in cc gas/l water STP). The composition of bubbling gases was expressed in either %vol or ppm vol. The accuracy to analyze dissolved gases following the method described by Capasso and Inguaggiato (1998) is within 5.0%.

$\delta^{13}C$ of the Total Dissolved Inorganic Carbon (TDIC)

Analyses of $\delta^{13}C$ of Total Dissolved Inorganic Carbon (TDIC) were carried out with the Analytical Precision 2003 (AP2003) mass spectrometer using the method outlined by Capasso et al. (2005) based on chemical and physical stripping. The results were expressed in ‰ vs. V-PDB standard and with standard deviations of $^{13}C/^{12}C$ ratios of $\pm 0.2\%$.

4.2.4.4. Geochemical calculations and modeling

In this study, the saturation index calculations and geothermometrical modeling were

performed with the (version 3-0-6) PHREEQC software (Parkhurst et al., 2013), using the phreeqc thermodynamic database distributed with the code.

Saturation index

A direct thermodynamic modeling of the multi-component system equilibrium has been performed from the composition of the waters and the physical-chemical parameters. The saturation index of waters with respect to possible minerals (SI_m) were calculated to test the equilibrium conditions or the departure from equilibrium of the system, following Equation 4-1:

$$SI_m = \log \Omega_m = \log \frac{\prod^i (\gamma_i [c_i])^{v_{im}}}{K_s(P, T)_m} \quad (4-1)$$

where $[c_i]$ and γ_i are the concentration and the activity coefficient of the ion i , v_{im} is the reaction coefficient for the ion i and the mineral m , and $K_s(P, T)_m$ is the solubility constant of the mineral m dependent on the temperature and pressure.

Chemical geothermometers and geobarometers

Chemical geothermometric techniques were used to estimate the theoretical reservoir temperature of the thermal waters. The application of the chemical geothermometers needs to satisfy the basic assumptions that the waters circulating at depth are in chemical equilibrium with the minerals of the host rocks (i.e., SI_m close to 0) and that their elemental contents have not changed significantly during the water ascent to the surface (including precipitation or dissolution of secondary mineral phases or degassing). Numerous chemical geothermometers have been described in the literature, including silica, Na/K, Na/K/Ca, K-Mg (D'Amore et al., 2000 and references therein). The silica geothermometers are the most common geochemical investigations of geothermal systems, widely used in different contexts around the world (Verma, 2000). SiO₂-quartz geothermometers from Fournier (1977), Fournier and Potter (1982), Michard (1979), and Verma (2000) and SiO₂-chalcedony geothermometers from Arnórsson et al. (1983) and Michard (1990) were applied for the studied thermal waters. Although cationic (Na/K, Na/K/Ca, K-Mg) geothermometers have been proven efficient in high temperature systems (> 180°C), they are usually considered as unsuitable in low temperature systems due to the different mineral assemblage governing the water chemistry and equilibrium (Blasco et al., 2017; Chiodini et al., 1995). Due to these limitations, the Na/K, Na/K/Ca and K-

Mg geothermometers have not been applied in this study. The Ca-Mg geothermometer, developed in the first place by Marini et al. (1986) and revised by Chiodini et al. (1995), is more appropriate for low temperature carbonate-evaporitic system and was therefore used here. This geothermometer assumes equilibrium of the waters with calcite, dolomite and anhydrite in the reservoir, which is a reasonable assumption in the investigated area where these minerals are extensively present.

In order to get an estimation of the partial pressure of CO₂ (pCO₂) in depth, the geobarometrical relationship based on the (HCO₃⁻)²/SO₄²⁻ ratio, pCO₂, and temperature (Chiodini et al., 1995) was applied using the following equation:

$$\log \frac{HCO_3^-}{SO_4^{2-}} = -4.807 + 0.9871 \log pCO_2 + \frac{794.8}{T} - 0.1655 \log \Sigma_{eq} \quad (4-2)$$

where Σ_{eq} is the sum of equivalents in the waters.

Geothermometrical modeling

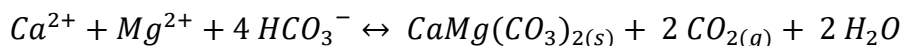
Another approach to estimate the reservoir temperature consists in simulating the variation of the saturation states with respect to a group of selected minerals, potentially present in the reservoir, to find the temperature at which the saturation indices simultaneously reach equilibrium (Blasco et al., 2018). This method is based on the same assumption as the classical chemical geothermometers: the thermal waters are in equilibrium with the mineral phases under reservoir conditions. Hence, the most realistic reservoir temperature corresponds to the temperature at which a group of minerals is at equilibrium (Asta et al., 2012; D'Amore et al., 1987; Tole et al., 1993).

Saturation indices were calculated in the temperature interval between the field temperature and 150°C for the following minerals: quartz, chalcedony, anhydrite, dolomite, calcite, Ca-montmorillonite, laumontite, Mg-chlorite, albite, anorthite, K-feldspar, and kaolinite. Due to the imprecision of the thermodynamic databases, the error on the SI at which the equilibrium is reached is considered to be $SI = 0 \pm 0.25$ (D'Amore et al., 1987). This geothermometrical modeling approach estimates the reservoir temperature within an uncertainty of $\pm 10^\circ\text{C}$ (Tole et al., 1993).

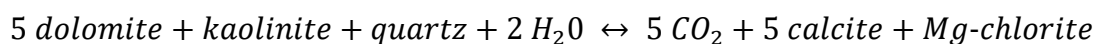
An additional set of geothermometrical simulations has been performed at the end of the study including addition of CO₂ to the initial solution to test the hypothesis of CO₂ degassing in an open system.

Hydrogeochemical modeling between surface and depth conditions in closed system

In order to assess the geochemistry of the waters in the reservoir conditions and the variation of the $p\text{CO}_2$ between the reservoir and the surface, we carried out hydrogeochemical simulations in closed system. In sedimentary environment, the pH and $p\text{CO}_2$ of the waters are highly dependent on the interaction with carbonate minerals. Dolomite is particularly important in the Central Betic Cordillera where large amount are present. CO_2 generation might occurs during dolomite precipitation as shown by the following reaction:



The $p\text{CO}_2$ in the system might also be controlled by reactions involving alumino-silicates and carbonates such as the conversion of kaolinite to Mg-chlorite proposed by Coudrain-Ribstein et al. (1998) and Hutcheon et al. (1993):



The modeling workflow was run with the PHREEQC code and includes the following three steps:

(1) Saturation calculations were carried out at the outlet temperature (T_{out}) and atmospheric pressure (P_{out}),

(2) An increase in temperature was simulated up to the temperature of the quartz geothermometer (T_{qz}) and the corresponding hydrostatic pressure of the reservoir (P_{hydro}) using a geothermal gradient of $30^\circ\text{C}/\text{km}$,

(3) Waters were equilibrated with a set of minerals at T_{qz} and P_{hydro} , to test two different hypotheses:

- Equilibrium with dolomite using $\text{CO}_{2(g)}$ as an alternative phase to reach the equilibrium,
- Equilibrium with carbonates and alumino-silicates using calcite, dolomite, kaolinite, quartz, Mg-chlorite as mineral assemblage.

The concentrations of chemical species, pH, $p\text{CO}_2$, and SI of minerals were computed during each step of modeling. By comparing the results of the geochemical modeling (Step 3) with the initial surface geochemical characteristics (Step 1), we evaluate the possible mineral assemblages in equilibrium in the reservoir conditions.

These geochemical simulations rely on the assumption that the difference in quartz saturation index ($\text{SI}_{\text{quartz}}$) during each step of the modeling do not lead to significant change in temperature. Even if $\text{SI}_{\text{quartz}}$ varies between -0.13 and 1.27, the H_4SiO_4 concentration remains

quite constant for all the thermal waters resulting in a change in apparent temperature (δT) lower than 5°C.

4.2.5. Results

4.2.5.1. Chemical characteristics of the waters

The investigated thermal waters have outlet temperature ranging from 20 to 50°C, corresponding to low to medium enthalpy waters, and pH values spanning between 5.8 and 7.6 (Table 4-1). The conductivity of the studied waters shows large range of values, from 1 to 34 mS/cm, corresponding to total dissolved solids (TDS) values from 0.67 to 18.17 g.L⁻¹.

The thermal waters show a large variability in their chemical composition and a relationship can be evidenced between the water-types and their location relative to the geological structures in the Central Betic Cordillera (Figure 4-2).

The waters located in the graben formed into the Alpujárride Complex and close to the SE-NW faults have a chemical composition of Ca²⁺-Mg²⁺-SO₄²⁻-HCO₃⁻ type, displaying interaction with both carbonates and sulfates.

The waters in the evaporitic basins are mainly Ca²⁺-Mg²⁺-SO₄²⁻ water-type resulting from clear interaction with evaporitic material and especially calcium sulfate. The samples BAG and BNAG have a higher HCO₃⁻ content, with a composition close to the samples from the graben in the Alpujárride Complex. The composition of the BZ water also differs from the others with a Ca²⁺-Na⁺-K⁺-SO₄²⁻-Cl⁻ water-type, showing significant interaction with evaporitic and detrital material.

The thermal waters located at contacts between metamorphic complexes display larger dispersion in their chemical composition. The samples BSL and CL are Na⁺-Cl⁻ type whereas BAA is Na⁺-Cl⁻-HCO₃⁻ type.

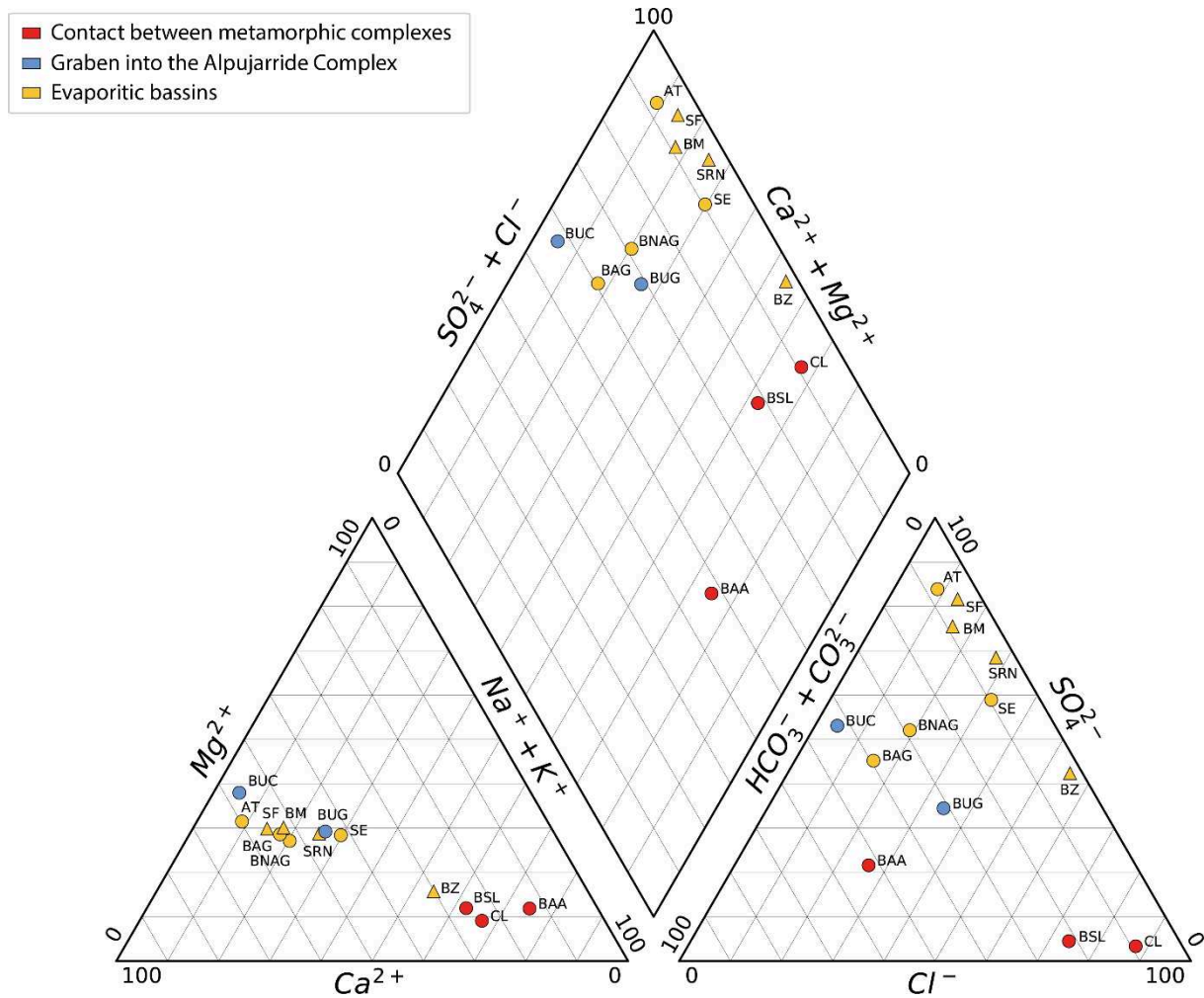


Figure 4-2: Piper diagram of the thermal waters from Central Betic Cordillera. Circles and triangles correspond to springs and wells respectively.

4.2.5.2. Saturation indices

The results of the saturation indices calculations at the outlet temperature are shown in Table 4-2. The waters are close to equilibrium or slightly oversaturated with respect to calcite and dolomite whereas they are undersaturated with respect to gypsum, anhydrite, and halite. Waters are oversaturated with respect to quartz and close to equilibrium with respect to chalcedony.

Concerning the saturation indices with respect to aluminosilicates, the waters are oversaturated with respect to kaolinite and Ca-montmorillonite whereas they display large range of saturation with respect to K-feldspar and albite, spanning from undersaturated to highly oversaturated, independently of the relationship with the tectonic structures.

4.2.5.1. CO₂

Dissolved CO₂ concentrations range from 4.2×10^{-4} to 2.7×10^{-2} cm³/L, corresponding to pCO₂ spanning from 0.02 to 0.78 atm (Table 4-3). The water samples characterized by higher amounts of dissolved CO₂ display lower pH values, suggesting that CO₂ is the main species responsible of water acidity. The high-CO₂ springs of CL, BAA and BUG are also characterized by bubbling gases with similar composition as the dissolved gases (Lix et al., 2018).

The pCO₂ values obtained from the speciation-solubility calculations at the outlet temperature range from 0.02 to 1.02 atm (Table 4-2).

The total dissolved inorganic carbon content of the thermal waters and its isotopic composition ($\delta^{13}\text{C}_{\text{TDIC}}$), listed in Table 4-3, range from 2.7×10^{-3} to 6.3×10^{-2} mol.L⁻¹ and from -9.04 to -1.54‰ vs. V-PDB respectively.

Various carbon sources control the $\delta^{13}\text{C}$ of the TDIC including: (1) the degradation of organic matter in the soil (of the recharge area), (2) carbonate dissolution, (3) mantellic CO₂. Biological degradation processes in soils usually results in $\delta^{13}\text{C}$ values ranging from -23‰ and -9‰ (Clark and Fritz, 1997), which is not well representative of the studied samples. Therefore, the $\delta^{13}\text{C}_{\text{TDIC}}$ values indicate mostly inorganic origin of CO₂. Although discriminating the carbon source between carbonate dissolution and mantellic CO₂ might be more complex as their $\delta^{13}\text{C}$ values overlap (range), the isotopic composition of dissolved and bubbling gases in these thermal waters show a dominant crustal component (Lix et al., 2018). Purely inorganic origin of CO₂ have been considered in these thermodynamical calculations, given the results of $\delta^{13}\text{C}$ of the TDIC.

Sample and location	Code	Type	Depth	Temp.	pH	EC	Ca	Mg	Na	K	Alk.	Cl	SO ₄	Si	Al	Ba	Fe	Sr	TDS	%
			(m)	(°C)																imbalance
Contacts metamorphic complexes																				
Banos Salado de Lanjaron 36°55.4189'N; 3°29.5869'W	BSL	S		26	5.8	8.18	6.59	3.06	29.46	2.60	12.86	43.95	1.31	1.56	8.85E-03	1.04E-03	3.13E-01	0.19	3.72	7.29
Capuchina de Lanjaron 36°55.1523'N, 3°29.4182'W	CL	S		21	6.1	34.15	32.57	12.29	166.99	13.96	28.65	274.78	5.24	1.53	7.13E-02	7.34E-04	4.98E-01	0.62	18.17	7.40
Banos de Alhamilla 36°57.6531'N; 2°23.7875'W	BAA	S		51	7.1	1.92	0.88	0.78	9.65	0.23	7.93	3.99	1.64	1.38	4.92E-04	4.62E-04	9.66E-04	0.02	1.15	7.04
Graben into Alp. Complex																				
Banos Urquizar Chico 36°58.3477'N; 3°34.5347'W	BUC	S		25	7.6	0.99	2.62	1.75	0.42	0.05	3.99	0.41	2.49	0.27	6.99E-04	2.28E-04	b.d.l	0.05	0.68	0.87
Banos Urquizar Grande 36°58.2261'N; 3°34.5854'W	BUG	S		23	7.3	1.50	2.92	1.92	3.22	0.22	4.21	4.66	2.33	0.24	1.23E-03	2.33E-04	b.d.l	0.04	0.91	1.49
Evaporitic basin																				
Banos de la Malaha 37°06.2946'N, 3°43.6034'W	BM	W	200	30	7.4	3.08	8.05	4.59	5.25	0.22	2.89	5.10	12.12	0.45	1.60E-03	1.18E-04	2.98E-02	0.16	2.13	2.35
Santa Fe 37°09.3813'N; 3°45.2023'W	SF	W	510	39	7.0	4.69	13.67	7.30	6.82	0.34	2.58	7.15	21.07	0.53	2.09E-03	5.10E-05	6.50E-03	0.16	3.38	2.73
Sondeo Romilla la Nueva 37°10.0216'N; 3°48.8567'W	SRN	W	740	32	7.3	6.13	14.32	8.80	15.45	0.41	2.72	18.88	23.16	0.45	5.13E-03	8.92E-05	4.25E-02	0.17	4.26	4.48
Sierra Elvira 37°13.7033'N; 3°43.3372'W	SE	S		30	6.9	3.82	7.80	5.28	10.76	0.27	3.77	12.43	11.61	0.43	3.74E-03	1.35E-04	b.d.l	0.11	2.52	2.93
Banos Alhama de Granada 37°01.1221'N; 3°58.9970'W	BAG	S		40	7.4	1.13	2.44	1.30	1.45	0.15	3.59	1.39	2.05	0.55	6.85E-04	3.49E-04	b.d.l	0.04	0.67	0.02
Banos Nuevo Alhama de Granada 37°01.3410'N; 3°58.7548'W	BNAG	S		39	7.2	1.24	2.63	1.36	1.87	0.17	2.89	1.89	2.60	0.72	6.95E-04	2.71E-04	4.42E-04	0.06	0.73	0.08
Alicun de las Torres 37°30.5418'N; 3°06.4172'W	AT	S		34	6.7	2.24	8.25	4.35	2.32	0.12	2.06	2.32	11.39	0.31	8.89E-04	1.38E-04	b.d.l.	0.11	1.83	0.87
Banos de Zujar 37°34.556'N, 2°49.463'W	BZ	W	-	35	6.8	12.82	15.83	8.01	56.11	0.62	2.91	61.40	23.32	0.62	1.71E-02	1.98E-04	5.74E-03	0.23	6.80	3.03

Table 4-1: Sample details including sample location and water chemistry. Location of sampling points refer to WGS84 system. Type of water points: S = spring; W = well. Conductivity is in mS/cm. Concentrations of dissolved elements and TDS are expressed in mmol/kg of solution and in mg/L respectively. b.d.l = below detection limit.

Sample	Calcite	Dolomite	Gypsum	Anhydrite	Halite	Quartz	Chalcedony	K-feldspar	Kaolinite	Albite	Anorthite	Ca-Mont.	CO ₂ (g)
Contacts metam. complexes													
BSL	-0.61	-1.39	-1.40	-1.61	-4.66	1.14	0.74	3.15	8.02	1.65	-1.03	7.96	0.01
CL	0.32	0.34	-0.63	-0.86	-3.21	1.25	0.83	5.42	10.44	3.90	1.93	11.01	-0.02
BAA	0.02	0.27	-1.83	-1.89	-6.17	0.74	0.42	0.14	2.52	-0.52	-2.79	1.65	-1.21
Graben into Alp. Complex													
BUC	0.41	0.75	-1.19	-1.42	-8.46	0.40	-0.01	-0.67	3.23	-2.31	-2.68	1.90	-2.23
BUG	0.16	0.23	-1.21	-1.44	-6.52	0.37	-0.05	0.18	4.36	-1.25	-2.25	3.05	-1.95
Evaporitic basin													
BM	0.43	0.78	-0.37	-0.57	-6.33	0.54	0.15	0.56	4.06	-0.57	-1.42	3.14	-2.22
SF	0.21	0.34	-0.07	-0.22	-6.13	0.48	0.12	0.37	4.18	-0.73	-1.20	3.23	-1.79
SRN	0.39	0.74	-0.06	-0.25	-5.35	0.52	0.14	1.15	5.12	0.25	-0.35	4.34	-2.10
SE	0.04	0.07	-0.43	-0.63	-5.65	0.52	0.13	0.91	5.65	0.00	-0.81	4.81	-1.60
BAG	0.32	0.62	-1.30	-1.44	-7.41	0.48	0.12	-0.39	2.49	-1.80	-2.54	1.31	-1.95
BNAG	0.06	0.06	-1.18	-1.33	-7.17	0.61	0.25	0.07	3.20	-1.29	-2.26	2.24	-1.87
AT	-0.32	-0.73	-0.37	-0.55	-7.03	0.31	-0.06	-0.83	4.02	-1.99	-2.45	2.63	-1.63
BZ	0.01	-0.07	-0.10	-0.27	-4.32	0.62	0.25	2.00	6.90	1.52	0.84	6.46	-1.62

Table 4-2: Saturation indices (SI) of the main mineral phases of interest in the investigated area. CO₂(g) corresponds to the log10 of CO₂ partial pressure (in atm). SI were calculated with the PHREEQC code at the outlet temperature (measured in the field).

Sample	O ₂ cc/L	N ₂ cc/L	CO ₂ cc/L	H ₂ ppm	CO ppm	CH ₄ ppm	TDIC mmol/L	δ ¹³ C _(TDIC) ‰	δ ¹³ C _(CO2) ‰
Contacts metam. complexes									
BSL	0.07	1.74	575.79	6.82E-04	2.88E-04	5.29E-03	46.6	-5.2	-6.6
CL	0.08	1.94	597.48	b.d.l	1.41E-04	8.66E-05	63.0	-4.7	-7.5
BAA	1.49	12.14	39.43	9.72E-04	3.16E-04	1.53E-02	9.1	-9.0	-13.6
Graben into Alp. Complex									
BUG	1.57	18.60	16.16	b.d.l	2.69E-05	6.36E-04	4.6	-9.0	-16.2
Evaporitic basin									
SF	1.81	17.04	9.51	b.d.l	3.51E-05	1.38E-02	2.9	-1.5	-6.6
SE	0.13	18.29	22.22	b.d.l	b.d.l	2.39E-04	4.5	-8.8	-14.5
BAG	0.67	17.59	10.71	b.d.l	b.d.l	7.43E-04	3.8	-7.6	-13.3
AT	0.44	16.74	27.02	1.10E-03	7.03E-05	2.48E-05	2.7	-5.0	-9.8
BZ	0.62	13.76	16.27	1.51E-03	2.02E-04	3.37E-02	3.5	-3.4	-8.4

Table 4-3: Dissolved gases and carbon isotopic composition of the selected investigated thermal waters. b.d.l = below detection limit.

4.2.5.2. Reservoir temperature and pressure

Chemical geothermometers and geobarometers

The temperatures provided by the silica and Ca-Mg geothermometers are compiled in Table 4-4. The mean reservoir temperatures estimated with the different SiO₂-quartz geothermometers range from 51 to 143°C and the relative standard deviation is less than 6°C. The SiO₂-chalcedony geothermometers yields lower temperature ranging from 20 to 109°C. The SiO₂-quartz are more reliable than the SiO₂-chalcedony geothermometers since quartz might be the phase controlling the dissolved silica in the thermal waters in the Betic Cordillera. Indeed, quartz occurrences and mineralizations have been described in the Internal Zones of the Betic Cordillera as well as in the Neogene basins whereas chalcedony have not been described in mineral assemblages.

The thermal waters located in the evaporitic basins (Granada and Guadix-Baza Basins) show estimated reservoir temperature from SiO₂-quartz ranging from 74 to 95°C. Assuming a thermal gradient of 30°C/km, which can be expected in the studied area (Fernández et al., 1998), these temperatures would correspond to depths and hydrostatic pressures varying from 2.5 to 3.2 km and from 250 to 320 atm respectively. The thermal waters BUC and BUG, located close to the SE-NW faults, show the lowest estimated reservoir temperature, ranging from 51 to 58°C and corresponding to hydrostatic pressure spanning between 170 and 200 atm respectively. The thermal waters located at the contacts between metamorphic complexes (BAA, CL, and BSL) show the highest estimated reservoir temperatures ranging from 126 and 142°C, corresponding to depths of 4 - 4.5 km and a hydrostatic pressures of – 400 to 450 atm.

The Ca-Mg geothermometer provides temperatures ranging mainly between 71 and 91°C with little variation between the different thermal waters (Table 4-4). The obtained temperatures are in good agreement with those of SiO₂-quartz geothermometers for the waters located in the evaporitic Granada Basin. However, the Ca-Mg geothermometer give similar reservoir temperatures regardless to the geological context of the studied thermal waters, due to low variations in their Ca/Mg ratios, ranging mainly from 1.5 to 2.4. Therefore, it seems that this geothermometer might not be suitable for all investigated thermal waters in the central Betic Cordillera.

The results of the geobarometrical method based on the (HCO₃⁻)²/SO₄²⁻ ratio (Chiodini et al., 1995) give values of pCO₂ in depth ranging from 0.04 to approximatively 23 atm. The high values (> 5 atm) are obtained for the thermal waters of located on the contact of metamorphic complexes (CL, BSL, and BAA).

Geothermometrical modeling

The first results of the geothermometrical modeling including all mineral phases (quartz, chalcedony, anhydrite, dolomite, calcite, Ca-montmorillonite, laumontite, Mg-chlorite, and kaolinite) do not reach a common equilibrium temperature (Figures 4-3 and 4-4).

Although we can expect the carbonates as part of the buffering mineral assemblage in depth due to their ubiquity in the sedimentary basin and in the Central Betic Cordillera, they cannot reach equilibrium in the reservoir conditions. As shown in Figures 4-3 and 4-4, the waters are close to equilibrium or oversaturated with respect to calcium calcite and dolomite in the outlet conditions and these minerals have retrograde solubility. The apparent oversaturation in the outlet conditions might result from CO₂ outgassing process during the ascent of the waters to the surface.

Sample	Outlet temp.	SiO ₂ -Quartz				SiO ₂ -chalcedony		Ca/Mg	pCO ₂
		Michard (1979)	Verma (2000)	Fournier and Potter (1982)	Fournier (1977)	Arnorsson (1983)	Michard (1990)	Chiodini (1995)	Chiodini (1995)
Contacts metam. complexes									
BSL	26	145	143	146	139	115	102	86	16.34
CL	21	133	130	134	129	103	92	88	23.82
BAA	51	128	124	128	127	97	87	60	5.63
Graben into Alp. Complex									
BUC	25	57	47	57	62	26	24	75	0.54
BUG	23	52	42	51	58	21	20	74	0.66
Evaporitic basin									
BM	30	76	67	76	79	45	41	81	0.08
SF	39	83	74	83	85	52	47	87	0.05
SRN	32	76	67	76	79	45	41	75	0.04
SE	30	74	66	75	78	43	40	71	0.16
BAG	40	84	76	85	86	53	48	89	0.74
BNAG	39	96	89	97	97	65	59	91	0.38
AT	34	61	52	61	66	30	28	88	0.05
BZ	35	90	82	90	91	58	53	84	0.06

Table 4-4: Temperature (°C) obtained with selected geothermometers and pCO₂ (atm) obtained with Chiodini et al. (1995)'s *geobarometer*.

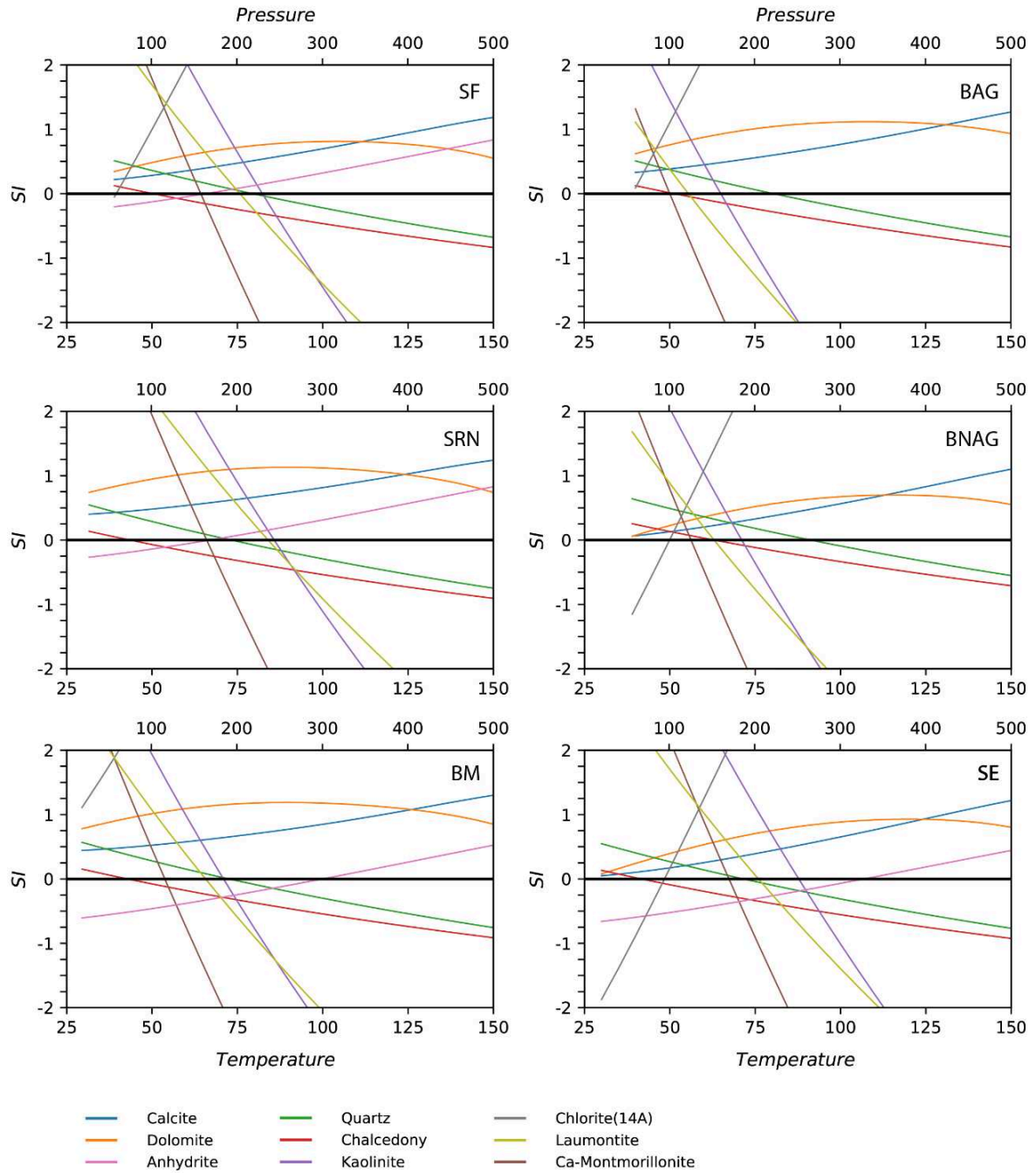


Figure 4-3: Evolution of the mineral saturation indices with temperature for the thermal waters located in the evaporitic Granada Basin by geothermometrical modeling.

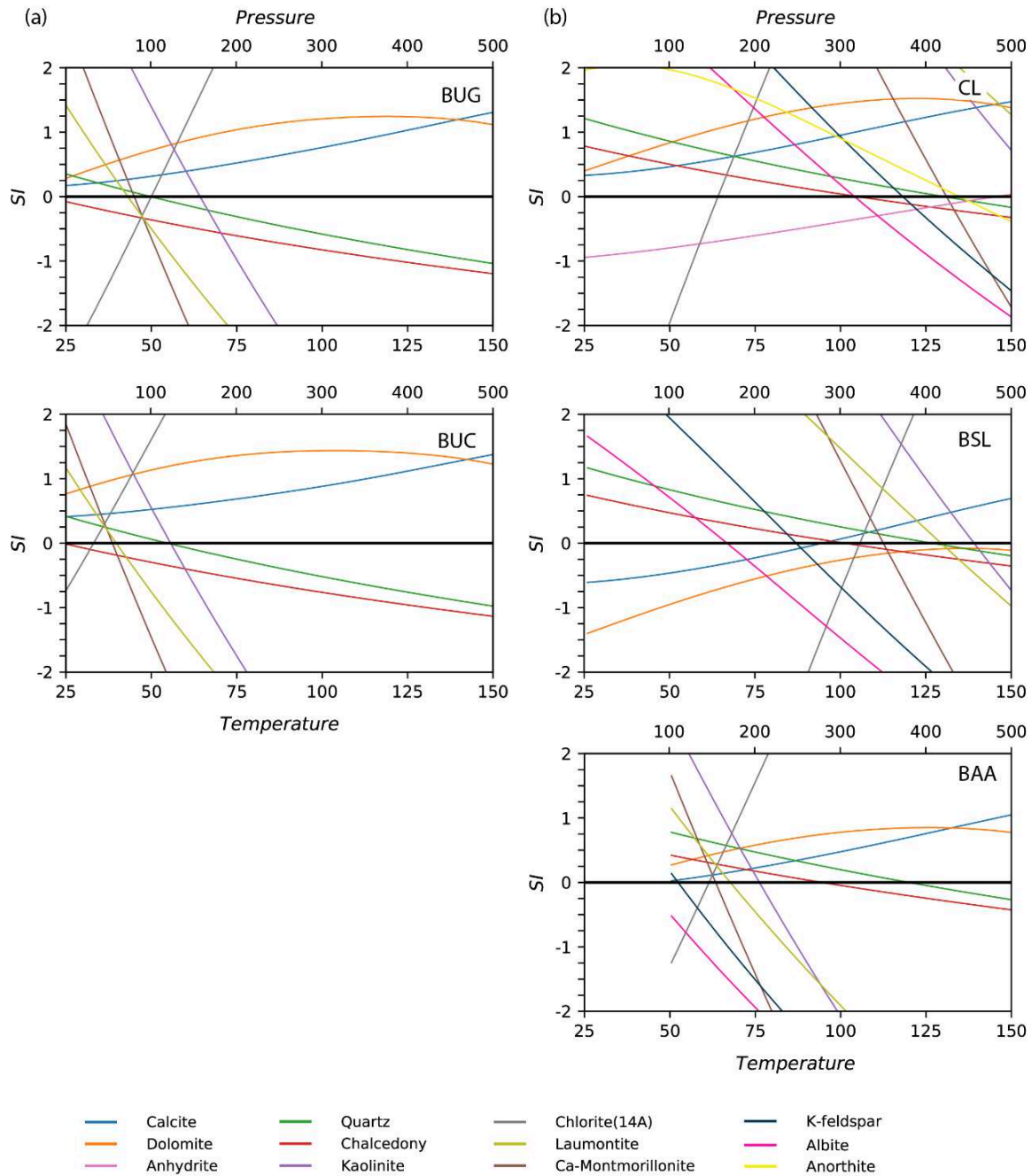


Figure 4-4: Evolution of the mineral saturation indices with temperature for the thermal waters located (a) in the graben in the Alpujarride Complex and (b) on the contacts of the metamorphic complexes.

Hydrogeochemical modeling

The results of the simulations show that, globally, $p\text{CO}_2$ in the outlet conditions varies between $\sim 6 \times 10^{-3}$ and 1 atm. The $p\text{CO}_2$ obtained in the third step of the simulation after equilibration with dolomite show values ranging from $\sim 2 \times 10^{-2}$ and 40 atm (Figure 4-5), whereas the values of $p\text{CO}_2$ after equilibration with aluminosilicates and carbonates vary

between 5.4×10^{-3} and 1.8×10^2 atm (Figure 4-6). The logarithmic relationship between $p\text{CO}_2$ and temperature for the waters equilibrated with the both carbonates and alumino-silicates might reflect strong constraints on the simulations.

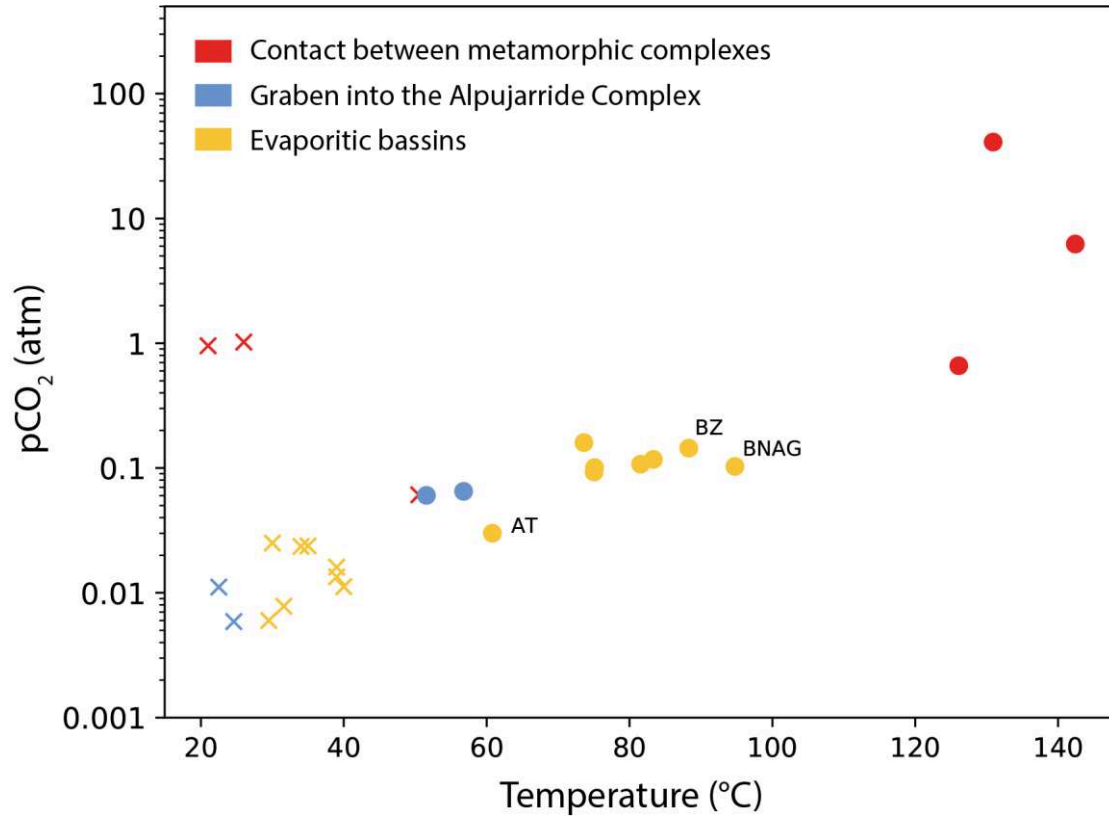


Figure 4-5: Relationship between $p\text{CO}_2$, (atm) and temperature ($^{\circ}\text{C}$), for the outlet (crosses) and reservoir (circles) conditions considering dolomite equilibrium in depth.

The geochemical modeling allows discriminating the three groups of waters, already distinguished by geology, regarding the $p\text{CO}_2$ in the reservoir conditions:

- Group of waters located in the evaporitic basins

The results of the simulations in the evaporitic basin Granada Basin give a pH of the waters in equilibrium with dolomite in the reservoir conditions ($74 < T < 95^{\circ}\text{C}$ and $250 < P_{\text{hydro}} < 320$ atm) ranging from 6.5 to 6.8 and an estimated $p\text{CO}_2$ spanning between 9×10^{-2} and 1.6×10^{-1} atm (Figures 4-5). The simulations taking into consideration carbonates and alumino-silicates give similar ranges of pH (from 6.5 to 6.7) and $p\text{CO}_2$ (from 6×10^{-2} to 2×10^{-1} atm) than those obtained with dolomite equilibrium for the water points located in the Granada basin (Figure 4-6). However, the two samples BNAG and BZ show slightly higher $p\text{CO}_2$ ranging from 3×10^{-1} and 6×10^{-1} atm. The thermal water of Alicun de las Torres (AT), showing a lower reservoir temperature similar to BUC and BUG samples, have an estimated low $p\text{CO}_2$ in depth for both

simulations ranging from 1×10^{-2} to 3×10^{-2} atm (Figure 4-5 and 4-6). The variation in $p\text{CO}_2$ between the steps 1 and 3 of the simulation, $\Delta p\text{CO}_2$, estimated for this group of thermal waters ranges from 3×10^{-2} to 6×10^{-1} atm (Figure 4-7), corresponding to ~ 1 to 20 mmol/L of CO_2 .

- Group of waters in the graben in the Alpujarride complex

The results of the equilibrium simulations with dolomite in the reservoir conditions ($51 < T < 58^\circ\text{C}$ and $170 < P_{\text{hydro}} < 200$ atm) for the waters located in the graben into the Alpujarride Complex give a pH of the waters of approximately 6.8 and an estimated $p\text{CO}_2$ of 6×10^{-2} atm (Figure 4-5). The simulation of these waters in equilibrium with both carbonates and aluminosilicates (calcite, dolomite, quartz, kaolinite, and Mg-chlorite) give higher values of pH ranging from 7.3 to 7.4 and lower values of $p\text{CO}_2$ spanning between 5×10^{-3} and 9×10^{-3} atm (Figure 4-6). The estimated variation in $p\text{CO}_2$ between the depth and the surface, $\Delta p\text{CO}_2$, ranges from ~ 0 to 6×10^{-2} atm (Figure 4-7), corresponding to maximum 2 mmol/L of CO_2 .

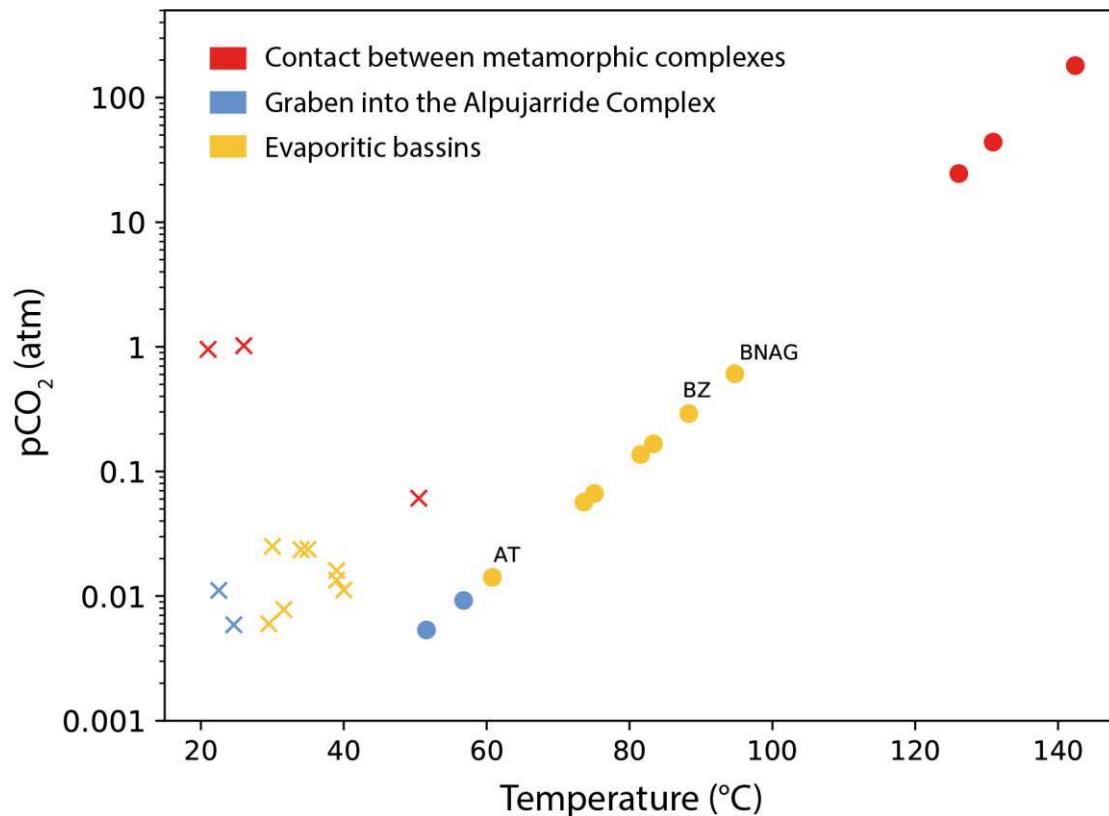
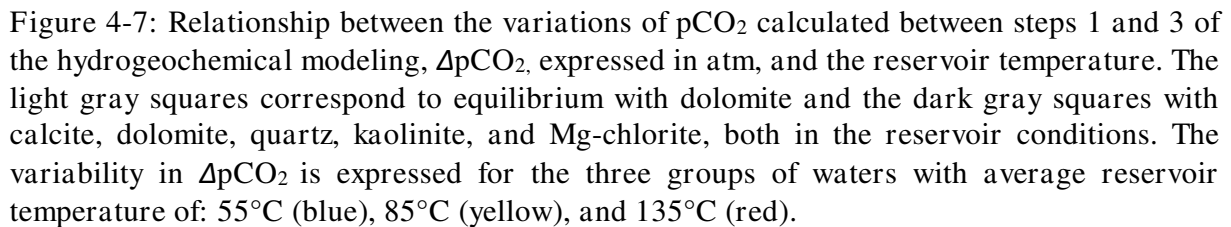


Figure 4-6: Relationship between $p\text{CO}_2$ (atm) and temperature ($^\circ\text{C}$) for the outlet (crosses) and reservoir (circles) conditions considering equilibrium with calcite, dolomite, quartz, kaolinite, and Mg-chlorite in depth.

- Both geochemical simulations show high $p\text{CO}_2$ values ($> 7 \times 10^{-1}$ atm) and low pH (ranging from 5.1 to 6.7) in the reservoir conditions ($126 < T < 142^\circ\text{C}$ and $400 < P_{\text{hydro}} < 450$ atm) for the thermal waters located at the contact with the metamorphic complexes. The estimated $p\text{CO}_2$ in depth is lower considering the equilibrium with dolomite only (ranging from 6×10^{-1} to 6 atm) than considering the equilibrium with the carbonate and alumino-silicate assemblage (ranging from 25 to 180 atm) (Figures 4-5 and 4-6). The estimated $\Delta p\text{CO}_2$ for this group of thermal waters spans from 6×10^{-1} to 1.8×10^2 atm (Figure 4-7), corresponding to 20 mmol/L to 5 mol/L of CO_2 .



Geothermometrical modeling with CO₂ degassing (open system)

- Group of waters located in the evaporitic basins

The geothermometrical simulations with the lowest estimation of CO₂ addition deduced from the hydrogeochemical modeling, 1 mmol/L, result in a common reservoir temperature of 75 to 90°C for the waters of the evaporitic basins (Figure 4-8). Waters are at potential equilibrium with the following mineral buffer: carbonates (calcite and dolomite), anhydrite, quartz, and possibly Mg-chlorite or Ca alumino-silicate (laumontite or a Ca-montmorillonite). These results show that low amount of CO₂ degassing (~ 1 mmol/L) are necessary in open system to reach equilibrium with dolomite and alumino-silicates. Evaporites is also part of the buffer mineral assemblage in this sedimentary environment.

- Group of waters in the graben in the Alpujarride Complex

The geothermometrical simulations in open system with addition of 0.5 mmol CO₂ show estimated reservoir temperatures ranging from 50 to 60°C for the waters located in the graben in the Alpujarride Complex (Figure 4-9) with the following mineral buffer: carbonates (calcite and dolomite), quartz, and Ca alumino-silicate (Ca-montmorillonite). Higher amount of added CO₂ do not lead to a common equilibrium of mineral phases at a specific temperature.

- Group of waters located at contact with metamorphic complexes

Modeling of CO₂ degassing in open system with geothermometrical simulations shows that 7 mmol/L to 1 mol/L of added CO₂ are necessary for the waters to be at equilibrium at temperature ranging from 120 and 140°C with the following mineral assemblage: quartz and dolomite, and sometimes Mg-chlorite and laumontite (Figure 4-10).

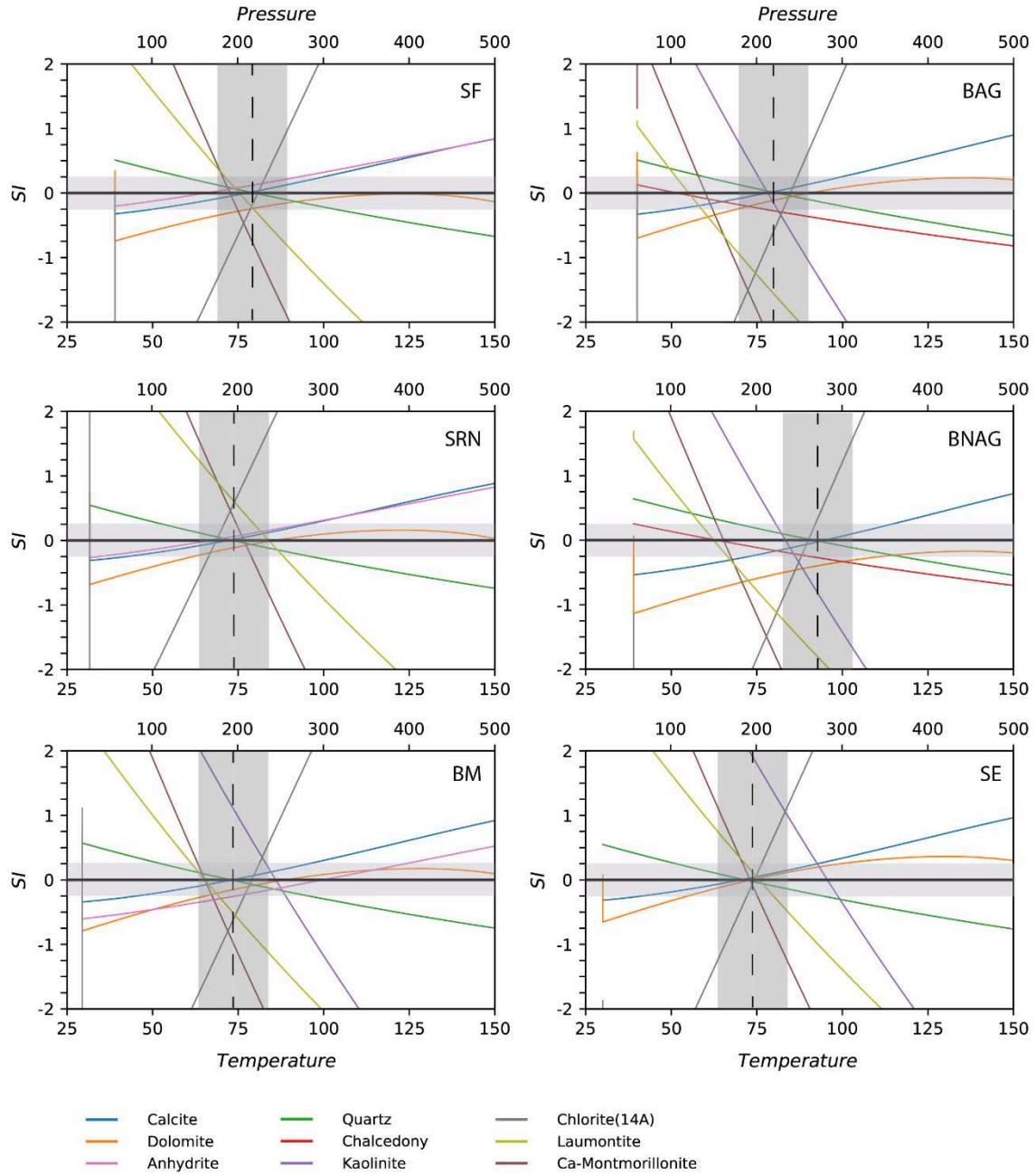


Figure 4-8: Evolution of the mineral saturation indices with temperature for the thermal waters located in the evaporitic Granada Basin by geothermometrical modeling with theoretical CO_2 addition (1 mmol/L) to compensate possible CO_2 outgassing during the ascent of the waters.

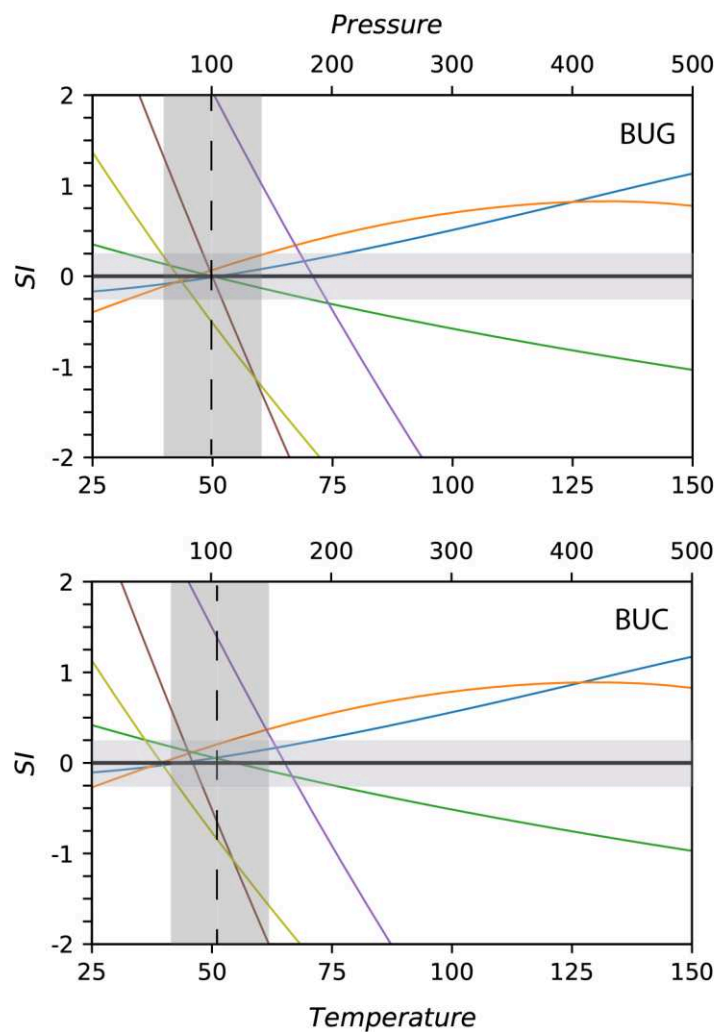


Figure 4-9: Evolution of the mineral saturation indices with temperature for the thermal waters located in the Valle de Lecrin graben by geothermometrical modeling with theoretical CO_2 addition (0.5 mmol/L) to compensate possible CO_2 outgassing during the ascent of the waters

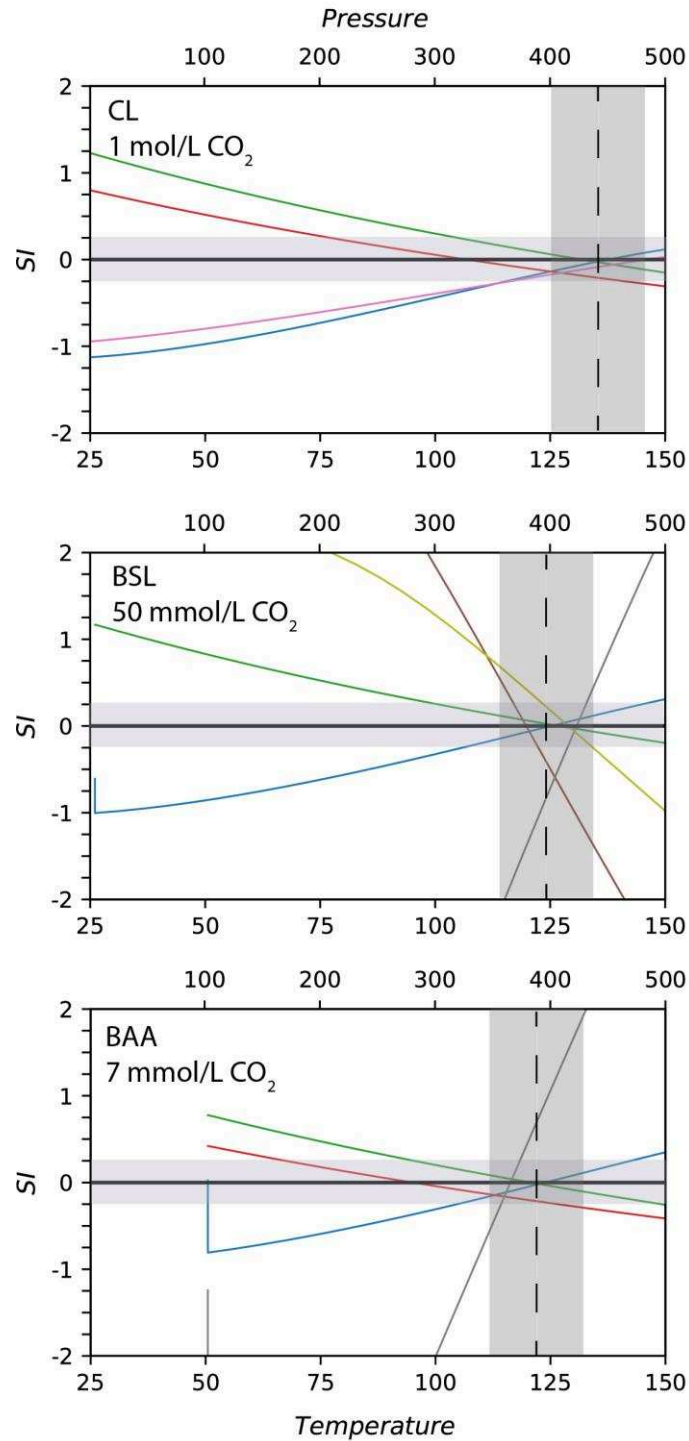


Figure 4-10: Evolution of the mineral saturation indices with temperature for the thermal waters located on the contacts of the metamorphic complexes. Geothermometrical modeling with theoretical CO₂ addition to compensate possible CO₂ outgassing during the ascent of the waters.

4.2.6. Discussion

4.2.6.1. Role of the mineral buffers in CO₂ estimation

The thermal waters in the Central Betic Cordillera are characterized by large heterogeneity in their geochemistry in the outlet conditions and in their geothermal characteristics. The three groups of waters, which were defined based on the geology at the thermal water locations, can be also distinguished from their temperature and pCO₂ in the reservoir. The groups of thermal waters have distinct reservoir temperatures, estimated with the SiO₂-quartz geothermometer, ranging from low-enthalpy (~55°C) to medium-enthalpy (~140°C) geothermal systems. Using the results of the geochemical and geothermometrical modeling we discuss in this section the mineralogical buffers and chemical properties of the reservoirs and the variations in pCO₂ between the depth and the surface ($\Delta p\text{CO}_2$) in both closed and open system for the three groups of waters. For all groups the assessed $\Delta p\text{CO}_2$ indicates CO₂ degassing during the ascent of the water to the surface. This CO₂ release is controlled by the equilibrium with respect to mineral phases in the reservoir conditions (Figure 4-7).

The group of thermal waters located in the sedimentary basins (Granada and Guadix-Baza Basins), whose reservoir temperatures range from 74 to 95°C, seem to be buffer in depth by mainly carbonates, evaporites, quartz and few alumino-silicates. The fact that there is a good agreement in $\Delta p\text{CO}_2$ with both dolomite buffer and carbonate/alumino-silicate buffer show that carbonates are the predominant buffer in this environment. The values of pCO₂ resulting from geochemical simulations in depth are in quite good agreement with those estimated by the geobarometer from Chiodini et al. (1995), ranging from 0.04 to 0.16 atm. This geobarometer, specifically established for low- to medium- geothermal systems hosted in carbonates and evaporites, might be an efficient tool to estimate the reservoir pCO₂ in this sedimentary context (similar range of temperature and pCO₂).

The presence of evaporites needs to be considered for the geothermal systems in sedimentary environment as it might enhance CO₂ release through dedolomitization process. Prado-Pérez and Pérez del Villar (2011) showed that the thermal water AT may result from dedolomitization in depth followed by CO₂ degassing. Dedolomitization, which is a process described in other natural systems (Auqué et al., 2009; López-Chicano et al., 2001b), corresponds to dolomite dissolution and calcite precipitation caused by the dissolution of gypsum and/or anhydrite. CO₂ loss, before or after outlet of the thermal waters, might occur as evidenced by the presence of fossil and present-day massive thermogenic travertine deposits (Prado-Pérez and Pérez del Villar, 2011) in the Alicun de las Torres site. This process of

dedolomitization is most probably occurring in other geothermal systems in the evaporitic Granada and Guadix-Baza basins.

For the thermal waters located in the graben in the Alpujarride Complex, which show the lowest estimated reservoir temperature, the buffer minerals are carbonates, quartz, and Ca alumino-silicate (Ca-montmorillonite). $\Delta p\text{CO}_2$ is higher considering the dolomite buffer than considering the carbonate/ alumino-silicate buffer. The difference in $p\text{CO}_2$ simulated with the two types of mineral buffers (dolomite only and the carbonate/alumino-silicate association) for the thermal waters in the graben might be the signature of the basement, whereas the similar $p\text{CO}_2$ estimated for the waters in sedimentary basin would be the signature of the sedimentary pile. Moreover, the values of $p\text{CO}_2$ for both simulations in depth are lower than those estimated by the geobarometer from Chiodini et al. (1995) of 0.54 and 0.66 atm for BUC and BUG samples respectively.

In the other hand, the group of waters located at contact with metamorphic complexes, whose display the highest estimated reservoir temperature (130 – 140°C), the mineral buffer in depth are more difficult to assess due to the large CO_2 degassing. Indeed, these waters show the highest measured dissolved CO_2 concentrations ($> 39 \text{ cm}^3/\text{L}$) distinguishing them from the other thermal springs in the Central Betic Cordillera. They are at equilibrium with the following mineral assemblage in the reservoir conditions: quartz and dolomite, and most probably with Mg-chlorite and laumontite. The $\Delta p\text{CO}_2$ is lower with dolomite buffer than with carbonate and alumino-silicate buffer (Figure 4-7).

The comparison between the results of simulations in closed and open systems for all the thermal waters show that lower CO_2 degassing is modeled in open system than in closed system. This point highlights the importance to evaluate the efficiency of the system to ascend rapidly water from the depth to the surface.

Calcite precipitation might result from the degassing process due to pH increase and driven kinetics compared to dolomite precipitation. The amount of precipitated calcite can be evaluated during a given time range using the amount of CO_2 loss during the ascent of the water and estimated flow rate of the springs found in literature and checked on the field (ranging from 0.2 to 100 L/s). Assuming a time range comprised between 1,000 and 100,000 yr, the amount of calcite precipitated is estimated to range from $\sim 10^2$ to 10^6 m^3 for the waters in the basins or their borders. This estimation can be compared to those of perched travertines deduced from the precise description of travertine proposed a complete This estimation is in good agreement with the volume of travertines that can be deduced from study of Martín-Algarra et al. (2003) in the northeastern part of the Granada Basin (from 10^4 to 10^5 m^3 for the last 200,000 yr).

4.2.6.2. Relationship $p\text{CO}_2$ and temperature

Using thermodynamic calculations (hydrogeochemical and geothermometrical simulations), we show the key role of the reservoir temperature and the buffer mineral assemblage assumptions on the estimation of $p\text{CO}_2$. Recent study on the geochemical characterization of geothermal system pointed out that CO_2 trapping mechanisms are controlled by reservoir temperature (Elidemir and Güleç, 2018). In our studied area, we found increasing reservoir $p\text{CO}_2$ with increasing reservoir temperature (Figure 4-9). The thermal water with intermediate reservoir temperature (70 to 90°C) show the lowest uncertainty on the variation of $p\text{CO}_2$ between the depth and the surface ($\Delta p\text{CO}_2$) with the two mineral buffers (dolomite only and assemblage of carbonates and alumino-silicates). Higher uncertainty on $\Delta p\text{CO}_2$ is observed for the thermal springs with the higher reservoir temperature (120-140°C): carbonates and alumino-silicates buffer predicts higher $\Delta p\text{CO}_2$ than dolomite as mineral buffer. The thermal waters with the lowest reservoir temperature also show a large uncertainty on $\Delta p\text{CO}_2$ but higher $\Delta p\text{CO}_2$ is assessed considering dolomite equilibrium in the reservoir condition rather than equilibrium with carbonates and alumino-silicates.

4.2.7. Conclusions

Our study provides the first characterization of the reservoir conditions (T, P, and geochemistry) for the thermal waters in the central part of the Betic Cordillera. The $p\text{CO}_2$ in depth were tentatively assessed with both a chemical geobarometer and direct geochemical simulations. The variation of $p\text{CO}_2$ ranges from approximately 6×10^{-3} to 10^2 atm at the scale of the area. Based on the geology of the thermal water locations and the results of the geothermometrical and thermodynamic geochemical simulations three groups of waters have been determined.

The group of the thermal waters located in the sedimentary basin has estimated reservoir temperatures ranging from approximately 70 to 90°C and $p\text{CO}_2$ varying between 6×10^{-2} and 6×10^{-1} atm. The estimated variations in $p\text{CO}_2$ between the depth and the surface ($\Delta p\text{CO}_2$) were quite similar considering both dolomite buffer and carbonate/alumino-silicate buffer for the thermal waters in the Granada Basin. A mineral assemblage buffering in depth mainly composed of carbonates, evaporites, and quartz characterizes this system.

The group of waters located in the graben in the Alpujarride Complex presents the lowest reservoir temperature of 55-60°C and $p\text{CO}_2$ ranging from 5×10^{-3} to 7×10^{-2} atm, depending of the considered buffering minerals. The $\Delta p\text{CO}_2$ between the depth and the surface is higher with dolomite buffer than with carbonate and alumino-silicate buffer. The buffering mineral assemblage in depth is estimated to be carbonates, quartz, and Ca alumino-silicates.

In the other hand, the group of waters located at contact with metamorphic complexes shows the highest reservoir temperature of 130 – 140°C and $p\text{CO}_2$ ranging from approximatively 1 to 100 atm. The $\Delta p\text{CO}_2$ between the depth and the surface is lower with dolomite buffer than with carbonate and alumino-silicate buffer. The buffering mineral assemblage in the reservoir might be dolomite, quartz, Mg and Ca alumino-silicates.

This study highlights the importance of evaluating the mineral buffers in the reservoir conditions of the geothermal systems. The mineral assemblage at equilibrium in the reservoir conditions constrains the estimated CO_2 generation and release in depth. In the study case of the Central Betic Cordillera, the CO_2 degassing is more constrained in the evaporitic basins thanks to a strong carbonate/evaporite/quartz buffers than in the surrounding areas of the basins where the alumino-silicates play a non-negligible role. Moreover, we pointed out the key role of the reservoir temperature on the estimation of the reactions between CO_2 , water, and rocks for the geothermal systems in sedimentary basins.

4.3. ADDITIONAL DATA

4.3.1. Relationship between hydrothermal characteristics and tectonics of the Central Betic Cordillera

In this section, I focus on the regional scope of this study by linking the hydrochemistry of the thermal waters with the tectonic structures of the Central Betic Cordillera. As seen in the previous article, the concentration in CO₂ depends mainly on the mineralogical control in the reservoir conditions. However, trying to interpret the physical-chemical characteristics of the thermal waters using the information on fault systems and hydrogeology might allow getting a more precise picture of the fluid circulations in this area.

4.3.1.1. Supplementary information on the sampling points: tectonics and hydrogeological background

The thermal waters in the Central Betic Cordillera are mainly situated close to major tectonic structures. These tectonic accidents are preferential drain for fluids in the investigated area, where the geothermal system is fracture-controlled. The thermal waters can be gathered into five groups depending on the nature of the accidents:

- (1) Baño Salado de Lanjaron and Capuchina de Lanjaron springs (BSL and CL) are located in the Sierra Nevada along the detachment between the Nevado-Filábride and Alpujárride complexes. Baños Alhamilla spring (BAA) is situated further to the east in the Sierra Alhamilla along the same tectonic contact, where it is also close to the trace of an important strike-slip fault of near N30E direction.
- (2) Baños de Zujar (BZ) and Baños de Alicún de las Torres (AT) are a well and a spring respectively, linked by faults with small Subbetic carbonate outcrops, and close to the above mentioned IEBZ and CAFS.
- (3) Sierra Elvira (SE) is located on the trace of an active fault, belonging to the NW to NNW directed fault system that continues toward the city of Granada, and also spatially linked with another small Subbetic outcrop. The thermal water fills partially a karstic cavity, from which it is pumped to supply the spa. Baños Urquizar Chico (BUC) and Baños Urquizar Grande (BUG) are springs aligned along a fault trace striking N30E. These fault systems are responsible of the termination to the west of the Sierra Nevada massif in the Valle de Lecrín tectonic graben in the Alpujárride Complex, where these two springs appear. They are also related with the recent sismicity that affects the area

surrounding the city of Granada. The sampling point Baños de la Malahá (BM) is also located in the intersection of the above mentioned NW-NNW fault system with another system striking roughly E-W that is particularly well developed in that south border of the Granada basin. BM was traditionally a spa supplied by a spring that was spatially linked to a very small ($< 0,1 \text{ km}^2$) outcrop of Triassic carbonates belonging to the Alpujárride Complex limited by faults, but since a few years the water is pumped by a well that has dried out the spring.

- (4) Baños Alhama de Granada (BAG) and Baños Nuevo Alhama de Granada (BNAG) springs belong to the same spa and is close to the IEBZ above mentioned. The site is spatially related to a small ($< 1 \text{ km}^2$) Subbetic outcrop by way of faults whose were active recently. The site of BAG originated after the important earthquake happened at the end of the XIX century.
- (5) Finally, Baños Santa Fe (SF), and Sondeo Romilla de la Nueva (SRN) are wells located in the Granada evaporitic basin. The other two points are relatively deep ($>500 \text{ m}$) artesian flowing wells.

The main regional aquifers in this part of the Cordillera are the Triassic carbonates from the Alpujárride Complex, and the Jurassic carbonates from the Subbetic, both permeable mostly by fracturation and karstification, respectively. The studied thermal springs, with the exception of those included in the first group above mentioned, have been mainly related with the flow through the Triassic carbonates. However, some mixing with groundwater coming from Subbetic aquifers may occur in the ascent of the thermal waters. In this case, is not uncommon that the groundwater exhibits a chemical signature due to the dissolution of Triassic gypsum and anhydrite that appear frequently in their clayey substratum. Other secondary porous aquifers can influence to different degrees the chemistry of the thermal waters by mixing in their way up flow. They are mainly calcareous sandstones and conglomerates in the Neogene sequence, and even the uppermost formation of Quaternary alluvial deposits that are particularly well developed in the Granada Basin.

4.3.1.2. Results

The different parameters investigated in the article (water chemistry, pCO_2 and temperature in the outlet and reservoir conditions respectively) have been represented using these five distinct tectonic groups.

Distinguishing the signature of the different tectonic accidents within the sedimentary basin is rather difficult. The results of $\delta^{13}\text{C}$ of the TDIC show clear variations according to the tectonic groups (Figure 4-11). The waters related to SE-NW faults displays the lowest $\delta^{13}\text{C}_{\text{TDIC}}$ (~ -9 ‰) whereas the $\delta^{13}\text{C}_{\text{TDIC}}$ values of the other thermal waters in the evaporitic basins or close to the CAFS range from -1.7 to -5 ‰. The waters at the contact between the metamorphic complexes show a larger range of $\delta^{13}\text{C}_{\text{TDIC}}$ (from -5 to -9 ‰).

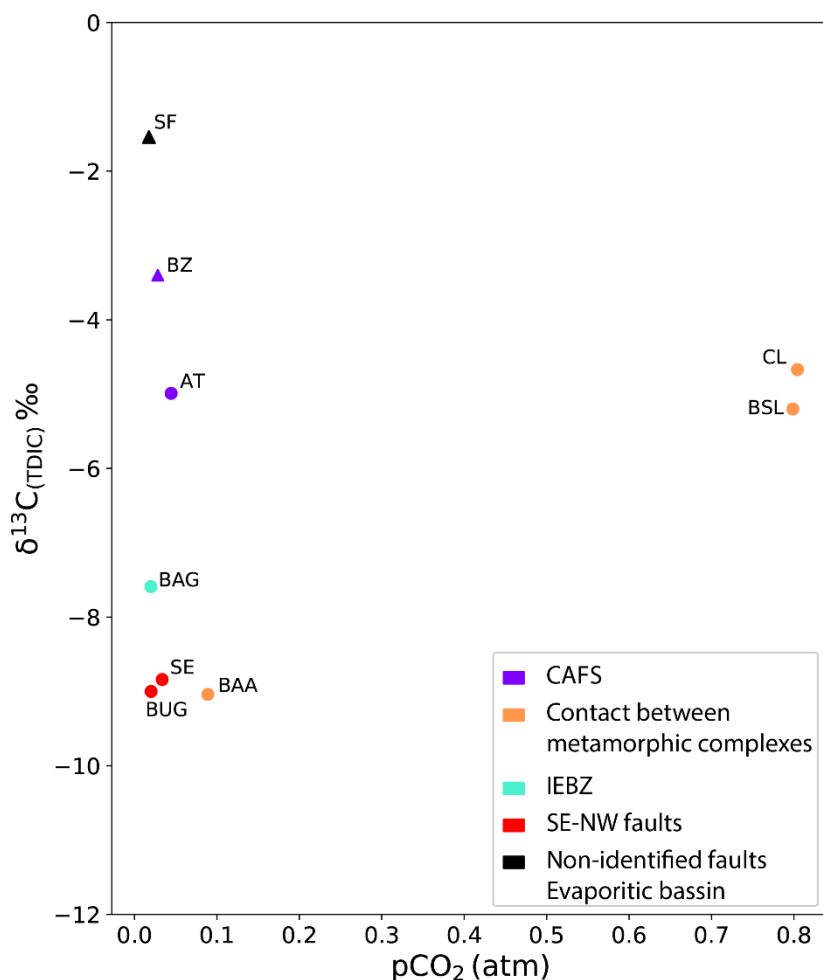


Figure 4-11: Co-variation of $\delta^{13}\text{C}_{\text{TDIC}}$ and CO_2 partial pressure (atm).

4.3.2. Details of the hydrogeochemical simulations

To complete the description of the geochemical simulations presented in the article (section 4.2.4.4), a schematic representation of the modeling workflow is shown in Figure 4-11. Simulations in both open and closed system were performed for all the thermal waters in the investigated area. The $\Delta p\text{CO}_2$ that are estimated in the closed-system modeling are used for the simulations in open system (geothermometrical simulations with CO_2 addition).

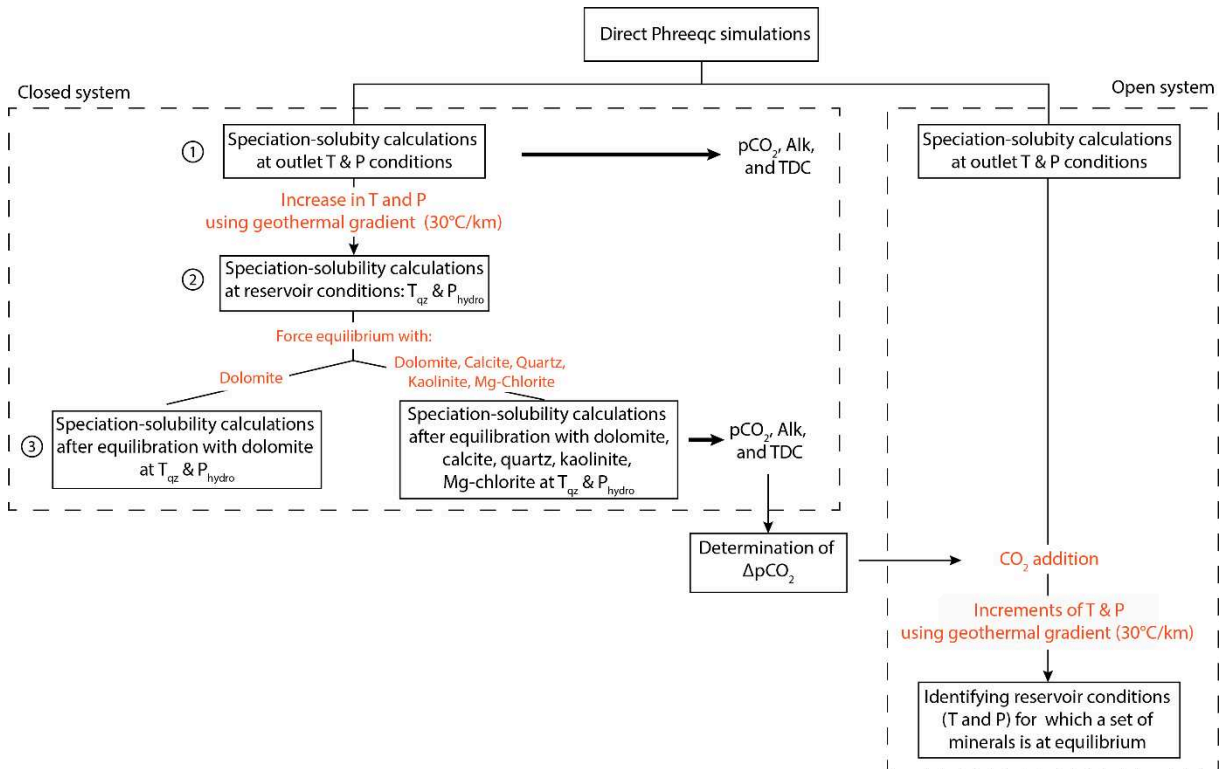


Figure 4-12: Schematic diagram of the Phreeqc simulations to estimate hydrochemistry at the temperature and pressure reservoir conditions and the variations of pCO₂ between the depth and the surface.

CHAPTER 5

WATER-ROCK INTERACTIONS IN THE GRANADA BASIN

CHAPTER 5: WATER-ROCK INTERACTIONS IN THE GRANADA BASIN

5.1. PRESENTATION

In this chapter, I focus on the evolution of the groundwater geochemistry within the sedimentary infilling of the Granada Basin. The goal of this study is to obtain a reaction model in the basin that could be then potentially coupled to a transport model for subsequent reactive transport modeling.

The focus on the water-evaporite interaction has been driven by the occurrence of several evaporite layers in the Granada Basin with various spatial distribution. As mentioned in section 1.2.3, two evaporite layers of different ages and composition are present in the sedimentary infilling of the basin. The Tortonian evaporites are composed of anhydrite and halite whereas the Messinian evaporites are mainly anhydrite and gypsum. The extension of the Messinian evaporites is larger than the Tortonian ones, covering almost all the basin (Figure 1-11). Two celestite orebodies, linked to the evaporites, have been also reported in the basin, forming one of the largest strontium deposit in the world (García-Veigas et al., 2015). Triassic evaporites (gypsum and halite) are also present in the basement of the basin, especially in the External Zone.

In addition, the Granada Basin has a semi-arid climate where water resource suffers from increasing anthropic pressure (agriculture, industry and tourism). Higher interaction with evaporites modify the water quality by increasing its salinity, and therefore decrease its potential utilizations by the population. Castillo (2005) pointed out this problem in the main aquifer of the Granada Basin, the Vega de Granada aquifer, where drastic changes in the piezometric levels have been observed between 1996 and 2004. He showed a strong correlation between the lowering of piezometry and increases in the electrical conductivity, clue of salinity. Waters with high salinity, improper for drinking usage and for most types of crops, are also well known in the basin. The water with the highest salinity (~ 180g/L of salts) is located in Salinas La Malaha in the evaporitic area of the basin and is exploited to collect salt since the Roman times.

In the present study, I attempt to get insights on the groundwater circulations at the scale of the whole Granada Basin using the evolution of the water composition. The groundwaters show large ranges of temperature (from 6 to 40°C), of pH (from 5.8 to 8.0), and of electrical

conductivity, i.e. EC, (from 0.09 to 187 mS/cm), which is used as the marker of the salinity throughout the study. Increasing EC from the borders of the basin, i.e. in the recharge areas, to the center of the basin was linked to the evolution from carbonate-dominated waters to sulfate and chlorine-dominated waters.

The control of the major elements (Ca, Mg, K, Na, HCO_3 and SO_4) were evaluated based on the saturation states with respect to carbonates, alumino-silicates (i.e., Korjinski diagrams) and sulfate minerals. Carbonates, including both calcite and dolomite, seem to control mainly Ca and Mg concentrations and pH within the whole basin. A strong control of K appears to be exercised by the alumino-silicates as sulfate-dominated waters are located on the triple point between kaolinite, pyrophyllite, and microcline. Considering Na, the sulfate-dominated waters evolve along the boundary between kaolinite and pyrophyllite.

The potential reactive flow paths were discussed using the distribution maps of the groundwater saturation with respect to sulfate minerals (barite, celestite, and gypsum). The saturation of the waters with respect to the sulfate minerals shows that waters become saturated with respect to barite, then celestite and finally gypsum with increasing EC from the border to the center of the basin. This evolution gives insights of potential groundwater flow paths at the scale of the whole Granada Basin.

5.2. WATER-ROCK INTERACTION IN THE GRANADA BASIN (SOUTHERN SPAIN): A REGIONAL STUDY FOR GROUNDWATER REACTIVITY IN SEDIMENTARY BASINS

C. Lix ^{1,2*}, P. Zuddas², X. Guichet¹, J. Benavente³, J.A. Luque-Espinar⁴, and M. Barbier¹

¹ IFP Energies Nouvelles, 1 et 4 avenue de Bois-Préau, 92852 Rueil-Malmaison, France

² Sorbonne Université, CNRS-INSU, Institut des Sciences de la Terre Paris, ITeP UMR 7193, F-75000 Paris, Campus Pierre et Marie Curie - 4 place Jussieu 75005 Paris, France

³ Departamento de Geodinámica e Instituto de Investigación del Agua, Universidad de Granada, Granada, Spain

⁴ Instituto Geológico y Minero de España, Granada, Spain

This section corresponds to an article in preparation to be later submitted in Applied Geochemistry.

5.2.1. Introduction

Understanding water-rock interaction is a major concern for water resource management in sedimentary basin. Groundwater geochemistry, in complement to surface and sub-surface hydrology, needs to be investigated in order to assess fluid reactivity at the scale of an entire sedimentary basin. Evolution in fluid reactivity, associated with potential flow paths, might allow performing reactive transport modeling.

The Granada Basin, located in a semi- arid area in the SW of Spain, is particularly impacted by the pressure on the water resource. The development of irrigated agriculture, tourism and industry drastically increased the groundwater use during the last decades (Vandenschrick et al., 2002) and have influenced locally groundwater hydrodynamics in the basin (Castillo, 2005, 1995). To satisfy the intensifying needs in waters many studies focused on the surface and sub-surface hydrology of the Granada Basin (Castillo, 2005; Castillo et al., 2004, 1997; Chica-Olmo et al., 2014; Mateos et al., 2017), as well as the recharge processes in the present watershed (Garrido, 2003; Kohfahl et al., 2008a). However, no studies from our knowledge tried to investigate the groundwater geochemistry and reactivity at the scale of the whole basin. Furthermore, the Granada Basin is also characterized by two layers of gypsum dated from the Tortonian and from the Messinian, as well as two celestite orebodies forming one of the largest strontium deposit in the world. These evaporites play an important role on the mineralization of waters in sedimentary basin and the interaction with these minerals needs to be evaluated.

The aim of this article is to evaluate the evolution of the groundwater composition in an

evaporitic basin using the Granada Basin as study case. The chemical composition and saturation state of the emerging waters was characterized, as well as the main geochemical controlling minerals and reactions in this basin. The evolution of the chemical composition and saturation with respect to carbonates, alumino-silicates, and sulfate minerals enables to estimate possible reactive flow paths from the border to the center of the basin.

5.2.2. Studied area

5.2.2.1. Geological and hydrogeological setting

The Granada Basin is a Neogene post-orogenic intramountainous basin in the Betic Cordillera. The Betic Cordillera is commonly subdivided into two units (1) the External Zone and (2) the Internal Zone (Figure 4.1).

The External Zone, which forms the northern border of the Cordillera, corresponds to mesozoic and tertiary sedimentary rocks of the continental Iberian paleo-margin of the Tethys Ocean. It consists of a non-metamorphic zone, which did not undergo the subduction of the Iberian plate under the Meso-Mediterranean micro-plate (Dyja, 2014; Vera, 2001, 1988).

The Internal Zone consists of three tectonically stacked metamorphic complexes from the base to the top: (1) the Nevado-Filábride, (2) the Alpujarride, and (3) the Maláguide. These complexes are distinguished from their metamorphism degree, their position in the subduction (geodynamic and structural histories). (1) The Nevado-Filábride Complex comprises Paleozoic or older metamorphic rocks (Gómez-Pugnaire et al., 2000), strongly affected by high-pressure Alpine metamorphism. This complex crops out in local tectonic windows in the Sierra Nevada and Sierra de los Filábres. This subunit consists of a pre-Triassic basement, mainly composed of mica schist, and a cover comprising from the base to the top: mica schists, a meta-evaporite interval, and marbles associated with calc-schists. (2) The Alpujarride Complex is composed of a series of nappes of Paleozoic-Mesozoic metasediments (Azañón et al., 1998). The pre-Mesozoic basement (graphite mica schists) is overlain by meta-sandstones, conglomerates, and schists, which are in turn overlain by Triassic carbonates (limestone, dolomitic limestone and dolostone). Mesozoic pelagic marls are at the top the complex. The Alpujarride Complex crops out extensively, in the sierras bordering the Granada Basin (Sierra Gorda, Sierra Tejeda, Sierra de la Pera, and parts of Sierra Nevada). (3) The Maláguide Complex is made up of non-metamorphic clastic and carbonate Paleozoic sediments covered by Mesozoic mixed sediments (carbonate, evaporite and siliciclastic). A small window of the Maláguide complex is situated at the east of the Granada Basin.

The Granada Basin infilling ranges from the early Miocene (around 8.3 Ma) to the Quaternary (Braga et al., 2003; Corbí et al., 2012) (Figure 5-1). The sedimentary sequence comprises from the bottom to the top: (1) deltaic siliciclastic sediments and marine carbonates dated of Langhian, Serravalian and lower Tortonian (Braga et al., 2003; Rodríguez-Fernández and Sanz de Galdeano, 2006a); (2) upper Tortonian proximal deltaic siliciclastic deposits and carbonates (temperate-water and coral-reef carbonates); (3) evaporites (gypsum and halite) and fluvial conglomerates, sandstones and silts dated from the latest Tortonian (7.3 to 7.2 Ma); (4) Messinian continental siliciclastic alluvial-fan and fluvial deposits, as well as lacustrine carbonates and evaporites (gypsum); (5) Pliocene and Quaternary siliciclastic materials, which accumulated in laterally limited fault-controlled, high-subsidence depocentres. The Granada Basin is also characterized by two celestite orebodies forming one of the largest strontium deposit in the world.

The hydro(geo)logy of the Granada Basin is characterized by a groundwater recharge mainly localized in the high elevation areas surrounding the basin (Sprenger, 2006). Two main types of aquifer can be distinguished in the studied area: (1) highly permeable aquifers (Vega de Granada aquifer and carbonate aquifers) and (2) low-permeability minor aquifers.

Within the highly permeable aquifer, the Vega de Granada aquifer is a wide (200 km² - 22x8 km) and thick (about 250 m locally) aquifer (Sprenger, 2006), which supplies water for a large part of the population and for irrigation of several cultures. Geologically, it is made of detrital alluvial material (gravel, sand, silt) deposited from the numerous rivers that flows in the area (Monachil, Darro, Dilar and Genil) (IGME, 1990). The direction of the flow of the aquifer from east to west is in accordance with the regional flow of the rivers (Sprenger, 2006).

The carbonate aquifers form the mountainous areas bordering the Granada Basin (IGME, 1990). The aquifers located in the Internal Zone are made up of Triassic and Jurassic limestones, dolostones, and marbles from the Alpujarride Complex, whereas those of the External Zone are composed of Jurassic carbonate formations. The carbonate aquifers have generally an high permeability due to karstification. The discharge of these carbonate aquifers is highly dependent of the precipitations as the residence time of the water is relatively short (Campos, 2006).

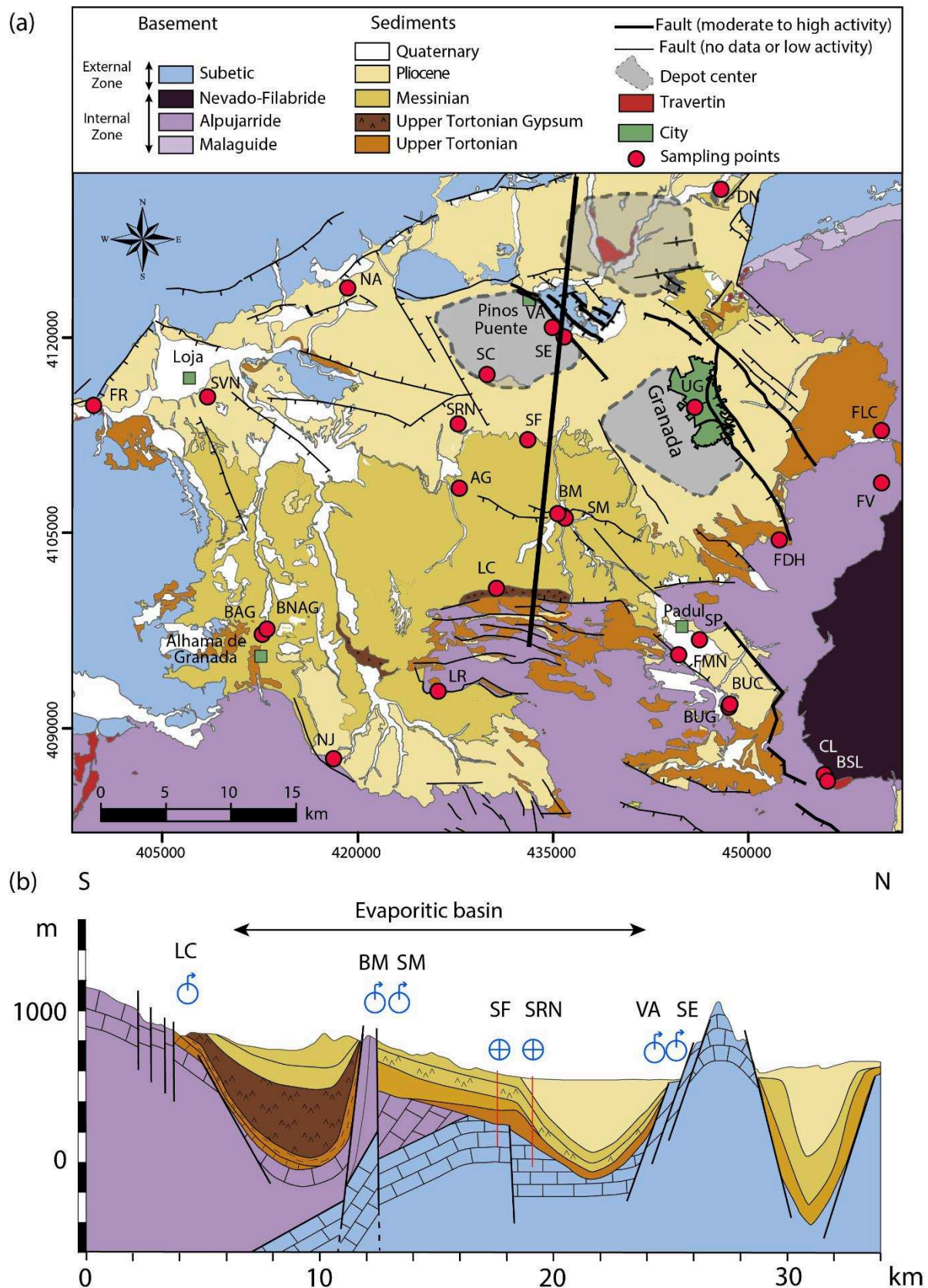


Figure 5-1: (a) Geological map of the Granada Basin with locations of the sampling points, modified after Galindo-Zalvidar et al. (2015) (b) S-N cross-section of the Granada Basin, modified after Rosino (2008).

Low-permeable to impermeable aquifers of the Granada Basin are composed of (a) the Triassic micaschists and quartzites of the Nevado-Filabride Complex located in the highest mountain area of the Sierra Nevada, (b) and the detrital and carbonated Mio-Pliocene basin deposits constituting most of the sedimentary infilling of the Granada Basin.

5.2.3. Materials and methods

5.2.3.1. Water sampling

Twenty-eight water samples were collected in the Granada Basin from 18 springs and 10 wells. The water samples were filtered with 0.45 μm membrane filters immediately after sampling to prevent loss of constituents through precipitation and sorption. Samples assigned to trace elements and Al analyses were filtered with 0.2 μm membrane filters to remove colloidal oxyhydroxides of iron and manganese and clay particles, which can pass through larger pores. The water samples dedicated to cations, minor and Al analyses were acidified using suprapure nitric acid (HNO_3). All Falcon® tubes and brown glass bottles were sealed with parafilm to avoid evaporation.

5.2.3.1. Water analyses

Physico-chemical properties

Physical-chemical parameters of the waters, including temperature, pH, electrical conductivity (EC), and alkalinity were measured directly on the field. Temperature and pH were measured with a portable pH-meter (VWR pH110) with a combination pH electrode. The electrode was calibrated with three buffer solutions at pH 4.0, 7.0 and 10.0 (25°C) (CertiPUR® Reference material). Electrical conductivity (EC) was measured with a portable conductimeter (VWR CO310). The electrode was calibrated with two potassium chloride standard solutions of 1.41 mS/cm and 12.8 mS/cm (25°C) (CertiPUR® Reference material) depending of the conductivity of the sample. The uncertainties on the measurements of temperature, pH, and EC were of $\pm 1^\circ\text{C}$, ± 0.1 , and ± 0.01 mS/cm respectively.

Alkalinity was determined by titration with an 0.01M or 0.1M hydrochloric acid solution depending on the encountered alkalinity range and by following the pH evolution with the pH-meter. The equivalent volume was determined with the Gran's method (Gran, 1952) and the analytical error of the alkalinity measurements was of approximately $\pm 5\%$.

Laboratory chemical analyses

The major cations and anions (Ca^{2+} , Mg^{2+} , K^+ , Na^+ , SO_4^{2-} , and Cl^-) were analyzed by ionic chromatography. Certified reference natural waters ION-96.4 and HAMIL-20.2 (Environment and Climate Change Canada) were analyzed at each series of analyses to detect analytical errors. The uncertainty of Mg^{2+} , K^+ , Na^+ , SO_4^{2-} determination is $\pm 5\%$ whereas that on Ca^{2+} and Cl^- is estimated to be $\pm 10\%$. Minor and trace elements (Ba, Sr, Al, Fe) were analyzed by Inductively Coupled Plasma Optical Emission Spectrometry ICP-OES. A certified reference material (TMDA-64.3 which is a trace element fortified water sample, Environment and Climate Change Canada) was analyzed at each series of analyses to detect analytical errors. The uncertainty of Ba and Sr determination is $\pm 10\%$ whereas that on Al is estimated to $\pm 20\%$.

The silica concentration were determined by spectrophotometric method following the protocol from Centre d'Expertise en Analyse Environnementale du Québec, (2016), suitable for natural groundwater with Si concentration ranging from 0 to 20 mg/l. This protocol allowing measuring only the reactive silica was adapted for waters with high ionic strength by preparing NaCl-enriched calibration solutions in the same range of ionic strength.

5.2.3.2. Geochemical calculations

Using the composition of the waters and the physical-chemical parameters, direct thermodynamic speciation-saturation calculations have been performed with the (version 3-0-6) PHREEQC software (Parkhurst et al., 2013). The saturation index of waters with respect to possible minerals (Equation 5-1) were calculated to test the equilibrium conditions or the departure from equilibrium of the system.

$$SI_m = \log \Omega_m = \log \frac{\prod^i (\gamma_i [c_i])^{v_{im}}}{K_s(P, T)_m} \quad (5-1)$$

where $[c_i]$ and γ_i are the concentration and the activity coefficient of the ion i , v_{im} is the reaction coefficient for the ion i and the mineral m , and $K_s(P, T)_m$ is the solubility constant of the mineral m dependent on the temperature and pressure.

The speciation-saturation calculations were performed with two different databases depending of the ionic strength of the waters. The phreeqc database was used for all samples except for those from Salinas La Malaha for which the Pitzer database was applied. Pitzer database is more appropriate for waters with high ionic strength as it uses the Pitzer equation to compute coefficient γ , and then calculate the activities of ions from the concentrations.

5.2.4. Results

5.2.4.1. Chemical composition of waters

All the results of the waters chemical composition of the waters are compiled in Tables 5-1 and 5-2. The investigated waters have an outlet temperature ranging from 6 to 40°C, corresponding to low to medium enthalpy waters, and pH values spanning between 5.8 and 8.1. The conductivity of the studied waters shows large range of values, from 0.09 to 187 mS/cm, corresponding to total dissolved solids (TDS) values from 0.08 to 175 g.L⁻¹. The total ionic balance does not exceed 8% for all water samples.

The composition of the water samples was reported in a Piper diagram as a function of the electrical conductivity in Figure 5-2. Assuming cogenetic waters, an evolution from carbonate-dominated waters to sulfate and chlorine-dominated waters with increasing conductivity is observed. Moreover, the dominants cations are also evolving from mainly calcium and magnesium to mainly sodium and potassium. We can see on the map (Figure 5-3) that the less conductive waters are located on the border of the basin in the mountain areas whereas the most conductive waters are located in the center of the basin. Therefore, there is an evolution of the water composition from carbonate-dominated waters at the border of the basin to sulfate- and chlorine- dominated waters in the center of the basin.

5.2.4.1. Saturation with respect to alumino-silicates

The evolution of the saturation with respect to alumino-silicates with increasing electrical conductivity was represented in activity diagrams, also known as Korjinski diagrams, for the system composed of H₄SiO₄, Al³⁺, K⁺, H₂O, the system H₄SiO₄, Al³⁺, Na⁺, H₂O and the system H₄SiO₄, Al³⁺, Ca²⁺, H₂O (Figures 5-4 and 5-5).

We can see that almost all waters are saturated or oversaturated with respect to quartz and kaolinite. Moreover, there are increasing trends of activity of potassium, sodium and silica with increasing electrical conductivity of the waters. The most conductive waters are in the field of stability of microcline and albite; i.e. saturated with respect to these minerals. A correlation is observed between the evolution of the saturation of waters with respect to alumino-silicate minerals (kaolinite, pyrophyllite and microcline) and the electrical conductivity (Figure 5-4). As mentioned before, the less conductive waters are located at the border of the basin with an increasing trend of electrical conductivity towards the center of the basin. Therefore, we can observe an increasing saturation with respect to alumino-silicates from the borders of the basin forming the recharge areas of the basin towards the center of the basin.

Name	Code	Type	Latitude	Longitude	Temperature °C	pH	EC mS/cm	Alkalinity mg/L	TDS g/L
Fuente de los 16 Canos	FLC	Spring	37°09.8611'N	3°26.6879'W	8	7.59	0.09	53.9	0.09
Sondeo surgente de Padul	SP	Well	37°01.046'N	3°36.147'W	15	7.78	0.49	237.4	0.37
Fuente del Hervidero	FDH	Spring	37°05.2530'N	3°32.0043'W	12	8.10	0.26	151.7	0.22
Deifontes Nacimiento	DN	Spring	37°19.9410'N	3°35.1730'W	15	7.34	0.45	241.0	0.43
Nacimiento de Alomartes	NA	Spring	37°15.6802'N	3°54.7070'W	16	7.49	0.35	198.5	0.30
Banos Urquizar Chico	BUC	Spring	36°58.3477'N	3°34.5347'W	25	7.58	0.99	243.2	0.68
					25	7.40	0.84	263.0	0.71
Fuente de la Viboras	FV	Spring	37°07.6694'N	3°26.6685'W	9	8.13	0.29	154.9	0.24
Fuente Alta	FA	Spring	37°06.2730'N	3°24.5655'W	6	8.12	0.11	31.9	0.09
University of Granada	UG	Well	37°10.7919'N	3°36.4675'W	18	7.16	1.26	421.3	0.86
Frontil	FR	Spring	37°10.6411'N	4°07.9549'W	17	7.49	0.67	224.5	0.45
Banos Alhama de Granada	BAG	Spring	37°01.1221'N	3°58.9970'W	40	7.36	1.13	218.8	0.67
					40	7.22	1.24	228.8	0.71
Banos Nuevo Alhama de Granada	BNAG	Spring	37°01.3410'N	3°58.7548'W	39	7.18	1.24	176.6	0.73
Arroyo de Granada	AG	Spring	37°07.3253'N	3°48.7641'W	16	7.05	3.39	169.6	2.91
Vivero Arco	VA	Well	37°14.0990'N	3°43.9615'W	17	7.05	2.01	454.0	1.28
Sondeo Venta Nueva	SVN	Well	37°11.0533'N	4°01.9903'W	17	6.92	2.02	375.0	1.44
Santa Clara	SC	Well	37°12.1029'N	3°47.3661'W	16	7.04	2.84	260.8	2.10
Banos de la Malaha	BM	Well	37°06.2946'N	3°43.6034'W	30	7.42	3.08	176.3	2.13
					27	7.78	2.84	203.2	2.21
Banos Urquizar Grande	BUG	Spring	36°58.2261'N	3°34.5854'W	23	7.31	1.50	256.7	0.91
					24	7.40	1.26	287.4	0.97
Santa Fe	SF	Well	37°09.3813'N	3°45.2023'W	39	6.99	4.69	157.2	3.38
					38	7.04	4.73	158.6	3.35
Sierra Elvira	SE	Spring	37°13.7033'N	3°43.3372'W	30	6.92	3.82	230.3	2.52
					30	7.05	2.68	309.4	2.04
Sondeo Romilla la Nueva	SRN	Well	37°10.0216'N	3°48.8567'W	32	7.26	6.13	166.1	4.26
Banos Salado de Lanjaron	BSL	Spring	36°55.4189'N	3°29.5869'W	26	5.81	8.18	784.9	3.70
Capuchina de Lanjaron	CL	Spring	36°55.1523'N	3°29.4182'W	21	6.06	34.15	1748.2	18.13
Salinas de La Malaha	SM	Spring	37°06.1982'N	3°43.3276'W	20	6.79	187.	232.5	167.79
					20	6.34	177	311.8	192.85
Salinas de La Malaha2	SM2	Spring	37°06.104'N	3°43.206'W	17	6.79	157	186.1	175.19
Nacimiento de Jatar	NJ	Spring	36°55.5051'N	3°55.0076'W	12	7.55	0.25	234.9	0.31
Los Rosas	LR	Well	36°58.3629'N	3°49.5737'W	18	7.27	0.45	360.0	0.48
Los Charcones	LC	Well	37° 03.0871'N	3°46.5296'W	17	7.4	0.54	339.2	0.54
Fuente Manantiales de la Nueva	FMN	Spring	37° 00.2467'N	3°37.2654'W	17	7.26	0.46	332.5	0.49

Table 5-1: Physicochemical measurements of investigated water samples.

Code	Temp	pH	Ca	Mg	Na	K	Alkalinity	Cl	SO ₄	SiO ₂	Al	Ba	Fe	Sr
FLC	8	7.59	0.27	0.25	0.10	0.02	0.88	0.04	0.12	0.13	2.55E-04	3.84E-05	1.78E-04	4.24E-04
SP	15	7.78	1.31	1.15	0.09	0.01	3.89	0.06	0.42	0.12	5.37E-04	6.05E-05	-	3.07E-03
FDH	12	8.10	0.92	0.39	0.07	0.01	2.49	0.06	0.13	0.10	4.88E-04	7.00E-05	-	2.09E-03
DN	15	7.34	1.78	0.86	0.18	0.02	3.95	0.17	0.77	0.12	6.24E-04	8.93E-05	-	1.19E-02
NA	16	7.49	1.14	0.68	0.32	0.03	3.25	0.21	0.14	0.12	5.06E-04	5.57E-05	-	1.07E-03
BUC	25	7.58	2.62	1.75	0.42	0.05	3.99	0.41	2.49	0.27	6.99E-04	2.28E-04	-	4.87E-02
		7.40	2.55	1.80	0.58	0.06	4.31	0.42	2.57	0.25	5.27E-06	2.25E-04	-	4.66E-02
FV	9	8.13	0.90	0.52	0.32	0.01	2.54	0.46	0.07	0.05	4.66E-04	2.33E-05	-	2.94E-03
FA	6	8.12	0.24	0.18	0.35	0.01	0.52	0.58	0.04	0.12	2.15E-04	2.92E-05	-	2.50E-04
UG	18	7.16	2.17	2.59	1.38	0.08	6.90	0.79	2.18	0.24	6.78E-04	2.11E-04	1.50E-05	1.45E-02
FR	17	7.49	1.79	0.85	0.86	0.03	3.68	0.87	0.74	0.10	6.19E-04	1.25E-04	-	1.06E-02
BAG	40	7.36	2.44	1.30	1.45	0.15	3.59	1.39	2.05	0.55	6.85E-04	3.49E-04	-	4.45E-02
		7.22	2.49	1.44	2.02	0.17	3.75	1.55	2.35	0.20	3.20E-05	3.64E-04	8.29E-06	4.26E-02
BNAG	39	7.18	2.63	1.36	1.87	0.17	2.89	1.89	2.60	0.72	6.95E-04	2.71E-04	4.42E-04	5.65E-02
AG	16	7.05	13.24	7.07	2.57	0.16	2.78	2.65	19.12	0.43	1.09E-03	1.99E-05	-	1.82E-01
VA	17	7.05	3.00	3.53	3.92	0.08	7.44	3.20	4.10	0.25	7.49E-04	1.92E-04	4.32E-04	7.07E-02
SVN	17	6.92	4.79	4.11	3.13	0.15	6.15	4.08	5.51	0.22	7.83E-04	3.25E-04	1.09E-03	6.40E-02
SC	16	7.04	7.84	5.88	4.90	0.09	4.27	4.09	11.36	0.25	9.69E-04	1.13E-04	1.16E-04	2.00E-01
BM	30	7.42	8.05	4.59	5.25	0.22	2.89	5.10	12.12	0.45	1.60E-03	1.18E-04	2.98E-02	1.59E-01
		7.78	8.26	4.12	7.50	0.24	3.33	7.70	11.26	0.38	6.70E-05	1.38E-04	5.42E-05	1.41E-01
BUG	23	7.31	2.92	1.92	3.22	0.22	4.21	4.66	2.33	0.24	1.23E-03	2.33E-04	-	4.21E-02
		7.40	3.11	2.00	3.67	0.21	4.71	4.29	2.40	0.52	2.89E-05	2.52E-04	8.04E-05	3.82E-02
SF	39	6.99	13.67	7.30	6.82	0.34	2.58	7.15	21.07	0.53	2.09E-03	5.10E-05	6.50E-03	1.59E-01
		7.04	14.35	7.36	7.89	0.36	2.60	7.33	20.21	0.45	3.68E-05	4.81E-05	7.16E-03	1.43E-01
SE	30	6.92	7.80	5.28	10.76	0.27	3.77	12.43	11.61	0.43	3.74E-03	1.35E-04	-	1.11E-01
		7.05	6.24	3.73	7.55	0.23	5.07	7.80	9.40	0.30	1.30E-05	2.10E-04	-	7.08E-02
SRN	32	7.26	14.32	8.80	15.45	0.41	2.72	18.88	23.16	0.45	5.13E-03	8.92E-05	4.25E-02	1.66E-01
BSL	26	5.81	6.59	3.06	29.46	2.60	12.86	43.95	1.31	1.56	8.85E-03	1.04E-03	3.13E-01	1.86E-01
CL	21	6.06	32.57	12.29	167.0	13.96	28.65	274.8	5.24	1.53	7.13E-02	7.34E-04	4.98E-01	6.18E-01
SM	20	6.79	78.97	46.49	2467	4.48	3.81	2841	58.01	0.38	4.54E-01	7.66E-04	-	3.73E-01
		6.34	40.97	1.18	3028	4.91	5.11	3240	64.47	0.12	-	1.24E-04	4.90E-04	9.13E-02
SM2	17	6.79	59.51	40.29	2748	4.92	3.05	2898	56.98	0.43	5.43E-01	8.23E-04	-	3.84E-01
NJ	12	7.55	1.16	0.64	0.05	0.02	3.85	0.14	0.04	0.06	3.15E-05	4.30E-05	4.66E-06	1.94E-03
LR	18	7.27	1.40	1.34	0.15	0.04	5.90	0.11	0.14	0.13	5.38E-06	8.81E-05	7.16E-03	3.65E-03
LC	17	7.4	1.47	1.43	0.87	0.10	5.56	0.56	0.58	0.15	5.31E-04	3.05E-04	3.58E-03	8.10E-03
FMN	17	7.26	1.41	1.35	0.25	0.05	5.45	0.23	0.37	0.20	1.78E-05	1.86E-04	-	1.00E-02

Table 5-2: Temperature (°C), pH, and hydrochemistry (mmol/L) of investigated samples

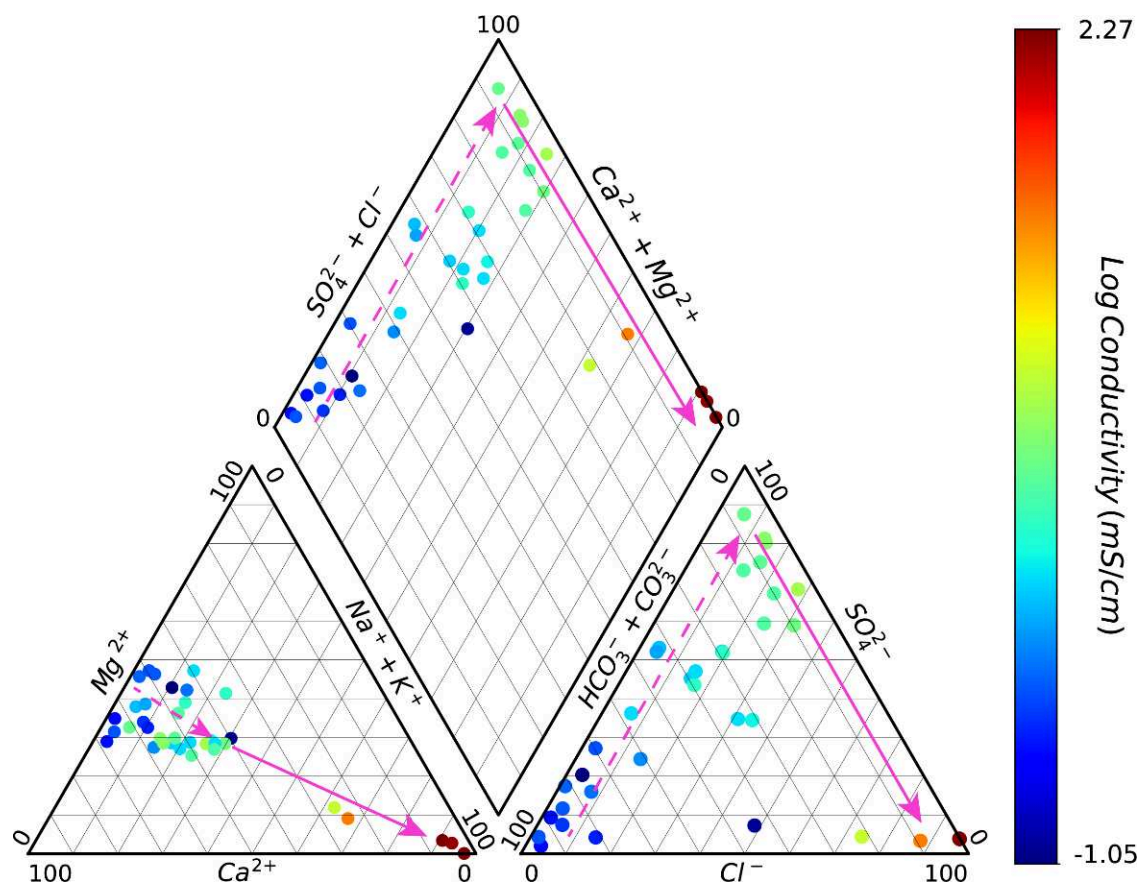


Figure 5-2: Piper diagram of the water samples with a color scale representing the logarithm of the electrical conductivity (mS/cm). The chemical evolution can be divided into two steps: (1) evolution from carbonate- to sulfate-dominated waters (dashed arrow), (2) evolution from sulfate- to chloride-dominated waters (solid arrows).

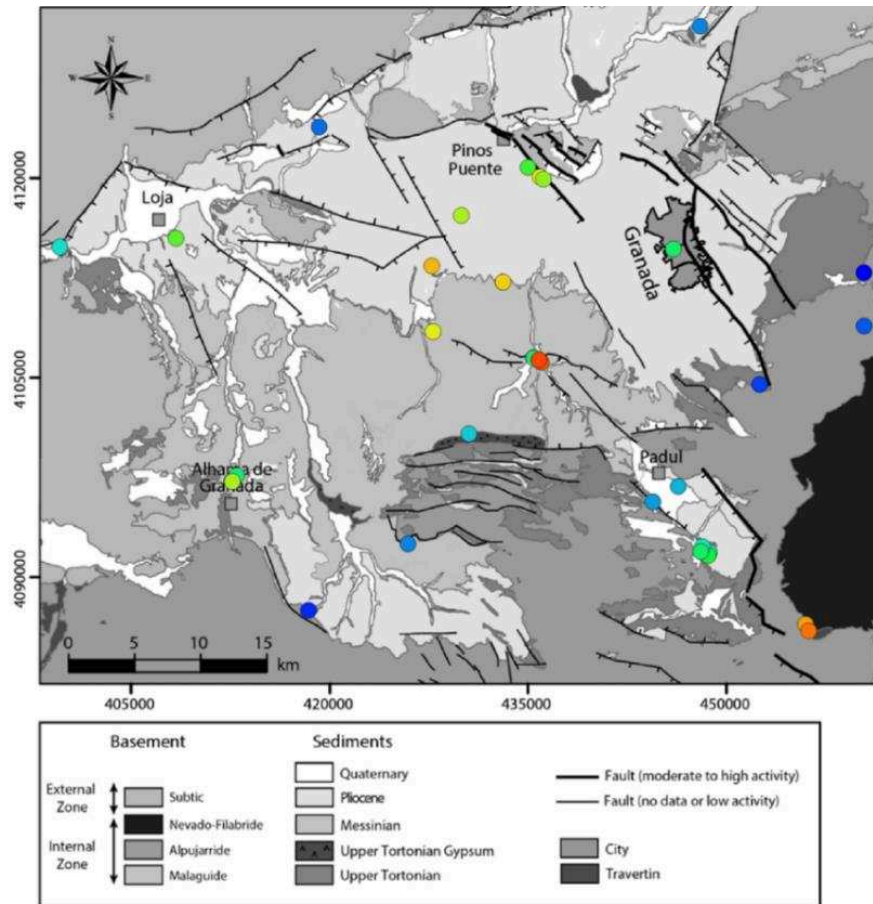


Figure 5-3: Map representing the electrical conductivity of the water samples. The colors correspond to the color scale of the logarithm of the electrical conductivity used in Figure 5-2. The background geological map was modified after Galindo-Zaldivar et al. (2015)

The saturations with respect to calcium carbonate minerals (calcite and dolomite) are compiled in Table 5-3 and represented in the activity diagrams for the system H_4SiO_4 , Al^{3+} , Ca^{2+} , H_2O in Figure 5-5. In this representation, calcite saturation was defined with a set of pCO_2 values (3×10^{-4} and 1 atm) corresponding to the extreme values obtained in these water samples. Dolomite saturation was determined by using a range of Mg^{2+} concentrations that were measured in the water samples (1.5×10^{-4} and 3.6×10^{-2} mol/L) and an average value of alkalinity of 4×10^{-3} mol/L. We can observe that waters are mainly saturated with respect to calcite and dolomite within the defined conditions (Figure 5-5). These results show that calcite and dolomite tend to control the pH of the waters.

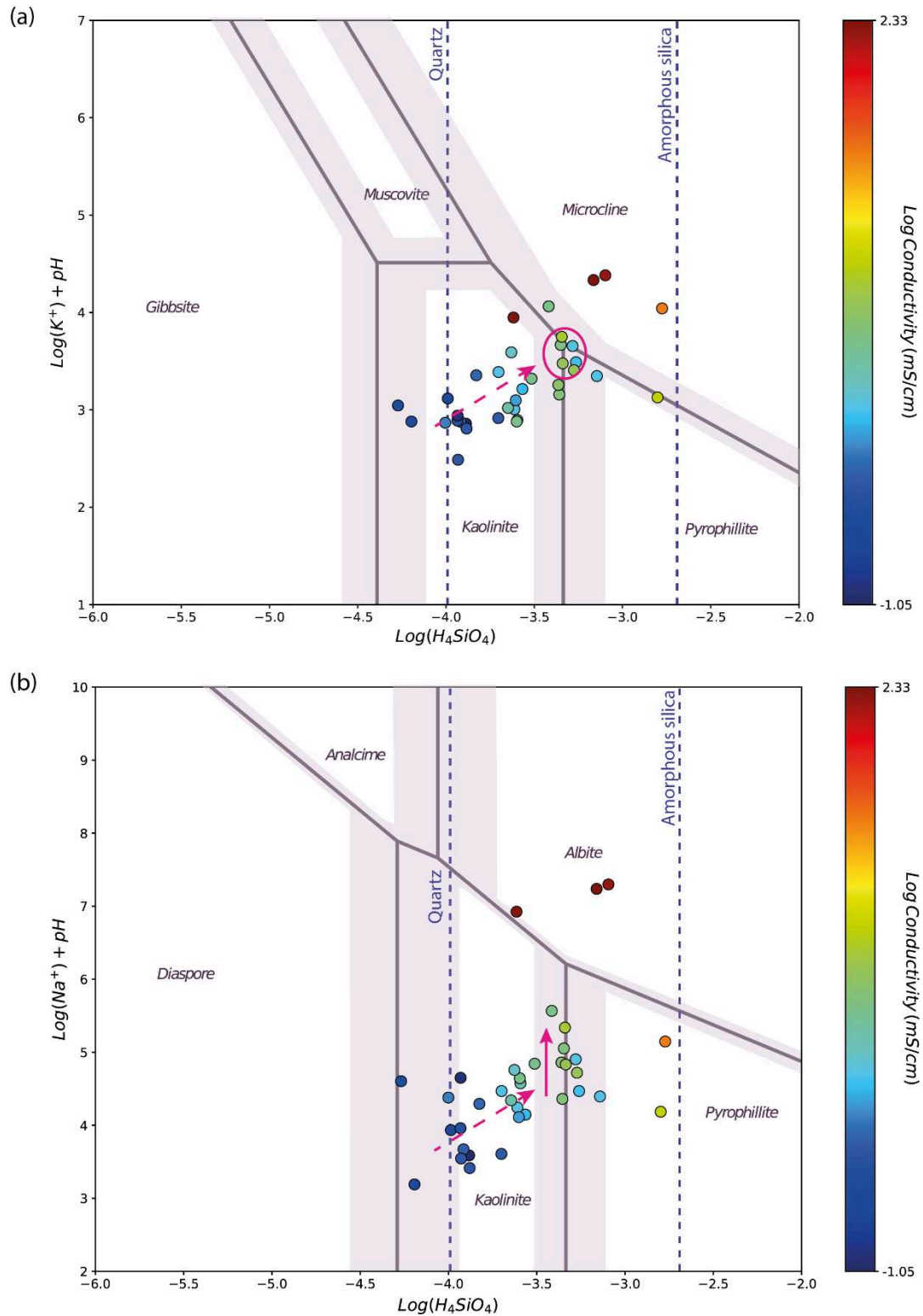


Figure 5-4: Activity diagrams for the systems (a) H_4SiO_4 , Al^{3+} , K^+ , H_2O and (b) H_4SiO_4 , Al^{3+} , Na^+ , H_2O . The limits of the mineral stability field are for $P = 1$ bar and T between 10 and 50°C . The blue dotted lines represent the saturation in quartz and amorphous silica. The chemical evolution can be divided as follows: (1) evolution within the kaolinite stability field (dashed pink arrow), (2a) K controlled by kaolinite, pyrophyllite, and microcline at the triple-point (pink circle) whereas (2b) evolution at the limit between the stability field of kaolinite and pyrophyllite for Na (pink solid arrows).

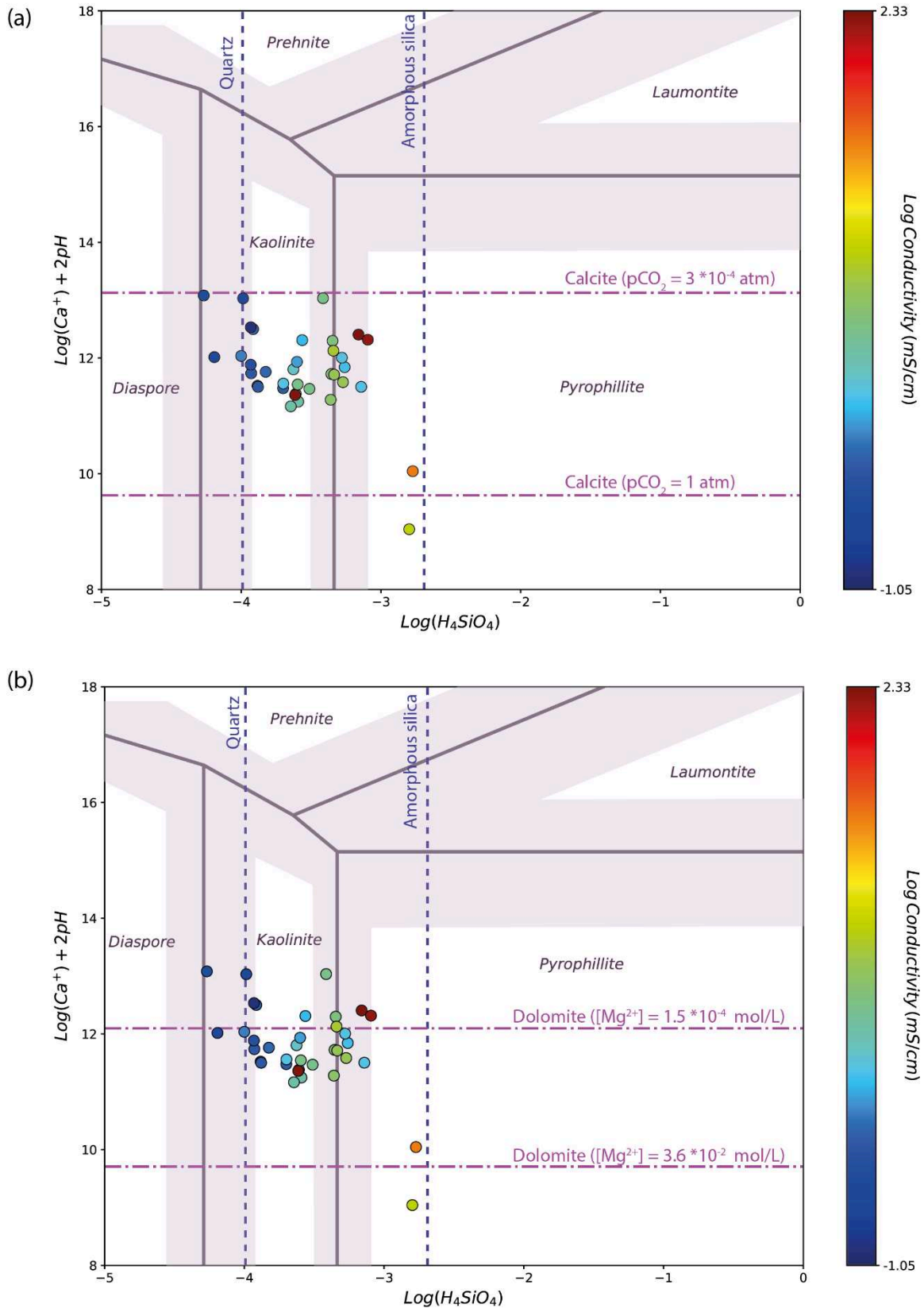


Figure 5-5: Activity diagrams for the system H_4SiO_4 , Al^{3+} , Ca^{2+} , H_2O . The limits of the mineral stability field are for $P = 1 \text{ bar}$ and T between 10 and 50°C . (a) Calcite saturation and (b) dolomite saturation are represented by the pink dotted line. The blue dotted lines represents the saturation in quartz and amorphous silica.

Sample	Calcite	Dolomite	Gypsum	Halite	Barite	Celestite	Quartz	K-feld.	Kaolinite	Albite
FLC	-1.26	-2.68	-3.09	-9.96	-1.52	-3.92	0.36	-1.07	3.91	-3.13
SP	0.26	0.43	-2.08	-9.96	-1.08	-2.69	0.22	-1.57	3.21	-3.47
FDH	0.25	0.06	-2.63	10.00	-1.37	-3.27	0.19	-1.71	2.67	-3.62
DN	-0.05	-0.43	-1.71	-9.16	-0.69	-1.86	0.20	-1.55	4.09	-3.19
NA	-0.11	-0.44	-2.57	-8.81	-1.54	-3.56	0.18	-1.49	3.46	-3.10
BUC	0.41	0.76	-1.19	-8.45	-0.06	-0.85	0.42	-0.67	3.23	-2.31
	0.25	0.46	-1.19	-8.28	-0.06	-0.86	0.39	-2.84	-0.73	-4.40
FV	0.22	0.08	-2.94	-8.45	-2.11	-3.44	-0.04	-2.41	2.44	-3.62
FA	-1.04	-2.37	-3.57	-8.28	-2.03	-4.58	0.35	-1.56	2.90	-2.66
UG	0.04	0.18	-1.34	-7.64	-0.09	-1.48	0.48	-0.09	4.78	-1.51
FR	0.09	-0.14	-1.74	-7.77	-0.58	-1.94	0.11	-1.65	3.46	-2.82
BAG	0.33	0.62	-1.28	-7.38	-0.08	-0.89	0.51	-0.39	2.49	-1.80
	0.21	0.41	-1.24	-7.19	-0.03	-0.87	0.07	-3.00	-0.78	-4.32
BNAG	0.06	0.06	-1.17	-7.14	-0.12	-0.71	0.64	0.07	3.20	-1.29
AG	0.02	-0.23	-0.03	-6.92	-0.72	0.13	0.76	1.22	6.03	-0.25
VA	0.02	0.14	-1.03	-6.60	0.01	-0.62	0.51	0.03	5.15	-0.96
SVN	-0.02	-0.09	-0.76	-6.60	0.29	-0.60	0.46	0.11	5.28	-1.23
SC	0.05	-0.02	-0.37	-6.43	-0.03	0.06	0.52	0.18	5.47	-0.73
BM	0.44	0.78	-0.35	-6.31	-0.13	0.03	0.57	0.56	4.06	-0.57
	0.84	1.50	-0.37	-5.98	-0.07	-0.06	0.54	-0.80	0.75	-1.84
BUG	0.16	0.23	-1.20	-6.51	-0.09	-0.99	0.39	0.18	4.36	-1.25
	0.33	0.58	-1.18	-6.49	-0.07	-1.03	0.72	-0.51	1.50	-1.85
SF	0.22	0.34	-0.05	-6.09	-0.54	0.13	0.51	0.37	4.18	-0.73
	0.28	0.45	-0.05	-6.02	-0.56	0.06	0.47	-1.45	0.61	-2.52
SE	0.05	0.08	-0.41	-5.63	-0.12	-0.17	0.55	0.91	5.65	0.00
	0.25	0.43	-0.53	-5.97	0.06	-0.38	0.39	-2.07	0.18	-3.05
SRN	0.40	0.74	-0.04	-5.33	-0.23	0.12	0.54	1.15	5.11	0.25
BSL	-0.61	-1.39	-1.39	-4.65	0.02	-0.86	1.17	3.16	8.03	1.66
CL	0.32	0.33	-0.62	-3.20	-0.04	-0.29	1.27	5.40	10.41	3.89
SM	0.94	1.85	0.31	-0.83	0.49	0.03	1.00	6.28	12.11	6.65
	0.46	-0.40	0.14	-0.62	-0.26	-0.46	0.57	-	-	-
SM2	0.68	1.38	0.18	-0.76	0.53	0.01	1.12	6.82	12.71	7.18
NJ	-0.03	-0.38	-3.07	-9.80	-2.11	-3.84	-0.01	-3.20	0.98	-5.62
LR	-0.01	0.00	-2.57	-9.41	-1.44	-3.12	0.21	-3.29	-0.14	-5.34
LC	0.09	0.18	-1.95	-7.96	-0.32	-2.17	0.28	-0.66	3.78	-2.39
FMN	-0.07	-0.14	-2.13	-8.90	-0.68	-2.25	0.41	-2.04	1.40	-4.02

Table 5-3: Saturation indices (SI) of the main mineral phases of interest in the investigated area. SI were calculated with the PHREEQC code, at the outlet conditions, with the phreeqc database and the pitzer database for SM and SM2 samples. The SI with respect to aluminosilicate were all calculated with the phreeqc database due to missing Al concentrations in the pitzer database.

5.2.4.1. Saturation with respect to sulfate minerals

Focusing on the water-evaporite interaction, the saturations of the waters with respect to some sulfate minerals: gypsum ($\text{CaSO}_4 \cdot 2\text{H}_2\text{O}$), celestite (SrSO_4), and barite (BaSO_4) are compiled in Table 5-3. An interpolated map of the saturation index of these minerals is represented in Figure 5-6. The interpolation was performed using the Inverse Distance Weighted (IDW) method with the open source QGIS software. This method is based on the decreasing influence of one point relative to another with increasing distance. The principal problem of this interpolation method in the studied area is the uneven spatial distribution of sampling points in the basin. The results of the interpolation were slightly adjust manually to take into account the known particularities of the studied area (e.g., topography) ignored in this method.

We can see that the waters close to equilibrium or saturated with respect to barite in the whole basin, whereas waters are undersaturated with respect to celestite at the borders of the basin and are saturated only in the center of the basin. Finally the waters are undersaturated with respect to gypsum at the basin border and slightly undersaturated (close to equilibrium) in the basin center. Therefore, the saturation of the waters with respect to these sulfate minerals shows that waters became saturated with respect to barite, then celestite and finally gypsum with increasing electrical conductivity from the border to the center of the basin. A reaction path involving the sulfate minerals is defined from the border to the center of the basin.

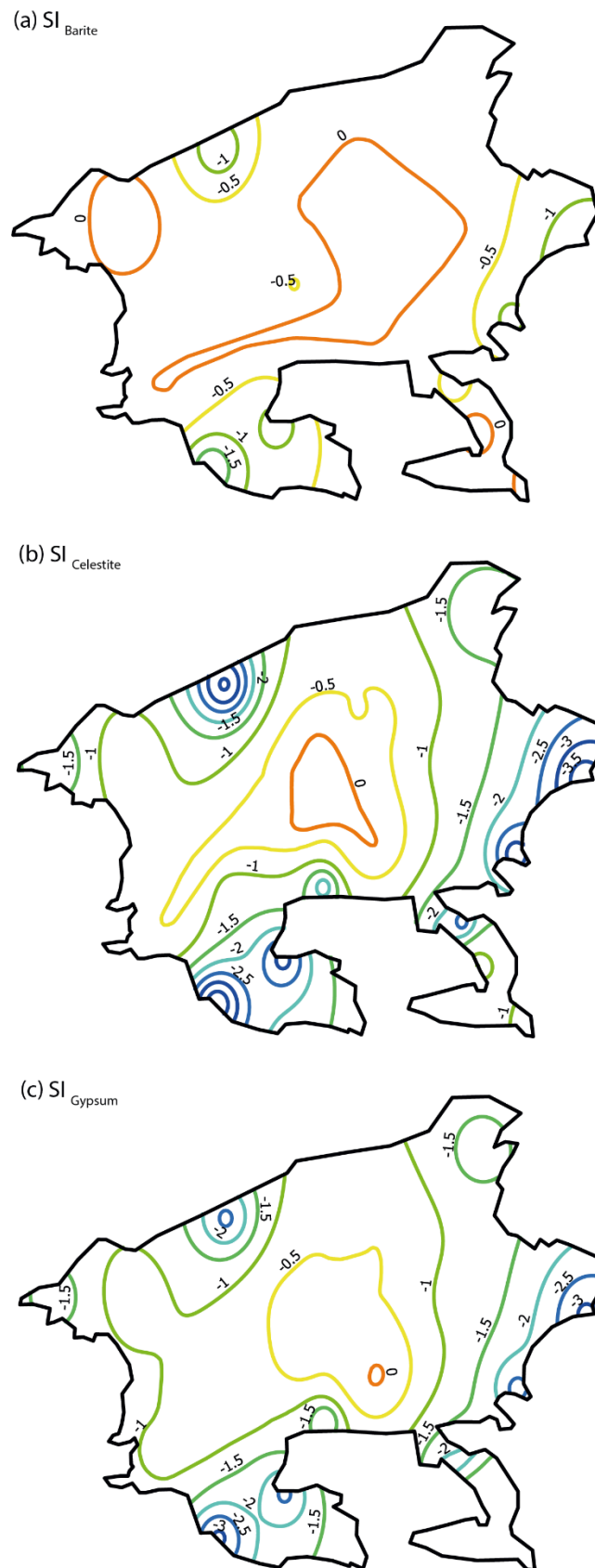


Figure 5-6: Interpolated map of the saturation index of (a) barite, (b) celestite, and (c) gypsum. Interpolation was performed using the Inverse Distance Weighted (IDW) method.

5.2.5. Discussion

5.2.5.1. Geochemical evolution

In order to apprehend the evolution of the water composition at the scale of the basin, changes in both water chemistry and electrical conductivity (EC) were investigated. The EC evolve from low values at the border of the basin to high values in the center of the basin, reflecting a gradient in salinity. Castillo (2005) has also observed a gradient in electrical conductivity at smaller scale in the Granada Basin, between the western and the eastern borders of the Vega de Granada aquifer.

Concerning the chemical composition of the water, a reactive path in two steps can be defined with, first, an evolution from carbonate- to sulfate-dominated waters and then to chloride-dominated waters (Figure 5-2). This two steps evolution is marked by the change in anion dominance whereas the evolution of cations is less marked. During the evolution from carbonate- to sulfate-dominated waters, the dominant cations are mainly Ca^{2+} and Mg^{2+} and do not evolve significantly whereas the chloride-dominated waters are characterized by Na^+ dominance in cations. The mineralization of the groundwaters reveals interaction with carbonate minerals in the mountainous recharge areas (e.g. Sierra Nevada or Sierra de la Pera) and in the basin. The quite stable $\text{Mg}^{2+}/\text{Ca}^{2+}$ ratio reflects interaction with both calcite and dolomite (Figure 5-2). The increasing interaction with the sulfate minerals might include Neogene evaporites in the basin and Triassic evaporites in the basement. The overall evolution is in agreement with the interpretations of Kohfahl et al. (2008a) in the Granada aquifer system, where calcite dissolution and precipitation, dolomite precipitation and gypsum dissolution were invoked to explain the changes in water chemistry. Their study, however, did not investigate the chemical evolution up to the Na-Cl waters.

This reaction path in two stages can be also observed considering the equilibrium with alumino-silicates in Korjinski diagrams. The first step of the evolution from carbonate- to sulfate-dominated waters seems to be correlated with the evolution of the Na^+ and K^+ control by alumino-silicates. Concerning Na^+ , the waters progress within the stability field of kaolinite, from purely kaolinite to the limit between the stability field of kaolinite and pyrophyllite where the sulfate-dominated waters evolve along (Figure 5-4b). The K element seems to be more strongly controlled by alumino-silicates as the sulfate-dominated waters are located on a triple point at the junction between kaolinite, pyrophyllite, and microcline (Figure 5-4a). A potential control by KCl could be excluded as no evidence of potash was found in the basin by the investigations of the Rio Tinto company. The most conductive waters, i.e. the chloride-

dominated waters reach the stability field of microcline and albite for both Na^+ and K^+ . However, the chloride-dominated waters do not reach the stability field of laumontite and evolve in the stability fields of pyrophyllite or close to equilibrium with kaolinite when considering Ca (Figure 5-5). As previously seen, both carbonates and calcium sulfate seem to control Ca concentration and pH and the influence of Ca aluminosilicates is less pronounced.

5.2.5.2. A possible conceptual reactive transport modeling?

In addition to the geochemical evolution and the hydrochemical processes previously defined, estimates of the flow paths, the transport mechanisms and residence time would be necessary to perform reactive transport modeling. In first approach, the geochemical results give some clues of the potential groundwater flow paths in the Granada Basin. The joint evolution of the chemical composition and EC along the E-W and N-S transects give a first insight on the flow paths, mainly from the eastern and southern part to the northwestern part of the basin. The gradient in EC, defined by Castillo (2005) in the Vega de Granada aquifer, was linked to the piezometric levels and the westward direction of the flow. These results, including those of both surface and subsurface data, show that physical-chemical parameters might help to constrain indirectly groundwater fluid flow. Globally, the qualitative chemical evolution defined in this study is in good agreement with the current understanding of groundwater flow paths in the Granada Basin defined in the literature (Castillo, 2005; Kohfahl et al., 2008a). Kohfahl et al. (2008a) showed that the recharge areas of several groundwater springs in the basin were located in the Sierra Nevada at an altitude > 1700 masl (meter above sea level) according to the water isotopic data ($\delta^{18}\text{O}$ and δD). Moreover, the general hydrographic system of the Granada Basin is characterized by river flowing mainly from the eastern and southern high altitude part to the northwestern part of the basin. The groundwater flow system is most probably related to this surface hydrographic system driven by a strong altitude gradient.

Furthermore, the evolution of the saturation state with respect to sulfate minerals allow us to discuss the spatial distribution of the chemical reactions at the scale of the basin. A reaction path is defined by the progressive saturation of the waters with respect to barite first, then celestite and finally gypsum from the border to the center of the basin. This reaction path shows the importance of the interactions with evaporites-bearing rocks in the sedimentary basin. As the two cations Sr^{2+} and Ba^{2+} are minor elements in groundwater composition, compared to SO_4^{2-} and Ca^{2+} , oversaturation with respect to celestite or barite and subsequent precipitation would not significantly change the sulfate concentrations. However, the difference in saturation

with respect to the three minerals might reveal potential flow paths. Both celestite and gypsum display sharp gradient in saturation between the borders and the center of the basin reflecting stronger control of these minerals in the basin. In addition to common ion effect of SO_4^{2-} , the control of Ca^{2+} on both carbonate and gypsum saturation state might also explain the saturation with respect to gypsum in the basin.

Our approach allows us to describe the reactivity at the scale of the basin using both major elements (SO_4^{2-} and Ca^{2+}) and minor elements (Ba^{2+} and Sr^{2+}). It is worth noting that none of the waters are highly oversaturated with respect to the three minerals in the basin center. Only small variations in saturation are sufficient to assess potential reaction and flow paths at the scale of the whole basin. The precise location of Sr and Ba source is unconstrained in the sedimentary infilling of the Granada Basin and in its basement (both in the Internal and External Zones) and numerical reactive transport modeling would not therefore allow a precise quantification of these reaction paths. More generally, numerical reactive transport modeling would necessitate the definition of mineralogical maps at the scale of the whole basin, which are more precise than geological maps or maps of facies.

An important parameter that is under-constrained in this study and that is crucial for reactive transport modeling is the water residence time and kinetics of the reactions. Although little data are available concerning the groundwater residence time of the Granada Basin (Cardenal et al., 1994; Kohfahl et al., 2008a; López-Chicano et al., 2001b), a time range of 1,000 to 100,000 years might be estimated. López-Chicano et al. (2001a) found that the thermal waters of Alhama de Granada show a residence time ranging from 8,600 to 12,300 years determined from $\delta^{14}\text{C}$ data and with possible strong influence of young waters (< 50 years). Our previous studies, based on the evaluation of the He crustal production in the studied area and on the volume of precipitated travertine in thermal springs (see Chapters 3 and 4), allow to evaluate the residence time at ~10,000 years.

In addition to groundwater residence time, the flow rates are necessary to perform reactive transport modeling. Although no direct measurements of flow rates were carried out, values can be generally estimated from the literature or the IGME (Instituto Geológico y Minero de España) water database. The large variability of flow rates, ranging from 0.2 to >100 L/s for both springs and wells, would need to be taken into consideration into reactive transport modeling.

5.2.6. Conclusions

The present study provides the first characterization of the groundwater geochemistry at the scale the whole Granada Basin from the collection of twenty-eight groundwater samples. The groundwaters display a large range of electrical conductivity (0.09 to 187 mS/cm), used as marker of the salinity, and chemical composition evolving from carbonate-dominated waters at the basin border to sulfate- and chlorine- dominated water in the basin center.

The groundwater saturation state with respect to carbonates, alumino-silicates and sulfate minerals allow assessing possible reactive flow paths in the Granada Basin. The rather constant saturation with respect to carbonates (calcite and dolomite) show the importance of these minerals to control the pH, Ca^{2+} and Mg^{2+} . The alumino-silicates seem to strongly constrain K^+ concentration, and in a lesser extend Na^+ , in the sulfate-dominated waters. The evolution of the groundwater saturation with respect to sulfate mineral allows to assess the possible flow paths in the basin and to apprehend a conceptual reactive transport.

The reactivity at the scale of the basin can be summarized regarding the N-S cross-section presented in Figure 5-7. At the borders of the basin, forming the main recharge areas of this basin, the waters are at equilibrium with the following mineral assemblage: quartz, kaolinite, calcite, dolomite and barite. Waters evolve to equilibrium with the following mineral assemblage when circulating towards the center of the basin: quartz, pyrophyllite, calcite, dolomite, and celestite, whereas the equilibrium with gypsum, K-feldspar and albite is reach only in the center of the extension area of evaporites. As the ionic interaction models for high ionic strength waters (e.g. pitzer model) present some limitations concerning Al phases, these equilibria with K-feldspar and albite in the basin center bring into question the prospect of apparent equilibrium due to the high salinities of these groundwaters. This question should be consider in future investigations.

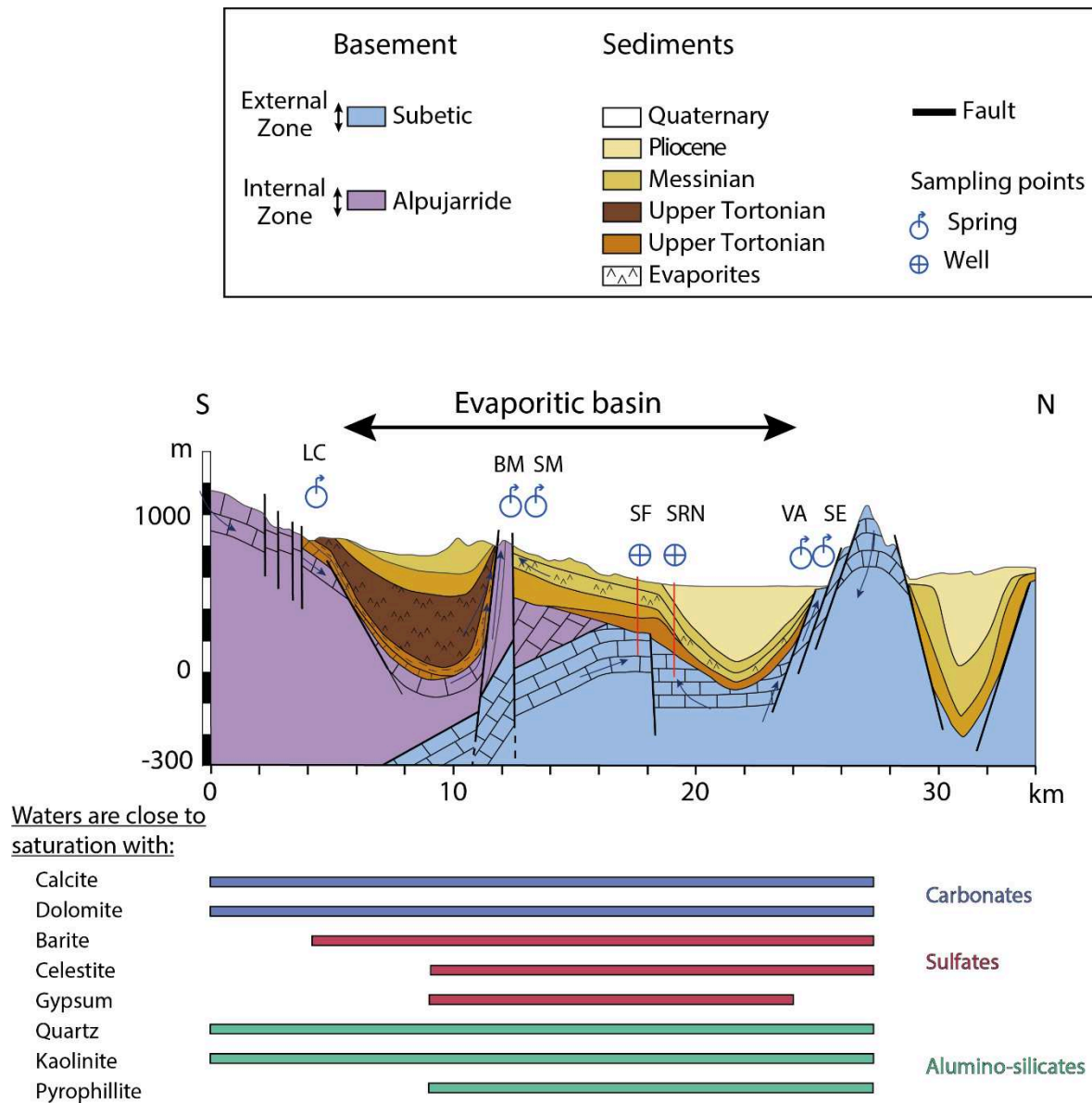


Figure 5-7: Summary of the reactivity of the groundwaters and possible flow paths (dark blue arrows) in the Granada Basin along a S-N cross-section.

5.3. ADDITIONAL RESULTS AND DISCUSSIONS

5.3.1. Kinetics and transport modeling

This study was initiated in the objective to perform reactive transport modeling after completing the reaction model and using classical transport equations. Insights on the groundwater flow paths in the Granada Basin have been defined thanks to the groundwater saturation with respect to sulfate minerals. However, a characterization of the transport mechanisms and of the hydrodynamism have not been developed in this thesis. The studied area presents some limitations in regards to these points.

The Granada Basin is characterized by the occurrence of very few wells, and especially deep wells (> 500 m), and in-situ data. The lack of deep wells and in-situ data is a limiting parameter to constrain the groundwater circulation at the scale of the sedimentary basin. The fact that most of data come from spring or shallow-depth well limits the spatial distribution and the depth constraints of the fluid flow and reactivity.

The geometry of the basement, and particularly of the structure of the Internal and External Zones beneath the Granada Basin, is under constrained and few data on the structure are available in the studied area. The structure in depth of the basement is particularly important to perform reactive transport modeling in the studied area. Although the chemical reactions have been estimated at various scales in the sedimentary basin, the transport parameters cannot be sufficiently constrained in the Granada Basin.

5.3.2. Influence of the Triassic evaporites in the External Zone

5.3.2.1. Motivations and geological setting

Two springs have been sampled in the External Zone outside of the Granada Basin to get insights in the geochemical signature of the Triassic evaporites. These two springs are the Salinas Fuente de Camacho (SFC) spring, at the west of the Granada Basin, at the limit between the Granada and the Málaga provinces, and the Manantial del Nacimiento de Arbuniel (MNA) spring in the north of the basin, in the Jaén province (Figure 5-8). These water points were selected for their saline character.

The SFC spring is a known hyper-saline spring, with a low flow rate (< 2 L/s), located at the eastern border of the Salinas – Los Hoyos diapiric structure (Figure 5-9 and 5-10). This diapiric structure belongs to the Chaotic Subbetic Complexes Unit (Vera and Martín-Algarra, 2004), which corresponds to a chaotic mega-breccia made up of Upper Triassic (Keuper)

versicolor clays, evaporites (gypsum, anhydrite, and halite) and sandstones blocks (Figure 5-9 and 5-10). The recharge takes place in the structure by infiltration of rainwater through swallow holes, dolines, and gypsum blocks (Gil-Márquez et al., 2016). The SFC spring is one of the discharge points with the Aguileras spring in the western border of the Salinas – Los Hoyos diapiric structure. Large salt mineralization coatings have been formed on the surface of this structure at the spring emergence (Figure 5-11 and 5-12) evidencing the high salinity of the water.

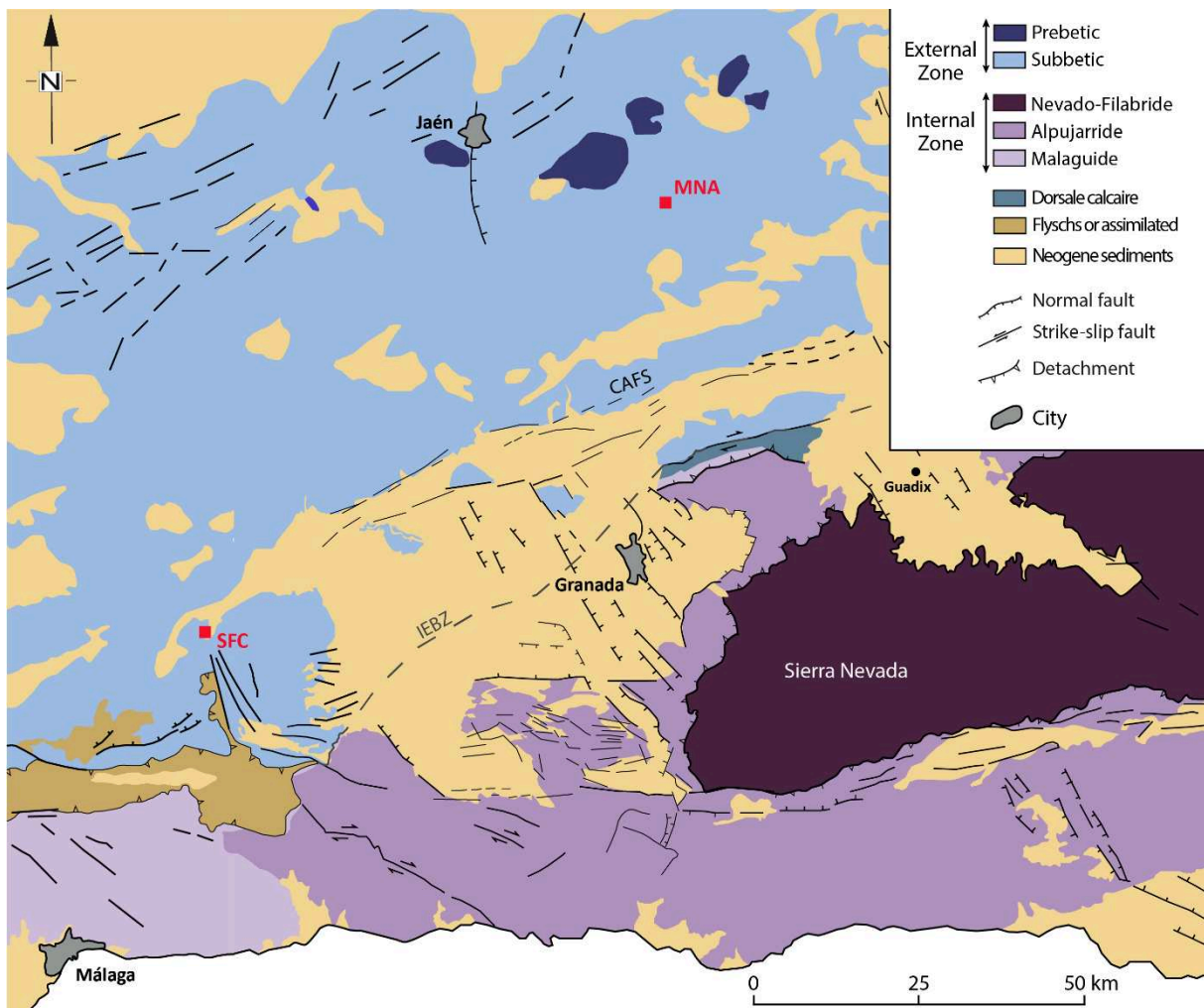


Figure 5-8: Location map of the Salinas Fuente de Camacho (SFC) and Manantial del Nacimiento de Arbuniel (MNA) springs (modified after Sanz de Galdeano and Peláez (2011))

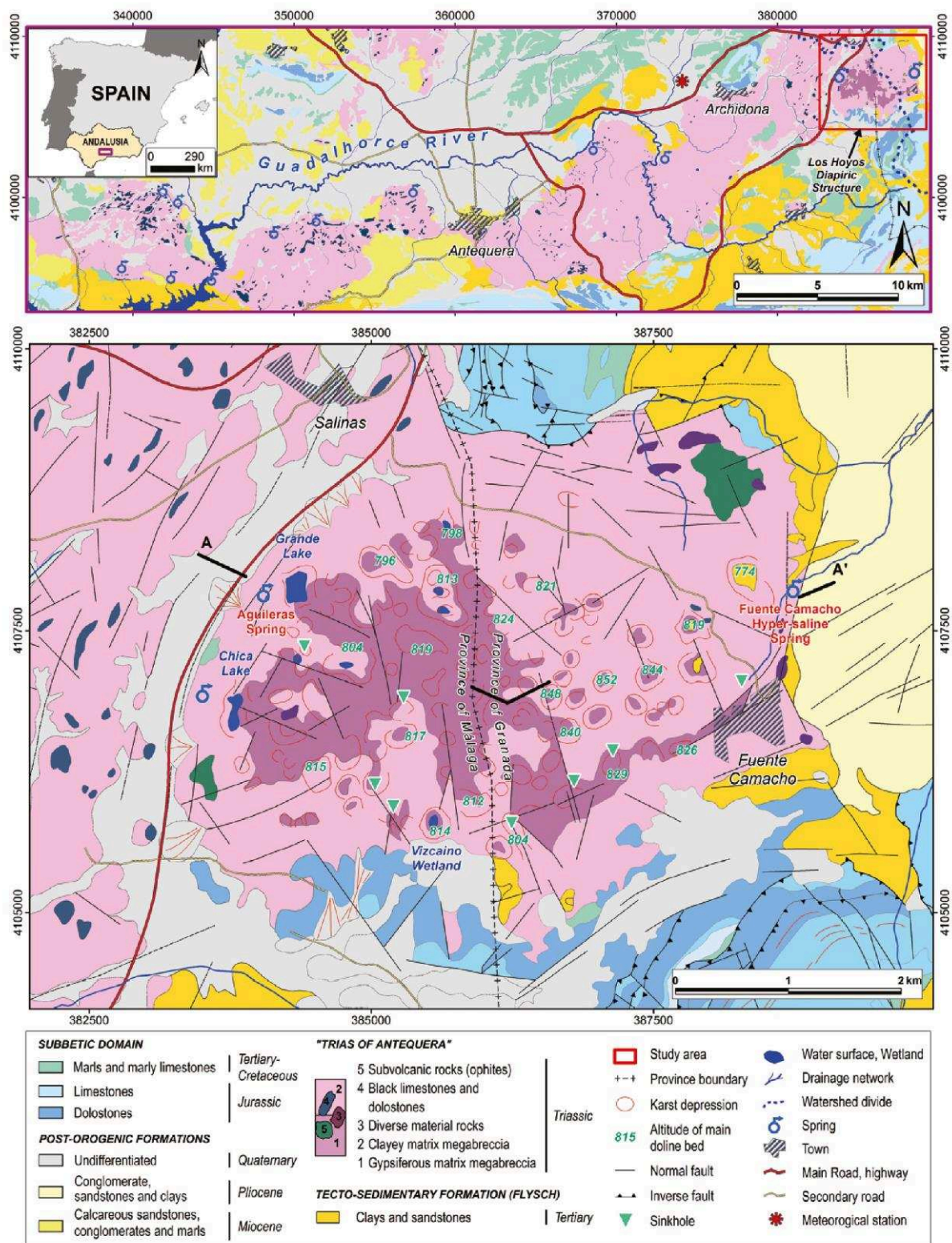


Figure 5-9: Geological map of the Salinas Fuente de Camacho spring area (Gil-Márquez et al., 2016). The cross-section A-A' is presented in Figure 5-10.

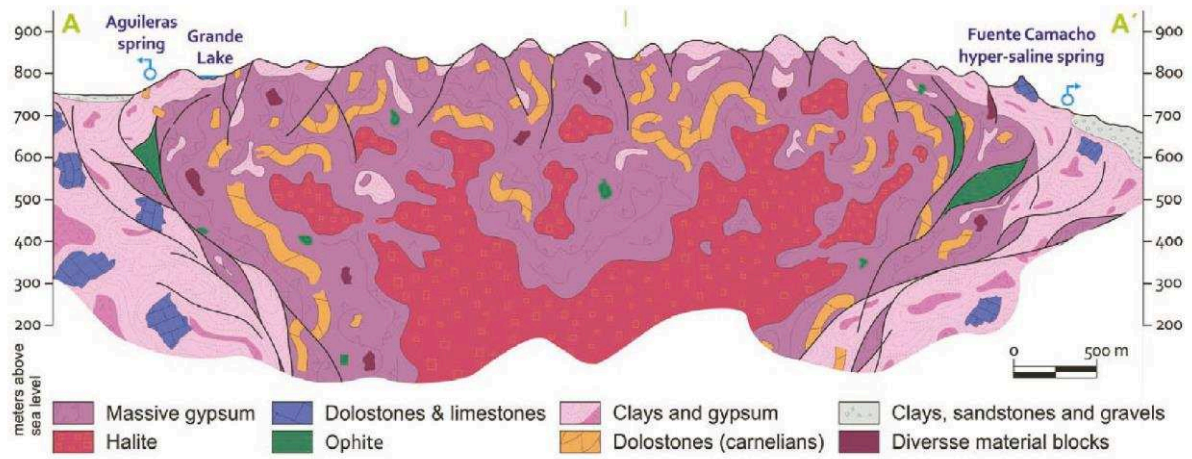


Figure 5-10: Cross-section of the Salinas - Los Hoyos diapiric structure (Gil-Márquez et al., 2016).



Figure 5-11: Photography of the salt mineralization at the emergence of the SFC spring.



Figure 5-12: Zoomed photography of the salt coatings at the emergence of the SFC spring.

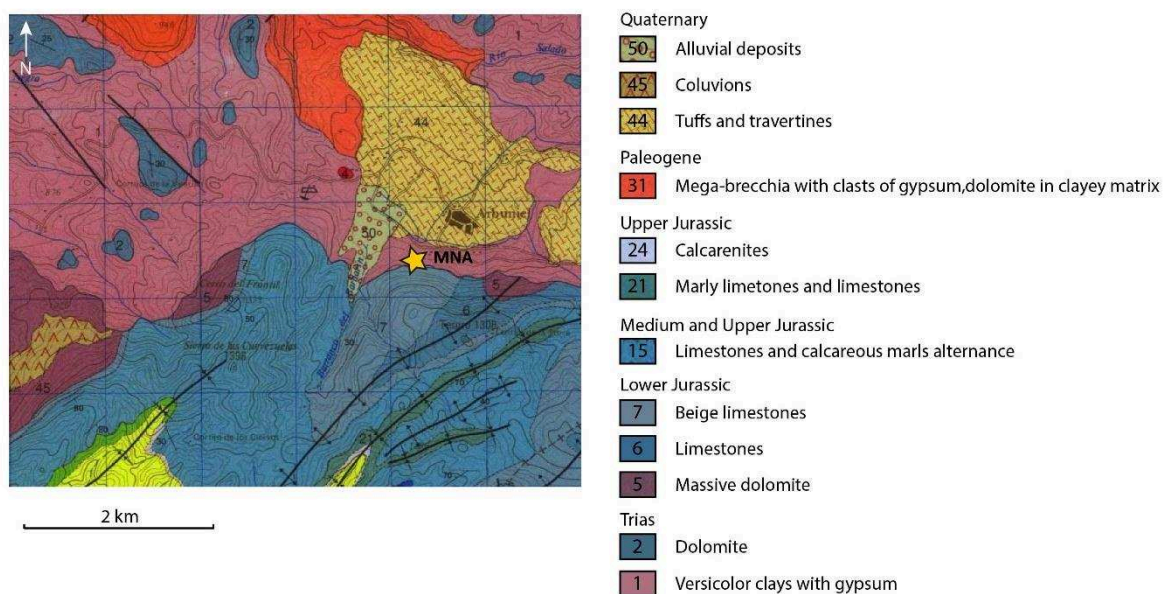


Figure 5-13: Geological map of the MNA spring, modified after the geological map of Valdepeñas de Jaén, scale 1:50 000 from IGME (Díaz de Neira et al., 1992).

The MNA water point is one of the largest springs of the Jaén province, with a flow rate of > 100 L/s, and is located in the Subbetic Unit of the External Zone (Figure 5-13). The substratum is mainly formed of Triassic (Keuper) versicolor clays and evaporites, carbonates clasts and sandstone levels. Large folds deform the External and Medium domains of the Subbetic Unit (Figure 5-13). The waters flows through the Liassic carbonate (limestones and

dolomites) aquifer and arises from marl with Triassic gypsum (IGME, 2005). The marked saline chemistry results from this latter characteristic.

5.3.2.2. Materials and methods

The materials and methods are similar to those presented in section 2.2.2.

Special care was paid to sample the SFC spring, especially to rinse the pH and EC electrodes, due to the very highly saline waters. In the other hand, the sampling of the MNA spring were carried out in the retention pool used to regulate the water utilization for olive grove irrigation.

5.3.2.3. Results and discussion

The physical-chemical characteristics of the two springs are presented in Table 5-3 and the chemical composition is reported in a Piper diagram in Figure 5-14. Both waters have quite low temperature (16-17°C) but SFC sample displays a slightly more acidic pH (6.0) than that of MNA sample. The difference in electrical conductivity (EC) between the two waters reflect a large difference in ionic strength.

The composition in major elements of the SFC sample is dominated by Na^+ and Cl^- ions, similar to the Salinas de La Malaha (SM) composition. As expected, the major elements do not allow distinguishing the influence of the Triassic evaporites from the Tortonian evaporites. The MNA water sample shows a different composition corresponding to a $\text{Ca-Mg-HCO}_3\text{-SO}_4$ type, with a clear influence of the Triassic evaporites and the Jurassic carbonates.

The geochemistry of these springs shows the influence of the Triassic evaporites (both gypsum and halite), which is present beneath the Granada Basin in the basement rocks of the External Zone and probably, in the form of meta-evaporites, in the Internal Zone. The composition in trace elements of these samples might be necessary to distinguish between the Triassic and the Tortonian evaporites. These results might be interesting to incorporate into the reactive transport modeling.

Name	Manantial del Nacimiento de Arbuniel	Salinas de Fuente Camacho
Code	MNA	SFC
Type	Spring	Spring
Latitude	37°37.4460'N	37°06.5753'N
Longitude	3°32.4529'W	4°15.2323'W
Temperature (°C)	16	17
pH	7.0	6.0
EC (mS/cm ²)	1.38	211.4
Ca	5.00E+00	5.34E+01
Mg	2.74E+00	3.40E+01
Na	8.80E-01	3.02E+03
K	1.84E-02	4.72E+00
Alkalinity	4.71E+00	4.32E+00
Cl	6.12E-01	3.38E+03
SO ₄	6.26E+00	3.94E+01
SiO ₂	1.60E-01	1.21E-01
Al	8.22E-04	4.54E-01
Ba	1.11E-04	4.19E-04
Sr	6.97E-02	3.61E-01

Table 5-4: Physical-chemical parameters and hydrochemistry (mmol/L) for the MNA and SFC springs.

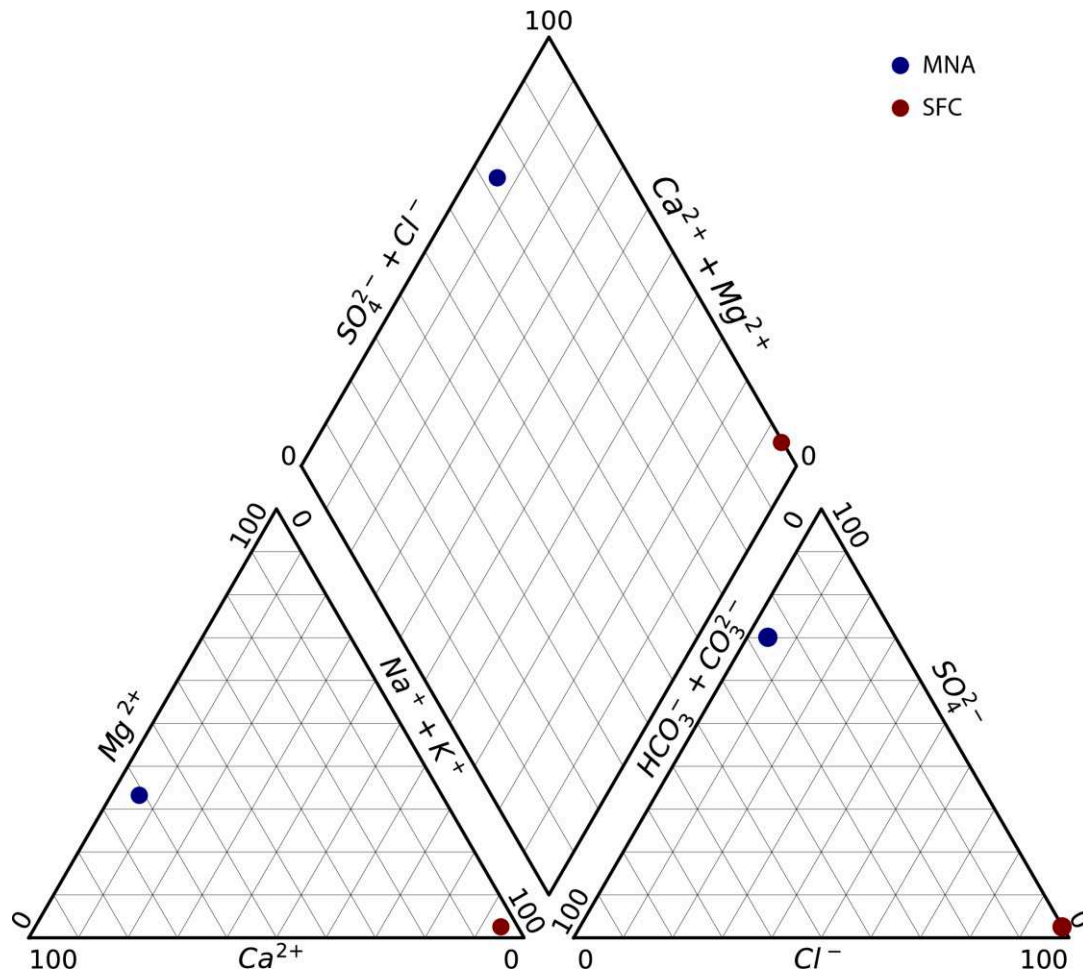


Figure 5-14: Representation of the SFC and MNA hydrochemistry on a Piper diagram

5.3.3. Origin of the salinity

In addition to the temperature of the groundwaters, the salinity is an important parameter to trace fluid reactive circulations in sedimentary basins. The different sources of dissolved chloride in the saline waters include (i) marine connate waters, (ii) chloride derived from evaporite dissolution, and (iii) subaerially evaporated surface brines. The Cl/Br ratio has been used as a tool to constrain the origin of chloride in the water, and by extension the origin of salinity. Both elements are good tracers because of their ideal conservative behaviour resulting from their hydrophilic character and small ionic size (Alcalá and Custodio, 2008; Kharaka and Hanor, 2014).

The Br concentration has been analyzed for a limited number of groundwater samples ($n=11$) in the Central Betic Cordillera. The distribution of Cl and Br in these samples is represented in Figure 5-15.

We can see on Figure 5-15, that the dissolved chloride mainly result from the evaporite

dissolution, including both halite dissolution and halite-bearing gypsum dissolution. The Cl/Br ratios of the samples SFC and SM are of 5.7×10^3 and 8.6×10^4 respectively, reflecting direct halite dissolution. The difference between the two samples might show the distinction between the Triassic halite signature for the SFC sample and the Tortonian halite signature for the SM sample. The higher Cl/Br ratio displayed by the SM sample compared to the SFC sample might lead to propose a potential hypothesis on the formation process of the Tortonian halite. As mentioned in Chapter 1, Tortonian corresponds to a transition period from marine to continental environment in the Granada Basin and halite seems to be formed in these continental conditions (e.g. lakes). In these lacustrine environments, possible leaching of outcropped evaporites are known to play a role into the precipitation of new evaporites (Kohfahl et al., 2008b). This process would result in an increase of the Cl/Br ratio at rather constant Cl concentration, creating fractionation. The hypothesis of Triassic halite dissolution implication into the Tortonian halite precipitation could be advanced to explain the large discrepancy in Cl/Br ratio between the Triassic and Tortonian evaporites.

The values of a local rainwater from the Sierra Nevada (Alcalá and Custodio, 2008) and those of local recharge waters, i.e. less evolved waters in the recharge mountain areas (Alcalá and Custodio, 2008; Sánchez-Martos et al., 2002), have been indicated in Figure 5-15.

The majority of the samples, corresponding to mainly sulfate-dominated waters, scatter on a mixing line between two end-members: an atmospheric recharge (the rainwater sample and the recharge waters) and the brine samples (SFC and SM). This signature might indicate both dissolution of gypsum containing small amount of halite and mixing with less mineralized waters (Alcalá and Custodio, 2008; Gil et al., 2017). The investigated samples are mainly from thermal groundwaters that have circulate in depth (> 1 km, see Chapter 4). The Cl/Br ratio seems to show possible mixing between recharge waters and groundwater resulting from interactions with the Triassic evaporites and the Tortonian evaporites. Therefore, waters might flow in the basement, where they would react with Triassic evaporites, and then in the basin infilling with Tortonian evaporites, before potentially mixing with less-mineralized surface waters.

The values of the fluid inclusions in veins of quartz from (Dyja-Person et al., 2018) have been also indicated in the Figure 5-15. Their data plot between halite-saturated evaporated seawater and halite dissolution brines. They also mentioned in their study the possible influence of diluted magmatic brines, which have intermediate Cl/Br ratios (ranging from 500 to 1,200) and higher Cl concentrations ($> 2.3 \times 10^5$ mg/kg). Their study proposed that the brines originate

from dissolution of Triassic metaevaporites by metamorphic fluids with variable enrichment in Br by interaction with graphitic schists.

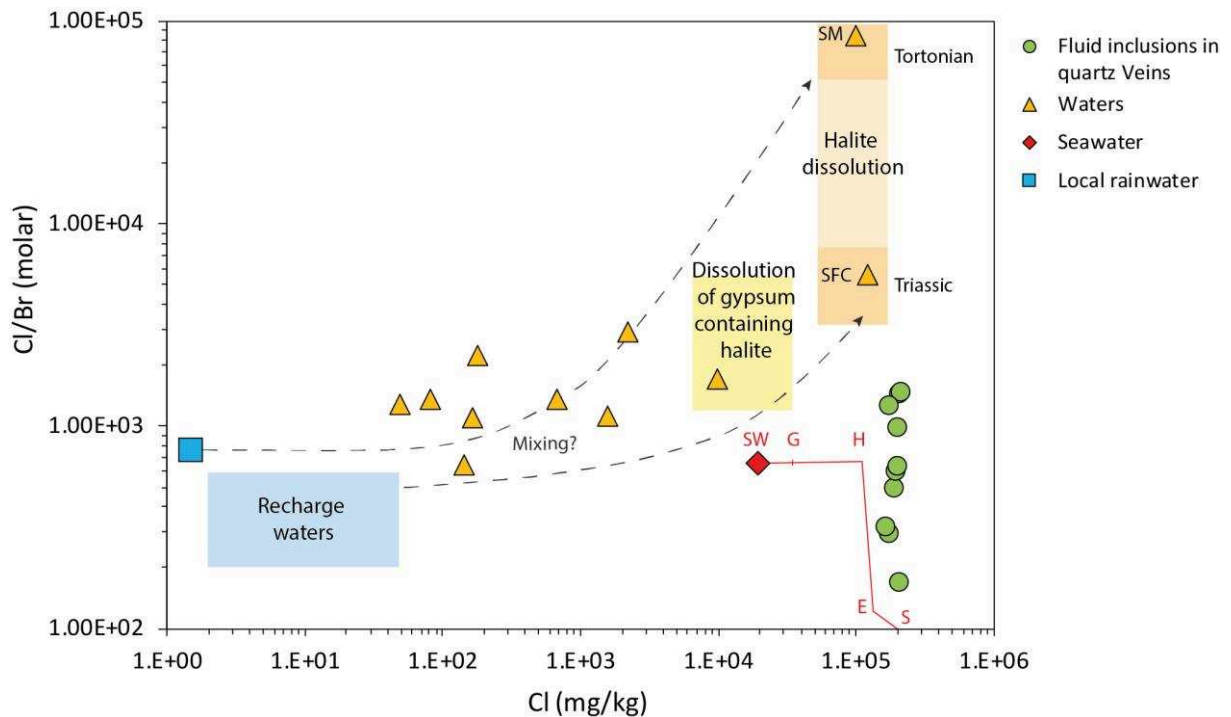


Figure 5-15: Molar Cl/Br ratios vs. Cl concentrations in samples located in the Central Betic Cordillera including: groundwater samples, local rainwater sample from the Sierra Nevada (Alcalá and Custodio, 2008), recharge waters (Alcalá and Custodio, 2008; Sánchez-Martos et al., 2002), and brine samples from fluid inclusion in veins of quartz in the Sierra Nevada (Dyja-Person et al., 2018). The seawater evaporation trend, up to sylvite, is indicated (Fontes and Matray, 1993): SW: Seawater, G: Gypsum, H: Halite, E: Epsomite, S: Sylvite,

5.3.4. Mineralization

Mineralizations are often observed at the emergence of the springs or wells, resulting from precipitation of neo-formed minerals in the outlet physical-chemical conditions. These mineralizations are the direct products of the waters and can be therefore compared with the estimated water saturation states. In the Central Betic Cordillera, the occurrence of large travertine deposits is an illustration of these precipitations of neo-formed carbonates resulting from degassing processes, related or not to thermal waters. Smaller precipitations are also observed, such as the sample presented in Figure 5-16, collected at the well head of the Sondeo Venta de la Nueva (SVN) in the northwestern part of the Granada Basin.



Figure 5-16: Photography of the mineralizations formed in the well "Sondeo Venta de la Nueva".

These mineralizations are so abundant and rapidly formed that they have to be regularly removed to prevent the plugging of the well. The investigated well is located close to outcrops of Triassic and Messinian evaporites although the saturation states of the waters does not reach gypsum equilibrium. The mineralogical shape is rather unusual and might suggest evaporite precipitates.

This sample was analyzed in XRD at Sorbonne University to determine its mineralogical composition. Calcite is in fact the predominant mineral in this sample. The “sheet” shape does not probably correspond to a crystalline structure but to small crystals aggregate in thin layers at the surface of the water or in the flow and deposited at the well head. The mineralogy of the mineralization is therefore in agreement with the saturation states calculated in this specific location.

SYNTHESIS AND CONCLUSIONS

SYNTHESIS AND CONCLUSIONS

In this thesis, I presented a combined study of the fluid reactivity and circulations in a sedimentary basin. A geochemical approach has been conducted to describe the reactions affecting the sedimentary system. As mentioned in introduction, fluids in sedimentary basin can interact with the sedimentary part itself, the atmosphere, and the basement. A sedimentary basin can therefore be viewed as the interface between these three domains. The studies presented in Chapters 3 to 5 enabled to comprehensively assess the fluid reactivity in the complete atmosphere/sedimentary basin/basement system.

The sampling surveys, from their planning to their completion, had a central role into the achievement of this study (Chapter 2). The sampling points (Figure C-1) were selected after querying a geochemical database with a numerical program that I developed thanks to the collaborative work with Granada University and IGME.

The study of the helium isotopic composition in the bubbling and dissolved gases in groundwater samples of the Granada Basin, and more generally in the Central Betic Cordillera, allowed us to obtain insights on the interaction between fluids (gas) and the deep lithosphere (Chapter 3). I found that helium isotopic composition have a dominant radiogenic component with a mantle-derived He contribution reaching mainly 1 % for the investigated area. From the estimation of He diffusion within the ductile crust, the crust seems to be dissociated from the mantle with no evidence of asthenospheric influx. After re-analyzing the crustal metamorphic complexes history and considering the other potential source of ^3He by crustal production of Li-rich rocks, I proposed that the slight ^3He excess observed in the present-day fluids results from a fossil mantle signature, induced by mantle incorporation during the metamorphic complexes exhumation, diluted by local radiogenic production over time. In this study, I was therefore able to evaluate the origin of gases, to estimate the transport mechanisms of deep fluids, and to set constraints on the lithospheric structure of the Central Betic Cordillera.

The thermal water chemistry, closely related to the geological features and the fault systems in the Granada Basin, and again more generally in the Central Betic Cordillera, enabled to assess the CO_2 reactivity in the basement of the basin and the sedimentary infilling (Chapter 4). The overall water-gas-rock system was taken into consideration to describe the relationship between water chemistry, temperature, and CO_2 by the evolution of the mineral buffers in the reservoir conditions. Based on geothermometrical and geochemical thermodynamic modeling, three main groups of waters have been defined depending on their geology, the temperature, the

buffering mineral assemblage, and the $p\text{CO}_2$ in their reservoir. The thermal waters located in the ‘Valle de Lecrin’ graben displays the lowest temperature and $p\text{CO}_2$ in the reservoir (50 - 60°C and 10^{-3} - 10^{-2} atm respectively) whereas the waters located in the sedimentary basins exhibit reservoir temperatures ranging from 70 to 90°C and reservoir $p\text{CO}_2$ spanning between 10^{-2} and 10^{-1} atm. Finally, the waters located on the detachments of the metamorphic complexes, show the highest estimated temperatures and $p\text{CO}_2$ in the reservoir (130 – 140°C and 1 to 10^2 atm respectively). Although the reservoir chemistry of waters in the sedimentary basins seems to be mainly controlled by carbonates and evaporites, the two other groups show increasing buffering effect of aluminosilicates, in addition to carbonates and quartz. This study at the pluri-kilometric scale in depth contributes to distinguish the influence of the sedimentary basin from the metamorphic complexes of the basement based on the temperature and the partial pressure of CO_2 . A strong relationship between the temperature and the $p\text{CO}_2$ in the reservoir has been hence evidenced in this study, as well as the role of the potential mineral buffers on the estimation of the $p\text{CO}_2$ in depth.

The study of the water-rock interactions in the Granada Basin allows us to get insights on the groundwater circulations at the scale of the whole basin (Chapter 5). This part of the PhD project focused on the reactivity within the first 1-3 km depth based on the evolution of the mineral buffer in the rocks forming the basement and the surroundings of the basin and then with evaporites with the basin. I showed that the groundwaters evolve from carbonate-dominated waters in the basin borders to sulfate and chlorine-dominated waters within the basin. The control of the major ions (Ca^{2+} , Mg^{2+} , K^+ , Na^+ , HCO_3^- and SO_4^{2-}) were evaluated based on the saturation states with respect to carbonates, aluminosilicates and sulfate minerals. Carbonates, including both calcite and dolomite, appear to constrain the Ca and Mg concentrations and pH within the whole basin. For sulfate-dominated waters, aluminosilicate minerals display a stronger control on K than on Na. Discussing the potential reactive flow paths based on the distribution maps of the groundwater saturation with respect to sulfate minerals (barite, celestite, and gypsum), I showed that waters become saturated with respect to barite, then celestite and finally gypsum from the border to the center of the basin. This evolution details potential groundwater flow paths at the scale of the whole Granada Basin and allows discussing a conceptual reactive transport model.

The present study, therefore, has helped understanding fluid reaction paths in the Granada Basin from pluri-metric to pluri-kilometric scales, which has not been attempted so far. Besides, this work integrates the groundwater and gases geochemistry for the whole sedimentary basin.

Although numerous hydrogeological and hydrochemical studies were carried out in the basin, they mainly focused on specific aquifers (e.g. Vega de Granada aquifer, Sierra Elvira aquifer, recharge within the Sierra Nevada) and did not include both water and gas geochemical data.

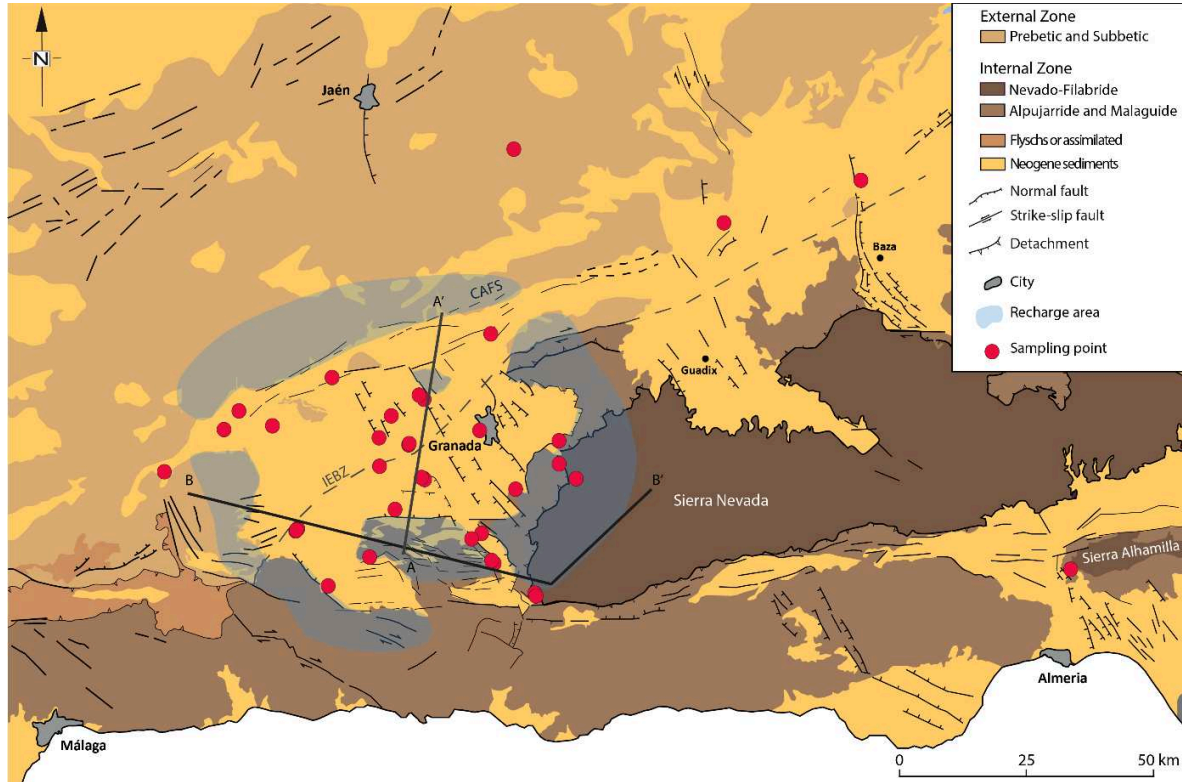


Figure C-1: Geological map of the investigated area including the location of the sampling points, the orientation of the two schematic cross-sections presented in Figure C-2 and C-3, and the recharge areas of the Granada Basin.

The regional present-day fluid reactivity and circulations were represented on two cross-sections, where the graphic charter follows that of the introduction to avoid unnecessary details on stratigraphy. I constrained fluid flows in the Granada Basin to the crust, with possible fossilized mantle-derived contribution on the noble gas composition (Figure C-3). Rainwater infiltrates into the mountain areas forming the borders of the basin and circulates through the basement and the sedimentary basin (Figure C-2 and C-3), resulting in meteoric origin of both the thermal waters and the groundwaters within the basin. The waters show large ranges of salinity and geochemical composition, which requires adaptation of the analytical protocols. These are buffered by different mineral assemblages at varied depths ranging from about a hundred meters to ~ 4 km (Figure C-2 and C-3).

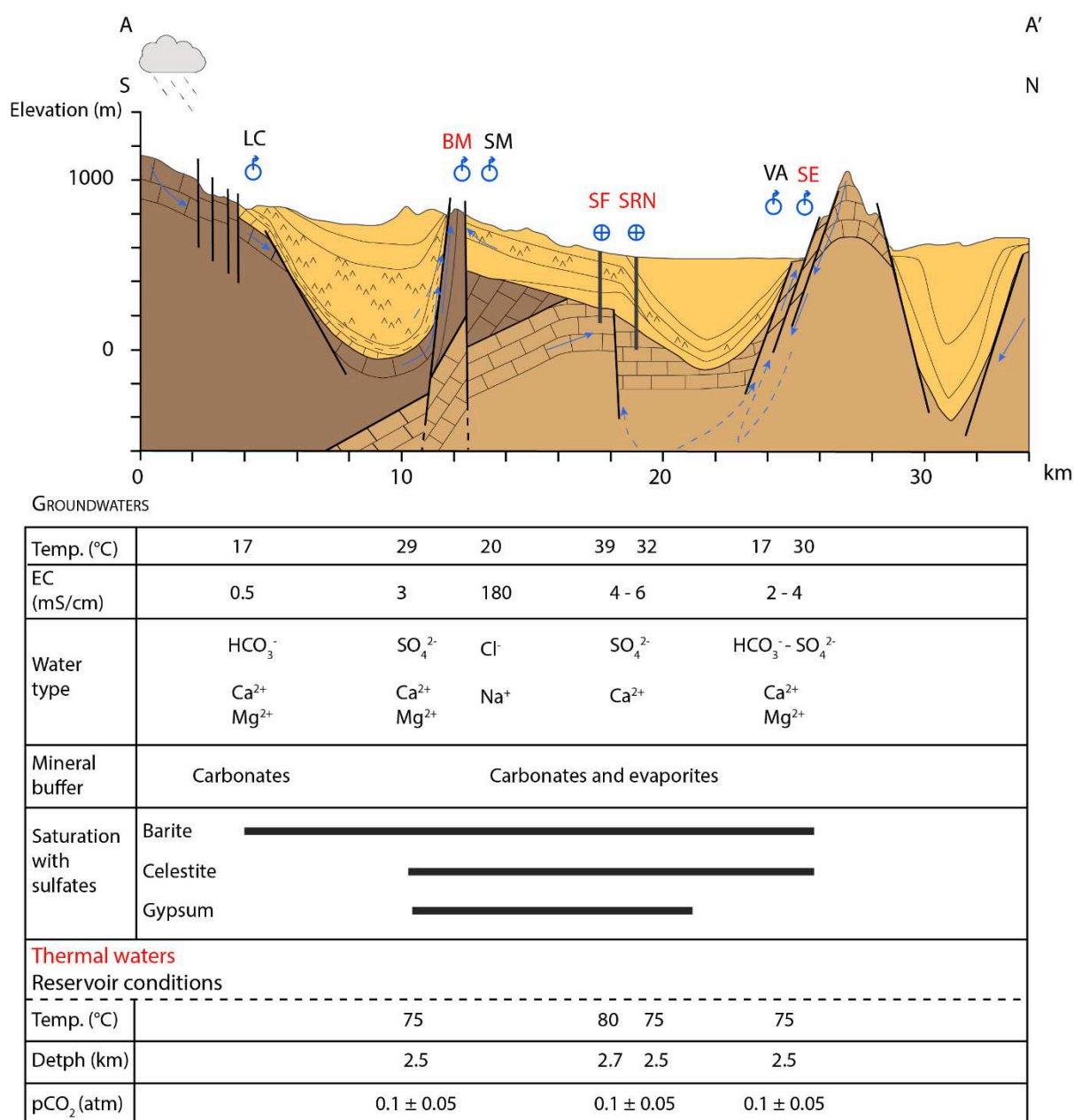
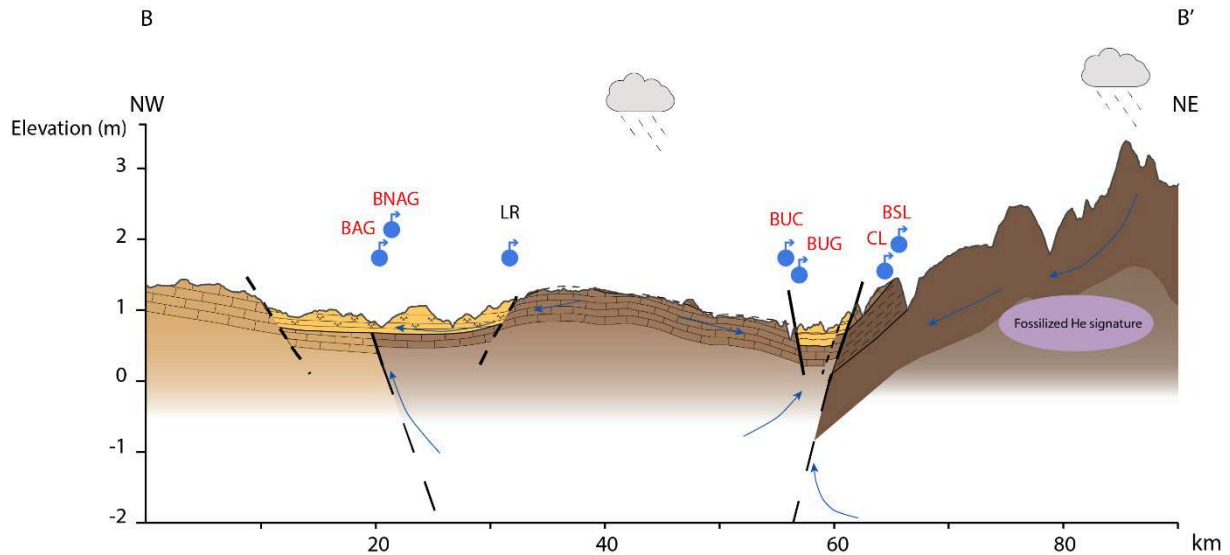


Figure C-2: Schematic N-S cross-section of the Granada Basin, modified after Rosino (2008) showing the groundwater characteristics and possible groundwater circulations. Thermal springs and wells are indicated in red.

The buffering minerals are dominated by carbonates and evaporites in the Granada Basin whereas the influence of the alumino-silicates is more pronounced at the border of the basin at the interface with the metamorphic complexes. Carbonates (calcite and/or dolomite) are the main buffering minerals in the whole Central Betic Cordillera and ubiquitously present in the investigated area, except in the Nevado-Filabride Complex. Moreover, waters interact with gases, and specifically CO₂, with different reactivities between the metamorphic complexes at the border of the basin and the center. At the contact of the metamorphic complexes, large

quantity of CO_2 is produced and degassed from potential reservoir of $\sim 130^\circ\text{C}$ (4 km) whereas smaller quantities are generated in the center of the basin (Figure C-2 and C-3). Overall, this PhD work contributes to a more detailed representation of the fluid reactivity and circulations in the Granada Basin and, more globally, in the Central Betic Cordillera.



GROUNDWATERS

Temp. ($^\circ\text{C}$)	40 39	18	25 23	21 26
EC (mS/cm)	1.2 - 1.3	0.5	0.9 1.4	34 8
Water type	SO_4^{2-} Ca^{2+} Mg^{2+}	HCO_3^- Ca^{2+} Mg^{2+}	$\text{HCO}_3^- - \text{SO}_4^{2-}$ Ca^{2+} Mg^{2+}	Cl^- Na^+
Mineral buffer	Carbonates Evaporites	Carbonates	Carbonates Ca aluminosilicates	Dolomite Mg aluminosilicates
Thermal waters				
Reservoir conditions				
Temp. ($^\circ\text{C}$)	85 90		55 70	130 140
Depth (km)	2.5 - 3		1.5 - 2	3 - 4
pCO_2 (atm)	0.2 ± 0.1		0.01 ± 0.01	50 ± 40
Helium isotopes				
$^3\text{He}/^4\text{He}_c$	0.11		0.02 - 0.06	1.1

Figure C-3: Schematic W-E cross-section of the southern border of the Granada Basin and through the Sierra Nevada, showing the groundwater chemical characteristics, the He isotopic ratio, and the potential groundwater circulations. Thermal springs are indicated in red.

PERSPECTIVES

PERSPECTIVES

The results of this study reveal several perspectives that are presented in the following paragraphs. These perspectives could be classified in decreasing scales with the first at the lithospheric scale, the second at the kilometric scale whereas the third one try to link the microscopic and macroscopic scales.

Investigating He isotopic composition in the springs located close to the peridotites:

We have proposed in Chapter 3 that asthenospheric material might have been incorporated in the crust of the Betic Cordillera during the exhumation of the metamorphic complexes, leading to a relative enrichment in ^3He (Chapter 3). The presence of xenoliths, and peridotites in particular in the western Betic Cordillera, is an evidence of incorporation of mantle material in the crust. A number of springs are located close to the peridotite massifs showing low incidence of shallow flow systems although their absence or low thermal character. Investigating He isotopic composition of gases in these springs might give some clues to test the relevance of this hypothesis, independently of the He mass-balance calculations.

Towards reactive transport modeling

This study has shown that the water geochemistry give us interesting insights on the fluid reactivity and possible reactions paths in the Granada Basin (Chapter 5). Hence, this work has allowed to evaluate the regional groundwater circulations and to qualitatively discuss transport without explicitly modeling flows via coupled numerical equations. Substantial efforts should be put into estimations of mineralogical distribution and groundwater residence times. It would be interesting to test simple reactive transport modeling along specific flow paths, in 1D or 2D, within the basin by integrating known hydrodynamics (e.g., flow rates, pressure gradients, and residence time ranges) found in the literature and derived from my observations. I could therefore test whether the orientation of the metamorphic complex stack, the faults, or the low-permeability evaporite layers could be possible controlling parameters of the transport in this basin. This could be performed using the numerical tools (software) developed at IFPEN. The porosity, permeability, pressure, and fluid salinity values could be extracted from modeling with the TemisFlow software to complete the dataset where no information is available. Then, I would be able to perform reactive transport modeling with the Coores software by simulating flow and geochemical reactions (Arxim) in a fixed grid and in a shorter time scale (during

100,000 years).

Being able to perform reactive transport modeling could be very useful to estimate the water quality in the Granada Basin for public governance. The investigated region is indeed a semi-arid area, facing an increasing pressure on the water resource. This approach would allow a better understanding of the distribution and the controlling parameters of the water quality.

Determining the controlling parameters of evaporite kinetics

This work provides a good description of the groundwater thermodynamics in the Granada Basin (Chapters 4 and 5) and especially those related to the evaporite interactions. There are, however, limitations of these thermodynamic calculations for waters at high ionic strength, as the ionic interaction models considering the deviation of ideal behavior of solutes (e.g. pitzer model) do not include Al. Moreover, the kinetic approach was not addressed in this study. The question of the parameters controlling evaporite dissolution/precipitation kinetics (e.g. ionic strength, common ion effect) still remains unsolved. As the initial objective of this study was to understand the fluid flows at this basin scale, it would be important to discuss kinetics at this scale too. An approach coupling laboratory experiments with reactive column experiments (open system) and monitoring of the geochemistry on the field could be considered. Although discrepancies between the evaporite kinetics determined in laboratory and in the field are well-known, the Granada Basin could be a suitable study case to carry out mass-balance calculations because of the large contrasts in salinities. It might be interesting to identify the controlling parameters of evaporite kinetics at a relatively long time scale (1,000 to 10,000 years) within a sedimentary basin.

REFERENCES

REFERENCES

- Alcalá, F.J., Custodio, E., 2008. Using the Cl/Br ratio as a tracer to identify the origin of salinity in aquifers in Spain and Portugal. *J. Hydrol.* 359, 189–207. <https://doi.org/10.1016/j.jhydrol.2008.06.028>
- Ármannsson, H., 2003. CO₂ emission from geothermal plants, in: International Geothermal Conference. pp. 56–62.
- Ármannsson, H., Fridriksson, T., Kristjánsson, B.R., 2005. CO₂ emissions from geothermal power plants and natural geothermal activity in Iceland. *Geothermics* 34, 286–296. <https://doi.org/10.1016/j.geothermics.2004.11.005>
- Arnórsson, S., Gunnlaugsson, E., Svavarsson, H., 1983. The chemistry of geothermal waters in Iceland. III. Chemical geothermometry in geothermal investigations. *Geochim. Cosmochim. Acta* 47, 567–577. [https://doi.org/10.1016/0016-7037\(83\)90278-8](https://doi.org/10.1016/0016-7037(83)90278-8)
- Arrizabalaga, I., De Gregorio, M., García del la Noceda, C., Hidalgo, R., Urchueguía, J.F., 2015. Country Update for the Spanish Geothermal Sector, in: World Geothermal Congress 2015. p. 9.
- Asta, M.P., Gimeno, M.J., Auqué, L.F., Gómez, J., Acero, P., Lapuente, P., 2012. Hydrochemistry and geothermometrical modeling of low-temperature Panticosa geothermal system (Spain). *J. Volcanol. Geotherm. Res.* 235–236, 84–95. <https://doi.org/10.1016/j.jvolgeores.2012.05.007>
- Augier, R., 2004. Evolution tardi-orogénique des Cordillères Bétiques (Espagne): Apports d’une étude intégrée. Université de Pierre et Marie Curie - Paris VI.
- Augier, R., Agard, P., Monié, P., Jolivet, L., Robin, C., Booth-Rea, G., 2005. Exhumation, doming and slab retreat in the Betic Cordillera (SE Spain): In situ ⁴⁰Ar/³⁹Ar ages and P-T-d-t paths for the Nevado-Filabride complex. *J. Metamorph. Geol.* <https://doi.org/10.1111/j.1525-1314.2005.00581.x>
- Auqué, L.F., Acero, P., Gimeno, M.J., Gómez, J.B., Asta, M.P., 2009. Hydrogeochemical modeling of a thermal system and lessons learned for CO₂ geologic storage. *Chem. Geol.* 268, 324–336. <https://doi.org/10.1016/j.chemgeo.2009.09.011>
- Azañón, J.M., Azor, A., Booth-Rea, G., Torcal, F., 2004. Small-scale faulting, topographic steps and seismic ruptures in the Alhambra (Granada, southeast Spain). *J. Quat. Sci.* 19, 219–227. <https://doi.org/10.1002/jqs.838>
- Azañón, J.M., Crespo-Blanc, A., García-Dueñas, V., Sánchez-Gómez, M., 1995. The Alpujárride Complex structure and its contribution to the ESCI-Béticas2 deep seismic reflection profile interpretation (Alborán Domain, Betic Chain). *Rev. Soc. Geol. España* 8, 491–501.
- Azañón, J.M., Crespo-Blanc, A., 2000. Exhumation during a continental collision inferred from the tectonometamorphic evolution of the Alpujárride Complex in the central Betics (Alboran Domain, SE Spain). *Tectonics* 19, 549–565. <https://doi.org/10.1029/2000TC900005>
- Azañón, J.M., García-Dueñas, V., Goffé, B., 1998. Exhumation of high-pressure metapelites and coeval crustal extension in the Alpujárride complex (Betic Cordillera). *Tectonophysics* 285, 231–252. [https://doi.org/10.1016/S0040-1951\(97\)00273-4](https://doi.org/10.1016/S0040-1951(97)00273-4)

- Ballentine, C.J., Burgess, R., Marty, B., 2002. Tracing fluid origin, transport and interaction in the crust, *Reviews in mineralogy and geochemistry*. Mineral Soc America. <https://doi.org/10.2138/rmg.2002.47.13>
- Ballentine, C.J., Burnard, P.G., 2002. Production, release and transport of noble gases in the continental crust, *Reviews in mineralogy and geochemistry*. Mineralogical Society of America. <https://doi.org/10.2138/rmg.2002.47.12>
- Battistel, M., Hurwitz, S., Evans, W.C., Barbieri, M., 2016. The chemistry and isotopic composition of waters in the low-enthalpy geothermal system of Cimino-Vico Volcanic District, Italy. *J. Volcanol. Geotherm. Res.* 328, 222–229. <https://doi.org/10.1016/j.jvolgeores.2016.11.005>
- Behr, W.M., Platt, J.P., 2012. Kinematic and thermal evolution during two-stage exhumation of a Mediterranean subduction complex. *Tectonics* 31. <https://doi.org/10.1029/2012TC003121>
- Benavente Herrera, J., Sanz de Galdeano, C., 1985. Relacion de las direcciones de karstificacion y del termalismo con la fracturacion en las Cordilleras Beticas. *Estud. Geológicos* 41, 177–188.
- Benson, B.B., Krause, D., 1980. Isotopic fractionation of helium during solution: A probe for the liquid state. *J. Solution Chem.* 9, 895–909.
- Bjorlykke, K., 1993. Fluid flow in sedimentary basins. *Sediment. Geol.* 86, 137–158. [https://doi.org/10.1016/0037-0738\(93\)90137-T](https://doi.org/10.1016/0037-0738(93)90137-T)
- Blanco, M.J., Spakman, W., 1993. The P-wave velocity structure of the mantle below the Iberian Peninsula: evidence for subducted lithosphere below southern Spain. *Tectonophysics* 221, 13–34. [https://doi.org/10.1016/0040-1951\(93\)90025-F](https://doi.org/10.1016/0040-1951(93)90025-F)
- Blasco, M., Auqué, L.F., Gimeno, M.J., Acero, P., Asta, M.P., 2017. Geochemistry, geothermometry and influence of the concentration of mobile elements in the chemical characteristics of carbonate-evaporitic thermal systems. The case of the Tiernas geothermal system (Spain). *Chem. Geol.* 466, 696–709. <https://doi.org/10.1016/J.CHEMGEO.2017.07.013>
- Blasco, M., Gimeno, M.J., Auqué, L.F., 2018. Low temperature geothermal systems in carbonate-evaporitic rocks: Mineral equilibria assumptions and geothermometrical calculations. Insights from the Arnedillo thermal waters (Spain). *Sci. Total Environ.* 615, 526–539. <https://doi.org/10.1016/J.SCITOTENV.2017.09.269>
- Boné, E., Dabrio, C.J., Michaux, J., Peña, José Andrés de la, Ruiz Bustos, A., 1978. Stratigraphie et paleontologie du Miocene Superieur d'Arenas del Rey, Bass 1 N de Grenade (Andalous 1 E, Espagne)(1). *Bull. la Société belge géologie* 87, 87–99.
- Bonnin, M., Nolet, G., Villaseñor, A., Gallart, J., Thomas, C., 2014. Multiple-frequency tomography of the upper mantle beneath the African/Iberian collision zone. *Geophys. J. Int.* 198, 1458–1473.
- Booth-Rea, G., Azañón, J.-M., Azor, A., García-Dueñas, V., 2004a. Influence of strike-slip fault segmentation on drainage evolution and topography. A case study: the Palomares Fault Zone (southeastern Betics, Spain). *J. Struct. Geol.* 26, 1615–1632.
- Booth-Rea, G., Azañón, J.M., García-Dueñas, V., 2004b. Extensional tectonics in the northeastern Bethics (SE Spain): Case study of extension in a multilayered upper crust with contrasting rheologies. *J. Struct. Geol.* 26, 2039–2058. <https://doi.org/10.1016/j.jsg.2004.04.005>

- Braga, J.C., Martín, J.M., Alcalá, B., 1990. Coral reefs in coarse-terrigenous sedimentary environments (Upper Tortonian, Granada Basin, southern Spain). *Sediment. Geol.* 66, 135–150.
- Braga, J.C., Martín, J.M., Quesada, C., 2003. Patterns and average rates of late Neogene--Recent uplift of the Betic Cordillera, SE Spain. *Geomorphology* 50, 3–26. [https://doi.org/10.1016/S0169-555X\(02\)00205-2](https://doi.org/10.1016/S0169-555X(02)00205-2)
- Bräuer, K., Geissler, W.H., Kämpf, H., Niedermann, S., Rman, N., 2016. Helium and carbon isotope signatures of gas exhalations in the westernmost part of the Pannonian Basin (SE Austria/NE Slovenia): Evidence for active lithospheric mantle degassing. *Chem. Geol.* 422, 60–70. <https://doi.org/10.1016/j.chemgeo.2015.12.016>
- Brouwer, H.A., 1926. Zur Geologie der Sierra Nevada. *Geol. Rundschau* 17, 118–137. <https://doi.org/10.1007/BF01801854>
- Buform, E., Bezzeghoud, M., Udías, A., Pro, C., 2004. Seismic Sources on the Iberia-African Plate Boundary and their Tectonic Implications. *Pure Appl. Geophys.* 161, 623–646. <https://doi.org/10.1007/s00024-003-2466-1>
- Burov, E., Jolivet, L., Le Pourhiet, L., Poliakov, A., 2001. A thermomechanical model of exhumation of high pressure (HP) and ultra-high pressure (UHP) metamorphic rocks in Alpine-type collision belts. *Tectonophysics* 342, 113–136. [https://doi.org/10.1016/S0040-1951\(01\)00158-5](https://doi.org/10.1016/S0040-1951(01)00158-5)
- Calvert, A., Sandvol, E., Seber, D., Barazangi, M., Roecker, S., Mourabit, T., Vidal, F., Alguacil, G., Jabour, N., 2000. Geodynamic evolution of the lithosphere and upper mantle beneath the Alboran region of the western Mediterranean: Constraints from travel time tomography. *J. Geophys. Res. Solid Earth* 105, 10871–10898. <https://doi.org/10.1029/2000JB900024>
- Campos, J.C.R., 2006. Guía de manantiales de la provincia de Granada: Una visión sobre su origen y naturaleza. Publicaciones de Diputación Provincial de Granada.
- Capasso, G., Favara, R., Grassa, F., Inguaggiato, S., Longo, M., 2005. On-line technique for preparing and measuring stable carbon isotope of total dissolved inorganic carbon in water samples ($\delta^{13}\text{C}$ TDIC). *Ann. Geophys.* 48.
- Capasso, G., Inguaggiato, S., 1998. A simple method for the determination of dissolved gases in natural waters. An application to thermal waters from Vulcano Island. *Appl. Geochemistry* 13, 631–642. [https://doi.org/10.1016/S0883-2927\(97\)00109-1](https://doi.org/10.1016/S0883-2927(97)00109-1)
- Capecchiacci, F., Tassi, F., Vaselli, O., Bicocchi, G., Cabassi, J., Giannini, L., Nisi, B., Chiocciara, G., 2015. A combined geochemical and isotopic study of the fluids discharged from the Montecatini thermal system (NW Tuscany, Italy). *Appl. Geochemistry* 59, 33–46. <https://doi.org/10.1016/j.apgeochem.2015.03.010>
- Caracausi, A., Paternoster, M., 2015. Radiogenic helium degassing and rock fracturing: A case study of the southern Apennines active tectonic region. *J. Geophys. Res. Solid Earth* 120, 2200–2211. <https://doi.org/10.1002/2014JB011462>
- Cardenal, J., Benavente, J., Cruz-Sanjulián, J.J., 1994. Chemical evolution of groundwater in Triassic gypsum-bearing carbonate aquifers (Las Alpujarras, southern Spain). *J. Hydrol.* 161, 3–30.
- Castillo, A., 2005. El acuífero de la Vega de Granada: Ayer y hoy (1966–2004). *Agua, Minería y Medio Ambient. Libr. Homen. al Profr. Rafael Fernández Rubio*. López Geta al.(eds). IGME 161–172.

- Castillo, A., 2000. Parque Nacional de Sierra Nevada, Clima e Hidrología, Canseco Ed. ed, Parque nacional de Sierra Nevada.
- Castillo, A., Pulido-Bosch, A., Martínez-Carmona, N., 1997. Evolution de la pollution par fertilisants dans un grand aquifère detritique du sud de l'Espagne. IAHS Publ. Proc. Reports-Intern Assoc Hydrol. Sci. 243, 203–210.
- Castillo, A., Sánchez-Díaz, L., Chica-Olmo, M., Luque-Espinar, J.A., 2004. Distribución espacial de nitratos en el acuífero de la Vega de Granada: análisis de las situaciones en 1983 y 2003. *Geogaceta* 36, 111–114.
- Castillo, A.M., 1995. El embalse subterráneo de la Vega de Granada, uno de los más importantes de Andalucía. *Tierra y Tecnol. Rev. Inf. geológica* 37–42.
- Centre d'Expertise en Analyse Environnementale du Québec, 2016. Détermination de la silice réactive dans l'eau : méthode par spectrophotométrie UV-visible, MA. 303 – SiO₂ 1.0, rév. 1. Ministère du Développement durable, de l'Environnement, de la Lutte contre les changements climatiques.
- Cerón, J.C., López-Chicano, M., 2002. Thermal waters in Andalucía. *Newsl. Int. Geotherm. Assoc.* 48, 4–5.
- Cherniak, D.J., Watson, E.B., Thomas, J.B., 2009. Diffusion of helium in zircon and apatite. *Chem. Geol.* 268, 155–166. <https://doi.org/10.1016/J.CHEMGEO.2009.08.011>
- Chica-Olmo, M., Luque-Espinar, J.A., Rodríguez-Galiano, V., Pardo-Iguzquiza, E., Chica-Rivas, L., 2014. Categorical Indicator Kriging for assessing the risk of groundwater nitrate pollution: the case of Vega de Granada aquifer (SE Spain). *Sci. Total Environ.* 470–471, 229–239. <https://doi.org/10.1016/j.scitotenv.2013.09.077>
- Chiodini, G., Frondini, F., Marini, L., 1995. Theoretical geothermometers and PCO₂ indicators for aqueous solutions coming from hydrothermal systems of medium-low temperature hosted in carbonate-evaporite rocks. Application to the thermal springs of the Etruscan Swell, Italy. *Appl. Geochemistry* 10, 337–346. [https://doi.org/10.1016/0883-2927\(95\)00006-6](https://doi.org/10.1016/0883-2927(95)00006-6)
- Clark, I., 2015. *Groundwater Geochemistry and Isotopes*. CRC Press.
- Clark, I.D., Fritz, P., 1997. *Environmental isotopes in hydrogeology*. CRC Press/Lewis Publishers, Boca Raton, FL.
- Clarke, W.B., Jenkins, W.J., Top, Z., 1976. Determination of tritium by mass spectrometric measurement of ³He. *Int. J. Appl. Radiat. Isot.* 27, 515–522. [https://doi.org/10.1016/0020-708X\(76\)90082-X](https://doi.org/10.1016/0020-708X(76)90082-X)
- Comas, M.C., Platt, J.P., Soto, J.I., Watts, A.B., 1999. 44. the origin and tectonic history of the alboran basin: insights from leg 161 results, in: *Proceedings of the Ocean Drilling Program Scientific Results*. pp. 555–580.
- Corbí, H., Lancis, C., García-García, F., Pina, J.-A., Soria, J.M., Tent-Manclús, J.E., Viseras, C., 2012. Updating the marine biostratigraphy of the Granada Basin (central Betic Cordillera). Insight for the Late Miocene palaeogeographic evolution of the Atlantic -- Mediterranean seaway. *Geobios* 45, 249–263. <https://doi.org/10.1016/j.geobios.2011.10.006>
- Coudrain-Ribstein, A., Gouze, P., de Marsily, G., 1998. Temperature-carbon dioxide partial pressure trends in confined aquifers. *Chem. Geol.* 1.
- Crespo-Blanc, A., Frizon de Lamotte, D., 2006. Structural evolution of the external zones

- derived from the Flysch trough and the South Iberian and Maghrebian paleomargins around the Gibraltar arc: A comparative study. *Bull. la Soc. Geol. Fr.* 177, 267–282. <https://doi.org/10.2113/gssgfbull.177.5.267>
- Cruz-Sanjulián, J., Rossell, L.G., Blasco, J.G., 1972. Aguas termales de la provincia de Granada. *Bol. Geológico y Min. T.LXXXIII-III* 266–275.
- Cruz Sanjulián, J., Granda, J.M., 1979. Temperatura de base de las aguas termales de la provincia de Granada, in: *II Simposio Nacional de Hidrogeología*. pp. 547–568.
- D’Amore, F., Arnórsson, S., Geothermometry, S.A., 2000. Isotopic and Chemical Techniques in Geothermal Exploration. *Dev. Use Sampl. Methods, Data Handl. Interpret. Int. At. Energy Agency, Vienna, Austria* 152–199.
- D’Amore, F., Fancelli, R., Caboi, R., 1987. Observations on the application of chemical geothermometers to some hydrothermal systems in Sardinia. *Geothermics* 16, 271–282.
- Dabrio, C.J., Fernández, J., Peña, J.A., Ruiz Bustos, A., de Galdeano, C.M., 1978. Rasgos sedimentarios de los conglomerados miocénicos del borde noreste de la Depresión de Granada. *Estud. Geológicos* 34, 89–97.
- Dabrio, C.J., Martín, J.M., 1981. Yesos diagenéticos en la Depresión de Granada. *Boletín la Real Soc. Española Hist. Nat. Sección Geológica* 79, 215–223.
- Dabrio, C.J., Martin, J.M., Megias, A.G., 1982. Signification sédimentaire des évaporites de la dépression de Grenade (Espagne). *Bull. la Société géologique Fr.* 705–710.
- Dewey, J.F., Helman, M.L., Knott, S.D., Turco, E., Hutton, D.H.W., 1989. Kinematics of the western Mediterranean. *Geol. Soc. London, Spec. Publ.* 45, 265–283. <https://doi.org/10.1144/GSL.SP.1989.045.01.15>
- Díaz de Neira, J.A., Enrile Albir, A., Hernaiz Huerta, P.P., López Olmedo, F., 1992. Geological map. Sheet Valdepeñas de Jaén, 969, scale 1:50 000.
- Diaz, J., Gallart, J., Carbonell, R., 2016. Moho topography beneath the Iberian-Western Mediterranean region mapped from controlled-source and natural seismicity surveys. *Tectonophysics* 692, 74–85. <https://doi.org/10.1016/j.tecto.2016.08.023>
- Do Couto, D., 2014. Evolution géodynamique de la Mer d’Alboran par l’étude des bassins sédimentaires. Université Pierre et Marie Curie-Paris VI.
- Durand Delga, M., 1980. Considérations sur les flyschs du Crétacé inférieur dans les chaînes alpines d’Europe. *Bsgf*.
- Dyja-Person, V., Tarantola, A., Richard, A., Hibsich, C., Siebenaller, L., Boiron, M., Cathelineau, M., Boulvais, P., 2018. Metamorphic brines and no surficial fluids trapped in the detachment footwall of a Metamorphic Core Complex (Nevado-Filábride units, Betics, Spain). *Tectonophysics* 727, 56–72. <https://doi.org/10.1016/j.tecto.2018.02.001>
- Dyja, V., 2014. Interaction entre fluides de différents réservoirs lors de l’évolution d’un prisme orogénique en contexte de déformation partitionnée: les Cordillères bétiques internes (Espagne): Implications sur le transfert de métaux dans la croûte. Université de Lorraine.
- Einsele, G., 2013. Sedimentary basins: evolution, facies, and sediment budget. Springer Science & Business Media.
- Elidemir, S., Güleç, N., 2018. Geochemical characterization of geothermal systems in western Anatolia (Turkey): implications for CO₂trapping mechanisms in prospective CO₂-EGS sites. *Greenh. Gases Sci. Technol.* 8, 63–76. <https://doi.org/10.1002/ghg.1747>

- Faccenna, C., Piromallo, C., Crespo-Blanc, A., Jolivet, L., Rossetti, F., 2004. Lateral slab deformation and the origin of the western Mediterranean arcs. *Tectonics* 23. <https://doi.org/10.1029/2002TC001488>
- Faulkner, D.R., Lewis, A.C., Rutter, E.H., 2003. On the internal structure and mechanics of large strike-slip fault zones: field observations of the Carboneras fault in southeastern Spain. *Tectonophysics* 367, 235–251.
- Fernández-Ibáñez, F., Soto, J.I., Morales, J., 2005. Profundidad de la transición dúctil-frágil en la corteza de Béticas-Rif y Mar de Alborán. *Geogaceta* 37, 155–158.
- Fernández, M., Marzán, I., Correia, A., Ramalho, E., 1998. Heat flow, heat production, and lithospheric thermal regime in the Iberian Peninsula. *Tectonophysics* 291, 29–53. [https://doi.org/10.1016/S0040-1951\(98\)00029-8](https://doi.org/10.1016/S0040-1951(98)00029-8)
- Fontes, J.C., Matray, J.M., 1993. Geochemistry and origin of formation brines from the Paris Basin, France: 1. Brines associated with Triassic salts. *Chem. Geol.* 109, 149–175.
- Foucault, A., 1974. Travaux et titres scientifiques et universitaires. Univ. Paris VI, Paris.
- Fournier, R.O., 1977. Chemical geothermometers and mixing models for geothermal systems. *Geothermics* 5, 41–50. [https://doi.org/10.1016/0375-6505\(77\)90007-4](https://doi.org/10.1016/0375-6505(77)90007-4)
- Fournier, R.O., Potter, R.W., 1982. An equation correlating the solubility of quartz in water from 25° to 900°C at pressures up to 10,000 bars. *Geochim. Cosmochim. Acta* 46, 1969–1973. [https://doi.org/10.1016/0016-7037\(82\)90135-1](https://doi.org/10.1016/0016-7037(82)90135-1)
- Fusari, A., Carroll, M.R., Ferraro, S., Giovannetti, R., Giudetti, G., Invernizzi, C., Mussi, M., Pennisi, M., 2017. Circulation path of thermal waters within the Laga foredeep basin inferred from chemical and isotopic ($\delta^{18}\text{O}$, δD , ^3H , $^{87}\text{Sr}/^{86}\text{Sr}$) data. *Appl. Geochemistry* 78, 23–34. <https://doi.org/10.1016/J.APGEOCHEM.2016.11.021>
- Galindo-Zaldívar, J., Gil, A.J., Sanz de Galdeano, C., Lacy, M.C., García-Armenteros, J.A., Ruano, P., Ruiz, A.M., Martínez-Martos, M., Alfaro, P., 2015. Active shallow extension in central and eastern Betic Cordillera from CGPS data. *Tectonophysics* 663, 290–301. <https://doi.org/10.1016/j.tecto.2015.08.035>
- Galindo-Zaldívar, J., Jabaloy, A., Serrano, I., Morales, J., González-Lodeiro, F., Torcal, F., 1999. Recent and present-day stresses in the Granada Basin (Betic Cordilleras): Example of a late Miocene-present-day extensional basin in a convergent plate boundary. *Tectonics* 18, 686–702. <https://doi.org/10.1029/1999TC900016>
- García-Alix, A., Minwer-Barakat, R., Martín, J.M., Suárez, E.M., Freudenthal, M., 2009. Dating the change from endorheic to exorheic conditions in the drainage system of the Granada Basin (southern Spain). *Palaios* 24, 544–549.
- García-Alix, A., Minwer-Barakat, R., Martín, J.M., Suárez, E.M., Freudenthal, M., 2008. Biostratigraphy and sedimentary evolution of Late Miocene and Pliocene continental deposits of the Granada Basin (southern Spain). *Lethaia* 41, 431–446. <https://doi.org/10.1111/j.1502-3931.2008.00097.x>
- García-Hernández, M., López-Garrido, A.C., Rivas, P., Sanz de Galdeano, Carlos, Vera, J.A., 1980. Mesozoic palaeogeographic evolution of the external zones of the Betic Cordillera.
- García-Tortosa, F.J., López-Garrido, A.C., Sanz de Galdeano, C., 2000. Présence du complexe tectonique Malaguide à l'est de Carthagène (zone interne Bétique, Espagne). *Comptes Rendus l'Académie des Sci. IIA-Earth Planet. Sci.* 330, 139–146. [https://doi.org/10.1016/S1251-8050\(00\)00124-5](https://doi.org/10.1016/S1251-8050(00)00124-5)

- García-Veigas, J., Cendón, D.I., Rosell, L., Ortí, F., Torres Ruiz, J., Martín, J.M., Sanz, E., 2013. Salt deposition and brine evolution in the Granada Basin (Late Tortonian, SE Spain). *Palaeogeogr. Palaeoclimatol. Palaeoecol.* 369, 452–465. <https://doi.org/10.1016/j.palaeo.2012.11.010>
- García-Veigas, J., Rosell, L., Cendón, D.I., Gibert, L., Martín, J.M., Torres-Ruiz, J., Ortí, F., 2015. Large celestine orebodies formed by early-diagenetic replacement of gypsified stromatolites (Upper Miocene, Montevive--Escúzar deposit, Granada Basin, Spain). *Ore Geol. Rev.* 64, 187–199. <https://doi.org/10.1016/j.oregeorev.2014.07.009>
- Garrido, J.R., 2003. Composición isotópica del vapor de agua atmosférico en el sureste de la Península Ibérica. Granada: Universidad de Granada.
- Garven, G., 1995. Continental-scale groundwater flow and geologic processes. *Annu. Rev. Earth Planet. Sci.* 23, 89–117.
- Gautheron, C., Moreira, M., 2002. Helium signature of the subcontinental lithospheric mantle. *Earth Planet. Sci. Lett.* 199, 39–47. [https://doi.org/10.1016/S0012-821X\(02\)00563-0](https://doi.org/10.1016/S0012-821X(02)00563-0)
- Gil-Márquez, J.M., Mudarra, M., Andreo, B., Linares, L., 2016. Hydrogeological characterization of the Salinas-Los Hoyos evaporitic karst (Malaga province , S Spain) using topographic , hydrodynamic, hydrochemical and isotopic methods. *Acta Carsologica* 45, 147–160.
- Gil, A.J., Galindo-Zaldívar, J., Sanz de Galdeano, C., Borque, M.J., Sánchez-Alzola, A., Martínez-Martos, M., Alfaro, P., 2017. The Padul normal fault activity constrained by GPS data: Brittle extension orthogonal to folding in the central Betic Cordillera. *Tectonophysics* 712–713, 64–71. <https://doi.org/10.1016/j.tecto.2017.05.008>
- Gil, A.J., Rodríguez-Caderot, G., Lacy, M.C., Ruiz, A.M., De Galdeano, C.S., Alfaro, P., 2002. Establishment of a non-permanent GPS network to monitor the recent NE-SW deformation in the Granada Basin (Betic Cordillera, Southern Spain). *Stud. Geophys. Geod.* 46, 395–410.
- Gilfillan, S.M.V., Wilkinson, M., Haszeldine, R.S., Shipton, Z.K., Nelson, S.T., Poreda, R.J., 2011. He and Ne as tracers of natural CO₂ migration up a fault from a deep reservoir. *Int. J. Greenh. Gas Control* 5, 1507–1516. <https://doi.org/10.1016/j.ijggc.2011.08.008>
- Gilli, É., Mangan, C., Mudry, J., 2008. *Hydrogéologie: objet, méthodes, applications*. Dunod.
- Gómez-Pugnaire, M.T., 1979. Evolución del metamorfismo alpino en el complejo nevado-filabride de la sierra de Baza (cordilleras béticas, España).
- Gómez-Pugnaire, M.T., Braga, J.C., Martín, J.M., Sassi, F.P., Del Moro, A., 2000. The age of the Nevado--Filábride cover (Betic Cordilleras, S Spain): regional implications. *Schweiz. Miner. Petrogr. Mitt* 80, 45–52.
- Gómez-Pugnaire, M.T., Fernández-Soler, J.M., 1987. High-pressure metamorphism in metabasites from the Betic Cordilleras (S.E. Spain) and its evolution during the Alpine orogeny. *Contrib. to Mineral. Petrol.* 95, 231–244. <https://doi.org/10.1007/BF00381273>
- Gran, G., 1952. Determination of the equivalence point in potentiometric titrations. Part II. *Analyst* 77, 661–671. <https://doi.org/10.1039/AN9527700661>
- Gutscher, M.-A., Malod, J., Rehault, J.-P., Contrucci, I., Klingelhoefer, F., Mendes-Victor, L., Spakman, W., 2002. Evidence for active subduction beneath Gibraltar. *Geology* 30, 1071–1074.
- Heit, B., Mancilla, F. de L., Yuan, X., Morales, J., Stich, D., Martín, R., Molina-Aguilera, A.,

2017. Tearing of the mantle lithosphere along the intermediate-depth seismicity zone beneath the Gibraltar Arc: The onset of lithospheric delamination. *Geophys. Res. Lett.* 44, 4027–4035. <https://doi.org/10.1002/2017GL073358>
- Hunt, T.M., 2001. Five Lectures on Environmental Effects of Geothermal Utilization, Geothermal Training Programme.
- Hutcheon, I.A.N., Shevalier, M., Abercrombie, H.J., 1993. pH buffering by metastable mineral-fluid equilibria and evolution of carbon dioxide fugacity during burial diagenesis. *Geochim. Cosmochim. Acta* 57, 1017–1027.
- Hyndman, R.D., Klemperer, S.L., 1989. Lower-crustal porosity from electrical measurements and inferences about composition from seismic velocities. *Geophys. Res. Lett.* 16, 255–258.
- Hyndman, R.D., Shearer, P.M., 1989. Water in the lower continental crust: modelling magnetotelluric and seismic reflection results. *Geophys. J. Int.* 98, 343–365. <https://doi.org/10.1111/j.1365-246X.1989.tb03357.x>
- IGME, 2005. Propuesta de perímetros de protección Cambil.
- IGME, 1990. Atlas Hidrogeológico de la Provincia de Granada. IGME-Excma Diput. Prov. Granada 107.
- Inguaggiato, C., Censi, P., D'Alessandro, W., Zuddas, P., 2016. Geochemical characterisation of gases along the dead sea rift: Evidences of mantle-CO₂ degassing. *J. Volcanol. Geotherm. Res.* 320, 50–57. <https://doi.org/10.1016/j.jvolgeores.2016.04.008>
- Inguaggiato, S., Rizzo, A., 2004. Dissolved helium isotope ratios in ground-waters: a new technique based on gas--water re-equilibration and its application to Stromboli volcanic system. *Appl. Geochemistry* 19, 665–673. <https://doi.org/10.1016/j.apgeochem.2003.10.009>
- Jabaloy, A., Galindo-Zaldívar, J., González-Lodeiro, F., Aldaya, F., 1997. Main features of the deep structure of the central Betic Cordillera (SE Spain) from the ESCI-Béticas deep seismic reflection profiles. *Rev. la Soc. Geológica España* 8.
- Jähne, B., Heinz, G., Dietrich, W., 1987. Measurement of the diffusion coefficients of sparingly soluble gases in water. *J. Geophys. Res. Ocean.* 92, 10767–10776. <https://doi.org/10.1029/JC092iC10p10767>
- Janowski, M., Loget, N., Gautheron, C., Barbarand, J., Bellahsen, N., Van Den Driessche, J., Babault, J., Meyer, B., 2016. Neogene exhumation and relief evolution in the eastern Betics (SE Spain): Insights from the Sierra de Gador. *Terra Nov.* 29, 91–97. <https://doi.org/10.1111/ter.12252>
- Jolivet, L., Augier, R., Faccenna, C., Negro, F., Rimmelé, G., Agard, P., Robin, C., Rossetti, F., Crespo-Blanc, A., 2008. Subduction, convergence and the mode of backarc extension in the Mediterranean region. *Bull. la Société Géologique Fr.* 179, 525–550. <https://doi.org/10.2113/gssgfbull.179.6.525>
- Jolivet, L., Faccenna, C., 2000. Mediterranean extension and the Africa-Eurasia collision. *Tectonics* 19, 1095–1106.
- Jolivet, L., Faccenna, C., Goffé, B., Burov, E., Agard, P., 2003. Subduction tectonics and exhumation of High-pressure metamorphic rocks in the Mediterranean orogens. *Am. J. Sci.* 303, 353–409. <https://doi.org/10.2475/ajs.303.5.353>
- Jolivet, L., Faccenna, C., Piromallo, C., 2009. From mantle to crust: Stretching the

- Mediterranean. *Earth Planet. Sci. Lett.* 285, 198–209. <https://doi.org/10.1016/j.epsl.2009.06.017>
- Keller, J.V.A., Hall, S.H., Dart, C.J., McClay, K.R., 1995. The geometry and evolution. *J. Geol. Soc. London* 152, 339–351.
- Kharaka, Y.K., Hanor, J.S., 2014. Deep Fluids in Sedimentary Basins, in: *Treatise on Geochemistry*. Elsevier, pp. 471–515. <https://doi.org/10.1016/B978-0-08-095975-7.00516-7>
- Kipfer, R., Aeschbach-Hertig, W., Peeters, F., Stute, M., 2002. Noble gases in lakes and ground waters. *Rev. Mineral. geochemistry* 47, 615–700.
- Kirchner, K.L., Behr, W.M., Loewy, S., Stockli, D.F., 2016. Early Miocene subduction in the western Mediterranean: Constraints from Rb-Sr multimineral isochron geochronology. *Geochemistry Geophys. Geosystems* 17, 1842–1860. <https://doi.org/10.1002/2015GC006208>
- Kohfahl, C., Sprenger, C., Herrera, J.B., Meyer, H., Chacón, F.F., Pekdeger, A., 2008a. Recharge sources and hydrogeochemical evolution of groundwater in semiarid and karstic environments: A field study in the Granada Basin (Southern Spain). *Appl. Geochemistry* 23, 846–862. <https://doi.org/10.1016/j.apgeochem.2007.09.009>
- Kohfahl, C., Rodríguez-Rodríguez, M., Fenk, C., Menz, C., Benavente, J., Hubberten, H., Meyer, H., Paul, L., Knappe, A., López-Geta, J.A., Pekdeger, A., 2008b. Characterising flow regime and interrelation between surface-water and ground-water in the Fuente de Piedra salt lake basin by means of stable isotopes, hydrogeochemical and hydraulic data. *J. Hydrol.* 351, 170–187. <https://doi.org/10.1016/j.jhydrol.2007.12.008>
- Lehmann, B.E., Love, A., Purtschert, R., Collon, P., Loosli, H.H., Kutschera, W., Beyerle, U., Aeschbach-Hertig, W., Kipfer, R., Frapre, S.K., Herczeg, A., Moran, J., Tolstikhin, I.N., Gröning, M., 2003. A comparison of groundwater dating with ^{81}Kr , ^{36}Cl and ^4He in four wells of the Great Artesian Basin, Australia. *Earth Planet. Sci. Lett.* 211, 237–250. [https://doi.org/10.1016/S0012-821X\(03\)00206-1](https://doi.org/10.1016/S0012-821X(03)00206-1)
- Lepiller, M., 2006. Aquifères et eaux souterraines de France, Tom 1, III, 6. Val d'Orléans. BRGM 200–214.
- Lippolt, H.J., Weigel, E., 1988. ^4He diffusion in ^{40}Ar -retentive minerals. *Geochim. Cosmochim. Acta* 52, 1449–1458. [https://doi.org/10.1016/0016-7037\(88\)90215-3](https://doi.org/10.1016/0016-7037(88)90215-3)
- Lix, C., Zuddas, P., Inguaggiato, C., Guichet, X., Benavente, J., Barbier, M., 2018. New insights on Betic Cordillera structure from gas geochemistry. *Geochemistry, Geophys. Geosystems* 1–12. <https://doi.org/10.1029/2018GC007712>
- Lonergan, L., Platt, J.P., Gallagher, L., 1994. The internal-external zone boundary in the eastern Betic Cordillera, SE Spain. *J. Struct. Geol.* 16, 175–188.
- Lonergan, L., White, N., 1997. Origin of the Betic-Rif mountain belt. *Tectonics* 16, 504–522.
- López-Chicano, M., Cerón, J.C., Vallejos, A., Pulido-Bosch, A., 2001a. Geochemistry of thermal springs, Alhama de Granada (southern Spain). *Appl. Geochemistry* 16, 1153–1163. [https://doi.org/10.1016/S0883-2927\(01\)00020-8](https://doi.org/10.1016/S0883-2927(01)00020-8)
- López-Chicano, M., Bouamama, M., Vallejos, A., Pulido-Bosch, A., 2001b. Factors which determine the hydrogeochemical behaviour of karstic springs. A case study from the Betic Cordilleras, Spain. *Appl. Geochemistry* 16, 1179–1192. [https://doi.org/10.1016/S0883-2927\(01\)00012-9](https://doi.org/10.1016/S0883-2927(01)00012-9)

- López-Quirós, A., Barbier, M., Martín, J.M., Guichet, X., 2018. Sedimentology and diagenetic evolution of the Neogene ‘Intermediate Sandstone Unit’ in the halite deposits of the Granada Basin (SE Spain): the turning point in the change from marine to continental sedimentation. *J. Iber. Geol.* 44, 513–537. <https://doi.org/10.1007/s41513-018-0069-z>
- López-Quirós, A., Barbier, M., Martín, J.M., Puga-Bernabéu, Á., Guichet, X., 2016. Diagenetic evolution of Tortonian temperate carbonates close to evaporites in the Granada Basin (SE Spain). *Sediment. Geol.* 335, 180–196. <https://doi.org/10.1016/j.sedgeo.2016.02.011>
- Mancilla, F. d. L., Stich, D., Berrocoso, M., Martin, R., Morales, J., Fernandez-Ros, A., Paez, R., Perez-Pena, A., 2013. Delamination in the Betic Range: Deep structure, seismicity, and GPS motion. *Geology* 41, 307–310. <https://doi.org/10.1130/G33733.1>
- Mancilla, F. de L., Booth-Rea, G., Stich, D., Pérez-Peña, J.V., Morales, J., Azañón, J.M., Martin, R., Giaconia, F., 2015. Slab rupture and delamination under the Betics and Rif constrained from receiver functions. *Tectonophysics* 663, 225–237. <https://doi.org/10.1016/j.tecto.2015.06.028>
- Mancilla, F. de L., Heit, B., Morales, J., Yuan, X., Stich, D., Molina-Aguilera, A., Azañón, J.M., Martin, R., 2018. A STEP fault in Central Betics, associated with lateral lithospheric tearing at the northern edge of the Gibraltar arc subduction system. *Earth Planet. Sci. Lett.* 486, 32–40. <https://doi.org/10.1016/j.epsl.2018.01.008>
- Marini, L., Chiodini, G., Cioni, R., 1986. New geothermometers for carbonate-evaporite geothermal reservoirs. *Geothermics* 15, 77–86. [https://doi.org/10.1016/0375-6505\(86\)90030-1](https://doi.org/10.1016/0375-6505(86)90030-1)
- Martelli, M., Bianchini, G., Beccaluva, L., Rizzo, A., 2011. Helium and argon isotopic compositions of mantle xenoliths from Tallante and Calatrava, Spain. *J. Volcanol. Geotherm. Res.* 200, 18–26. <https://doi.org/10.1016/j.jvolgeores.2010.11.015>
- Martín-Algarra, A., Martín-Martín, M., Andreo, B., Julià, R., González-Gómez, C., 2003. Sedimentary patterns in perched spring travertines near Granada (Spain) as indicators of the paleohydrological and paleoclimatological evolution of a karst massif. *Sediment. Geol.* 161, 217–228. [https://doi.org/10.1016/S0037-0738\(03\)00115-5](https://doi.org/10.1016/S0037-0738(03)00115-5)
- Martín, J.M., Bernabéu, Á.P., Rodríguez, J.A., Alarcón, Juan Carlos Braga, 2014. Miocene Atlantic-Mediterranean seaways in the Betic Cordillera (Southern Spain). *Rev. la Soc. Geológica España* 27, 175–186.
- Martín, J.M., Braga, J.C., 1987. Alpujárride carbonate deposits (southern Spain) - Marine Sedimentation in a Triassic Atlantic. *Palaeogeogr. Palaeoclimatol. Palaeoecol.* 59, 243–260.
- Martín, J.M., Ortega-Huertas, M., Torres-Ruiz, J., 1984. Genesis and evolution of strontium deposits of the Granada Basin (southeastern Spain): Evidence of diagenetic replacement of a stromatolite belt. *Sediment. Geol.* 39, 281–298.
- Martin Suarez, E., Freudenthal, M., Agusti, J., 1993. Micromammals from the Middle Miocene of the Granada Basin (Spain). *Geobios* 26, 377–387. [https://doi.org/10.1016/S0016-6995\(93\)80028-P](https://doi.org/10.1016/S0016-6995(93)80028-P)
- Martínez-Martínez, J.M., Azañón, J.M., 1997. Mode of extensional tectonics in the southeastern Betics SE Spain Implications for the tectonic evolution of the periAlborn orogenic system. *Tectonics* 16, 205–225.
- Martínez-Martínez, J.M., Booth-Rea, G., Azañón, J.M., Torcal, F., 2006. Active transfer fault zone linking a segmented extensional system (Betics, southern Spain): Insight into

- heterogeneous extension driven by edge delamination. *Tectonophysics* 422, 159–173. <https://doi.org/10.1016/j.tecto.2006.06.001>
- Marty, B., Onions, R.K., Oxburgh, E.R., Martel, D., Lombardi, S., 1992. Helium isotopes in Alpine Regions. *Tectonophysics* 206, 71–78. [https://doi.org/10.1016/0040-1951\(92\)90368-G](https://doi.org/10.1016/0040-1951(92)90368-G)
- Mateos, R.M., Ezquerro, P., Luque-Espinar, J.A., Béjar-Pizarro, M., Notti, D., Azañón, J.M., Montserrat, O., Herrera, G., Fernández-Chacón, F., Peinado, T., Galve, J.P., Pérez-Peña, V., Fernández-Merodo, J.A., Jiménez, J., 2017. Multiband PSInSAR and long-period monitoring of land subsidence in a strategic detrital aquifer (Vega de Granada, SE Spain): An approach to support management decisions. *J. Hydrol.* 553, 71–87. <https://doi.org/10.1016/j.jhydrol.2017.07.056>
- Michard, G., 1990. Behaviour of major elements and some trace elements (Li, Rb, Cs, Sr, Fe, Mn, W, F) in deep hot waters from granitic areas. *Chem. Geol.* 89, 117–134. [https://doi.org/10.1016/0009-2541\(90\)90062-C](https://doi.org/10.1016/0009-2541(90)90062-C)
- Michard, G., 1979. Géothermomètres chimiques. *Bull. BRGM* 2, 183–189.
- Monié, P., Galindo-Zaldívar, J., Lodeir, F.G., Goffé, B., Jalaboy, A., 1991. $^{40}\text{Ar}/^{39}\text{Ar}$ geochronology of Alpine tectonism in the Betic Cordilleras (southern Spain). *J. Geol. Soc. London.* 148, 289–297. <https://doi.org/10.1144/gsjgs.148.2.0289>
- Morales, J., Serrano, I., Vidal, F., Torcal, F., 1997. The depth of the earthquake activity in the Central Betics (Southern Spain). *Geophys. Res. Lett.* 24, 3289–3292.
- Morales, J., Vidal, F., de Miguel, F., Alguacil, G., Am Posadas, Ibáñez, J.M., Guzmán, A., Guirao, J.M., 1990. Basement structure of the Granada basin, Betic Cordilleras, southern Spain. *Tectonophysics* 177, 337–348.
- Oelkers, E.H., Helgeson, H.C., 1988. Calculation of the thermodynamic and transport properties of aqueous species at high pressures and temperatures: Aqueous tracer diffusion coefficients of ions to 1000°C and 5 kb. *Geochim. Cosmochim. Acta* 52, 63–85. [https://doi.org/10.1016/0016-7037\(88\)90057-9](https://doi.org/10.1016/0016-7037(88)90057-9)
- Ozima, M., Podosek, F.A., 2002. Noble gas geochemistry (2nd Edition). Cambridge University Press. <https://doi.org/10.1017/CBO9781107415324.004>
- Palomeras, I., Villaseñor, A., Thurner, S., Levander, A., Gallart, J., Harnafi, M., 2017. Lithospheric structure of Iberia and Morocco using finite-frequency Rayleigh wave tomography from earthquakes and seismic ambient noise. *Geochemistry, Geophys. Geosystems* 18, 1824–1840. <https://doi.org/10.1002/2016GC006679>. Received
- Parkhurst, D.L., Appelo, C.A.J., others, 2013. Description of input and examples for PHREEQC version 3 - a computer program for speciation, batch-reaction, one-dimensional transport, and inverse geochemical calculations. *US Geol. Surv. Tech. methods*, B. 6, 497. [https://doi.org/10.1016/0029-6554\(94\)90020-5](https://doi.org/10.1016/0029-6554(94)90020-5)
- Pérez-Peña, J.V., Azañón, J.M., Azor, A., Sánchez-Almazo, I.M., Tuccimei, P., Della Seta, M., Soligo, M., 2012. Reply to comment by J.L. Díaz-Hernández and R. Julià on “Quaternary landscape evolution and erosion rates for an intramontane Neogene basin (Guadix-Baza basin, SE Spain).” *Geomorphology* 171–172, 204–209. <https://doi.org/10.1016/j.geomorph.2012.05.019>
- Pérez-Peña, J.V., Azor, A., Azañón, J.M., Keller, E.A., 2010. Active tectonics in the Sierra Nevada (Betic Cordillera, SE Spain): Insights from geomorphic indexes and drainage pattern analysis. *Geomorphology* 119, 74–87.

- <https://doi.org/10.1016/j.geomorph.2010.02.020>
- Pérez-Peña, J. V., Azañón, J.M., Azor, A., Booth-Rea, G., Galve, J.P., Roldán, F.J., Mancilla, F., Giaconia, F., Morales, J., Al-Awabdeh, M., 2015. Quaternary landscape evolution driven by slab-pull mechanisms in the Granada Basin (Central Betics). *Tectonophysics* 663, 5–18. <https://doi.org/10.1016/j.tecto.2015.07.035>
- Pérez del Villar, L., 2009. Almacenamiento geológico de CO₂: Análogos del almacenamiento y escape. Fundamentos, ejemplos y aplicaciones para la predicción de riesgos y la evaluación del comportamiento a largo plazo. Congr. Nac. del Medio Ambient.
- Pérez, N.M., Nakai, S., Wakita, H., Albert Bertrán, J.F., Redondo, R., 1996. Preliminary results on 3He/4He isotopic ratios in terrestrial fluids from Iberian peninsula: seismotectonic and neotectonic implications. *Geogaceta*.
- Platt, J.P., Behr, W.M., Johanesen, K., Williams, J.R., 2013. The Betic-Rif Arc and Its Orogenic Hinterland: A Review. *Annu. Rev. Earth Planet. Sci.* 41, 313–357. <https://doi.org/10.1146/annurev-earth-050212-123951>
- Platt, J.P., Vissers, R.L.M., 1989. Extensional collapse of thickened continental lithosphere: a working hypothesis for the Alboran Sea and Gibraltar Arc. *Geology* 17, 540–543. [https://doi.org/10.1130/0091-7613\(1989\)017<0540:ECOTCL>2.3.CO;2](https://doi.org/10.1130/0091-7613(1989)017<0540:ECOTCL>2.3.CO;2)
- Prado-Pérez, A.J., Pérez del Villar, L., 2011. Dedolomitization as an analogue process for assessing the long-term behaviour of a CO₂ deep geological storage: The Alicún de las Torres thermal system (Betic Cordillera, Spain). *Chem. Geol.* 289, 98–113. <https://doi.org/10.1016/j.chemgeo.2011.07.017>
- Rey, A., Etiope, G., Belelli-Marchesini, L., Papale, D., Valentini, R., 2012. Geologic carbon sources may confound ecosystem carbon balance estimates: Evidence from a semiarid steppe in the southeast of Spain. *J. Geophys. Res. Biogeosciences* 117, 1–10. <https://doi.org/10.1029/2012JG001991>
- Rizzo, A.L., Caracausi, A., Chavagnac, V., Nomikou, P., Polymenakou, P.N., Mandalakis, M., Kotoulas, G., Magoulas, A., Castillo, A., Lampridou, D., 2016. Kolumbo submarine volcano (Greece): An active window into the Aegean subduction system. *Sci. Rep.* 6, 1–9. <https://doi.org/10.1038/srep28013>
- Rodríguez-Fernández, J., Sanz de Galdeano, C., 2006a. Late orogenic intramontane basin development: the Granada basin, Betics (southern Spain). *Basin Res.* 18, 85–102. <https://doi.org/10.1111/j.1365-2117.2006.00284.x>
- Rodríguez-Fernández, J., Sanz de Galdeano, C., 2006b. Late orogenic intramontane basin development: the Granada basin, Betics (southern Spain). *Basin Res.* 18, 85–102. <https://doi.org/10.1111/j.1365-2117.2006.00284.x>
- Rosell, O., Martí, A., Marcuello, À., Ledo, J., Queralt, P., Roca, E., Campanyà, J., 2011. Deep electrical resistivity structure of the northern Gibraltar Arc (western Mediterranean): evidence of lithospheric slab break-off. *Terra Nov.* 23, 179–186. <https://doi.org/10.1111/j.1365-3121.2011.00996.x>
- Rosenbaum, G., Lister, G.S., Duboz, C., 2002. Reconstruction of the tectonic evolution of the western Mediterranean since the Oligocene. *J. Virtual Explor.* 8. <https://doi.org/10.3809/jvirtex.2002.00053>
- Rosino, J.M., 2015. Inventario y caracterización de las aguas carbogaseosas españolas., in: Congreso Internacional Del Agua – Termalismo y Calidad de Vida. Campus Da Auga, Ourense, Spain.

- Rosino, J.M., 2008. Modelo hidrogeológico conceptual de las aguas termo-minerales de la Depresión de Granada. En: J. A. López-Geta et al. (Editores), Agua y Cultura., in: IGME (Ed.), VII Simposio Sobre El Agua En Andalucía (SIAGA).
- Rouchy, J.M., Pierre, C., 1979. Données sédimentologiques et isotopiques sur les gypses des séries évaporitiques messiniennes d'Espagne méridionale et de Chypre. *Rev. Géogr. Phys. Géol. Dyn* 21, 267–280.
- Royden, L.H., 1993. Evolution of retreating subduction boundaries formed during continental collision. *Tectonics* 12, 629–638.
- Rudnick, R.L., Fountain, D.M., 1995. Nature and composition of the continental crust: a lower crustal perspective. *Rev. Geophys.* 33, 267–309. <https://doi.org/10.1029/95rg01302>
- Sánchez-Gómez, M., Balanyá, J.C., García-Dueñas, V., Azañón, J.M., 2002. Intracrustal tectonic evolution of large lithosphere mantle slabs in the western end of the Mediterranean orogen (Gibraltar arc). *J. Virtual Explor.* 8, 23–34.
- Sánchez-Martos, F., Pulido-Bosch, A., Molina-Sánchez, L., Vallejos-Izquierdo, A., 2002. Identification of the origin of salinization in groundwater using minor ions (Lower Andarax, Southeast Spain). *Sci. Total Environ.* 297, 43–58. [https://doi.org/10.1016/S0048-9697\(01\)01011-7](https://doi.org/10.1016/S0048-9697(01)01011-7)
- Sánchez Guzmán, J., García de la Noceda, C., 2010. The Evolution of Geothermal Energy in Spain - Country Update (2005-2009), in: *Proceedings World Geothermal Congress*.
- Sano, Y., Marty, B., 1995. Origin of carbon in fumarolic gas from island arcs. *Chem. Geol. (Isotope Geosci. Sect.* 119, 265–274. [https://doi.org/10.1016/0009-2541\(94\)00097-R](https://doi.org/10.1016/0009-2541(94)00097-R)
- Sano, Y., Wakita, H., 1985. Geographical distribution of $^3\text{He}/^4\text{He}$ ratios in Japan: Implications for arc tectonics and incipient magmatism. *J. Geophys. Res.* 90, 8729–8741. <https://doi.org/10.1029/JB090iB10p08729>
- Sanz de Galdeano, C., 2008. The Cadiz-Alicante fault: an important discontinuity in the Betic Cordillera. *Rev. la Soc. Geológica España* 21.
- Sanz de Galdeano, C., 1990. Geologic evolution of the Betic Cordilleras in the Western Mediterranean, Miocene to the present. *Tectonophysics* 172, 107–119. [https://doi.org/10.1016/0040-1951\(90\)90062-D](https://doi.org/10.1016/0040-1951(90)90062-D)
- Sanz de Galdeano, C., 1983. Los accidentes y fracturas principales de las Cordilleras Béticas. *Estud. Geológicos* 39, 157.
- Sanz de Galdeano, C., Alfaro, P., 2004. Tectonic significance of the present relief of the Betic Cordillera. *Geomorphology* 63, 175–190. <https://doi.org/10.1016/j.geomorph.2004.04.002>
- Sanz de Galdeano, C., Peláez, J.A., 2011. Fallas activas en la Cordillera Bética: una aproximación a partir de la información tectónica y sísmica. Editorial Universidad de Granada.
- Sanz de Galdeano, C., Peláez, J.A., 2011. Fallas activas en la Cordillera Bética: una aproximación a partir de la información tectónica y sísmica.
- Sanz de Galdeano, C., Peláez Montilla, J.A., López Casado, C., 2003. Seismic potential of the main active faults in the Granada Basin (southern Spain). *Pure Appl. Geophys.* 160, 1537–1556.
- Sanz de Galdeano, C., Vera, J.A., 1992. Stratigraphic record and palaeogeographical context of

- the Neogene basins in the Betic Cordillera, Spain. *Basin Res.* 4, 21–36. <https://doi.org/10.1111/j.1365-2117.1992.tb00040.x>
- Sonney, R., 2010. Groundwater flow, heat and mass transport in geothermal systems of a Central Alpine Massif. The cases of Lavey-les-Bains, Saint-Gervais-les-Bains and Val d'Illeiez. Université de Neuchâtel.
- Soria, J.M., Esteyez, A., Rodriguez-Perez, M., 1993. Materiales afines al Complejo del Campo de Gibraltar en el sector oeste del Mencal (Subbetico medio, tercio central de la Cordillera Betica). *Rev. Soc. Geol. Espana* 6, 3–4.
- Spakman, W., Wortel, R., 2004. A tomographic view on western Mediterranean geodynamics. *TRANSMED Atlas-The Mediterr. Reg. from Crust to Mantle* 31–52. https://doi.org/10.1007/978-3-642-18919-7_2
- Sprenger, C., 2006. Groundwater Study for the Regional Granada Aquifer System (southern Spain): Hydrochemistry and Isotope Study. Freie Universität Berlin (FUB).
- Steiger, R.H., Jäger, E., 1977. Subcomission on geochronology: Convention on the use of decay constants in geo- and cosmochemistry. *Earth Planet. Sci. Lett.* 36, 359–362. [https://doi.org/10.1016/0012-821x\(77\)90060-7](https://doi.org/10.1016/0012-821x(77)90060-7)
- Turner, S., Palomeras, I., Levander, A., Carbonell, R., Lee, C.T., 2014. Ongoing lithospheric removal in the western Mediterranean: Evidence from Ps receiver functions and thermobarometry of Neogene basalts (PICASSO project). *Geochemistry, Geophys. Geosystems* 15, 1113–1127. <https://doi.org/10.1002/2013GC005124>
- Tole, M.P., Ármannsson, H., Zhong-He, P., Arnórsson, S., 1993. Fluid/mineral equilibrium calculations for geothermal fluids and chemical geothermometry. *Geothermics* 22, 17–37.
- Tolstikhin, I., Lehmann, B.E., Loosli, H.H., Gautschi, A., 1996. Helium and argon isotopes in rocks, minerals, and related ground waters: A case study in northern Switzerland. *Geochim. Cosmochim. Acta* 60, 1497–1514. [https://doi.org/10.1016/0016-7037\(96\)00036-1](https://doi.org/10.1016/0016-7037(96)00036-1)
- Tolstikhin, I., Waber, H.N., Kamensky, I., Loosli, H.H., Skiba, V., Gannibal, M., 2011. Production, redistribution and loss of helium and argon isotopes in a thick sedimentary aquitard-aquifer system (Molasse Basin, Switzerland). *Chem. Geol.* 286, 48–58. <https://doi.org/10.1016/j.chemgeo.2011.04.017>
- Tolstikhin, I.N., Lehmann, B.E., Loosli, H.H., Kamensky, I.L., Nivin, V.A., Orlov, S.P., Ploschansky, L.M., Tokarev, I.V., Gannibal, M.A., 1999. Radiogenic helium isotope fractionation: the role of tritium as ^3He precursor in geochemical applications. *Geochim. Cosmochim. Acta* 63, 1605–1611. [https://doi.org/10.1016/S0016-7037\(99\)00105-2](https://doi.org/10.1016/S0016-7037(99)00105-2)
- Tubía, J.M., Cuevas, J., Navarro-Vilá, F., Alvarez, F., Aldaya, F., 1992. Tectonic evolution of the Alpujárride Complex (Betic Cordillera, southern Spain). *J. Struct. Geol.* 14, 193–203. [https://doi.org/10.1016/0191-8141\(92\)90056-3](https://doi.org/10.1016/0191-8141(92)90056-3)
- Vandenschrick, G., van Wesemael, B., Frot, E., Pulido-Bosch, A., Molina, L., Stiévenard, M., Souchez, R., 2002. Using stable isotope analysis (δD – $\delta^{18}\text{O}$) to characterise the regional hydrology of the Sierra de Gador, south east Spain. *J. Hydrol.* 265, 43–55. [https://doi.org/10.1016/S0022-1694\(02\)00097-5](https://doi.org/10.1016/S0022-1694(02)00097-5)
- Vera, J.A., 2001. Evolution of the South Iberian continental margin. *Mémoires du Muséum Natl. d'histoire Nat.* 186, 109–143.
- Vera, J.A., 1988. Evolución de los sistemas de depósito en el margen ibérico de la Cordillera

- Bética. *Rev. la Soc. Geológica España* 1, 373–391.
- Vera, J.A., Martín-Algarra, A., 2004. Cordillera bética, in: Vera, J.A. (Ed.), *Geología de España*. IGME-Sociedad Geológica de España, pp. 345–464.
- Vergés, J., Fernàndez, M., 2012. Tethys – Atlantic interaction along the Iberia – Africa plate boundary: The Betic – Rif orogenic system. *Tectonophysics* 579, 144–172. <https://doi.org/10.1016/j.tecto.2012.08.032>
- Verma, M.P., 2000. Chemical thermodynamics of silica: A critique on its geothermometer. *Geothermics* 29, 323–346. [https://doi.org/10.1016/S0375-6505\(99\)00064-4](https://doi.org/10.1016/S0375-6505(99)00064-4)
- Weiss, R.F., 1971. Solubility of helium and neon in water and seawater. *J. Chem. Eng. Data* 16, 235–241. <https://doi.org/10.1021/je60049a019>

APPENDIX

APPENDIX

This table gives the geographical coordinates of the sampling points for gas analyses (Chapter 3) and is included in supplementary material of the article. The major gas compositions are plotted in Figure 3-3 (Section 3.2.5.1).

Sampling points ^a	Code	Latitude	Longitude	Gas type ^b	O ₂	N ₂	CO ₂
Baños Santa Fe (W)	SF	37°09.3813'N	3°45.2023'W	D	1.81	17.04	9.51
Sierra Elvira (S)	SE	37°13.7033'N	3°43.3372'W	D	0.13	18.29	22.22
Vivero Arco (W)	VA	37°14.0990'N	3°43.9615'W	D	4.23	18.65	45.60
Baños Alicun de las Torres (S)	AT	37°30.5418'N	3°06.4172'W	D	0.44	16.74	27.02
Baños Alhama de Granada (S)	BAG	37°01.1221'N	3°58.9970'W	D	0.67	17.59	10.71
Baños Salado de Lanjaron (S)	BSL	36°55.4189'N	3°29.5869'W	D	0.07	1.74	575.79
Baños de Zujar (W)	BZ	37°34.556'N	2°49.463'W	D	0.62	13.76	16.27
Salinas Malaha (S)	SM	37°06.1982'N	3°43.3276'W	D	0.09	4.97	13.73
Baños Alhamilla (S)	BAA	36°57.6531'N	2°23.7875'W	D B	1.49 11.81	12.14 81.64	39.43 4.13E-04
Baños Urquizar Grande (S)	BUG	36°58.2261'N	3°34.5854'W	D B	1.57 10.82	18.60 87.20	16.16 8.40E-05
Capuchina Lanjaron (S)	CL	36°55.1523'N	3°29.4182'W	D B	0.08 5.53	1.94 20.11	597.48 7.30E-03
Frontil (S)	FR	37°10.6411'N	4°07.9549'W	B	17.77	80.15	3.90E-05

Table A-1. Table of the geographical coordinates of the waters sampling sites and major gas compositions. ^a Sample collected in: Spring (S) and Well (W); ^b B: bubbling gas, D: dissolved gas. Major gas concentrations are expressed in cm³ (STP)/L_{water} for dissolved gases and in % vol. for bubbling gases.

LIST OF FIGURES

Introduction

Figure I-1: Schematic representation of a sedimentary basin and the fluid circulations.....7

Chapter 1

Figure 1-1: Tectonic map of the Mediterranean modified after Jolivet et al., 2009 and Do Couto, 2014 showing the position of the thrust fronts and subduction zones and the nature of crust. 11

Figure 1-2: Models of the four upper mantle processes beneath the Alboran Domain invoked to explain geodynamics (Platt et al., 2013). (a) Delamination (e.g., Calvert et al. 2000), (b) slab break-off (e.g., Blanco and Spackman, 1993), (c) convective removal of the lithosphere (Platt and Vissers, 1989), (d) slab rollback (Lonergan and White, 1997; Royden, 1993)..... 12

Figure 1-3: EW- and NS-interpreted cross-sections across the Betic Cordillera from Mancilla et al. (2015), localized in Figure 3.4. The topography is displayed at the top of the profiles. 13

Figure 1-4: Moho depths of the Iberian and Maghrebian subducted continental slabs. The continuous red line marks the interpretation of the edge of the south Iberian Moho imaged by the P-receiver functions and the dashed red line the extrapolation of the torn slab edge toward the east (modified from Mancilla et al. (2015)). The two green solid lines correspond to the cross-sections presented in Figure 1-5. 14

Figure 1-5: Map of the Betics showing the locations of the magnetotelluric sites (black dots) and the cross-sections. AA' side view cross section of the 3D resistivity model, from Rosell et al. (2011). 15

Figure 1-6: Geological sketch map of the Gibraltar Arc in the western Mediterranean, modified after Dyja (2014), Sánchez-Gómez et al. (2002), and Comas et al. (1999) 16

Figure 1-7: Structural map of the Betics modified from Sanz de Galdeano et al. (2003). Red line: Cadix-Alicante fault; blue line: transfert fault; green line: Palomeras Fault Zone; and yellow line: Carboneras fault. 19

Figure 1-8: Map of the network of active faults in the Granada Basin modified after Sanz de Galdeano and Peláez (2011). Colors indicate the calculated velocity of the displacement. 20

Figure 1-9: Simplified map of the Granada Basin (Modified from Martín et al. (1984) and Dabrio et al. (1982)). The Unit I, II, III and IV are described in section 1.2.2. 21

Figure 1-10: Stratigraphy of the Granada Basin (Modified from Braga et al. (1990)). 23

Figure 1-11: Presumed distribution map of the Tortonian and Messinian evaporites in the Granada Basin defined after Dabrio et al. (1982) and García-Veigas et al. (2013). 25

Figure 1-12: Map of the aquifers of the Granada Basin modified after Campos (2006). 28

Figure 1-13: Current drainage of the Granada Basin from García-Alix et al. (2009). 29

Chapter 2

Figure 2-1: Map of the 1749 springs in the Granada Basin and its surrounding. The background geological map has been modified after Sanz de Galdeano and Peláez, (2011). 34

Figure 2-2: Algorithm scheme of the developed numerical program.....	35.
--	-----

Chapter 3

Figure 3-1: (a) Structural map of the Betic Cordillera (Spain) including the main lithological units and structures. Bold red lines shows the location of the cross-sections presented in Figure 3-2 and discussed in text. Structural map modified after Augier (2004). Inset indicates the main tectonic domains of the peri-Alboran orogenic system modified after Janowski et al. (2016). (b) Detailed structural map of the Central Betic Cordillera, modified after Sanz de Galdeano and Peláez (2011), showing the main tectonic domains and faults. SN and SA are Sierra Nevada and Sierra Alhamilla massifs respectively. Sampling points are: (1) Baños Salado de Lanjaron, (2) Capuchina de Lanjaron, (3) Baños Alhamilla, (4) Baños Zujar, (5) Baños Alicun de las Torres, (6) Frontil, (7) Sierra Elvira, (8) Vivero Arco, (9) Baños Santa Fe, (10) Salinas la Malaha, (11) Baños Urquizar Grande and (12) Baños Alhama de Granada.	49
Figure 3-2: (a) Original W-E cross-section showing the lithospheric structure of the Betic Cordillera. Five sampling points have been projected on the topographic section. Moho profile was constrained using Diaz et al. (2016)'s data from deep seismic sounding experiments and receiver functions studies. (b) NNW-SSE cross-section of the Betic Cordillera modified from Crespo-Blanc and Frizon de Lamotte (2006). Two sampling points have been projected on the topographic section.	50
Figure 3-3: Triangular plot of the relative pressure of CO ₂ , N ₂ , and O ₂ . The air value is also reported for comparison; the green dotted line represents the theoretical mixing between air dominated system and CO ₂ -rich fluid.	54
Figure 3-4: ³ He/ ⁴ He (R/R _A) values vs. ⁴ He/ ²⁰ Ne ratios diagram. <i>The uncertainties (1σ) are within the size of the symbols.</i>	57
Figure 3-5: Comparison of ⁴ He and ³ He concentrations in water between measured and calculated values for groundwater residence time of 10 ³ , 10 ⁴ and 10 ⁵ years. He concentrations in water from crustal production are calculated with the hypothesis of 3 % porosity.	62
Figure 3-6: Geodynamic evolution of the Betic Cordillera since the last 20 Ma. NFC: Nevado-Filábride Complex; AC: Alpujárride Complex; MC: Maláguide Complex. Insets represents the pressure-temperature exhumation paths for the Alpujárride Complex in green (Azañón and Crespo-Blanc, 2000) and for the Nevado-Filábride Complex in red (Augier et al., 2005; Gómez-Pugnaire and Fernández-Soler, 1987). Green and red symbols correspond to the pressure-temperature conditions of the metamorphic complexes during their exhumation path	64
Figure 3-7: Crustal He isotopic production (lines) and measured He isotopic abundance in our water samples (circles). The crustal helium isotopic production is represented for different rocks (shale, granite, sandstone).	65
Figure 3-8: Structural map of the Central Betic Cordillera, modified after Sanz de Galdeano and Peláez (2011), showing the main tectonic domains, faults, and the location of the dissolved gas samples collected in four springs during the 2018 survey. SN and SA are Sierra Nevada and Sierra Alhamilla massifs respectively.	66
Figure 3-10: Triangular plot of the relative pressure of CO ₂ , N ₂ , and O ₂ . The air value is also reported for comparison; the green dotted line represents the theoretical mixing between air dominated system and CO ₂ -rich fluid.	67
Figure 3-11: ³ He/ ⁴ He (R/R _A) values vs. ⁴ He/ ²⁰ Ne ratios diagram. The circles and triangle symbols correspond to dissolved and bubbling gas samples respectively and the blue and red	

colors designate samples from the 2016 and 2018 surveys respectively. The uncertainties (1σ) are within the size of the symbols. 69

Chapter 4

Figure 4-1: Location of the thermal water samples in the Central Betic Cordillera and geological map of the area modified after Sanz de Galdeano and Peláez (2011). 79

Figure 4-2: Piper diagram of the thermal waters from Central Betic Cordillera. Circles and triangles correspond to springs and wells respectively. 87

Figure 4-3: Evolution of the mineral saturation indices with temperature for the thermal waters located in the evaporitic Granada Basin by geothermometrical modeling. 95

Figure 4-4: Evolution of the mineral saturation indices with temperature for the thermal waters located (a) in the graben in the Alpujárride Complex and (b) on the contacts of the metamorphic complexes. 96

Figure 4-5: Relationship between $p\text{CO}_2$ (atm) and temperature ($^{\circ}\text{C}$), for the outlet (crosses) and reservoir (circles) conditions considering dolomite equilibrium in depth. 97

Figure 4-6: Relationship between $p\text{CO}_2$ (atm) and temperature ($^{\circ}\text{C}$) for the outlet (crosses) and reservoir (circles) conditions considering equilibrium with calcite, dolomite, quartz, kaolinite, and Mg-chlorite in depth. 98

Figure 4-7: Relationship between the variations of $p\text{CO}_2$ calculated between steps 1 and 3 of the hydrogeochemical modeling, $\Delta p\text{CO}_2$, expressed in atm, and the reservoir temperature. The light gray squares correspond to equilibrium with dolomite and the dark gray squares with calcite, dolomite, quartz, kaolinite, and Mg-chlorite, both in the reservoir conditions. The variability in $\Delta p\text{CO}_2$ is expressed for the three groups of waters with average reservoir temperature of: 55°C (blue), 85°C (yellow), and 135°C (red). 99

Figure 4-8: Evolution of the mineral saturation indices with temperature for the thermal waters located in the evaporitic Granada Basin by geothermometrical modeling with theoretical CO_2 addition (1 mmol/L) to compensate possible CO_2 outgassing during the ascent of the waters. 101

Figure 4-9: Evolution of the mineral saturation indices with temperature for the thermal waters located in the Valle de Lecrin graben by geothermometrical modeling with theoretical CO_2 addition (0.5 mmol/L) to compensate possible CO_2 outgassing during the ascent of the waters. 102

Figure 4-10: Evolution of the mineral saturation indices with temperature for the thermal waters located on the contacts of the metamorphic complexes. Geothermometrical modeling with theoretical CO_2 addition to compensate possible CO_2 outgassing during the ascent of the waters. 103

Figure 4-11: Co-variation of $\delta^{13}\text{C}_{(\text{TDIC})}$ and CO_2 partial pressure (atm). 110

Figure 4-12: Schematic diagram of the Phreeqc simulations to estimate hydrochemistry at the temperature and pressure reservoir conditions and the variations of $p\text{CO}_2$ between the depth and the surface. 111

Chapter 5

- Figure 5-1: (a) Geological map of the Granada Basin with locations of the sampling points. modified after Galindo-Zalvidar et al. (2015) (b) S-N cross-section of the Granada Basin, modified after Rosino (2008). 120
- Figure 5-2: Piper diagram of the water samples with a color scale representing the logarithm of the electrical conductivity (mS/cm). The chemical evolution can be divided into two steps: (1) evolution from carbonate- to sulfate-dominated waters (dashed arrow), (2) evolution from sulfate- to chloride-dominated waters (solid arrows). 126
- Figure 5-3: Map representing the electrical conductivity of the water samples. The colors correspond to the color scale of the logarithm of the electrical conductivity used in Figure 5-2. The background geological map was modified after Galindo-Zaldivar et al. (2015) 127
- Figure 5-4: Activity diagrams for the systems (a) H_4SiO_4 , Al^{3+} , K^+ , H_2O and (b) H_4SiO_4 , Al^{3+} , Na^+ , H_2O . The limits of the mineral stability field are for $P = 1$ bar and T between 10 and 50°C . The blue dotted lines represents the saturation in quartz and amorphous silica. The chemical evolution can be divided as the following: (1) evolution within the kaolinite stability field (dashed pink arrow), (2a) K controlled by kaolinite, pyrophyllite, and microcline at the triple-point (pink circle) whereas (2b) evolution at the limit between the stability field of kaolinite and pyrophyllite for Na (pink solid arrows). 128
- Figure 5-5: Activity diagrams for the system H_4SiO_4 , Al^{3+} , Ca^{2+} , H_2O . The limits of the mineral stability field are for $P = 1$ bar and T between 10 and 50°C . (a) Calcite saturation and (b) dolomite saturation are represented by the pink dotted line. The blue dotted lines represents the saturation in quartz and amorphous silica. 129
- Figure 5-6: Interpolated map of the saturation index of (a) barite, (b) celestite, and (c) gypsum. Interpolation was performed using the Inverse Distance Weighted (IDW) method. 132
- Figure 5-7: Summary of the reactivity of the groundwaters and possible flow paths (dark blue arrows) in the Granada Basin along a S-N cross-section. 137
- Figure 5-8: Location map of the Salinas Fuente de Camacho (SFC) and Manantial del Nacimiento de Arbuniel (MNA) springs (modified after Sanz de Galdeano and Peláez (2011)) 139
- Figure 5-9: Geological map of the Salinas Fuente de Camacho spring area (Gil-Márquez et al., 2016). The cross-section A-A' is presented in Figure 5-10. 140
- Figure 5-10: Cross-section of the Salinas - Los Hoyos diapiric structure (Gil-Márquez et al., 2016). 141
- Figure 5-11: Photography of the salt mineralization at the emergence of the SFC spring. ... 141
- Figure 5-12: Zoomed photography of the salt coatings at the emergence of the SFC spring. 142
- Figure 5-13: Geological map of the MNA spring, modified after the geological map of Valdepeñas de Jaén, scale 1:50 000 from IGME (Díaz de Neira et al., 1992). 142
- Figure 5-14: Representation of the SFC and MNA hydrochemistry on a Piper diagram 145
- Figure 5-15: Molar Cl/Br ratios vs. Cl concentrations in samples located in the Central Betic Cordillera including: groundwater samples, local rainwater sample from the Sierra Nevada (Alcalá and Custodio, 2008), recharge waters (Alcalá and Custodio, 2008; Sánchez-Martos et al., 2002), and brine samples from fluid inclusion in veins of quartz in the Sierra Nevada (Dyja-Person et al., 2018). The seawater evaporation trend, up to sylvite, is indicated (Fontes and Matray, 1993): SW: Seawater, G: Gypsum, H: Halite, E: Epsomite, S: Sylvite, 147

Figure 5-16: Photography of the mineralizations formed in the well "Sondeo Venta de la Nueva".....	148
--	-----

Synthesis and conclusions

Figure C-1: Geological map of the investigated area including the location of the sampling points, the orientation of the two schematic cross-sections presented in Figure C-2 and C-3, and the recharge areas of the Granada Basin.....	153
--	-----

Figure C-2: Schematic N-S cross-section of the Granada Basin, modified after Rosino (2008) showing the groundwater characteristics and possible groundwater circulations. Thermal springs and wells are indicated in red.....	154
---	-----

Figure C-3: Schematic W-E cross-section of the southern border of the Granada Basin and through the Sierra Nevada, showing the groundwater chemical characteristics, the He isotopic ratio, and the potential groundwater circulations. Thermal springs are indicated in red.....	155
---	-----

LIST OF TABLES

Chapter 3

Table 3-1: Physical and chemical parameters of the waters sampling sites and helium isotopic composition of dissolved and bubbling gases	55
Table 3-2: Physical and chemical parameters of the waters sampling sites and helium isotopic composition of dissolved gases, which were sampled during the second sampling survey in June 2018.	68

Chapter 4

Table 4-1: Sample details including sample location and water chemistry. Location of sampling points refer to WGS84 system. Type of water points: S = spring; W = well. Conductivity is in mS/cm. Concentrations of dissolved elements and TDS are expressed in mmol/kg of solution and in mg/L respectively. b.d.l = below detection limit.	89
Table 4-2: Saturation indices (SI) of the main mineral phases of interest in the investigated area. CO ₂ (g) corresponds to the log ₁₀ of CO ₂ partial pressure (in atm). SI were calculated with the PHREEQC code at the outlet temperature (measured in the field).	90
Table 4-3: Dissolved gases and carbon isotopic composition of the selected investigated thermal waters. b.d.l = below detection limit.	91
Table 4-4: Temperature (°C) obtained with selected geothermometers and pCO ₂ (atm) obtained with Chiodini (1995)'s geobarometer.	94

Chapter 5

Table 5-1: Physicochemical measurements of investigated water samples.	124
Table 5-2: Temperature (°C), pH, and hydrochemistry (mmol/L) of investigated samples ..	125
Table 5-3: Saturation indices (SI) of the main mineral phases of interest in the investigated area. SI were calculated with the PHREEQC code, at the outlet conditions, with the phreeqc database and the pitzer database for SM and SM2 samples. The SI with respect to alumino-silicate were all calculated with the phreeqc database due to missing Al concentrations in the pitzer database.	130
Table 5-4: Physical-chemical parameters and hydrochemistry (mmol/L) for the MNA and SFC springs.	144